

**A SEARCH FOR LONG-LIVED  
PARTICLES THAT STOP IN THE CMS  
DETECTOR AND DECAY TO MUONS**

by

**Juliette Alimena**

M.Sc. in Physics, Brown University, 2010

B.A. in Physics, University of Pennsylvania, 2008

A DISSERTATION SUBMITTED IN PARTIAL FULFILLMENT OF THE REQUIREMENTS

FOR

THE DEGREE OF DOCTOR OF PHILOSOPHY

IN THE DEPARTMENT OF PHYSICS AT BROWN UNIVERSITY

Providence, Rhode Island

May 2016

© Copyright 2016 by Juliette Alimena

This dissertation by Juliette Alimena is accepted in its present form by  
the Department of Physics as satisfying the  
dissertation requirement for the degree of  
Doctor of Philosophy

Date .....  
David Cutts, Advisor

Recommended to the Graduate Council

Date .....  
Meenakshi Narain, Reader

Date .....  
JiJi Fan, Reader

Approved by the Graduate Council

Date .....  
Peter M. Weber  
Dean of the Graduate School

# Juliette Alimena

Physics Department                      juliette.alimena@cern.ch                      203-362-7287 (cell)  
Barus and Holley Building  
Brown University  
182 Hope Street  
Providence, RI 02906

## Education

**Brown University**, Providence, RI

Candidate for Doctor of Philosophy in Physics, Expected May 2016

Thesis: “A Search for Delayed Muons in the CMS Experiment”

Advisor: Prof. David Cutts

Master of Science in Physics, May 2010

**University of Pennsylvania**, College of Arts and Sciences, Philadelphia, PA

Bachelor of Arts in Physics with Honors, Math and English Minors, *cum laude*, May 2008

## Awards

**CMS Achievement Award**, December 2012

For “implementation of triggers for long-lived particles and outstanding contributions to the High Level



Trigger (HLT) code and trigger menu integration.”

## Selected Publications

D0 Collaboration, “Search for charged massive long-lived particles at  $\sqrt{s} = 1.96$  TeV”, *Phys. Rev. D* **87** (2013) 052011.

D0 Collaboration, “Search for charged massive long-lived particles”, *Phys. Rev. Lett.* **108** (2012) 121802.

## Research Experience

**Physics Research Assistantship**, Brown University, September 2009 – present

Primary analyst for long-lived exotica searches:

**Search for Delayed Muons**, Run I data, CMS Experiment, January 2012 – present

Performed a search for long-lived particles predicted by theories beyond the Standard Model, which stop

in the detector material and decay to delayed and displaced muons

Created and maintained an analysis-specific trigger for the 2012 run

Developed a new muon reconstruction for highly displaced muons, for offline and HLT

**Search for Charged Massive Long-Lived Particles**, Run II data, D0 Experiment, May 2009 – March 2013

Performed a search for long-lived particles with long time-of-flight and large ionization energy loss ( $dE/dx$ )

Detector experience:

**Trigger Convener**, CMS Exotica, March 2011 – December 2014

Supervised the exotica analysts when developing their triggers within the operational limits of the HLT

**Member of STORM**, CMS Trigger Studies Group, March 2011 – December 2014

Co-led integration all the HLT paths into the trigger menus for the 2011, 2012, and 2015 runs

## Research Details

### Compact Muon Solenoid (CMS) Experiment

#### Analysis: **Search for Delayed Muons**

We search for long-lived exotic particles, which arise in many theories beyond the Standard Model, that are stopped in the detector material and decay to muons sometime after the bunch crossing. If a new particle were sufficiently massive, slow-moving, and long-lived, it could traverse part of the detector and stop somewhere in the material and then decay between nanoseconds and days later. Using Run I data, we search for long-lived particles, which have been stopped somewhere between the inner tracker and the muon system and which decay to muons. We require these delayed muons to be out-of-time with respect to the bunch crossing, and they would typically not point back to the primary vertex. For this search, I created and maintained a new analysis-specific trigger that was implemented in the CMS collisions trigger menu for the entire 2012 run. I also developed a new muon reconstruction for highly displaced muons using only the muon system, which has been incorporated into the CMS software and used by other long-lived exotica searches involving muons. I then implemented an online version of this new reconstruction for the delayed muons triggers, which will be used in the HLT in 2015. I have also developed algorithms to measure the time-of-flight of the muons, which can help distinguish the primary background, cosmic ray muons, from the signal. Furthermore, I have customized

the Monte Carlo (MC) for this search, generating stopped long-lived particles that decay to muons, using MC simulations of long-lived particles as input. I doubled the stopping efficiency of the benchmark model with several simulation improvements. I have developed the event selection, estimated the background, and will obtain the results for this search.

### Detector Experience: **Trigger Studies Group**

The CMS High Level Trigger (HLT) performs the final online selection of events that are recorded for physics analyses. Within the HLT Trigger Studies Group (TSG), I had three separate tasks:

I was a Trigger Convener for the Exotica Physics Analysis Group, primarily working with the Long-Lived Particle Sub-Group. This task involves communicating between the long-lived exotica trigger developers and the TSG, to ensure that the physics analysis requirements are met within the operational limits. I worked with the analysts to develop and maintain their trigger paths for the 2012 and 2015 runs.

For my work within the HLT Software, Tools, Online Releases and Menus (STORM) group, I integrated trigger paths into the master HLT trigger menu and then validated this menu. The two conveners of STORM and I integrated all the changes to the HLT menu, which consists of approximately 400 trigger paths and goes through about five major and 25 minor revisions per year. I did this task for the HLT menus in 2011, 2012, and in preparation for the 2015 run. This task involves maintaining an intimate knowledge of the current state of the HLT trigger paths and of confDB, the tool used to work on the HLT configuration database.

I designed code that I used to study and monitor any differences between online and offline HLT results. In general, whether or not an event passed a trigger path (the HLT results) should be reproducible offline, but various differences in online and offline code and release conditions occasionally produce discrepancies that need to be studied.

In addition to my trigger tasks, I also took about 20 online trigger shifts in the Point 5 control room during the 2012 run.

## **DØ Experiment**

### Analysis: **Search for Charged Massive Long-Lived Particles**

We performed a search for charged massive long-lived particles (CMLLPs), using Run II data collected with the D0 detector. We searched for events in which one or more particles are reconstructed as muons but have speed and ionization energy loss ( $dE/dx$ ) inconsistent with muons produced in beam collisions. I developed data corrections and Monte Carlo (MC) smearing for our key variables, studied and applied event selection criteria, and modeled the background with a data-driven technique. I used a multivariate technique known as Boosted Decision Trees (BDTs) to further separate the signal from background, studied the systematic uncertainties, and obtained confidence levels (CLs) cross-section limits for our different signal models. This work was published in PRL, with a longer article in PRD. The latter describes this analysis, an analysis our group performed in parallel for a pair of CMLLPs, and an earlier version of this analysis, in more detail.

## **Presentations and Posters**

**Brown Astrophysics Seminar Series**, “Search for Stopped Particles from Decays to Delayed Muons”, October 2015.

**Large Hadron Collider Physics Conference**, Columbia University, “Performance of Muon-Based Triggers at the CMS High Level Trigger”, June 2014.

**Division of Particles and Fields Conference**, American Physical Society, "A Search for Single Charged Massive Long-Lived Particles at the Fermilab Tevatron", August 2011.

**April Meeting**, American Physical Society, "A Search for Single Charged Massive

Long-Lived Particles at the Fermilab Tevatron", May 2011.

**Brown Astrophysics Journal Club**, "A Search for Charged Massive Long-Lived Particles at D0", April 2011.

## Teaching Experience

**Physics Teaching Assistantship**, Brown University, September 2008 – December 2009

TA for undergraduate introductory physics labs for physics and engineering concentrators (Phys 0050/0070,

Fall 2008; Phys 0160, Spring 2009)

TA for undergraduate introductory physics drop-in sections (Phys 0030, Fall 2009)

## Additional Training and Skills

Fermilab-CERN Hadron Collider Physics Summer School, August 2012.

Knowledge of ROOT, C++, Python, UNIX shell, L<sup>A</sup>T<sub>E</sub>X, Maple, Mathematica.

Conversational French.

# Preface and Acknowledgments

There have been many people who have helped me with this thesis work and getting to this point in my career. I'm sure I've forgotten someone, and for that, I'm very sorry.

I would first like to thank Dave Cutts, who has tirelessly advised me all these years. Your constant support and guidance really got me through. I would also like to thank the other professors in our group, Ulrich Heintz, Greg Landsberg, and Meenakshi Narain, as they have also helped me with various physics and non-physics things over the years. Thanks also to Meenakshi and JiJi Fan for being my thesis readers. Sorry it turned out so long!

There have been a lot of postdocs at Brown over the years, and I relied on all of their help at some point: Alexey Ferapontov, Thomas Speer, Gena Kukarzev, Grant Christopher, John Paul Chou, Ted Laird, Josh Swanson, and Edmund Berry.

I also have to thank all of the Brown graduate students in the group: Saptaparna Bhattacharya, Zeynep Demiragli, Alex Garabedian, Mary Hadley, Mike Luk, Zaixing Mao, Sinan Sagir, Mike Segala, Tutanon Sinthuprasith (201 lab partners 4 life!), Steve Sirisky, Dave Tersegno, Rizki Syarif, and Yunhe Xie. Yunhe got me started on the new version of her thesis analysis, so I have to thank her for explaining lots of D0 code and helping me understand long-lived particles. The Mikes were like my little brothers: annoying, but you wouldn't trade them just the same. Plus, they might know something about physics. Mary Hadley had the patience to actually read all

of this thesis and make very helpful suggestions, for which I am eternally grateful. There's also a lot of grad students in other fields who were also supportive - thank you all!

There are also several people in CMS that I need to thank. There were many people in the TSG who made my time with them productive yet enjoyable: Andrea Bocci, Tulika Bose, Roberto Carlin, and Wesley Smith. Wesley, Roberto, and also Juan Alcaraz wrote me recommendation letters, and I'd like to thank them for that. Ted Kolberg, Loic Quertenmont, and Wells Wulsin from the Long-Lived Exotica group gave me a lot of guidance for the analysis. Carlo Battilana and Daniele Trocino from the Muon POG helped me so much with the muon reconstruction. In addition to all these people, there were many others at CMS who gave me feedback or commiserated with me - I value it all.

Thanks to the D0 CMLLP crew (those who aren't mentioned elsewhere): Sudeshna Banerjee, Sungwoong Cho, and Mike Eads. I learned a lot with you all (see the Appendix) and it was fun, too!

There have also been a number of friends who have provided moral support over the years. The ones who have continued to stick (not sure why or how they put up with me) are: Melissa King, Samantha Rosenberg, and Julie Verespej.

Thanks to the unwavering love and support from my family.

[REDACTED]

My extended family has always also been supportive, and I'm very grateful for that.

I'd also like to thank any random reader (or more likely, the graduate student

or undergraduate who will do the next version of this analysis with more data and better tools) who picks up this thesis and finds they are curious about long-lived exotic particles. I hope you can learn something from the way I've organized my thoughts on all the particle physics I know.



# Contents

Curriculum Vitae	iv
Preface and Acknowledgments	x
Contents	xiii
List of Tables	xxi
List of Figures	xxiv
<b>1 INTRODUCTION</b>	<b>1</b>
<b>2 THE STANDARD MODEL AND BEYOND</b>	<b>4</b>
2.1 The Standard Model (SM) . . . . .	4
2.1.1 The Particle Content of the SM . . . . .	5
2.1.1.1 Fermions . . . . .	6
2.1.1.2 Bosons . . . . .	7
2.1.1.3 Mass and Gauge Eigenstates . . . . .	9
2.1.2 The Fundamental Forces . . . . .	10
2.1.3 Quantum Electrodynamics (QED) . . . . .	11
2.1.4 Weak Interactions . . . . .	15
2.1.5 Electroweak Unification . . . . .	15
2.1.6 Quantum Chromodynamics (QCD) . . . . .	16

2.1.7	The SM before the Higgs Mechanism . . . . .	17
2.1.8	Spontaneous Symmetry Breaking . . . . .	19
2.1.8.1	Discrete Spontaneous Symmetry Breaking . . . . .	19
2.1.8.2	Continuous Spontaneous Symmetry Breaking . . . . .	20
2.1.8.3	The Higgs Mechanism in an Abelian Theory . . . . .	23
2.1.8.4	The Higgs Mechanism in the the Electroweak Sector of the SM . . . . .	24
2.1.9	Measurements of the SM . . . . .	31
2.1.10	Summary of the Fundamental Forces . . . . .	33
2.2	Why the SM is Incomplete . . . . .	34
2.2.1	Unexplained Phenomena . . . . .	34
2.2.1.1	Gravity . . . . .	34
2.2.1.2	Neutrino Oscillations . . . . .	34
2.2.1.3	Dark Matter and Dark Energy . . . . .	35
2.2.1.4	The Baryon-Antibaryon Asymmetry . . . . .	36
2.2.2	Theoretical Problems . . . . .	37
2.2.2.1	Arbitrary Assumptions and Parameters . . . . .	37
2.2.2.2	The Hierarchy Problem, Naturalness, and Fine Tuning	37
2.2.2.3	Strong CP Problem . . . . .	39
2.3	Theories Beyond the SM . . . . .	40
2.3.1	Supersymmetry (SUSY) . . . . .	40
2.3.1.1	SUSY Breaking . . . . .	43
2.3.2	Extra Dimensions . . . . .	43
2.3.2.1	Kaluza-Klein Theories . . . . .	44
2.3.2.2	Large Extra Dimensions . . . . .	44
2.3.2.3	Warped Extra Dimensions . . . . .	45
2.3.3	New Strong Dynamics and Little Higgs . . . . .	45

2.3.4	Hidden Valley Theories . . . . .	46
2.3.5	Grand Unified Theories and Theories of Everything . . . . .	47
<b>3</b>	<b>THE COMPACT MUON SOLENOID EXPERIMENT AT THE LARGE HADRON COLLIDER</b>	<b>49</b>
3.1	The Large Hadron Collider (LHC) . . . . .	49
3.1.1	The Proton Acceleration . . . . .	52
3.1.2	Luminosity, Vertices, and Pileup . . . . .	54
3.1.3	Data-Taking at the LHC . . . . .	57
3.2	The Compact Muon Solenoid Experiment (CMS) . . . . .	58
3.2.1	Particle Interactions in Matter . . . . .	60
3.2.2	The Coordinate System . . . . .	66
3.2.3	The Superconducting Magnet . . . . .	67
3.2.4	The Inner Tracker . . . . .	68
3.2.4.1	The Pixel Detector . . . . .	69
3.2.4.2	The Silicon Strip Tracker . . . . .	70
3.2.5	The Electromagnetic Calorimeter (ECAL) . . . . .	71
3.2.5.1	The ECAL Barrel . . . . .	73
3.2.5.2	The ECAL Endcaps . . . . .	74
3.2.5.3	The ECAL Preshower Detector . . . . .	74
3.2.6	The Hadronic Calorimeter (HCAL) . . . . .	74
3.2.6.1	The HCAL Barrel . . . . .	76
3.2.6.2	The HCAL Endcaps . . . . .	77
3.2.6.3	The HCAL Outer Calorimeter . . . . .	77
3.2.6.4	The HCAL Forward Calorimeter . . . . .	77
3.2.7	The Muon System . . . . .	78
3.2.7.1	The Drift Tubes . . . . .	80
3.2.7.2	The Cathode Strip Chambers . . . . .	81

3.2.7.3	The Resistive Plate Chambers . . . . .	82
3.2.8	The Trigger and Data Acquisition . . . . .	83
3.2.8.1	Level 1 Trigger . . . . .	84
3.2.8.2	High Level Trigger . . . . .	86
3.2.8.3	Data Acquisition . . . . .	88
3.2.9	The Detector Infrastructures . . . . .	89
3.2.9.1	Detector Powering . . . . .	89
3.2.9.2	Detector Cooling . . . . .	90
3.2.9.3	Detector Cabling . . . . .	91
3.2.9.4	Detector Safety System (DSS) . . . . .	91
3.2.9.5	Beam and Radiation Monitoring (BRM) Systems . .	92
3.2.10	Computing . . . . .	94
3.2.10.1	MC Event Simulation . . . . .	95
3.2.10.2	Data Formats and Distribution . . . . .	96
3.2.10.3	Calibration and Alignment . . . . .	98
3.2.10.4	Data Quality Monitoring and Certification . . . . .	98
3.2.11	The Event and Object Reconstruction . . . . .	99
3.2.11.1	Particle Flow Algorithm . . . . .	101
3.2.11.2	Muons . . . . .	104
3.2.11.3	Electrons and Photons . . . . .	106
3.2.11.4	Jets . . . . .	107
3.2.11.5	Taus . . . . .	108
3.2.11.6	Missing Transverse Energy . . . . .	109
<b>4</b>	<b>EXOTIC LONG-LIVED PARTICLES</b>	<b>111</b>
4.1	Motivation for LLP Searches . . . . .	112
4.2	Theoretical Models Predicting LLPs . . . . .	113
4.2.1	Minimal Supersymmetry . . . . .	113

4.2.2	Gauge Mediated Supersymmetry Breaking . . . . .	114
4.2.3	Anomaly Mediated Supersymmetry Breaking . . . . .	116
4.2.4	Split Supersymmetry . . . . .	117
4.2.5	$R$ -Parity Violating Supersymmetry . . . . .	117
4.2.6	Models with Multiply or Fractionally Charged Particles . . .	118
4.2.7	Supersymmetric Left-Right Model . . . . .	118
4.2.8	Hidden Valley Models . . . . .	119
4.2.9	Untracked Signals of SUSY . . . . .	119
4.2.10	Magnetic Monopoles . . . . .	120
4.3	LLP Interactions in Matter . . . . .	121
4.3.1	Ionization of Electrically and Magnetically Charged LLPs . .	121
4.3.2	Hadronization of LLPs . . . . .	123
4.4	Detector Signatures of LLPs . . . . .	124
4.4.1	Signature of Particles that Pass Through the Detector . . . .	124
4.4.2	Signature of Particles that Decay in the Detector . . . . .	128
4.4.3	Signature of Particles that Stop in the Detector . . . . .	130
4.4.4	Signature of Monopoles . . . . .	132
4.5	Previous and Present Searches for LLPs . . . . .	133
4.5.1	Previous and Present Searches for CMLLPs . . . . .	134
4.5.2	Previous and Present Searches for Displaced Vertices . . . . .	134
4.5.3	Previous and Present Searches for Weird Tracks . . . . .	136
4.5.4	Previous and Present Searches for Stopped Particles . . . . .	137
4.5.5	Previous and Present Searches for Monopoles . . . . .	137
<b>5</b>	<b>A SEARCH FOR DELAYED MUONS</b>	<b>139</b>
5.1	Introduction and Motivation . . . . .	139
5.2	Data and Monte Carlo Samples . . . . .	141
5.2.1	Trigger . . . . .	141

5.2.2	Data Samples . . . . .	145
5.2.2.1	Search Sample . . . . .	145
5.2.2.2	Cosmic Muon Background Sample . . . . .	149
5.2.3	Signal Samples . . . . .	149
5.2.3.1	Models . . . . .	149
5.2.3.2	Signal Generation . . . . .	150
5.2.3.3	Stopping Probability . . . . .	155
5.2.3.4	Event Weight for Doubly Charged Higgs . . . . .	159
5.2.4	Cosmic Muon MC Simulation Sample . . . . .	164
5.3	Analysis Strategy and Techniques . . . . .	164
5.3.1	Displaced Standalone Muon $p_T$ . . . . .	164
5.3.2	DT Time of Flight . . . . .	169
5.3.3	RPC BX Assignments . . . . .	172
5.4	Event Selection . . . . .	174
5.4.1	Trigger and Reconstruction Efficiency . . . . .	174
5.4.2	Preselection Criteria . . . . .	175
5.4.3	Signal and Background Comparison . . . . .	176
5.4.4	Cosmic Muon TOF . . . . .	183
5.4.5	Final Selection Criteria . . . . .	187
5.5	Background Modeling . . . . .	191
5.5.1	ABCD Method . . . . .	191
5.5.2	Choice of Momentum Variable for Background Estimation . . . . .	192
5.5.3	Choice of $\beta_{Free}^{-1}$ and $p$ Cuts . . . . .	194
5.5.4	Background Closure Test . . . . .	196
5.5.5	Background Estimation . . . . .	197
5.5.6	Other Backgrounds . . . . .	198
5.6	Systematic Uncertainties . . . . .	200

5.7	Results	203
5.8	Results with at Least One Upper Hemisphere DSA Track	211
5.9	Preparation for 13 TeV	217
<b>6</b>	<b>SUMMARY</b>	<b>224</b>
<b>A</b>	<b>A SEARCH FOR CHARGED MASSIVE LONG-LIVED PARTICLES AT D0</b>	<b>225</b>
A.1	Motivation and Signal Samples	226
A.1.1	Motivation and Models	226
A.1.2	Signal Generation	228
A.1.3	Detection of Top Squarks	228
A.2	The D0 Experiment at the Tevatron Collider	231
A.2.1	The Tevatron and the D0 Detector	231
A.2.2	The Central Tracker	233
A.2.3	The Calorimeter	235
A.2.4	The Muon System	235
A.2.5	The Trigger	237
A.3	Analysis Strategy and Techniques	239
A.3.1	Time-of-Flight Measurement	239
A.3.2	$dE/dx$ Measurement	243
A.4	Event Selection	246
A.5	Background Estimation	255
A.5.1	Background Normalization	256
A.5.2	Differences in Kinematic Distributions and Additional Event Weight	256
A.6	Analysis Method	258
A.7	Systematic Uncertainties	266

A.7.1	Flat Systematic Uncertainties . . . . .	267
A.7.2	Shape Systematic Uncertainties . . . . .	269
A.8	Results . . . . .	271
<b>Bibliography</b>		<b>278</b>



# List of Tables

2.1	The SM fermions and their fields. . . . .	9
2.2	The SM gauge fields. . . . .	9
2.3	The SM scalar field for the Higgs boson. . . . .	10
2.4	The SM particles and their superpartners. . . . .	41
2.5	The superpartner mixing states. . . . .	42
3.1	The variables used in the definition of instantaneous luminosity. . . . .	55
3.2	The variables used in the Bethe formula. . . . .	61
3.3	Power requirements for CMS. . . . .	90
3.4	Cooling power for each CMS subsystem. . . . .	90
3.5	The BRM systems in CMS. . . . .	92
4.1	The chiral supermultiplets in the MSSM. . . . .	114
4.2	The gauge supermultiplets in the MSSM. . . . .	114
4.3	The variables used in the modified Bethe formula for monopoles. . . . .	122
5.1	Delayed muon triggers at the end of 2012. . . . .	142
5.2	RECO data samples. . . . .	146
5.3	RECO data samples. . . . .	146
5.4	The trigger livetime fraction for each of the LHC filling schemes used in 2012.. . . .	148
5.5	Stage 1 GEN-SIM signal samples. . . . .	152

5.6	Stage 2 signal samples. . . . .	153
5.7	Stage 2 RECO signal samples. . . . .	153
5.8	Cumulative selection cut efficiencies for collision data and cosmic muon data events. . . . .	189
5.9	Cumulative selection cut efficiencies (fraction of events) for 100 GeV, 500 GeV, and 1000 GeV mchamps. . . . .	190
5.10	Number of events in each region in Figure 5.43 for cosmic muon data.	197
5.11	Systematic uncertainties. . . . .	203
5.12	Signal acceptance, number of expected background events, and number of observed events for each mchamp mass. . . . .	205
5.13	Counting experiment results for different lifetimes, for 100, 500, and 1000 GeV mchamps. . . . .	208
5.14	LO cross sections and cross section limits for mchamps with a lifetime of 1 sec. . . . .	210
5.15	Cumulative selection cut efficiencies for the one upper hemisphere DSA track selection, for collision data and cosmic muon data events. . . . .	212
5.16	Cumulative selection cut efficiencies (fraction of events) for the one upper hemisphere DSA track selection, for 100 GeV, 500 GeV, and 1000 GeV mchamps. . . . .	213
5.17	Signal acceptance, number of expected background events, and number of observed events for the one upper hemisphere DSA track selection, for each mchamp mass. . . . .	215
5.18	LO cross-sections and cross-section limits for the one upper hemisphere DSA track selection, for mchamps with a lifetime of 1 sec. . . . .	216
5.19	Relative improvement for each change at L1 and HLT. . . . .	221
5.20	Delayed muon triggers for 2015. . . . .	222
A.1	The measured muon scintillator timing resolutions. . . . .	241

A.2	The muon scintillator readout and trigger gates. . . . .	241
A.3	Selection cut efficiencies for data events. . . . .	251
A.4	Selection cut efficiencies for stau MC events. . . . .	252
A.5	Selection cut efficiencies for top squark MC events. . . . .	253
A.6	Selection cut efficiencies for gaugino-like chargino MC events. . . . .	254
A.7	Selection cut efficiencies for higgsino-like chargino MC events. . . . .	255
A.8	Summary of systematic uncertainties. . . . .	271
A.9	Expected event table for staus. . . . .	271
A.10	Expected event table for top squarks. . . . .	272
A.11	Expected event table for gaugino-like charginos. . . . .	272
A.12	Expected event table for higgsino-like charginos. . . . .	272
A.13	NLO cross-sections and cross-section limits for staus. . . . .	275
A.14	NLO cross-sections and cross-section limits for top squarks. . . . .	275
A.15	NLO cross-sections and cross-section limits for gaugino-like charginos. . . . .	275
A.16	NLO cross-sections and cross-section limits for higgsino-like charginos. . . . .	275
A.17	Acceptance times cross-section for 100 GeV staus: pair produced and cascade decays. . . . .	277

# List of Figures

2.1	The standard model fundamental particles. . . . .	5
2.2	The particles of the SM and their interactions. . . . .	12
2.3	The interactions of the SM. . . . .	13
2.4	Feynman diagrams of the basic QED processes. . . . .	14
2.5	Graph of $V(\phi)$ for the Lagrangian in equation (2.9). . . . .	20
2.6	Graph of $V(\phi_1, \phi_2)$ for the Lagrangian in equation 2.11. . . . .	21
2.7	The Higgs boson self-interactions and couplings to the gauge bosons and fermions. . . . .	31
2.8	Differences between the SM prediction and the measured parameter. .	32
2.9	Coupling constants as a function of energy scale in the SM and the MSSM. . . . .	33
2.10	Percentages of types of matter in the universe. . . . .	35
2.11	One-loop quantum corrections to the Higgs squared mass, due to (a) a fermion and (b) a scalar. . . . .	39
3.1	Diagram of the LHC. . . . .	51
3.2	Diagram of an LHC dipole. . . . .	52
3.3	Diagram of the CERN accelerator complex. . . . .	53
3.4	Diagram of the LHC bunch filling scheme, at 25 ns and with 3564 total bunches (2808 colliding). . . . .	54

3.5	Diagram of a $pp$ collision at the LHC. . . . .	56
3.6	Event display of a collision in CMS, showing 29 distinct pileup vertices. . . . .	56
3.7	Distribution of the average pileup in CMS in 2012. . . . .	57
3.8	The delivered integrated luminosity at CMS for $pp$ collisions in 2010-2012. . . . .	58
3.9	Diagram of the CMS detector. . . . .	59
3.10	Photograph of the CMS detector. . . . .	60
3.11	Stopping power for muons in copper. . . . .	63
3.12	Fractional energy loss per radiation length for electrons in lead. . . . .	64
3.13	Photon cross sections as a function of energy in carbon and lead. . . . .	65
3.14	Probability that a photon interaction will result in conversion to an $e^+e^-$ pair. . . . .	66
3.15	Ratio of stored energy to cold mass for major detector solenoids. . . . .	68
3.16	Diagram of the CMS inner tracker. . . . .	69
3.17	Diagram of the CMS pixel detector. . . . .	70
3.18	Photograph of the CMS silicon strip tracker. . . . .	71
3.19	Diagram of the CMS electromagnetic calorimeter. . . . .	72
3.20	Photograph of the CMS hadronic calorimeter. . . . .	75
3.21	Diagram of the CMS barrel muon system. . . . .	78
3.22	Diagram of the subdetectors of the CMS muon system. . . . .	79
3.23	Diagram of a drift tube cell. . . . .	81
3.24	Diagram of a cathode strip chamber. . . . .	82
3.25	Diagram of the barrel resistive plate chambers. . . . .	83
3.26	Diagram of the L1 trigger architecture. . . . .	85
3.27	Diagram of the DAQ architecture. . . . .	89
3.28	YB+2 and YE+1 cable-chains in the UXC55 basement trenches. . . . .	91
3.29	WLCG sites. . . . .	97
3.30	Diagram of the Grid hierarchy. . . . .	97

3.31	Diagram of how different particles appear in the CMS detector. . . .	100
3.32	The muon $p_T$ resolution as a function of the $p_T$ . . . . .	105
4.1	Stopping power and ratio of range to mass for Dirac monopoles in aluminum. . . . .	123
4.2	Diagram of the behavior of different particles in general-purpose par- ticle experiments. . . . .	125
4.3	Generator level speed distribution for CMLLPs. . . . .	126
4.4	Stopping power for muons in copper. . . . .	127
4.5	The distribution of $dE/dx$ as a function of $p$ . . . . .	128
4.6	Illustration of the experimental signature of a stopped LLP. . . . .	130
4.7	Diagram of the SQUID apparatus used by the H1 experiment. . . . .	133
5.1	The WBM plots showing the trigger rate for L1_SingleMu6_NotBptxOR (top) and HLT_L2Mu20_NoVertex_2Cha_NoBPTX3BX_NoHalo (middle) and the instantaneous luminosity (bottom) during run 208307. . . . .	143
5.2	The trigger rate for HLT_L2Mu20_NoVertex_2Cha_NoBPTX3BX_NoHalo and the instantaneous luminosity at the start of a fill as a function of the number of colliding bunches. . . . .	144
5.3	Turn-on curve for HLT_L2Mu20_NoVertex_2Cha_NoBPTX3BX_NoHalo.	145
5.4	Diagram of the LHC bunch filling scheme, at 25 ns and with 3564 total bunches (2808 colliding). . . . .	147
5.5	BX distribution for events passing HLT_L2Mu20_NoVertex_2Cha_NoBPTX3BX_NoHalo during collision data in Run2012D. . . . .	148
5.6	The fraction of stopped particle decays per mchamp pair production, as a function of mchamp mass. . . . .	156

5.7	The stopping efficiency as a function of mass for each of the possible signal samples. . . . .	157
5.8	Stopping positions for 500 GeV mchamps. . . . .	158
5.9	Fraction of events that stop in each detector region, for one mass point for all signal samples. . . . .	159
5.10	Distributions of $p_T$ , $\eta$ , and $\phi$ at the generator level for the positively charged 500 GeV mchamps and the positively charged 500 GeV doubly charged Higgs. . . . .	160
5.11	Distributions of $p_T$ , $\eta$ , and $\phi$ at the generator level for the negatively charged 500 GeV mchamps and the negatively charged 500 GeV doubly charged Higgs. . . . .	161
5.12	Distributions of the positively charged versus the negatively charged 500 GeV mchamps $p_T$ (left) and of the positively charged versus negatively charged 500 GeV doubly charged Higgs $p_T$ (right), at the generator level. . . . .	161
5.13	Distributions of $p_T$ , $\eta$ , and $\phi$ at the generator level for the positively charged 500 GeV mchamps and the positively charged 500 GeV doubly charged Higgs, after the reweighting. . . . .	162
5.14	Distributions of $p_T$ , $\eta$ , and $\phi$ at the generator level for the negatively charged 500 GeV mchamps and the negatively charged 500 GeV doubly charged Higgs, after the reweighting. . . . .	163
5.15	Distributions of the positively charged versus the negatively charged 500 GeV mchamps $p_T$ (left) and of the positively charged versus negatively charged 500 GeV doubly charged Higgs $p_T$ (right), at the generator level, after the reweighting. . . . .	163
5.16	DSA muon $p_T$ for 500 GeV mchamps, $Z \rightarrow \mu\mu$ data, cosmic muon MC simulation, and cosmic muon data. . . . .	165

5.17	Generator muon $p_T$ distribution for mchamps with masses of 100 GeV, 500 GeV, and 1000 GeV. . . . .	166
5.18	Reconstructed muon $p_T$ distribution in 53X for mchamps with masses of 100 GeV, 200 GeV, 300GeV, 500 GeV, and 1000 GeV. SA muon $p_T$ (left) and RSA muon $p_T$ (right). . . . .	166
5.19	SA muon $p_T$ distribution in 53X and 72X for mchamps with a mass of 500 GeV, which predominantly decay to two generator muons with a $p_T$ of 250 GeV each. The black histogram shows the default SA muon $p_T$ distribution in 53X, and the blue histogram shows the DSA muon $p_T$ , as reconstructed in CMSSW_7_2_0_pre6. The blue histogram is the final version of the $p_T$ distribution, whereas the red histogram shows an intermediate step, before the reconstruction was finalized. . .	167
5.20	$p_T$ resolution and charge divided by $p_T$ resolution for different muon reconstruction algorithms, for prompt and displaced muon samples. . .	168
5.21	A diagram showing the direction and thus, the sign of $\beta^{-1}$ , of muons coming from signal and background. . . . .	170
5.22	DSA track $\beta_{Free}^{-1}$ for 500 GeV mchamps, $Z \rightarrow \mu\mu$ data, cosmic muon MC simulation, and cosmic muon data. . . . .	171
5.23	The $\beta_{Free}^{-1}$ distribution for 500 GeV mchamps and cosmic muon data, plotting the upper and lower hemisphere muons separately. . . . .	171
5.24	A diagram showing the RPC BX assignments of muons coming from signal (left) and cosmic muon background (right). . . . .	172
5.25	DSA muon RPC BX pattern for 500 GeV mchamps, $Z \rightarrow \mu\mu$ data, cosmic muon MC simulation, and cosmic muon data. . . . .	173
5.26	The RPC BX pattern for 500 GeV mchamps and cosmic muon data, plotting the upper and lower hemisphere muons separately. . . . .	173



5.27	The trigger efficiency (left) and the reconstruction efficiency (right) as a function of mchamp mass. . . . .	174
5.28	DSA track kinematics for 500 GeV mchamps, $Z \rightarrow \mu\mu$ data, cosmic muon MC simulation, and cosmic muon data. . . . .	177
5.29	DSA muon track quality distributions for 500 GeV mchamps, $Z \rightarrow \mu\mu$ data, cosmic muon MC simulation, and cosmic muon data. . . . .	178
5.30	DSA muon track timing variables for 500 GeV mchamps, $Z \rightarrow \mu\mu$ data, cosmic muon MC simulation, and cosmic muon data. . . . .	179
5.31	The TimeInOut distribution for 500 GeV mchamps (top left), $Z \rightarrow \mu\mu$ data (bottom left), cosmic muon data (top right), and cosmic muon MC simulation (bottom right). . . . .	181
5.32	The $\beta_{Free}^{-1}$ distribution for 500 GeV mchamps (top left), $Z \rightarrow \mu\mu$ data (bottom left), cosmic muon data (top right), and cosmic muon MC simulation (bottom right). . . . .	182
5.33	The RPC BX pattern for 500 GeV mchamps (top left), $Z \rightarrow \mu\mu$ data (bottom left), cosmic muon data (top right), and cosmic muon MC simulation (bottom right). . . . .	183
5.34	A scatter plot of the TimeInOut distribution for the lower hemisphere muon as a function of that of the upper hemisphere muon, for cosmic muon data. . . . .	185
5.35	A scatter plot of $\beta_{Free}^{-1}$ as a function of TimeInOut for cosmic muon data in the upper hemisphere (left) and in the lower hemisphere (right). . . . .	186
5.36	DSA muon track timing variables for cosmic muon data and collision data passing the prescaled control trigger. . . . .	187
5.37	Schematic of the ABCD regions for the background estimation. . . . .	192

5.38	$S/\sqrt{(S+B)}$ as a function of the upper hemisphere $p$ (top left), the average $p$ (top right), and the highest $p$ (bottom), for three mchamp masses. . . . .	193
5.39	$S/\sqrt{(S+B)}$ as a function of the upper hemisphere $p_T$ (top left), the average $p_T$ (top right), and the highest $p_T$ (bottom), for three mchamp masses. . . . .	194
5.40	DSA track free $\beta^{-1}$ (left) and $p$ (right) for 100, 500, and 1000 GeV mchamps. . . . .	195
5.41	$S/\sqrt{(S+B)}$ as a function of $\beta_{Free}^{-1}$ for three mchamp masses. . . . .	195
5.42	$S/\sqrt{(S+B)}$ as a function of $p$ for all mchamp masses. . . . .	196
5.43	A scatter plot of the DSA track $\beta_{Free}^{-1}$ as a function of $p$ for 500 GeV mchamps and cosmic muon data. . . . .	197
5.44	A scatter plot of the DSA track $\beta_{Free}^{-1}$ as a function of $p$ for 500 GeV mchamps and Run2012 collision data. . . . .	198
5.45	A scatter plot of the $\beta_{Free}^{-1}$ distribution for the lower hemisphere muon as a function of that of the upper hemisphere muon for cosmic muon data. . . . .	199
5.46	Number of CSC segments in the event for 500 GeV mchamps, cosmic muon data, cosmic muons from collision events passing the prescaled control trigger, and $Z \rightarrow \mu\mu$ data. . . . .	200
5.47	The DSA track $p_T$ (left) and $\beta_{Free}^{-1}$ (right) for cosmic muon data and cosmic muon MC simulation. . . . .	201
5.48	Turn-on curve for HLT_L2Mu20_NoVertex_2Cha_NoBPTX3BX_NoHalo in data passing the prescaled control trigger and in cosmic MC simulation. . . . .	202
5.49	$p$ and $\beta_{Free}^{-1}$ distributions for Run2012 collision data, background, and 500 GeV mchamps. . . . .	204

5.50	A scatter plot of the DSA track $\beta_{Free}^{-1}$ as a function of $p$ for 500 GeV mchamps and Run2012 collision data. . . . .	204
5.51	Event display of a data event (run 206859, event 704221955) passing all selection criteria, including $p > 200$ GeV and $\beta_{Free}^{-1} > 0.5$ . . . . .	205
5.52	Event display of a data event (run 200245, event 20270933) passing all selection criteria, including $p > 200$ GeV and $\beta_{Free}^{-1} > 0.5$ . . . . .	206
5.53	Event display of a data event (run 199021, event 1349217580) passing all selection criteria, including $p > 200$ GeV and $\beta_{Free}^{-1} > 0.5$ . . . . .	206
5.54	95% CL cross section limits as a function of lifetime, for 100 (top left), 500 (top right), and 1000 (bottom) GeV mchamps. . . . .	209
5.55	95% CL cross section limits as a function of mchamp mass, for a lifetime of 1 sec. . . . .	210
5.56	$p$ and $\beta_{Free}^{-1}$ distributions for the one upper hemisphere DSA track selection, for Run2012 collision data, background, and 500 GeV mchamps. . . . .	214
5.57	A scatter plot of the DSA track $\beta_{Free}^{-1}$ as a function of $p$ for the one upper hemisphere DSA track selection, for 500 GeV mchamps and Run2012 collision data. . . . .	214
5.58	95% CL cross section limits as a function of mchamp mass for a lifetime of 1 sec, for the one upper hemisphere DSA track selection. . . . .	216
5.60	The L2 muon $p_T$ distribution in 72X for mchamps with a mass of 500 GeV. The black histogram shows the default L2 muon $p_T$ distribution, and the red histogram shows the L2 muon $p_T$ distribution with the meantimer and the cosmic muon seeding. . . . .	218
5.59	Acceptance of different cuts applied at the HLT, for data and a 500 GeV mchamp signal at 8 TeV, relative to the control trigger. . . . .	219

5.61	The L1 muon $p_T$ distribution in 72X for mchamps with a mass of 500 GeV. The black histogram shows the events that pass L1_SingleMu6_NotBptxOR, and the red histogram shows the events that pass L1_SingleMuOpen. . . . .	220
5.62	The L2 muon $p_T$ distribution in 72X for mchamps with a mass of 500 GeV. The black histogram shows the default L2 muon $p_T$ distribution, the red histogram shows the L2 muon $p_T$ distribution with L1_SingleMuOpen as the L1 seed, and the blue histogram shows the L2 muon $p_T$ distribution with the meantimer and the cosmic muon seeding and L1_SingleMuOpen as the L1 seed. . . . .	221
5.63	The rate of the signal HLT path in 2012 and 2015, as a function of the number of colliding bunches. . . . .	223
A.1	Diagram of the D0 detector. . . . .	230
A.2	A diagram of the Fermilab Tevatron. . . . .	232
A.3	A picture of the D0 detector. . . . .	233
A.4	A diagram of the D0 central tracking system. . . . .	234
A.5	A diagram of the D0 calorimeter. . . . .	235
A.6	A picture of the D0 muon system. . . . .	236
A.7	The trigger efficiency for staus. . . . .	238
A.8	The speed distribution for data, background, and signal. . . . .	240
A.9	The $dE/dx$ distribution for data, background, and signal. . . . .	244
A.10	Mean $dE/dx$ as a function of delivered integrated luminosity. . . . .	245
A.11	(a) Distribution of the difference between the A-layer and C-layer times for a single muon. (b) Distribution of the absolute value of the difference between the A-layer times of the two muons in the event. . . .	248
A.12	The transverse mass distribution. . . . .	249
A.13	The speed $\chi^2$ distribution. . . . .	250

A.14 The absolute value of the detector $\eta$ distribution for signal-free back-	
ground and signal-free data. . . . .	257
A.15 $\eta$ distribution for background and data, before the new event weight	
(left) and after (right). . . . .	257
A.16 Adjusted $dE/dx$ as a function of $\beta$ . . . . .	258
A.17 Final distributions related to the speed. . . . .	259
A.18 Final distributions related to the $dE/dx$ . . . . .	260
A.19 TMVA correlation matrices. . . . .	261
A.20 TMVA overtraining check. . . . .	261
A.21 Final BDT distributions for stau cases. . . . .	263
A.22 Final BDT distributions for top squark cases. . . . .	264
A.23 Final BDT distributions for gaugino-like chargino cases. . . . .	265
A.24 Final BDT distributions for higgsino-like chargino cases. . . . .	266
A.25 Plots of the L1 timing gate systematic. . . . .	270
A.26 Plots of the timing smearing systematic. . . . .	270
A.27 Event displays for a candidate event (event # 12813686, run # 243293).273	
A.28 Event displays for a candidate event (event # 22550709, run # 247800).274	
A.29 95% CL cross-section limits. . . . .	276

# Chapter 1

## INTRODUCTION

Particle physics describes the fundamental particles that make up the universe and the forces that they feel. Humankind has always wondered about nature at its most basic level, from at least the time of the ancient Greek philosophers. 19<sup>th</sup> century scientists developed atomic theory and the periodic table, and around the turn of the 20<sup>th</sup> century, we discovered that the supposedly “indivisible” atom was in fact composed of smaller particles such as electrons. The discovery of the electron by J.J. Thompson in 1897 really kick-started the field of elementary particle physics. During the 20<sup>th</sup> century, we discovered the other main constituents of atoms: the proton and neutron.

Today, we understand that there are more particles besides protons, neutrons, and electrons; for example, protons and neutrons are made up of smaller particles called quarks. The theory that describes the current understanding of the elementary particles and their interactions is called the Standard Model (SM) of particle physics. The SM has been developed over the past forty years or so, and it has been shown to accurately describe the behavior of elementary particles. Many measurements taken over decades have confirmed the SM predictions and parameter values.

The SM has been experimentally verified to a high level of precision, but it is

incomplete because it fails to incorporate, for instance, gravity, dark matter, or the matter-antimatter asymmetry in the universe. These and other experimental observations are not included in the SM. Furthermore, there are a number of failings of the theory itself, such as the hierarchy problem. As a result, several theories beyond the SM (BSM), such as supersymmetry, extra dimensions, and hidden valley theories, have been proposed over the past few decades. These BSM theories provide theoretical frameworks that bring us closer to explaining everything in our universe in one complete, consistent theory.

The SM and theories beyond it can be tested experimentally at particle colliders such as the Tevatron, outside Chicago, and the Large Hadron Collider (LHC), outside Geneva. The Tevatron was a particle collider at Fermilab, and the two largest experiments there were D0 and the Collider Detector at Fermilab (CDF). The Tevatron is the former highest energy particle collider in the world; that title has now shifted to the LHC at CERN. The two largest experiments at the LHC are the Compact Muon Solenoid (CMS) Experiment and A Toroidal LHC Apparatus (ATLAS). These four experiments use general purpose detectors to search for the Higgs boson, which was the last particle in the SM to be discovered, and new physics beyond the SM.

This thesis describes a search for particles beyond the SM at the CMS Experiment at the LHC. Some theories beyond the SM predict new, long-lived particles. The main analysis described here searches for long-lived particles that decay to muons, which an elementary particle in the SM that is basically a heavy cousin of the electron. The search exploits the experimental signature of the long-lived exotic particles, and the data are examined to determine whether it is consistent with background processes. If the data are not consistent with background, it could indicate new physics; if the data are consistent with background, limits can be placed on BSM theories.

This thesis is organized as follows: Chapter 2 introduces the theoretical background for this study; that is, it describes the SM, the problems with the SM, and

some theories beyond the SM. Chapter 3 describes the experimental apparatus: the LHC and the CMS detector. Chapter 4 provides an introduction to long-lived exotic particles: why we should search for them, the theories beyond the SM that predict them, their detector signature, and previous searches for long-lived particles at colliders. Chapter 5 describes the main analysis, which is the search for delayed muons at CMS, and includes the preparations done for this analysis for Run 2. Chapter 6 summarizes this analysis. Appendix A describes another search for long-lived particles, which was conducted at D0 at the Fermilab Tevatron Collider.



## Chapter 2

# THE STANDARD MODEL AND BEYOND

The Standard Model (SM) of particle physics is a precise theory of elementary particles and their interactions, but it is incomplete for many reasons. For instance, the SM fails to incorporate one of the fundamental forces, gravity. This chapter will first describe the SM in detail, then explain the many reasons why the theory is incomplete, and lastly introduce some theoretical models beyond the SM.

### 2.1 The Standard Model (SM)

The SM of particle physics is a theory of the elementary particles and three forces that govern their interactions: electromagnetism and the strong and weak forces (see Fig. 2.1) [1–5]. The SM, which is defined by a local  $SU(3)_C \times SU(2)_L \times U(1)_Y$  symmetry, is generally considered to be a highly successful theory, as it has precisely predicted the properties of many particles that have been experimentally discovered.

One of the first breakthroughs that led to the SM was the unification of the electromagnetic and weak forces by Sheldon Glashow in 1960, resulting in the so-called electroweak theory. The Higgs Mechanism was proposed in the early 1960's

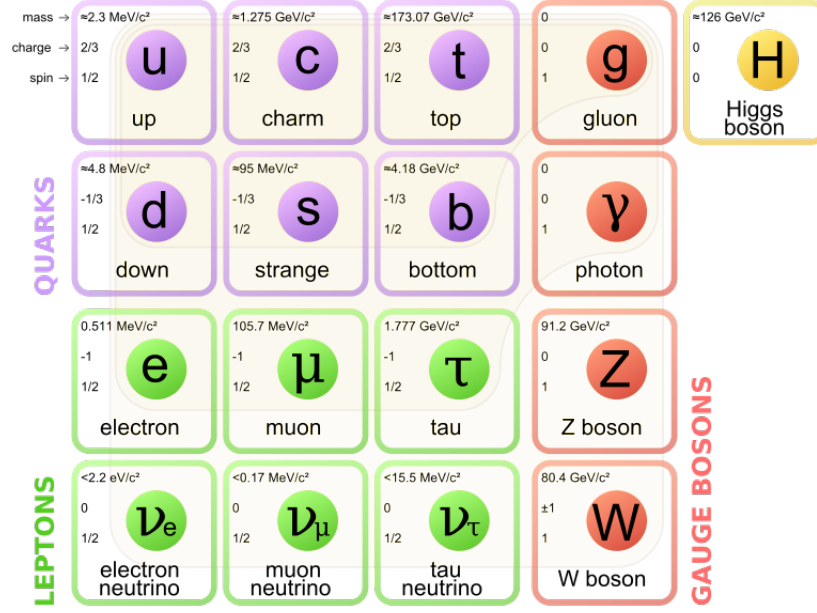


Figure 2.1: The standard model fundamental particles.

by Robert Brout and Francois Englert, independently by Peter Higgs, and by Gerald Guralnik, C. R. Hagen, and Tom Kibble in order to generate the masses of the gauge bosons and the fermions in the SM. The Higgs Mechanism was then incorporated into the electroweak theory in 1967 by Steven Weinberg and Abdus Salam. The full electroweak theory and Quantum Chromodynamics (QCD), which is the theory of the strong force, make up the SM as it is known today.

### 2.1.1 The Particle Content of the SM

There are two main classes of particles in the SM: *fermions* and *bosons*. Fermions, such as protons, neutrons, and electrons, are the particles that make up matter, while bosons are basically the force carriers. Fermions have spins of  $\frac{1}{2}$ , and bosons have spins of 0, 1, and 2. Fermions are further classified into *leptons* and *quarks*; bosons may be the *gauge bosons* or the *Higgs boson*.

There are also composite particles in the SM called *hadrons*, which are made up of quarks. There are two types of hadrons observed in nature: *baryons*, which are

fermionic hadrons, and *mesons*, which are bosonic hadrons.

#### 2.1.1.1 Fermions

Fermions are the SM particles that form matter. They have half-integer spin and obey Fermi-Dirac statistics. Each fermion has an antiparticle, which has the same spin and mass but opposite electric charge. Fermions are organized into three known, successive generations. The mass of the fermions increases with each generation, but the particles in all three generations share the same quantum numbers. Fermions come in two types: leptons and quarks.

**Leptons** The mass eigenstates of the leptons are shown in blue in Fig.2.1. The three leptons with charge -1, given in units of the proton charge, are the electron ( $e^-$ ), the muon ( $\mu^-$ ), and the tau ( $\tau^-$ ). They have corresponding antiparticles with charge +1, denoted  $e^+$  (called the positron),  $\mu^+$ , and  $\tau^+$ . These particles interact electromagnetically, since they are charged, as well as via the weak force. Each of these three leptons has a corresponding neutrino and antineutrino: the electron neutrino ( $\nu_e^-$ ), the muon neutrino ( $\nu_\mu^-$ ), and the tau neutrino ( $\nu_\tau^-$ ). All the neutrinos are electrically neutral and have been measured to have very small but nonzero masses. Since the neutrinos are neutral, they interact only via the weak force, which made them difficult to discover. The electron, electron neutrino, and their antiparticles are in the first generation; the muon, muon neutrino, and their antiparticles are in the second generation; and the tau, tau neutrino, and their antiparticles are in the third generation, for a total of 12 leptons.

**Quarks** The mass eigenstates of the quarks are shown in green in Fig.2.1. Quarks carry fractional charge. The up ( $u$ ), charm ( $c$ ), and top ( $t$ ) quarks have charge  $2/3$ , while the down ( $d$ ), strange ( $s$ ), and bottom ( $b$ ) quarks have charge  $-1/3$ . These six quarks give the six different *flavors* of quarks. Each quark also has a weak hy-

percharge, denoted  $Y$ , and a weak isospin, denoted  $I$ . Thus, quarks interact electromagnetically and via the weak force. The antiparticles of the quarks are  $(\bar{u}, \bar{d})$ ,  $(\bar{c}, \bar{s})$ , and  $(\bar{t}, \bar{b})$ . The up quark, the down quark, and their antiparticles are in the first generation; the charm quark, the strange quark, and their antiparticles are in the second generation; and the top quark, the bottom quark, and their antiparticles are in the third generation.

Quarks also interact via the strong force because, in addition to electric charge, they carry *color* or *color charge*. There are three kinds of color: red, green, and blue. Quarks are bound by *confinement*, which results in quarks only being found in color-neutral composite particles called hadrons. The process by which quarks form hadrons is called *hadronization*. There are two forms of hadrons: baryons and mesons. Baryons are of the form  $qqq$  and anti-baryons are of the form  $\bar{q}\bar{q}\bar{q}$ , where each quark in the baryon or anti-baryon has a different color. Mesons are of the form  $q\bar{q}$ , where the  $q$  will be, for example, blue, and the  $\bar{q}$  will be anti-blue. Baryons are fermionic hadrons because they carry half-integer spin, while mesons are bosonic hadrons because they carry integer spin. Commonly known baryons are the proton ( $p$ ), which has quark content  $uud$  and charge  $+1$ , and the neutron ( $n$ ), which has quark content  $udd$  and charge  $0$ . A commonly known meson is the pion ( $\pi^+$ ), which has quark content  $u\bar{d}$  and charge  $+1$ . As there are six flavors of quarks, every quark has an antiquark, and there are three colors, there are a total of 36 different quarks. Hadronization and confinement are further described in Section 2.1.6.

### 2.1.1.2 Bosons

In addition to fermions, there are also bosons in the SM. Bosons obey Bose-Einstein statistics and have integer spin. The mass eigenstates of the bosons are shown in red in Fig. 2.1.

**Gauge Bosons** The fermions interact with each other by exchanging gauge bosons, which are the force mediators. All of the gauge bosons have spin 1, and each gauge boson mediates a different fundamental force.

The photon ( $\gamma$ ) mediates the electromagnetic force among charged particles. The photon is massless and has no electric charge. See Section 2.1.3 for a description of Quantum Electrodynamics (QED), the quantum theory of electromagnetism.

The  $W^\pm$  and Z bosons mediate the weak force among quarks and leptons. The  $W^\pm$  bosons have charge  $\pm 1$  and a mass of 80.4 GeV, while the Z boson is electrically neutral and has a mass of 91.2 GeV. See Section 2.1.5 for a description of the electroweak force, the quantum theory of electromagnetism and the weak force.

The gluon ( $g$ ) mediates the strong force among color charged particles, which are quarks and other gluons. The gluon is massless, electrically neutral, and carry a color-anticolor charge. There are eight gluons because there are eight interacting linear combinations of red, blue and green. See Section 2.1.6 for a description of Quantum Chromodynamics (QCD), the quantum theory of the strong force.

**Higgs Boson** The Higgs boson, finally observed at the LHC in 2012, was the last SM particle to be discovered [6–9]. Theory states that the Higgs boson has spin zero, making it a *scalar* boson, and the measurements of the observed particle are consistent with that of a spin zero particle. The Higgs boson plays a key role in explaining the origins of the mass of the other elementary particles. See Section 2.1.8 for more on the Higgs boson and the Higgs Mechanism, by which particles acquire mass.

In summary, there are 12 leptons, 36 quarks, 12 gauge bosons, and 1 Higgs boson in the SM.

### 2.1.1.3 Mass and Gauge Eigenstates

It should be noted that all of the particles discussed above are the mass eigenstates, which are the states with definite mass, and therefore the ones that are observed. However, in the theory, we often deal with the gauge eigenstates, which are the states that have definite interactions with the gauge bosons in the Lagrangian. Indeed, we will refer to the gauge eigenstates later in this chapter, when each of the pieces of the SM are discussed in more detail. The gauge eigenstates mix to form the mass eigenstates. The gauge eigenstates are right- and left-handed quarks and leptons. For example, the electron  $e^-$  we are familiar with is the mass eigenstate formed from the linear combination of  $e_L$  and  $e_R$ , which are gauge eigenstates. The  $U(1)_Y$  gauge boson is known as the B boson and the  $SU(2)_L$  gauge bosons are the  $W^+$ ,  $W^-$ , and the  $W^0$ . After spontaneous symmetry breaking, the B and  $W^0$  mix to form the photon and Z boson. The gauge eigenstates and their associated fields are described in Tables 2.1 - 2.3.

Table 2.1: The SM fermions and their fields. Right-handed (RH) and left-handed (LH) fields.

Particles	Field
LH leptons	$L_L$
LH quarks	$Q_L$
RH leptons	$L_R$
RH up-type quarks	$U_R$
RH down-type quarks	$D_R$

Table 2.2: The SM gauge fields.

Gauge Group	Field
$U(1)_Y$	$B_\mu$
$SU(2)_L$	$W_\mu^i$
$SU(3)_C$	$G_\mu$

Table 2.3: The SM scalar field for the Higgs boson.

Description	Field
Complex scalar doublet	$\phi$

### 2.1.2 The Fundamental Forces

There are four fundamental forces that govern all of the interactions we observe in nature: electromagnetism, the weak force, the strong force, and gravity. The first three forces are incorporated into the SM, but gravity is not explained in the SM, which is a major hole in the theory.

Electromagnetism describes the interaction among charged and magnetized objects. The quantum mechanical version of electromagnetism is Quantum Electrodynamics (QED).

The weak force governs radioactive decay and describes the interaction among particles with flavor. The full quantum version is described by the unified electroweak theory.

The strong force is responsible for binding quarks and gluons into hadrons and for binding hadrons together. The strong force is what keeps protons and neutrons bound together in the nucleus of the atom and is responsible for nuclear fusion. The strong force acts on particles with color, and it is the strongest of the four fundamental forces. The full quantum mechanical version of the strong force is described by Quantum Chromodynamics (QCD).

The most complete theory of gravity we have today is Einstein’s theory of General Relativity (GR). GR states that spacetime is curved in the presence of mass. Gravity is the weakest of the fundamental forces. We currently have no accepted quantum theory of gravity.

See Fig. 2.2 for a summary of the particles (mass eigenstates) and interactions of the SM. Figure 2.3 shows the allowed interactions of the SM in the form of vertices

of Feynman diagrams.

We will now describe the fundamental forces in more detail and explain their Lagrangians in the context of the SM. We will first introduce QED, weak interactions, electroweak unification, and QCD without including the Higgs mechanism, and then we will describe the Higgs mechanism and how that effects the different SM sectors.

### 2.1.3 Quantum Electrodynamics (QED)

QED is the relativistic quantum field theory of electromagnetism. It describes the interaction of charged particles, mediated by the photon. The gauge invariant U(1) QED Lagrangian is:

$$\mathcal{L}_{\mathcal{QED}} = \bar{\psi}(i\gamma^\mu D_\mu - m)\psi - \frac{1}{4}F_{\mu\nu}F^{\mu\nu} \quad (2.1)$$

where  $\psi$  is a fermion field with mass  $m$  and  $\bar{\psi} = \psi^\dagger \gamma^0$ .  $D_\mu$  is the covariant derivative, which is defined as  $D_\mu \equiv \partial_\mu - ieA_\mu$  for QED.  $F_{\mu\nu}$  is the electromagnetic field tensor, given by  $F_{\mu\nu} = \partial_\mu A_\nu - \partial_\nu A_\mu$ .  $A_\mu$  is the electromagnetic gauge field of the photon. The first term in the QED Lagrangian is the Dirac Lagrangian with an additional U(1) symmetry, and the second term is the gauge invariant kinematic term for the photon. The photon is required to be massless to preserve the invariance over local gauge transformations, and of course, we observe a massless photon in nature.

If we expand the covariant derivative, we find:

$$\begin{aligned} \mathcal{L}_{\mathcal{QED}} &= \bar{\psi}(i\gamma^\mu \partial_\mu - m)\psi - \frac{1}{4}F_{\mu\nu}F^{\mu\nu} - J^\mu A_\mu \\ &= \mathcal{L}_{Dirac} + \mathcal{L}_{EM} \end{aligned} \quad (2.2)$$

where  $\mathcal{L}_{Dirac}$  is the Dirac Lagrangian, which describes the field of fermions, where  $\mathcal{L}_{EM}$  is the Lagrangian of classical electrodynamics, and where we have identified the



# Standard Model of FUNDAMENTAL PARTICLES AND INTERACTIONS

The Standard Model summarizes the current knowledge in Particle Physics. It is the quantum theory that includes the theory of strong interactions (quantum chromodynamics or QCD) and the unified theory of weak and electromagnetic interactions (electroweak). Gravity is included on this chart because it is one of the fundamental interactions even though not part of the "Standard Model."

## FERMIONS

**matter constituents**  
spin = 1/2, 3/2, 5/2, ...

Leptons			Quarks		
Flavor	Mass GeV/c <sup>2</sup>	Electric charge	Flavor	Approx. Mass GeV/c <sup>2</sup>	Electric charge
$\nu_e$ electron neutrino	<1x10 <sup>-8</sup>	0	u up	0.003	2/3
e electron	0.000511	-1	d down	0.006	-1/3
$\nu_\mu$ muon neutrino	<0.0002	0	c charm	1.3	2/3
$\mu$ muon	0.106	-1	s strange	0.1	-1/3
$\nu_\tau$ tau neutrino	<0.02	0	t top	175	2/3
$\tau$ tau	1.7771	-1	b bottom	4.3	-1/3

**Spin** is the intrinsic angular momentum of particles. Spin is given in units of  $\hbar$ , which is the quantum unit of angular momentum, where  $\hbar = h/2\pi = 6.58 \times 10^{-35}$  GeV s =  $1.05 \times 10^{-34}$  J s.

**Electric charges** are given in units of the proton's charge. In SI units the electric charge of the proton is  $1.6 \times 10^{-19}$  Coulombs.

The **energy** unit of particle physics is the electronvolt (eV), the energy gained by one electron in crossing a potential difference of one volt. **Masses** are given in GeV/c<sup>2</sup> (remember  $E = mc^2$ ), where 1 GeV =  $10^9$  eV =  $1.6 \times 10^{-10}$  joule. The mass of the proton is 0.938 GeV/c<sup>2</sup> =  $1.67 \times 10^{-27}$  kg.

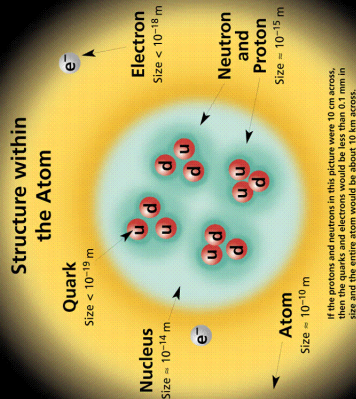
Baryons qq <sub>q</sub> and Antibaryons qq <sub>q</sub>				
Baryons are fermions. Hadrons. There are about 120 types of baryons.				
Symbol	Name	Quark content	Mass GeV/c <sup>2</sup>	Spin
p	proton	uud	0.938	1/2
$\bar{p}$	anti-proton	$\bar{u}\bar{u}\bar{d}$	0.938	1/2
n	neutron	udd	0.940	1/2
$\bar{n}$	anti-neutron	$\bar{u}\bar{d}\bar{d}$	0.940	1/2
$\Lambda$	lambda	uds	1.116	1/2
$\bar{\Lambda}$	anti-lambda	$\bar{u}\bar{d}\bar{s}$	1.116	1/2
$\Omega^-$	omega minus	sss	1.672	3/2

## Matter and Antimatter

Every particle has a corresponding antiparticle type, denoted by a bar over the particle symbol (unless s or c charge is shown). Particle and antiparticle have identical mass and spin but opposite charges. Some electrically neutral bosons (e.g.,  $Z^0$ ,  $\gamma$ , and  $\eta_c = c\bar{c}$ ) are their own antiparticles.

These diagrams are an artist's conception of physical processes. They are not to scale. The electron and positron annihilate to produce a cloud of gluons or the gluon field, and red lines the quark paths.

Figures



## BOSONS

**force carriers**  
spin = 0, 1, 2, ...

Unified Electroweak			Strong (color)		
Name	Mass GeV/c <sup>2</sup>	Electric charge	Name	Mass GeV/c <sup>2</sup>	Electric charge
$\gamma$ photon	0	0	g gluon	0	0
$W^-$	80.4	-1			
$W^+$	80.4	+1			
$Z^0$	91.187	0			

## Color Charge

Each quark carries one of three types of "strong charge," also called "color charge." These charges have nothing to do with the colors of objects. Light, there are eight possible colors of color charge. There are eight possible types of color charge. The strong interaction, called color charge, is the force that binds quarks together. In strong interactions, color-charged particles interact by exchanging gluons. Leptons, photons, and  $W$  and  $Z$  bosons have no strong interactions and hence no color charge.

## Quarks Confined in Mesons and Baryons

Quarks and leptons are the only particles defined in color-neutral particles called hadrons. This confinement (binding) results from multiple exchanges of gluons among the color-charged constituents. As color-charged particles (quarks and gluons) move apart, the energy in the color-force field between them increases. This energy eventually is converted into additional quark-antiquark pairs (see figure below). The quarks and antiquarks then combine into hadrons; these are the particles seen to emerge. Two types of hadrons have been observed in nature: mesons qq and baryons qq<sub>q</sub>.

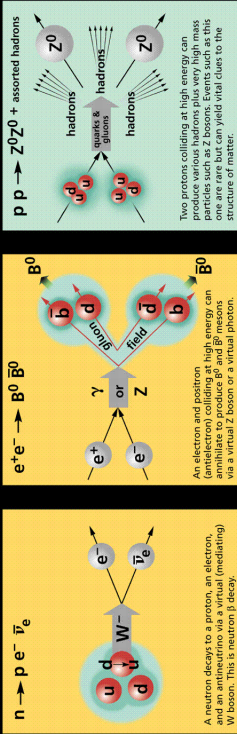
## Residual Strong Interaction

The strong binding of color-neutral protons and neutrons to form nuclei is due to residual strong interactions between their color-charged constituents. It is similar to the residual electrical interaction that binds electrically neutral atoms to form molecules. It can also be viewed as the exchange of mesons between the hadrons.

## PROPERTIES OF THE INTERACTIONS

Interaction		Weak (Electroweak)		Electromagnetic		Strong	
Property	Acts on:	Mass – Energy	Flavor	Electric Charge	Color Charge	Fundamental	Residual
Particles experiencing:	Particles mediating:	All	Quarks, Leptons	Electrically charged	Quarks, Gluons		See Residual Strong Interaction Note
		Graviton <small>(not yet observed)</small>	$W^+$ $W^-$ $Z^0$	$\gamma$	Gluons		Hadrons
		10 <sup>-41</sup>	0.8	1	25		Mesons
		10 <sup>-4</sup>	10 <sup>-4</sup>	1	60		Not applicable to quarks
for two u quarks at:	for two protons in nucleus	10 <sup>-36</sup>	10 <sup>-7</sup>	1	Not applicable to hadrons	20	

Mesons qq				
Mesons are bosonic hadrons. There are about 140 types of mesons.				
Symbol	Name	Quark content	Electric charge	Spin
$\pi^+$	pion	$u\bar{d}$	+1	0
$K^-$	kaon	$s\bar{u}$	-1	0
$\rho^+$	rho	$u\bar{d}$	+1	1
$B^0$	B-zero	$d\bar{b}$	0	0
$\eta_c$	eta-c	$c\bar{c}$	0	0



The Particle Adventure  
Visit the award-winning web feature *The Particle Adventure* at <http://ParticleAdventures.org>

This chart has been made possible by the generous support of:

U.S. Department of Energy  
Lawrence Berkeley National Laboratory  
National Science Foundation  
Department of Education  
American Physical Society, Division of Particle and Fields  
**BPURLE INDUSTRIES, INC.**

©2000 Contemporary Physics Education Project. CPEP is a non-profit organization that supports physics education research and the development of materials, hands-on classroom activities, and workshops; see: <http://CPEPweb.org>

Figure 2.2: The particles of the SM and their interactions.

**Standard Model Interactions**  
(Forces Mediated by Gauge Bosons)

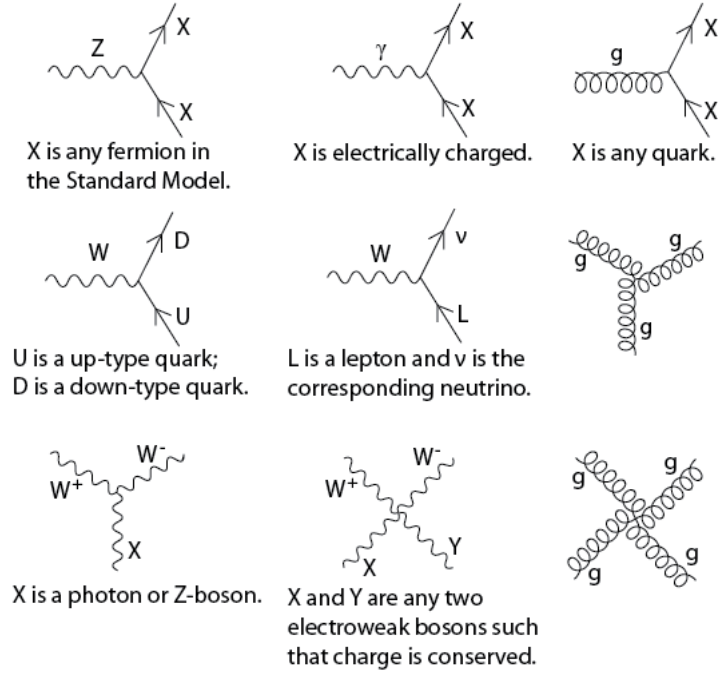


Figure 2.3: The interactions of the SM. Feynman diagrams are built from these vertices. Modifications involving Higgs boson interactions and neutrino oscillations are omitted. The conjugate of each listed vertex (i.e. reversing the direction of the arrows) is also allowed.

Noether current associated with the  $U(1)$  symmetry of the field  $A_\mu$  as:

$$J^\mu = ie\bar{\psi}\gamma^\mu\psi \quad (2.3)$$

Thus, electromagnetism arises from imposing a local  $U(1)$  symmetry on the Dirac Lagrangian.

QED involves the interaction of charged particles by exchange of a virtual photon. The basic QED vertex is the top middle vertex in Fig. 2.3, involving a photon and two charged particles. Each QED vertex is characterized by the coupling constant  $g_e = \sqrt{4\pi\alpha_e}$ .  $\alpha_e$  is the fine structure constant, given by  $\alpha_e = e^2/4\pi = 1/137$ , when

charge is measured in Heaviside-Lorentz units and setting  $\hbar = c = 1$ <sup>1</sup>.

The basic processes in QED, such as Compton scattering ( $\gamma + e^- \rightarrow \gamma + e^-$ ), pair production ( $\gamma + \gamma \rightarrow e^+ + e^-$ ), and pair annihilation ( $e^+ + e^- \rightarrow \gamma + \gamma$ ) are shown in Fig. 2.4. See Section 3.2.1 for more about QED processes in matter.

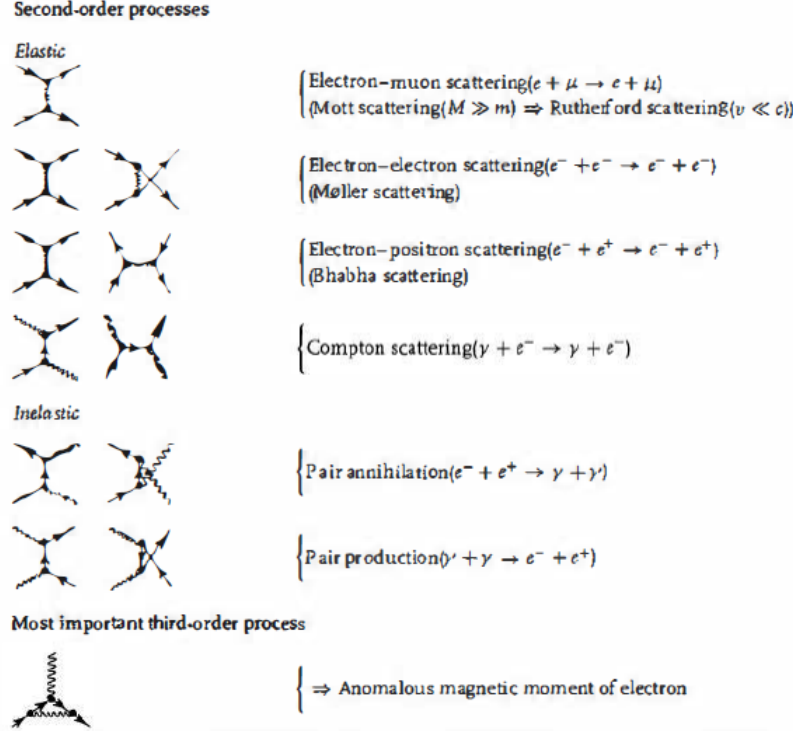


Figure 2.4: Feynman diagrams of the basic QED processes [2].

There are more complicated QED processes as well, but since the fine structure constant is small, every diagram with more and more vertices contributes less and less to the full physical processes. Thus, to a given degree of accuracy, the more complicated diagrams can be ignored.

An important feature of QED is that it is renormalizable. A number of Feynman diagrams in QED, namely, those involving closed loops, can give integrals that are divergent. A technique called renormalization, which absorbs the infinities into “renormalized” masses and coupling constants, was developed. Renormalization results in

<sup>1</sup>Throughout this thesis, we will use natural units where  $\hbar = c = k_B = 1$  for simplicity and because it is an often-adopted convention in particle physics.

a coupling constant that reflects what is actually measured in nature. Furthermore, the coupling constant will now depend on the momentum transferred in the collision and distance between the particles in the collision. This is the so-called “running” of the coupling constants, and it is further described in Section 2.1.9.

### 2.1.4 Weak Interactions

The weak force describes the interaction of particles with flavor. There are neutral weak interactions, mediated by the Z boson, and charged weak interactions, mediated by the W bosons.

The fundamental vertex for neutral weak interactions is the top left vertex in Fig. 2.3, involving a Z boson and two fermions. The Z boson mediates processes such as neutrino-electron scattering ( $\nu_\mu + e^- \rightarrow \nu_\mu + e^-$ ).

The charged weak interactions are shown in the two left-most diagrams in the second row in Fig. 2.3. They involve a W boson and either leptons or quarks. It is only the charged weak interactions that produce a change in flavor; a lepton converts into a neutrino (or vice-verse) or an up-type quark converts into a down-type quark (or vice-verse). Muon decay ( $\mu \rightarrow e + \nu_\mu + \bar{\nu}_e$ ), neutron decay ( $n \rightarrow p + e + \bar{\nu}_e$ ), and pion decay ( $\pi^- \rightarrow l^- + \bar{\nu}_l$ ) are all examples of charged weak interactions.

The W and Z bosons also can couple to themselves, each other, or the W can couple to the photon (see the two left-most diagrams in the bottom row in Fig. 2.3).

The weak coupling constant is  $g_w = \sqrt{4\pi\alpha_w}$ , where  $\alpha_w = 1/29$ .

### 2.1.5 Electroweak Unification

At sufficiently high energies, the electromagnetic and weak forces are unified into one force called the electroweak force. The gauge invariant  $SU(2)_L \times U(1)_Y$  electroweak Lagrangian is:

$$\begin{aligned}
\mathcal{L}_{EW} = & -\frac{1}{4}W_{\mu\nu}^a W_a^{\mu\nu} - \frac{1}{4}B_{\mu\nu}B^{\mu\nu} + \bar{L}_i i D_\mu \gamma^\mu L_i + \bar{e}_{Ri} i D_\mu \gamma^\mu e_{Ri} \\
& + \bar{Q}_i i D_\mu \gamma^\mu Q_i + \bar{u}_{Ri} i D_\mu \gamma^\mu u_{Ri} + \bar{d}_{Ri} i D_\mu \gamma^\mu d_{Ri}
\end{aligned} \tag{2.4}$$

The first two terms are kinematic terms for the generators of the  $SU(2)_L$  and  $U(1)_Y$  groups, respectively. The rest are the kinematic terms for the fermions, where  $D_\mu$  is the covariant derivative, which is defined as  $D_\mu \equiv \partial_\mu - ig_s \frac{\tau_a}{2} G_\mu^a - ig_2 \frac{\tau_a}{2} W_\mu^a - ig_1 \frac{Y_q}{2} B_\mu$ . However, for the weak singlet, the covariant derivative does not have the  $-ig_2 \frac{\tau_a}{2} W_\mu^a$  term.

All the particles in the electroweak theory are massless, as shown above; mass terms for the fermions and gauge bosons are forbidden by the gauge symmetry. The symmetry must be broken in order to obtain masses for the particles in the theory. Thus, electroweak symmetry breaking (EWSB) and the Higgs mechanism are required. This will be discussed in Section 2.1.8.4.

### 2.1.6 Quantum Chromodynamics (QCD)

QCD is the quantum theory of the strong interaction, governing the interactions between quarks and gluons. The gauge invariant  $SU(3)_C$  Lagrangian is analogous to the Lagrangian for QED and is given by:

$$\mathcal{L}_{QCD} = \bar{\psi}(i\gamma^\mu D_\mu - m)\psi - \frac{1}{4}G_{\mu\nu}G^{\mu\nu} \tag{2.5}$$

where  $\psi$  is a quark field with mass  $m$  and  $D_\mu$  is the covariant derivative for QCD.  $G_{\mu\nu}$  is the gluon field tensor, given by  $G_{\mu\nu} = \partial_\mu A_\nu^a - \partial_\nu A_\mu^a + gf_{bc}^a A_\mu^b A_\nu^c$ .  $A_\mu^a$  is the gauge field of the gluon.

The basic QCD vertices are in the right-most column of Fig. 2.3. They involve a gluon and two quarks, three gluons, or four gluons. As previously mentioned in

Section 2.1.1, quarks and gluons carry color; quarks can be blue, red, or green, and gluons have a color-anticolor charge. Thus, a quark can change color as it undergoes the first vertex. The diagrams with three or four gluons exist because the gluons themselves carry color.

Quarks and gluons are never observed as free particles; they obey the law of confinement. Only singlets of  $SU(3)_C$  are physically observable.

Each QCD vertex is characterized by the coupling constant  $g_s = \sqrt{4\pi\alpha_s}$ .  $\alpha_s$  has been experimentally determined to be large, which in principle would mean that more complicated diagrams would contribute more to the overall processes. However, the coupling constant is also highly dependent on the distance between the particles and is not constant at all. The coupling strength increases as the distance between the partons increases. As partons are pulled apart from each other, the potential energy increases, and eventually there is enough energy to spontaneously create new hadrons from the vacuum by drawing quarks from the quark sea. This process is known as hadronization. Conversely, at very short distances, that is, less than the size of a proton, the QCD coupling constant is very small. Thus, within a hadron, the partons interact very little; this phenomenon is called “asymptotic freedom.”

### 2.1.7 The SM before the Higgs Mechanism

Before the Higgs Mechanism was introduced, the SM Lagrangian stood as follows:

$$\begin{aligned}\mathcal{L}_{SM} = & -\frac{1}{4}G_{\mu\nu}^a G_{\mu\nu}^a - \frac{1}{4}W_{\mu\nu}^a W_{\mu\nu}^a - \frac{1}{4}B_{\mu\nu} B_{\mu\nu} + \bar{L}_i i D_\mu \gamma^\mu L_i + \bar{e}_{Ri} i D_\mu \gamma^\mu e_{Ri} \\ & + \bar{Q}_i i D_\mu \gamma^\mu Q_i + \bar{u}_{Ri} i D_\mu \gamma^\mu u_{Ri} + \bar{d}_{Ri} i D_\mu \gamma^\mu d_{Ri}\end{aligned}\tag{2.6}$$

where  $G_{\mu\nu}^a$ ,  $W_{\mu\nu}^a$ , and  $B_{\mu\nu}$  correspond to the generators of the  $SU(3)_C$ ,  $SU(2)_L$ , and  $U(1)_Y$  groups, respectively [2, 10]. More specifically, these three terms are the gluon,

$W$  boson, and  $B$  boson.  $L_i$  and  $Q_i$  are the left-handed lepton and quark doublets, while  $e_{Ri}$ ,  $u_{Ri}$ , and  $d_{Ri}$  are the right-handed lepton and quark singlets (electron, muon, and tau leptons; up, charm, and top quarks; down, strange, and bottom quarks). Finally,  $D_\mu$  is the covariant derivative, which is defined as  $D_\mu \equiv \partial_\mu - ig_s \frac{\tau_a}{2} G_\mu^a - ig_2 \frac{\tau_a}{2} W_\mu^a - ig_1 \frac{Y_q}{2} B_\mu$  for the quarks. In this expression,  $g_{s,1,2}$  are the coupling constants of the  $SU(3)_C$ ,  $SU(2)_L$ , and  $U(1)_Y$  groups, respectively,  $\tau_a$  are the  $2 \times 2$  Pauli matrices, and  $Y_q$  is the hypercharge.

This Lagrangian is invariant under local  $SU(3)_C \times SU(2)_L \times U(1)_Y$  gauge transformations. A local gauge transformation is a transformation of the form  $\psi(x) \rightarrow \psi'(x) = e^{i\alpha(x)}\psi(x)$ . As one can see, a transformation of this type is a change in phase that is generally different at each point in space.  $\mathcal{L}_{SM}$  can be shown to be invariant under local gauge transformations in the electroweak sector (i.e.  $SU(2)_L \times U(1)_Y$ ), for example, by making the following transformations:

$$\begin{aligned}
L(x) &\rightarrow L'(x) = e^{i\alpha_a(x)T^a + i\beta(x)Y} L(x) \\
R(x) &\rightarrow R'(x) = e^{i\beta(x)Y} R(x) \\
\vec{W}_\mu(x) &\rightarrow \vec{W}'_\mu(x) = \vec{W}_\mu(x) - \frac{1}{g_2} \partial_\mu \vec{\alpha}(x) - \vec{\alpha}(x) \times \vec{W}_\mu(x) \\
B_\mu(x) &\rightarrow B'_\mu(x) = B_\mu(x) - \frac{1}{g_1} \partial_\mu \beta(x)
\end{aligned} \tag{2.7}$$

The problem with the SM Lagrangian occurs when one tries to introduce mass terms for the fermions and gauge bosons. If mass terms are explicitly introduced, the local gauge invariance is violated:

$$\frac{1}{2} m^2 A_\mu A^\mu \rightarrow \frac{1}{2} m^2 (A_\mu + \frac{1}{e} \partial_\mu \alpha) (A^\mu + \frac{1}{e} \partial^\mu \alpha) \neq \frac{1}{2} m^2 A_\mu A^\mu \tag{2.8}$$

where we have introduced the transformation  $A_\mu \rightarrow A_\mu + \frac{1}{e} \partial_\mu \alpha$  to make the electro-

magnetic fields invariant. The Higgs Mechanism of spontaneous symmetry breaking was introduced to resolve this difficulty by providing a way to generate the fermion and gauge boson masses without violating local  $SU(2)_L \times U(1)_Y$  invariance.

## 2.1.8 Spontaneous Symmetry Breaking

We will first discuss the simplest case of spontaneous symmetry breaking, that is, a discrete spontaneous symmetry breaking. We will then gradually examine more complex examples until we can discuss the Higgs Mechanism in the SM.

### 2.1.8.1 Discrete Spontaneous Symmetry Breaking

Consider a simple Klein-Gordon Lagrangian of a massless scalar (spin-0) field in a potential:

$$\mathcal{L} = \frac{1}{2}(\partial_\mu \phi)(\partial^\mu \phi) - V(\phi) \quad (2.9)$$

where  $V(\phi) = -\frac{1}{2}\mu^2\phi^2 + \frac{1}{4}\lambda^2\phi^4$ ,  $\phi$  is a simple scalar field, and  $\mu$  and  $\lambda$  are real constants. This Lagrangian is invariant under the reflection symmetry  $\phi \rightarrow -\phi$  because there are no cubic terms. Note that the first term in the potential is not the mass term, since the sign would be wrong.

The minimum of the potential can easily be shown to be at  $\phi = \pm \frac{\mu}{\lambda}$  (see Fig. 2.5). This minimum is called the vacuum expectation value of the scalar field  $\phi$ .

One should consider Feynman calculus as a perturbation procedure and discuss fluctuations around the ground state. In this case, since the ground state is not at 0, we should introduce a new variable  $\eta$  defined by  $\eta \equiv \phi \pm \frac{\mu}{\lambda}$ . In terms of  $\eta$ , the Lagrangian is now:

$$\mathcal{L} = \frac{1}{2}(\partial_\mu \eta)(\partial^\mu \eta) - \mu^2 \eta^2 \pm \mu \lambda \eta^3 - \frac{1}{4} \lambda^2 \eta^4 + \frac{1}{4} \left( \frac{\mu^2}{\lambda} \right)^2 \quad (2.10)$$



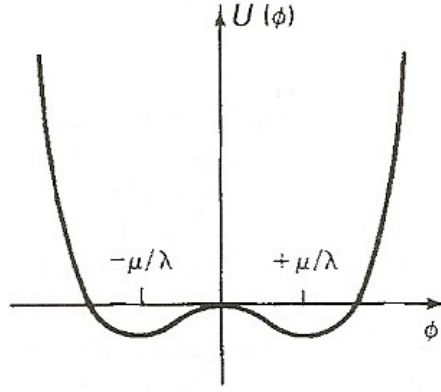


Figure 2.5: Graph of  $V(\phi)$  for the Lagrangian in equation (2.9) [2].

The second term is now the mass term, and so one can see that the mass associated with  $\eta$  is  $m_\eta = \sqrt{2}\mu$ . The third and fourth terms represent cubic and quartic couplings, respectively, while the last term is simply a constant. When one writes the Lagrangian in this way, the reflexive symmetry from before is now broken, due to the presence of the cubic term. This is the simplest example of spontaneous symmetry breaking. We refer to the symmetry breaking as “spontaneous” because there is no external agent to cause it and as “discrete” because there are only two ground states.

### 2.1.8.2 Continuous Spontaneous Symmetry Breaking

The example above can be easily extended to a continuous spontaneous symmetry breaking. Consider a Lagrangian that is very similar to equation 2.11, except now with two scalar fields:

$$\mathcal{L} = \frac{1}{2}(\partial_\mu \phi_1)(\partial^\mu \phi_1) + \frac{1}{2}(\partial_\mu \phi_2)(\partial^\mu \phi_2) + \frac{1}{2}\mu^2(\phi_1^2 + \phi_2^2) - \frac{1}{4}\lambda^2(\phi_1^2 + \phi_2^2)^2 \quad (2.11)$$

This Lagrangian is invariant under rotations in  $\phi_1, \phi_2$  space.

Figure 2.6 shows the graph of  $V(\phi_1, \phi_2)$ . The minima of the potential now lie on a circle of radius  $\frac{\mu}{\lambda}$ :

$$\phi_{1min}^2 + \phi_{2min}^2 = \frac{\mu^2}{\lambda^2} \quad (2.12)$$

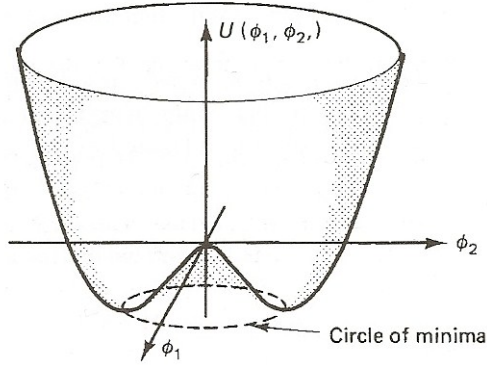


Figure 2.6: Graph of  $V(\phi_1, \phi_2)$  for the Lagrangian in equation 2.11 [2].

We must choose a particular ground state, that is, a particular vacuum expectation value, for example:

$$\phi_{1min} = \frac{\mu}{\lambda} \quad (2.13)$$

$$\phi_{2min} = 0 \quad (2.14)$$

We will then introduce new variables, which are fluctuations about the ground state we have chosen, as we did before:

$$\eta_1 \equiv \phi_1 - \frac{\mu}{\lambda} \quad (2.15)$$

$$\eta_2 \equiv \phi_2 \quad (2.16)$$

Substituting these new variables into the original Lagrangian gives:

$$\begin{aligned}
\mathcal{L} &= \frac{1}{2} \left( \partial_\mu \left[ \eta_1 + \frac{\mu}{\lambda} \right] \right) \left( \partial^\mu \left[ \eta_1 + \frac{\mu}{\lambda} \right] \right) + \frac{1}{2} (\partial_\mu \eta_2) (\partial^\mu \eta_2) \\
&\quad + \frac{1}{2} \mu^2 \left( \left[ \eta_1 + \frac{\mu}{\lambda} \right]^2 + \eta_2^2 \right) - \frac{1}{4} \lambda^2 \left( \left[ \eta_1 + \frac{\mu}{\lambda} \right]^2 + \eta_2^2 \right)^2 \\
&= \frac{1}{2} (\partial_\mu \eta_1) (\partial^\mu \eta_1) + \frac{1}{2} (\partial_\mu \eta_2) (\partial^\mu \eta_2) \\
&\quad + \frac{1}{2} \mu^2 \left( \eta_1^2 + 2 \frac{\mu}{\lambda} \eta_1 + \frac{\mu^2}{\lambda^2} + \eta_2^2 \right) - \frac{1}{4} \lambda^2 \left( \eta_1^2 + 2 \frac{\mu}{\lambda} \eta_1 + \frac{\mu^2}{\lambda^2} + \eta_2^2 \right)^2 \quad (2.17)
\end{aligned}$$

The last term above becomes:

$$- \frac{1}{4} \lambda^2 \left( \eta_1^4 + 4 \frac{\mu}{\lambda} \eta_1^3 + 6 \frac{\mu^2}{\lambda^2} \eta_1^2 + 4 \frac{\mu^3}{\lambda^3} \eta_1 + \eta_2^4 + 2 \frac{\mu^2}{\lambda^2} \eta_2^2 + 2 \eta_1^2 \eta_2^2 + 4 \frac{\mu}{\lambda} \eta_1 \eta_2^2 + \frac{\mu^4}{\lambda^4} \right) \quad (2.18)$$

And so the final Lagrangian is:

$$\begin{aligned}
\mathcal{L} &= \left[ \frac{1}{2} (\partial_\mu \eta_1) (\partial^\mu \eta_1) - \mu^2 \eta_1^2 \right] + \left[ \frac{1}{2} (\partial_\mu \eta_2) (\partial^\mu \eta_2) \right] \\
&\quad - \left[ \mu \lambda (\eta_1^3 + \eta_1 \eta_2^2) + \frac{1}{4} \lambda^2 (\eta_1^4 + \eta_2^4 + 2 \eta_1^2 \eta_2^2) \right] + \frac{1}{4} \left( \frac{\mu^2}{\lambda} \right)^2 \quad (2.19)
\end{aligned}$$

The first two terms above are free Klein-Gordon Lagrangians for the fields  $\eta_1$  and  $\eta_2$  with masses  $m_{\eta_1} = \sqrt{2}\mu$  and  $m_{\eta_2} = 0$ , the third term defines the couplings, and the last term is a constant. The second term with a zero mass points to the reason we have included this example, namely, to demonstrate Goldstone's Theorem. Goldstone's Theorem states that for every spontaneously broken continuous symmetry, a massless scalar (spin-0) particle, called the Goldstone boson, appears. The Goldstone boson is, of course, not a real particle that exists in nature, but rather a mathematical entity that must be overcome in order to eventually generate gauge bosons with mass.

### 2.1.8.3 The Higgs Mechanism in an Abelian Theory

We will now move to continuous spontaneous symmetry breaking in a local gauge invariant field. If we combine the two fields  $\phi_1$  and  $\phi_2$  into a complex field  $\phi \equiv \phi_1 + i\phi_2$ , introduce a massless vector (spin-1) field  $A^\mu$ , and replace the derivatives by the covariant derivative  $\mathcal{D}_\mu \equiv \partial_\mu + ieA_\mu$ , then our Lagrangian will be:

$$\mathcal{L} = -\frac{1}{4}F^{\mu\nu}F_{\mu\nu} + \frac{1}{2}(\mathcal{D}_\mu\phi^*)(\mathcal{D}^\mu\phi) + \frac{1}{2}\mu^2(\phi^*\phi) - \frac{1}{4}\lambda^2(\phi^*\phi)^2 \quad (2.20)$$

This Lagrangian is invariant under local U(1) transformations of the form  $\phi(x) \rightarrow e^{i\alpha(x)}\phi(x)$  and  $A_\mu(x) \rightarrow A_\mu(x) - \frac{1}{e}\partial_\mu\alpha(x)$ .

Since the potential is the same as in the previous section, it will have the same vacuum expectation value. We will need to introduce the same fields as before (see equations (2.15) and (2.16)) for the particular ground state. Substituting these fields into the Lagrangian in equation (2.20) will give:

$$\begin{aligned} \mathcal{L} = & \left[ -\frac{1}{4}F^{\mu\nu}F_{\mu\nu} + \frac{1}{2}\left(e\frac{\mu}{\lambda}\right)^2 A_\mu A^\mu \right] + \left[ \frac{1}{2}(\partial_\mu\eta_1)(\partial^\mu\eta_1) - \mu^2\eta_1^2 \right] + \left[ \frac{1}{2}(\partial_\mu\eta_2)(\partial^\mu\eta_2) \right] \\ & + e[\eta_1(\partial_\mu\eta_2) - \eta_2(\partial_\mu\eta_1)]A^\mu + e^2\frac{\mu}{\lambda}\eta_1 A_\mu A^\mu + \frac{1}{2}e^2(\eta_1^2 + \eta_2^2)A_\mu A^\mu \\ & - \mu\lambda(\eta_1^3 + \eta_1\eta_2^2) - \frac{1}{4}\lambda^2(\eta_1^4 + \eta_2^4 + 2\eta_1^2\eta_2^2) \\ & + e\frac{\mu}{\lambda}(\partial_\mu\eta_2)A^\mu + \frac{1}{4}\left(\frac{\mu^2}{\lambda}\right)^2 \end{aligned} \quad (2.21)$$

The first line in the Lagrangian is for the scalar particle  $\eta_1$  with mass  $\sqrt{2}\mu$ , the Goldstone boson  $\eta_2$ , and now we have the free gauge field  $A^\mu$  with a mass  $2\sqrt{\pi}e\frac{\mu}{\lambda}$ . In effect, we have given a mass to the photon! The second and third line of the Lagrangian describes the couplings of  $\eta_1$ ,  $\eta_2$ , and  $A^\mu$ , and the second term in the fourth line is the constant. However, the first term in the last line,  $e\frac{\mu}{\lambda}(\partial_\mu\eta_2)A^\mu$ , implies a vertex in which the Goldstone boson turns into a photon, which suggests

that we have incorrectly identified the particles in the theory.

So to summarize our issues, we have:

1. A Goldstone boson
2. A massive photon
3. A Goldstone boson becoming a photon

For the second issue, the massive photon will become the massive gauge bosons in the next section. However, we can deal with the first and third issues now by exploiting the local gauge invariance of the Lagrangian to transform  $\eta_2$  away entirely. We can choose a particular gauge, called the unitary gauge, such that when the field from equation (2.20) transforms (i.e.  $\phi \rightarrow \phi' = e^{i\alpha}\phi$ ),  $\phi'$  will be real.  $\phi'$  will be real if we choose  $\alpha = -\tan^{-1}\left(\frac{\phi_2}{\phi_1}\right)$ . Thus,  $\eta_2$  will now be 0. In this unitary gauge, the Lagrangian will now be:

$$\begin{aligned} \mathcal{L} = & \left[ -\frac{1}{4}F^{\mu\nu}F_{\mu\nu} + \frac{1}{2}\left(e\frac{\mu}{\lambda}\right)^2 A_\mu A^\mu \right] + \left[ \frac{1}{2}(\partial_\mu \eta_1)(\partial^\mu \eta_1) - \mu^2 \eta_1^2 \right] \\ & + \left\{ e^2 \frac{\mu}{\lambda} \eta_1 A_\mu A^\mu + \frac{1}{2} e^2 \eta_1^2 A_\mu A^\mu - \mu \lambda \eta_1^3 - \frac{1}{4} \lambda^2 \eta_1^4 \right\} \\ & + \frac{1}{4} \left( \frac{\mu^2}{\lambda} \right)^2 \end{aligned} \tag{2.22}$$

In essence, the photon, with two degrees of freedom, has absorbed the Goldstone boson and become massive, effectively taking on three degrees of freedom. Also, the offending term in the previous Lagrangian no longer exists. The U(1) gauge symmetry has been spontaneously broken, and this is what is called the Higgs Mechanism.

#### 2.1.8.4 The Higgs Mechanism in the the Electroweak Sector of the SM

Since the Higgs Mechanism will not affect QCD, we can just apply it to the electroweak sector of the SM, which is, of course, locally gauge invariant. Our goals in what follows

will be to:

1. Keep the photon massless
2. Keep Quantum Electrodynamics (QED) as an exact symmetry
3. Generate masses for the three gauge bosons, the fermions, and the Higgs boson
4. Generate the Higgs boson couplings to the gauge bosons and the fermions

We will first generate the gauge boson masses, then include the fermions, and then deal with the Higgs boson itself and its couplings.

**Generation of the Gauge Boson Masses** The simplest choice for the Higgs field will be a complex SU(2) doublet of scalar fields with a hypercharge ( $Y$ ) of 1:

$$\Phi = \begin{pmatrix} \phi^+ \\ \phi^0 \end{pmatrix} = \frac{1}{\sqrt{2}} \begin{pmatrix} \phi_1 + i\phi_2 \\ \phi_3 + i\phi_4 \end{pmatrix} \quad (2.23)$$

To the electroweak Lagrangian, which is the SM Lagrangian without the strong interaction part:

$$\begin{aligned} \mathcal{L}_{EW} = & -\frac{1}{4}W_{\mu\nu}^a W_a^{\mu\nu} - \frac{1}{4}B_{\mu\nu}B^{\mu\nu} + \bar{L}_i iD_\mu \gamma^\mu L_i + \bar{e}_{Ri} iD_\mu \gamma^\mu e_{Ri} \\ & + \bar{Q}_i iD_\mu \gamma^\mu Q_i + \bar{u}_{Ri} iD_\mu \gamma^\mu u_{Ri} + \bar{d}_{Ri} iD_\mu \gamma^\mu d_{Ri} \end{aligned} \quad (2.24)$$

we need to add the Lagrangian for the scalar field:

$$\mathcal{L}_S = (\mathcal{D}^\mu \Phi)^\dagger (\mathcal{D}_\mu \Phi) + \frac{1}{2}\mu^2(\Phi^\dagger \Phi) - \frac{1}{4}\lambda^2(\Phi^\dagger \Phi)^2 \quad (2.25)$$

where in this case,  $\mathcal{D}_\mu \equiv \partial_\mu - ig_2 \frac{\tau_a}{2} W_\mu^a - ig_1 \frac{1}{2} B_\mu$ .  $g_1$  is the strength of the B boson coupling to the weak hypercharge  $Y$ ,  $g_2$  is the strength of the W boson coupling to the left-handed weak isospin doublets, and  $\tau_a$  are the  $2 \times 2$  Pauli matrices.

If we preserve the symmetry of  $U(1)_{QED}$ , then the vacuum expectation value will have  $\phi^+ = 0$  such that:

$$\Phi_{min} = \frac{1}{\sqrt{2}} \begin{pmatrix} 0 \\ \mu/\lambda \end{pmatrix} \quad (2.26)$$

We will then introduce new fields  $\eta_{1,2,3,4}$ :

$$\Phi_\eta = \frac{1}{\sqrt{2}} \begin{pmatrix} \eta_1 + i\eta_2 \\ (\eta_3 + \frac{\mu}{\lambda}) + i\eta_4 \end{pmatrix} \quad (2.27)$$

Then, we will again chose the unitary gauge so that  $\Phi_\eta \rightarrow e^{i\alpha(x)}\Phi_\eta = \mathbb{R}$  . In other words,  $\eta_2 = \eta_4 = 0$  and

$$\Phi_\eta \rightarrow \frac{1}{\sqrt{2}} \begin{pmatrix} 0 \\ \eta_3 + \frac{\mu}{\lambda} \end{pmatrix} \quad (2.28)$$

With this choice, we will focus on the expansion of the  $|\mathcal{D}^\mu\Phi|^2$  term in the Lagrangian:

$$\begin{aligned}
|\mathcal{D}^\mu \Phi|^2 &= \left| \left( \partial_\mu - ig_2 \frac{\tau_a}{2} W_\mu^a - ig_1 \frac{1}{2} B_\mu \right) \frac{1}{\sqrt{2}} \begin{pmatrix} 0 \\ \eta_3 + \frac{\mu}{\lambda} \end{pmatrix} \right|^2 \\
&= \frac{1}{2} \left| \begin{pmatrix} \partial_\mu - \frac{i}{2}(g_2 W_\mu^3 + g_1 B_\mu) & -\frac{ig_2}{2}(W_\mu^1 - iW_\mu^2) \\ -\frac{ig_2}{2}(W_\mu^1 + iW_\mu^2) & \partial_\mu + \frac{i}{2}(g_2 W_\mu^3 - g_1 B_\mu) \end{pmatrix} \begin{pmatrix} 0 \\ \eta_3 + \frac{\mu}{\lambda} \end{pmatrix} \right|^2 \\
&= \frac{1}{2} \left| \begin{pmatrix} -\frac{ig_2}{2}(W_\mu^1 - iW_\mu^2) (\eta_3 + \frac{\mu}{\lambda}) \\ (\partial_\mu + \frac{i}{2}(g_2 W_\mu^3 - g_1 B_\mu)) (\eta_3 + \frac{\mu}{\lambda}) \end{pmatrix} \right|^2 \\
&= \frac{1}{2} \left( \partial_\mu \left( \eta_3 + \frac{\mu}{\lambda} \right) \right)^2 + \frac{1}{8} g_2^2 \left( \eta_3 + \frac{\mu}{\lambda} \right)^2 |W_\mu^1 - iW_\mu^2|^2 \\
&\quad - \frac{1}{8} \left( \eta_3 + \frac{\mu}{\lambda} \right)^2 |g_2 W_\mu^3 - g_1 B_\mu|^2 + \frac{i}{2} \left( \eta_3 + \frac{\mu}{\lambda} \right)^2 \partial_\mu |g_2 W_\mu^3 - g_1 B_\mu|^2 \\
&= \frac{1}{2} (\partial_\mu \eta_3)^2 + \frac{1}{8} g_2^2 \left( \eta_3 + \frac{\mu}{\lambda} \right)^2 |W_\mu^1 - iW_\mu^2|^2 \\
&\quad - \frac{1}{8} \left( \eta_3 + \frac{\mu}{\lambda} \right)^2 |g_2 W_\mu^3 - g_1 B_\mu|^2
\end{aligned} \tag{2.29}$$

The mass eigenstates will be defined as:

$$W^\pm \equiv \frac{1}{\sqrt{2}}(W_\mu^1 \mp iW_\mu^2) \tag{2.30}$$

$$Z_\mu \equiv \frac{1}{\sqrt{g_2^2 + g_1^2}}(g_2 W_\mu^3 - g_1 B_\mu) \tag{2.31}$$

$$A_\mu \equiv \frac{1}{\sqrt{g_2^2 + g_1^2}}(g_2 W_\mu^3 + g_1 B_\mu) \tag{2.32}$$

And then the mass terms,  $M_W^2 W_\mu^+ W^{-\mu}$ ,  $\frac{1}{2} M_Z^2 Z_\mu Z^\mu$ , and  $\frac{1}{2} M_A^2 A_\mu A^\mu$ , show that the masses are:



$$M_W = \frac{g_2}{2} \frac{\mu}{\lambda} \quad (2.33)$$

$$M_Z = \frac{\sqrt{g_2^2 + g_1^2}}{2} \frac{\mu}{\lambda} \quad (2.34)$$

$$M_A = 0 \quad (2.35)$$

Thus, we have generated the masses of the three gauge bosons, kept the photon massless, and kept the symmetry of QED unbroken.

**Generation of the Fermion Masses** We can generate the fermion masses by assuming a Higgs field  $\Phi$  with  $Y = 1$  as before, plus the isodoublet  $\tilde{\Phi} = i\tau_2\Phi^*$ , which has  $Y = -1$ . The Lagrangian will become  $\mathcal{L}_{EW} + \mathcal{L}_S + \mathcal{L}_F$ , where the first two terms are defined in equations (2.4) and (2.25) and the last term is:

$$\mathcal{L}_F = -\lambda_e \bar{L}\Phi e_R - \lambda_d \bar{Q}\Phi d_R - \lambda_u \bar{Q}\tilde{\Phi} u_R + h.c. \quad (2.36)$$

$\mathcal{L}_F$  is invariant under rotations in  $SU(2)_L \times U(1)_Y$ .

We will then repeat the same procedure as above, eventually getting the fermion masses:

$$m_{e,u,d} = \frac{\lambda_{e,u,d}}{\sqrt{2}} \frac{\mu}{\lambda} \quad (2.37)$$

One thing to note is that for quarks, the physical states are obtained by diagonalizing the up and down quark mass matrices by four unitary matrices. The charged weak interactions couple to the physical up and down-type quarks with couplings given by the Cabibbo-Kobayakshi-Maskawa (CKM) matrix:

$$V_{CKM} = \begin{pmatrix} V_{ud} & V_{us} & V_{ub} \\ V_{cd} & V_{cs} & V_{cb} \\ V_{td} & V_{ts} & V_{tb} \end{pmatrix} \quad (2.38)$$

The CKM matrix can be parametrized by the three mixing angles and a CP-violating phase:

$$V_{CKM} = \begin{pmatrix} c_{12}c_{13} & s_{12}c_{13} & s_{13}e^{-i\delta} \\ -s_{12}c_{23} - c_{12}s_{23}s_{13}e^{i\delta} & c_{12}c_{23} - s_{12}s_{23}s_{13}e^{i\delta} & s_{23}c_{13} \\ s_{12}s_{23} - c_{12}c_{23}s_{13}e^{i\delta} & -c_{12}s_{23} - s_{12}c_{23}s_{13}e^{i\delta} & c_{23}c_{13} \end{pmatrix} \quad (2.39)$$

where  $s_{ij} = \sin \theta_{ij}$ ,  $c_{ij} = \cos \theta_{ij}$ , and  $\delta$  is the phase responsible for all CP-violating phenomena in flavor changing processes in the SM.

### Generation of the Higgs Boson and its Couplings to the Gauge Bosons and

**Fermions** All that remains is to deal with the Higgs boson itself. In Equation 2.29, we found the kinetic part of the Higgs field,  $\frac{1}{2}(\partial_\mu \eta_3)^2$ , which came from the  $|\mathcal{D}^\mu \Phi|^2$  term. The mass and self-interaction parts will come from the potential  $V(\Phi) = -\frac{1}{2}\mu^2\Phi^+\Phi + \frac{1}{4}\lambda^2(\Phi^+\Phi)^2$ , so that the Higgs Lagrangian is:

$$\begin{aligned} \mathcal{L}_H &= \frac{1}{2}(\partial_\mu \eta_3)^2 + \frac{1}{2}\mu^2 \begin{pmatrix} 0 & \eta_3 + \frac{\mu}{\lambda} \end{pmatrix} \begin{pmatrix} 0 \\ \eta_3 + \frac{\mu}{\lambda} \end{pmatrix} - \frac{1}{4}\lambda^2 \left| \begin{pmatrix} 0 & \eta_3 + \frac{\mu}{\lambda} \end{pmatrix} \begin{pmatrix} 0 \\ \eta_3 + \frac{\mu}{\lambda} \end{pmatrix} \right|^2 \\ &= \frac{1}{2}(\partial_\mu \eta_3)^2 + \frac{1}{2}\mu^2 \left( \eta_3 + \frac{\mu}{\lambda} \right)^2 - \frac{1}{4}\lambda^2 \left( \eta_3 + \frac{\mu}{\lambda} \right)^4 \\ &= \left[ \frac{1}{2}(\partial_\mu \eta_3)^2 - \mu^2 \eta_3^2 \right] - \mu\lambda \eta_3^3 - \frac{1}{4}\lambda^2 \eta_3^4 + \frac{1}{4} \left( \frac{\mu^2}{\lambda} \right)^2 \end{aligned} \quad (2.40)$$

Clearly, the mass of the Higgs boson is  $m_{\eta_3} = \sqrt{2}\mu$ , and it has cubic and quartic

self-interactions. To get the couplings of the Higgs boson to the gauge bosons and fermions, we notice that the Lagrangians for the gauge bosons and fermions are such that:

$$\mathcal{L}_{M_{GB}} \sim M_{GB}^2 \left(1 + \frac{\lambda}{\mu} \eta_3\right)^2 \quad (2.41)$$

$$\mathcal{L}_{M_f} \sim M_f \left(1 + \frac{\lambda}{\mu} \eta_3\right) \quad (2.42)$$

Then the couplings can be found:

$$g_{H,f,f} = i \frac{\lambda}{\mu} M_f \quad (2.43)$$

$$g_{H,GB,GB} = -2i \frac{\lambda}{\mu} M_{GB}^2 \quad (2.44)$$

$$g_{H,H,GB,GB} = -2i \left(\frac{\lambda}{\mu}\right)^2 M_{GB}^2 \quad (2.45)$$

Figure 2.7 shows the Higgs boson self-interactions and couplings to the gauge bosons and fermions in terms of the vacuum expectation value  $v \equiv \frac{\mu}{\lambda}$  and the Fermi constant  $G_\mu$ . In the notation of the figure,  $V_\mu$  corresponds to a gauge boson.

**The Electroweak Lagrangian** In summary, the full gauge invariant electroweak Lagrangian is:

$$\mathcal{L}_{fullEW} = \mathcal{L}_{EW} + \mathcal{L}_S \quad (2.46)$$

where  $\mathcal{L}_{EW}$  is given by Equation 2.24 and  $\mathcal{L}_S$  is given by Equation 2.25.

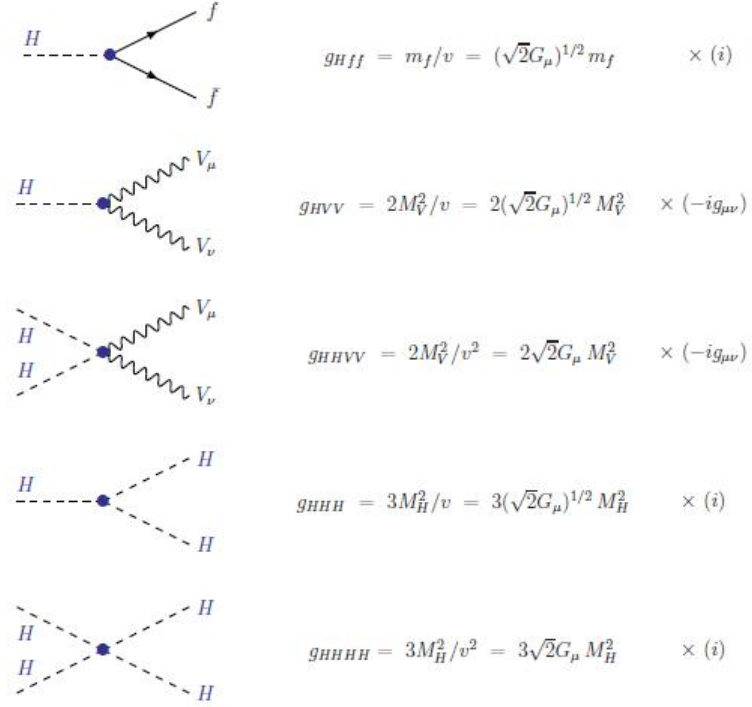


Figure 2.7: The Higgs boson self-interactions and couplings to the gauge bosons and fermions [10].

### 2.1.9 Measurements of the SM

The SM has been proven to be extremely accurate. It predicted particles such as the W and Z boson before they were observed. Fig. 2.8 shows a recent global fit of the SM, which displays the high agreement between theoretical predictions and experimental values.

There are 19 free parameters in the SM:

- The masses of the electron, muon, tau, and six quarks
- The four CKM angles
- The QCD vacuum angle
- The vacuum expectation value
- The Higgs mass

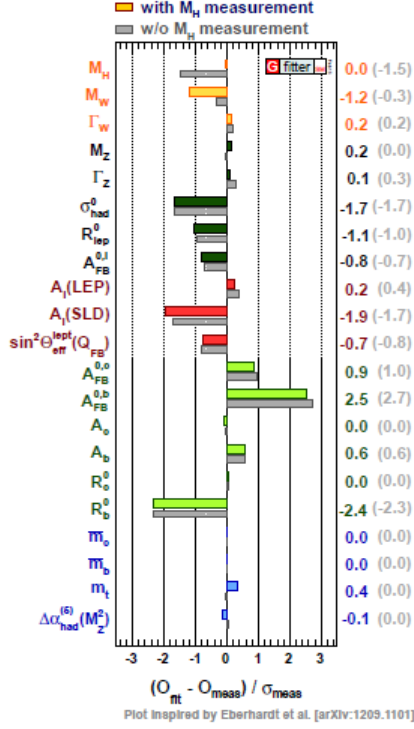


Figure 2.8: Differences between the SM prediction and the measured parameter, in units of the uncertainty for the fit including  $M_H$  (color) and without  $M_H$  (gray) [11].

- The three gauge couplings

The coupling constants  $g_e$ ,  $g_s$ , and  $g_w$  are actually not constant as a function of the energy or distance scale because of the contributions from virtual particles in higher order diagrams (see Fig. 2.9, left). That is, the strength of the force depends on how far away the particles in question are from one another; the coupling constants are said to “run” with the energy scale. The left side of Fig. 2.9 describes measurements that have been made in the accessible energy ranges, and then extrapolations to higher energies. As you can see, the coupling constants almost intersect at around  $10^{16}$  GeV. For some Grand Unified Theories (GUT) beyond the SM, the three lines actually intersect at a point because the particle content is different (see the right-hand side of Fig. 2.9). This describes the main idea behind GUTs: there is some energy scale where all the fundamental forces are unified into one. See more about GUTs and

beyond the SM in general in Section 2.3.

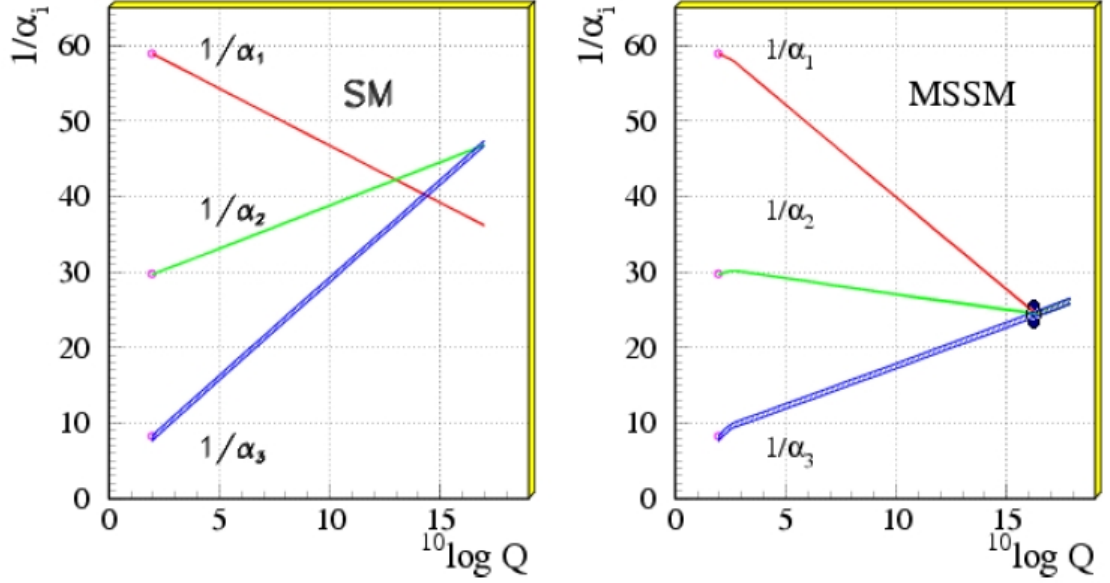


Figure 2.9: The inverse of the three coupling constants as a function of energy scale in the SM (left) and in the supersymmetric extension of the SM (MSSM) (right). In this figure,  $\alpha_1 = g_e$ ,  $\alpha_2 = g_w$ , and  $\alpha_3 = g_s$  [12].

### 2.1.10 Summary of the Fundamental Forces

The complete SM Lagrangian, governing the electromagnetic, weak, and strong forces, is:

$$\mathcal{L}_{SM} = \mathcal{L}_{fullEW} + \mathcal{L}_{QCD} \quad (2.47)$$

where  $\mathcal{L}_{fullEW}$  is given by Equation 2.46 and  $\mathcal{L}_{QCD}$  is given by Equation 2.5.

The last fundamental force, gravity, is described by Einstein's equations [13, 14]. The Lagrangian for GR is:

$$\mathcal{L}_{GR} = \frac{1}{128\pi G} R \sqrt{-g} \quad (2.48)$$

where  $R$  is the Ricci scalar,  $G$  is Newton's constant and  $g = \det g_{\mu\nu}$  is the determinant

of the metric tensor. GR is inherently non-renormalizable and therefore has not been quantized and incorporated into the SM.

## **2.2 Why the SM is Incomplete**

The SM is a highly precise theory of elementary particles and their interactions, but it is incomplete because it does not include some observed phenomena, such as gravity or neutrino oscillations, and because of a number of theoretical problems, such as the hierarchy problem and CP violation.

### **2.2.1 Unexplained Phenomena**

We will first describe several experimentally observed hints that the SM is incomplete.

#### **2.2.1.1 Gravity**

Gravity, which is one of the four fundamental forces, is not included in the SM. We have not found a gravity particle or gravitino. Although gravity is well described by Einstein's General Relativity, we do not have an accepted quantum theory of gravity [13,14]. Several quantum theories of gravity have been proposed, such as string theory and loop quantum gravity [15,16], but they have not been widely accepted, largely due to the lack of experimental evidence.

#### **2.2.1.2 Neutrino Oscillations**

In the SM, neutrinos have zero mass because there are only left-handed neutrinos and therefore, there can be no mass term in the Lagrangian. However, neutrinos have been observed to possess some, albeit small, mass. This non-zero mass is a direct consequence of the fact that neutrinos have been observed to oscillate between the different flavors. In other words, a neutrino will change its state as it travels through

space from, for example,  $\nu_e$  to  $\nu_\mu$  or  $\nu_\tau$ . Then, since the flavor eigenstates are linear superpositions of the mass eigenstates, changing from one flavor to another effectively means that the mass of the neutrino will change. Since the mass differences between the neutrinos are small, the coherence length for neutrino oscillations is long, and thus this quantum mechanical effect can be observed macroscopically [2].

Neutrino oscillations have been observed in solar and atmospheric neutrinos, and in neutrinos produced at nuclear reactors and particle accelerators. The first observation of neutrino oscillation was Ray Davis’s Homestake Experiment in the 1960s, which observed a deficit of solar neutrinos with respect to the Standard Solar Model, using a chlorine-based detector [17]. Since then, neutrino observations have famously been observed at the Sudbury Neutrino Observatory [18], with Kamiokande II [19], at Daya Bay [20], with the T2K Experiment [21], and others.

### 2.2.1.3 Dark Matter and Dark Energy

Ordinary matter, which is described by the particles in the SM, makes up only about 4% of the energy of the observable universe (see Fig. 2.10) [22]. 23% of the energy is dark matter, and 73% is dark energy.

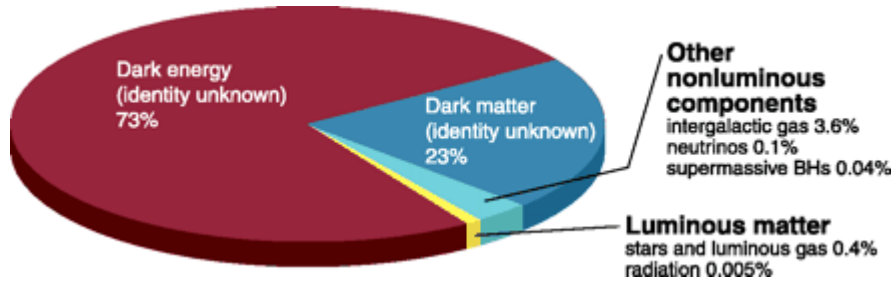


Figure 2.10: Pie chart showing the fractions of energy in the universe contributed by different sources. Ordinary matter is divided into luminous matter, that is, the stars, luminous gases, and radiation, and nonluminous matter, that is, intergalactic gas, neutrinos, and supermassive black holes. The majority of the universe, dark matter and dark energy, is unknown [22].

Dark matter accounts for some “missing mass” in the universe, which is inferred from the gravitational effects on ordinary matter. Dark matter is necessary to explain



the rotational curves of galaxies and galaxy clusters [23, 24], and there is evidence for it from studies of gravitational lensing and the cosmic microwave background (CMB) [25–27]. We have not yet found the particle responsible for dark matter; the most popular model for dark matter posits the existence of weakly interacting massive particles (WIMPs). This model is for cold dark matter, meaning that dark matter is non-relativistic, and in this model, WIMPs interact only via gravity and the weak force. There are many experiments that are searching for WIMPs, including LUX [28], XENON100 [29], CDMS [30], DAMA/LIBRA [31], PAMELA [32], and IceCube [33]. We can infer the existence of dark matter from experiments, but there is no corresponding neutral, stable, weakly interacting particle for it in the SM. Some theories beyond the SM have a natural dark matter candidate, such as SUSY, which predicts a lightest stable particle (LSP).

Most of the energy in the universe is due to dark energy, which is theorized to explain the acceleration of the expansion of the universe [34]. The fact that the universe is accelerating in its expansion has been observed by groups studying type Ia supernovae [35, 36], WMAP [25, 26], and Planck [27]. Dark energy is uniformly spread throughout the universe and is gravitationally self-repulsive. Like dark matter, there is no consideration of dark energy in the SM. Dark energy could be incorporated into General Relativity if the cosmological constant is reintroduced into the equations.

#### **2.2.1.4 The Baryon-Antibaryon Asymmetry**

There is more matter than antimatter in the universe. However, the Big Bang should have produced equal amounts of matter and antimatter, and they would have annihilated each other. Since that obviously did not happen, there must be some reason why there is more matter in the universe. Sakharov identified the necessary conditions for this to happen: a violation of baryon and lepton number, a universe out of thermal equilibrium, and a violation of charge-parity (CP) [37]. We have observed

CP violation in the weak interactions of quarks, but it is not enough to account for the matter dominance in the universe. The nature of the CP violation responsible for the baryon dominance in the universe is needed in order to understand why we have more matter than antimatter [2].

## **2.2.2 Theoretical Problems**

There are also several theoretical problems with the SM, which we will describe in this section [38].

### **2.2.2.1 Arbitrary Assumptions and Parameters**

There are a number of arbitrary assumptions and parameters in the SM. For example, there are many free parameters in the theory, including the masses of particles and parameters describing the mixings and couplings, such as the CKM angles and weak mixing angle. We know these values from experiments, but if the SM were a mature theory, it would explain them.

Furthermore, there are three generations of fermions in the SM, but why? Ordinary matter in an atom is made of up quarks, down quarks (which form protons and neutrons) and electrons, which are all in the first generation. What is the purpose of the other two generations? In addition, we could also ask why there are three generations and if there are more?

There are other questions about the assumptions of the SM, such as why are there three colors? Also, why are left-handed fermions in  $SU(2)$  doublets and right-handed fermions in  $SU(2)$  singlets?

### **2.2.2.2 The Hierarchy Problem, Naturalness, and Fine Tuning**

The Hierarchy Problem has to do with the fact that there is a large difference in the energy scales in particle physics: in particular, there is a large difference between the

electroweak scale ( $\sim 10^2 \text{ GeV}$ ) and the Planck scale ( $\sim 10^{19} \text{ GeV}$ ) [39].

The Higgs boson mass, to second order, is given by:

$$m_H^2 = 2\mu^2 + \Delta m_{H,i}^2 \quad (2.49)$$

where  $\Delta m_{H,i}^2$  indicates the quantum corrections from particle  $i$  (see Section 2.1.8.4). All massive particles couple to the Higgs boson, resulting in large quantum corrections to the Higgs boson mass. This is a problem because the Higgs boson has recently been discovered and its mass is about 125 GeV [6–9].

For example, the one-loop Feynman diagrams for fermions and scalars coupling to the Higgs boson are given in Fig. 2.11. These give corrections to the Higgs boson mass of:

$$\Delta m_{H,f}^2 = -\frac{|\lambda_f|^2}{8\pi^2} \Lambda_{\text{UV}}^2 + \dots \quad (2.50)$$

for the fermion and

$$\Delta m_{H,s}^2 = \frac{\lambda_s}{16\pi^2} \left[ \Lambda_{\text{UV}}^2 - 2m_s^2 \ln\left(\frac{\Lambda_{\text{UV}}}{m_s}\right) + \dots \right] \quad (2.51)$$

for the scalar.  $\lambda_f$  and  $\lambda_s$  are the coupling between the Higgs field and the fermion and scalar, respectively, and  $m_s$  is the mass of the scalar.  $\Lambda_{\text{UV}}$  is the ultraviolet momentum cutoff, which is the least energy scale at which new physics enters. If  $\Lambda_{\text{UV}}$  is of the order of the Planck scale, then these quantum corrections to the Higgs boson mass are several orders of magnitude larger than the observed mass of the Higgs boson.

It is possible that the quantum contributions to the Higgs boson mass could be made to cancel out, thus keeping the Higgs boson mass small. One way this could be done is by carefully choosing the parameters of the SM so that the quantum corrections cancel. However, this requires a large amount of fine tuning of the parameters,

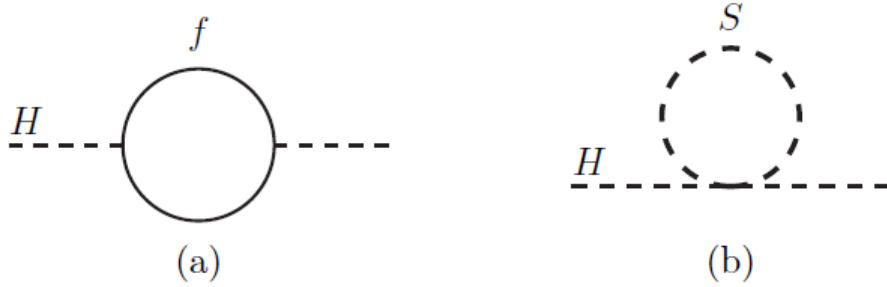


Figure 2.11: One-loop quantum corrections to the Higgs squared mass ( $m_H^2$ ), due to (a) a fermion  $f$  and (b) a scalar  $S$  [39].

and is generally considered to be “unnatural” and theoretically inelegant.

The quantum corrections could also cancel if a theory beyond the SM is introduced in which additional particles exist and more “naturally” cancel the quantum contributions. For example, in Supersymmetry (SUSY), additional bosons are introduced for every SM fermion, and additional fermions are introduced for every SM boson. The SUSY particle contributions would exactly cancel the contributions of their SM partners because the contributions would be the same but with opposite sign. See Section 2.3.1 for more on SUSY.

### 2.2.2.3 Strong CP Problem

As mentioned above, CP violation has been observed in the weak interactions, but a theoretical problem with the SM is that it has not been observed in QCD. In principle, there should be no reason why CP is violated in the electroweak interactions but not in the strong interactions, and so this creates a type of fine tuning problem. There are natural terms in the QCD Lagrangian that could break the CP symmetry, but no such symmetry breaking has been observed.

## 2.3 Theories Beyond the SM

There are many theories beyond the SM, and we will discuss some popular ones here [40]. Most of the theories try to incorporate gravity or dark matter, solve the hierarchy problem, or in some way, fix the problems with the SM. Here we will focus on different classes of theories, while in Section 4.2, we will focus on specific models that predict long-lived exotic particles.

### 2.3.1 Supersymmetry (SUSY)

Supersymmetry (SUSY) is a class of theories beyond the SM in which every particle in the SM has a *superpartner* that has a  $\frac{1}{2}$  difference in spin, but the remaining quantum numbers are the same [39]. In other words, every boson in the SM has a fermion superpartner, and every fermion in the SM has a boson superpartner. SUSY would double the number of elementary particles because none of the SM particles that differ by  $\frac{1}{2}$  in spin share other quantum numbers.

The SM particles and their superpartners are listed in Table 2.4. The leptons are paired with *sleptons*, the quarks with *squarks*, and the gauge bosons with *gauginos*. Slepton and squark are short for “scalar lepton” and “scalar quark,” respectively. As one can see in the table, the symbol for a superpartner is the same as its corresponding SM particle, except with a tilde ( $\tilde{\phantom{x}}$ ) over it. Each SM particle and superpartner form a chiral or gauge supermultiplet. The Higgs boson would be in a chiral supermultiplet, and there are two Higgs supermultiplets, in order to preserve the electroweak gauge symmetry.

Table 2.4: The SM particles and their superpartners. RH means right-handed, and LH mean left-handed.

SM Particle	SM Symbol	Superpartner	SUSY Symbol
<b>Leptons</b>		<b>Sleptons</b>	
RH electron, muon, tau	$e_R, \mu_R, \tau_R$	RH selectron, smuon, stau	$\tilde{e}_R, \tilde{\mu}_R, \tilde{\tau}_R$
LH electron, muon, tau	$e_L, \mu_L, \tau_L$	LH selectron, smuon, stau	$\tilde{e}_L, \tilde{\mu}_L, \tilde{\tau}_L$
Electron, muon, tau neutrino	$\nu_e, \nu_\mu, \nu_\tau$	Electron, muon, tau sneutrino	$\tilde{\nu}_e, \tilde{\nu}_\mu, \tilde{\nu}_\tau$
<b>Quarks</b>		<b>Squarks</b>	
RH up, charm, top quark	$u_R, c_R, t_R$	RH up, charm, top squark	$\tilde{u}_R, \tilde{c}_R, \tilde{t}_R$
LH up, charm, top quark	$u_L, c_L, t_L$	LH up, charm, top squark	$\tilde{u}_L, \tilde{c}_L, \tilde{t}_L$
RH down, strange, bottom quark	$d_R, s_R, b_R$	RH down, strange, bottom squark	$\tilde{d}_R, \tilde{s}_R, \tilde{b}_R$
LH down, strange, bottom quark	$d_L, s_L, b_L$	LH down, strange, bottom squark	$\tilde{d}_L, \tilde{s}_L, \tilde{b}_L$
<b>Gauge Bosons</b>		<b>Gauginos</b>	
W bosons	$W^\pm, W^0$	Winos	$\tilde{W}^\pm, \tilde{W}^0$
B boson	B	Bino	$\tilde{B}$
Gluon	$g$	Gluino	$\tilde{g}$
Neutral Higgs	$h^0, H^0, A^0$	Neutral Higgsinos	$\tilde{h}^0, \tilde{H}^0, \tilde{A}^0$
Charged Higgs	$H^\pm$	Charged Higgsinos	$\tilde{H}^\pm$
Graviton	$G$	Gravitino	$\tilde{G}$

Since many of the superpartners share the same quantum numbers, the gauge eigenstates listed in Table 2.4 will mix to form mass eigenstates, as listed in Table 2.5. The mass eigenstates of the first and second generation sleptons and squarks are the same as their gauge eigenstates because the amount of mixing is proportional to the Yukawa couplings, and these couplings for the first and second generations are small. The Yukawa couplings describe the interaction between a scalar field and a Dirac field: in this case, between the Higgs field and the fermion fields. The Yukawa couplings for the third generation, on the other hand, are large, and so the mass eigenstates are *staus*, *stops*, and *sbottoms*, as listed in the table. The winos, binos,

and Higgsinos mix to form *charginos* and *neutralinos*. The gluino is a color octet fermion, and so does not mix with any other states. Similarly, the gravitino's mass eigenstate is the same as its gauge eigenstate. The mass eigenstate subscript denotes how massive the state is, with one denoting the lowest mass eigenstate.

Table 2.5: The superpartner mixing states.

Names	Gauge Eigenstates	Mass Eigenstates
Sleptons	$\tilde{e}_R, \tilde{e}_L, \tilde{\nu}_e$	(same)
	$\tilde{\mu}_R, \tilde{\mu}_L, \tilde{\nu}_\mu$	(same)
	$\tilde{\tau}_R, \tilde{\tau}_L, \tilde{\nu}_\tau$	$\tilde{\tau}_1, \tilde{\tau}_2, \tilde{\nu}_\tau$
Squarks	$\tilde{u}_R, \tilde{u}_L, \tilde{d}_R, \tilde{d}_L$	(same)
	$\tilde{c}_R, \tilde{c}_L, \tilde{s}_R, \tilde{s}_L$	(same)
	$\tilde{t}_R, \tilde{t}_L, \tilde{b}_R, \tilde{b}_L$	$\tilde{t}_1, \tilde{t}_2, \tilde{b}_1, \tilde{b}_2$
	$\tilde{W}^\pm, \tilde{H}^\pm$	$\tilde{\chi}_1^\pm, \tilde{\chi}_2^\pm$
Gauginos	$\tilde{W}^0, \tilde{B}, \tilde{H}_u^0, \tilde{H}_d^0$	$\tilde{\chi}_1^0, \tilde{\chi}_2^0, \tilde{\chi}_3^0, \tilde{\chi}_4^0$
	$\tilde{g}$	(same)
	$\tilde{G}$	(same)

Once this symmetry between bosons and fermions is assumed, the hierarchy problem is solved naturally because the higher order contributions to the scalar masses are canceled. The correction from a scalar loop will be the opposite sign as the correction resulting from a fermion loop, so if the SM particles had exactly the same mass as their superpartners, the terms would cancel exactly. However, the superpartners have not been observed with the same mass as their SM partners. But if the superpartners have somewhat similar masses to their SM partners, there will still be a large cancellation in the correction factors and the Higgs mass can be kept relatively small.

A new symmetry called *R*-parity is often assumed in SUSY models. The SM particles have even *R*-parity ( $R = +1$ ), while the SUSY particles have odd *R*-parity ( $R = -1$ ). If *R*-parity is conserved, the superpartners will be produced in pairs, and the lightest supersymmetric particle (LSP) will be neutral and stable, thus making it a natural dark matter candidate.

### 2.3.1.1 SUSY Breaking

To explain why SUSY has not yet been observed, one usually assumes that the masses of the superpartners are somewhat large, thus making it difficult to detect them at particle colliders without having sufficiently high energies. If the masses of the SM particles and their superpartners are not the same, then the symmetry must be spontaneously broken; we call this SUSY breaking.

SUSY models can be classified by the mediation of the SUSY breaking. SUSY could be broken by interactions that take place at the gravitational strength; we call this gravity mediation. Some SUSY models where the SUSY breaking is mediated by gravity are *minimal supergravity* (mSUGRA) and *anomaly mediated supersymmetry breaking* (AMSB). SUSY could also be broken by gauge interactions; this model is called *gauge mediated supersymmetry breaking* (GMSB). SUSY might also be broken by bulk mediation. This class of models combines SUSY with extra dimensions theories, which are described below. Some or all of the SM fields are sequestered on a “brane,” a kind of slice through the full “bulk” space that includes the extra dimensions. SUSY is broken by dynamics on a different brane. The messengers of SUSY breaking to the SM sector are via fields that propagate in the full bulk space. An example of a bulk mediation SUSY model is *gaugino mediation*. See Section 4.2 for more on a few specific SUSY models.

### 2.3.2 Extra Dimensions

Theories with more than the usual three spatial dimensions have been proposed over the years, largely in an effort to unify the fundamental forces [1]. The first theory of extra dimensions was proposed by Kaluza and Klein in 1921 [41]. Since then, several types of extra dimensions have been proposed, including large extra dimensions and warped extra dimensions.



### 2.3.2.1 Kaluza-Klein Theories

Kaluza and Klein developed a theory of five spacetime dimensions in the early 1920s in order to try to unify gravity and electromagnetism [41–44]. In the theory, the fifth dimension would have to be very small, thus explaining why we do not observe it in our normal macroscopic lives. Kaluza-Klein theories, which extend this idea to more than five compact extra dimensions, are still being developed today. Kaluza-Klein theories gained momentum in the 1980s, after string theory proposed extra dimensions in order to create a quantum theory of gravity. See Section 2.3.5 for more on string theory.

### 2.3.2.2 Large Extra Dimensions

In 1998, Arkani-Hamed, Dimopoulos, and Dvali realized that theories with extra dimensions could be created where the dimensions were larger than the Planck length if only gravity were allowed to propagate in the extra dimensions [45, 46]. In the ADD theory, the weakness of gravity could be explained by having two or more extra dimensions in which only gravity could propagate. If gravity propagates in  $4 + d$  dimensions, then we know the force between two bodies of masses  $m_1$  and  $m_2$  separated by a distance  $r$  is given by:

$$F = G_{grav} \frac{m_1 m_2}{r^{2+d}} \quad (2.52)$$

where  $G_{grav}$  is the equivalent to Newton's constant in  $4 + d$  dimensions. If this is true, then the gravity force decreases faster as  $r$  increases, that is,  $F \propto 1/r^{2+d}$ , than for the gauge forces, where  $F \propto 1/r^2$ . These extra dimensions would be between 1 mm and  $1 \text{ TeV}^{-1}$ .

### 2.3.2.3 Warped Extra Dimensions

Shortly after the publication of the first ADD paper, Randall and Sundrum discovered that if extra dimensions were curved or “warped,” as opposed to the flat extra dimensions we have described so far, gravitons would behave differently than gauge bosons, which would explain why they couple differently to matter [47]. The RS theory is a 5D Anti-de Sitter (AdS) spacetime theory where the extra dimension is compactified. Because the fifth dimension is warped, gravity is strong on one brane, but not on the brane that we experience.

### 2.3.3 New Strong Dynamics and Little Higgs

There are several BSM theories that address electroweak symmetry breaking, but without introducing a Higgs boson [48]. Instead, electroweak symmetry breaking is governed by some new strong interactions, and in this way, mass is given to the W and Z bosons. New strong dynamics theories have a larger gauge group, which spontaneously breaks down to the SM gauge group, thus explaining why we have not observed these interactions at the energies we can currently probe. The first and simplest of these models was called Technicolor, and it was posited to be similar to QCD, but with a much larger characteristic energy scale. In order to produce the quark and lepton masses, Technicolor must be extended to include additional gauge interactions.

Theories with new strong dynamics are attractive because they avoid the hierarchy problem, as there is usually no Higgs boson in these theories. However, with the discovery of the Higgs boson, it has become more important to include the new boson in the BSM strong dynamics theories. These new theories do not usually predict a particle like the Higgs boson, but they can accommodate such a particle.

There are a number of Little Higgs theories, sometimes called pseudo-Nambu-Goldstone boson (PNGB) Higgs theories [49, 50]. These theories state that the Higgs

boson is a pseudo-Nambu-Goldstone boson, corresponding to a spontaneously broken global symmetry of a new strong interaction at about 10 TeV. This spontaneously broken global symmetry stabilizes the Higgs boson mass. The global symmetry is also explicitly broken because part of the global symmetry is gauged in order to become the weak interaction. Therefore, the Higgs boson is naturally light, compared to the 10 TeV scale.

The explicit breaking of the global symmetry requires that we make additional assumptions to avoid quadratic divergences from loops of gauge bosons and top quarks. What is typically done is to introduce heavy partners for the SM particles and have them cancel the divergences at the loop diagram level.

One of the simplest models of this type is the Little Higgs with T-parity model, in which every SM particle has a heavy partner with the same quantum numbers except the top quark, which has extra partners [51, 52]. The lightest partner particle is stable due to T-parity and therefore makes a good dark matter candidate. Another popular model is the Twin Higgs model, in which the partner particles form a mirror copy of their SM particles under some hidden gauge interactions [53].

### 2.3.4 Hidden Valley Theories

Hidden valley theories are BSM theories that propose new, hidden sectors that contain relatively light particles [54, 55]. We would have already found these new light particles, were it not for some barrier, possibly an energy barrier, preventing us from reaching this sector. The new particles would interact minimally with SM particles and could be subject to new conservation laws. SUSY or other BSM theories discussed above could have hidden sectors.

In hidden valley theories, the SM gauge group  $G_{\text{SM}}$  is extended by a non-Abelian group  $G_\nu$ . The new, low mass valley particles are charged under  $G_\nu$  but neutral under  $G_{\text{SM}}$ , while SM particles are neutral under  $G_\nu$ . Higher dimension operators

allow interactions between SM and hidden valley particles. In a confining hidden valley model, all the new particles assemble into  $G_\nu$ -neutral “ $\nu$ -hadrons,” which can decay to SM particles.

Hidden valley theories typically have a few common characteristics. There are often long-lived  $\nu$ -hadrons, which could decay at a displaced vertex in an LHC detector. Some long-lived  $\nu$ -hadrons could be absolutely stable, giving rise to a dark matter candidate. However, in general, hidden valley particles could have a wide range of lifetimes, such that they could decay promptly, produce displaced vertices, or decay after passing through the detector. Furthermore, some  $\nu$ -hadrons would decay preferentially to heavy flavor particles, while others would decay more democratically to any fermion-antifermion or fermion-antifermion plus another  $\nu$ -hadron state. Other final states could include two or three gluons, or pairs of W or Z bosons. Another common characteristic of hidden valley theories is that  $\nu$ -hadron production multiplicities at the LHC may be large, especially if the  $\nu$ -confinement scale is much less than 1 TeV.

Much work has been done recently to incorporate dark matter into hidden valley theories [56, 57]. If the dark matter particle existed in a hidden, dark sector, it would help to explain why we have not yet observed the dark matter particle. Models have been developed where a variety of particles can mediate between the dark sector and our visible sector.

### 2.3.5 Grand Unified Theories and Theories of Everything

Some theories beyond the SM have been developed with the goal of unifying the fundamental forces [2, 40]. Electricity and magnetism were unified into the theory of electromagnetism by James Clerk Maxwell in 1873, and then the weak force and electromagnetism were unified into the electroweak force in the 1960s. We could theoretically continue this trend and unify the electroweak force and the strong force;

such theories are called Grand Unified Theories (GUTs).

We might also take it one step further and unify all four fundamental forces; that is, add in gravity as well. Such theories are called Theories of Everything (TOE). However, as they are currently formulated, general relativity and quantum mechanics are fundamentally incompatible. One TOE that has gained popularity in recent years is Superstring Theory, often simply called String Theory. String Theory holds that the elementary particles are really vibrations of tiny supersymmetric strings, rather than tiny point particles. By modeling particles as one or more dimensional strings, and often by invoking the existence of several other extra dimensions, String Theory could provide a quantum theory of gravity. However, even if SUSY exists, it would be very difficult to prove String Theory was correct.

We can test the SM and theories beyond the SM at particle colliders, like the Large Hadron Collider (LHC), and with particle detectors, like the Compact Muon Solenoid (CMS) Experiment.

## Chapter 3

# THE COMPACT MUON SOLENOID EXPERIMENT AT THE LARGE HADRON COLLIDER

The Compact Muon Solenoid (CMS) Experiment is a general-purpose detector that measures the properties of particles produced from  $pp$  and heavy ion elastic collisions in the Large Hadron Collider (LHC). The LHC accelerates proton bunches around a ring that is 27 km in circumference and has a design center-of-mass (C.M.) energy  $\sqrt{s}$  of 14 TeV. The proton bunches collide at regular intervals along the ring, and one such collision point is at the center of the CMS detector. Then, the decay products of these collisions travel radially outward through the different sub-detectors of CMS. Depending on how these particles interact with the different materials in each of the sub-detectors, one can identify and characterize them.

### 3.1 The Large Hadron Collider (LHC)

The LHC is the world's largest high-energy particle accelerator and collider [58–60], located at the European Center for Nuclear Research (CERN) in Geneva, Switzerland.

The accelerator primarily collides protons, but it also collides heavy nuclei, usually lead ions, for a few months each year<sup>1</sup>.

The LHC was designed in the 1980s and 1990s, and the CERN Council approved the construction of the LHC in 1994. The four main experiments around the LHC ring, namely, A Large Ion Collider Experiment (ALICE), A Toroidal LHC Apparatus (ATLAS), CMS, and Large Hadron Collider beauty (LHCb), received official approval and started construction between 1996 and 1998. ATLAS and CMS are large, general-purpose detectors that can study a wide variety of fundamental processes. The primary aim of these two experiments is to discover and study the Higgs boson and other new physics beyond the SM. The ALICE experiment was built to study the quark-gluon plasma using collisions of heavy ions, and LHCb studies the matter-antimatter imbalance by focusing on B meson physics. Since the late 1990s, three other smaller experiments have been installed around the LHC: TOTal Elastic and diffractive cross section Measurement (TOTEM), Monopole and Exotics Detector at the LHC (MoEDAL), and Large Hadron Collider forward (LHCf). See Fig. 3.1 for a diagram of the layout of the LHC.

---

<sup>1</sup>Protons are accelerated around the LHC ring instead of electrons because they are more massive, so they lose less energy through synchrotron radiation, which is the radiation of charged particles in a curved trajectory





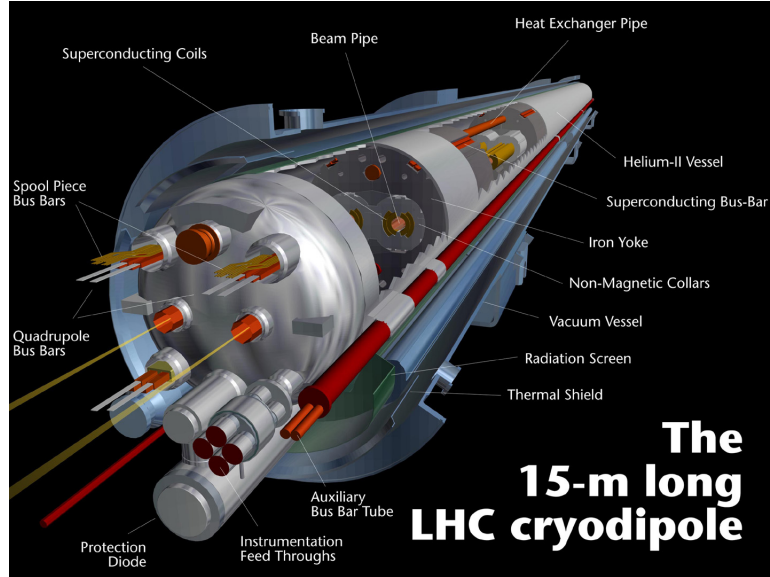


Figure 3.2: Diagram of an LHC dipole. The two beam pipes can be seen at the center of the dipole [62].

### 3.1.1 The Proton Acceleration

At the design specifications, the proton bunches will travel around the LHC ring at 7 TeV each. In order to get the protons to this energy, they are accelerated in several steps. First of all, protons are extracted from hydrogen atoms by stripping the electrons from the hydrogen atoms. The protons are accelerated to 50 MeV using the Linac2, a linear accelerator. They are then injected into the Proton Synchrotron Booster, which accelerates the protons to 1.4 GeV; then into the Proton Synchrotron, which accelerates them to 25 GeV; and finally into the Super Proton Synchrotron (SPS), which accelerates them to 450 GeV. After the SPS, the protons are fed into the LHC, which accelerated them to 4 TeV in 2012, but will eventually take them to 7 TeV. See Fig.3.3 for a diagram of the CERN accelerator complex. The proton beams usually circulate and collide around the LHC ring for several hours; one period of beam injection and circulation is called a *fill*. As the protons continue to collide during the fill, the number of protons per bunch decreases, and thus so too does the probability that any two protons will collide. Thus, the event rate naturally decreases

throughout the fill.

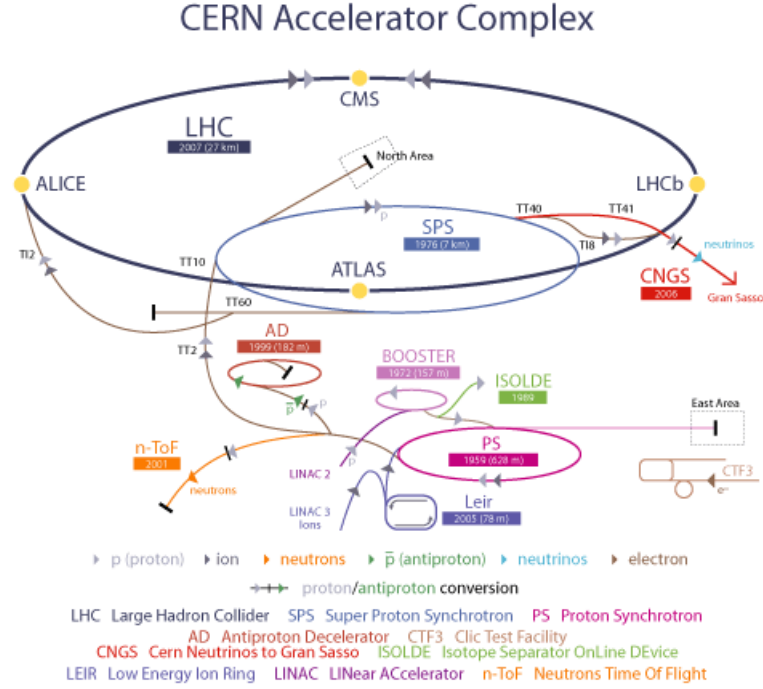


Figure 3.3: Diagram of the CERN accelerator complex.

Protons are accelerated in the LHC with eight radio frequency (RF) cavities per beam. RF cavities contain oscillating electromagnetic fields, and the phase of the oscillations is adjusted so that when protons enter the cavities, they become grouped together in bunches and are accelerated in the ring. The RF cavities, which operate at 400 MHz, keep the protons tightly bunched in order to maximize the number of proton collisions with each crossing. At the design specifications, each proton bunch will have  $1.1 \times 10^{11}$  protons, and there will be 2808 proton bunches per beam and 25 ns between each bunch. Figure 3.4 shows the bunch structure at design specifications.

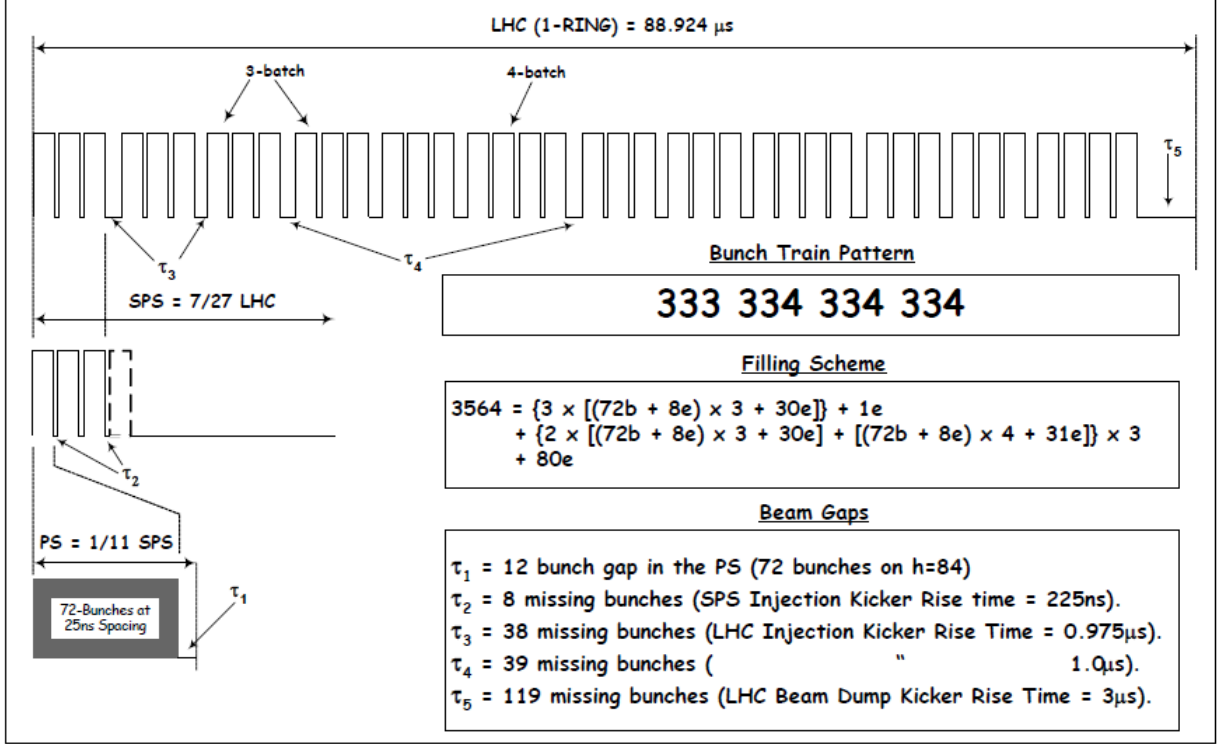


Figure 3.4: Diagram of the LHC bunch filling scheme, at 25 ns and with 3564 total bunches (2808 colliding) [63]. See also [64, 65] for updates.

### 3.1.2 Luminosity, Vertices, and Pileup

The number of events in a collider is given by:

$$N = \sigma \int \mathcal{L} dt \quad (3.1)$$

where  $\mathcal{L}$  is the instantaneous luminosity,  $\int \mathcal{L} dt$  is the integrated luminosity, and  $\sigma$  is the interaction cross section. The instantaneous luminosity depends only on the beam parameters and can be written for a Gaussian beam distribution, assuming the parameters for the two beams are the same, as:

$$\mathcal{L} = \frac{N_b^2 n_b f_{rev} \gamma}{4\pi \epsilon_n \beta * \sqrt{1 + \left(\frac{\theta_c \sigma_z}{2\sigma^*}\right)^2}} \quad (3.2)$$

See Table 3.1 for the definitions and design values of the parameters in Equation 3.2. A *lumi section* is the smallest period of time, defined to be 23 seconds, in which the instantaneous luminosity should be constant.

Table 3.1: The variables used in the definition of instantaneous luminosity [59].

Symbol	Definition	Value and/or Units
$N_b$	Number of protons per bunch	$1.1 \times 10^{11}$
$n_b$	Number of proton bunches per beam	2808
$f_{rev}$	Frequency of revolution	11.245 kHz
$\gamma$	$\frac{1}{\sqrt{1-\beta^2}}$ for the protons	7461
$\epsilon_n$	Normalized transverse beam emittance	$3.75 \mu\text{m rad}$
$\beta^*$	Optical $\beta$ function at the interaction point	55 cm
$\theta_c$	Beam crossing angle	$285 \mu\text{ rad}$
$\sigma_z$	RMS longitudinal bunch length	7.55 cm
$\sigma^*$	RMS transverse beam size	$16.7 \mu\text{m}$

When two protons collide in a head-on, high energy collision, they create a *primary vertex*. Subsequent decays of the daughter particles of this interaction happen at *secondary vertices*. In addition, there could be more than one head-on proton collision in a single bunch crossing, due to the large number of protons per bunch. This phenomenon is called *in-time pileup*; only the most energetic proton collision is considered, and the other primary vertices created from less energetic proton collisions are called *pileup vertices*. See Fig. 3.5 for a sketch of an LHC collision and the different types of vertices, and Fig. 3.6 for a pileup event in CMS in 2012 data. There is also *out-of-time pileup*, which is when there are particles still in the detector from previous bunch crossings. Most of the time when *pileup* is mentioned, it refers to in-time pileup, and so that is what we will do here. At the LHC, especially in 2012, pileup was a significant problem, with an average of about 21 and a maximum of 35 pileup interactions per crossing recorded at CMS [66], even though this was about the number of pileup interactions expected at the LHC design specifications (almost twice the C.M. energy and 20-40% increased instantaneous luminosity). Fig. 3.7 shows the

distribution of the average pileup in CMS in 2012.

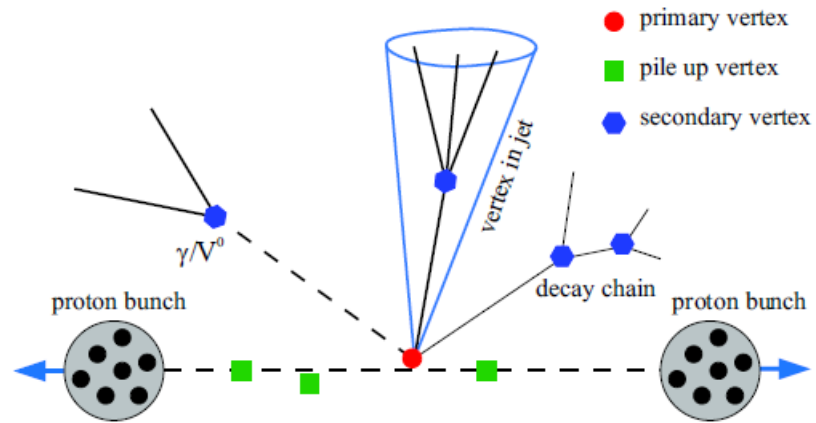


Figure 3.5: Diagram of a  $pp$  collision at the LHC [67].

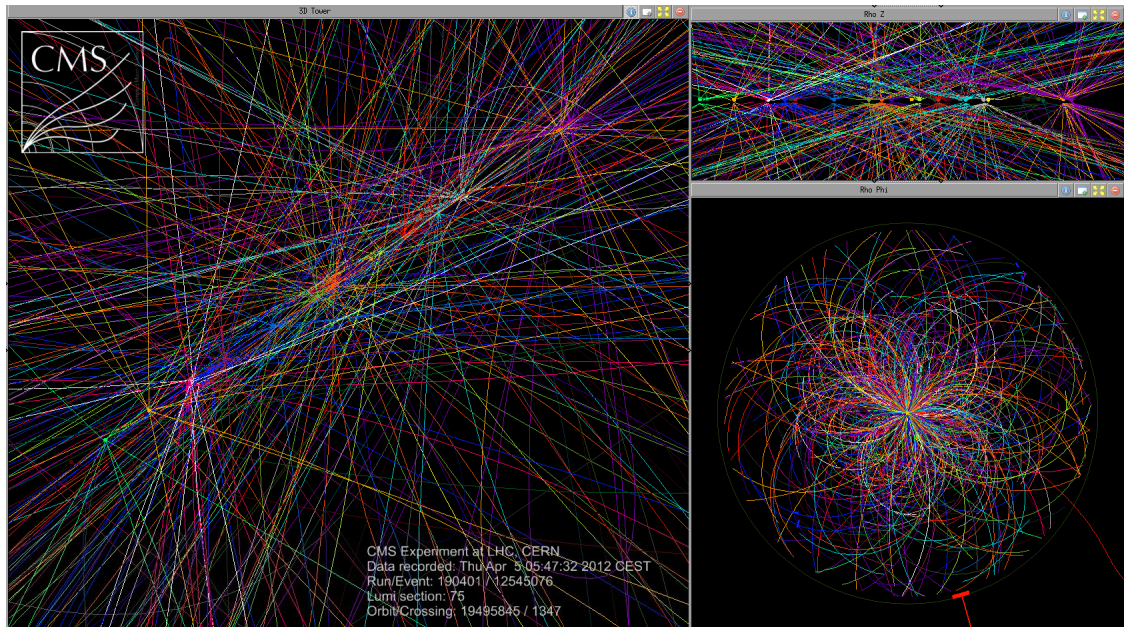


Figure 3.6: Event display of a collision in CMS, showing 29 distinct pileup vertices [68].

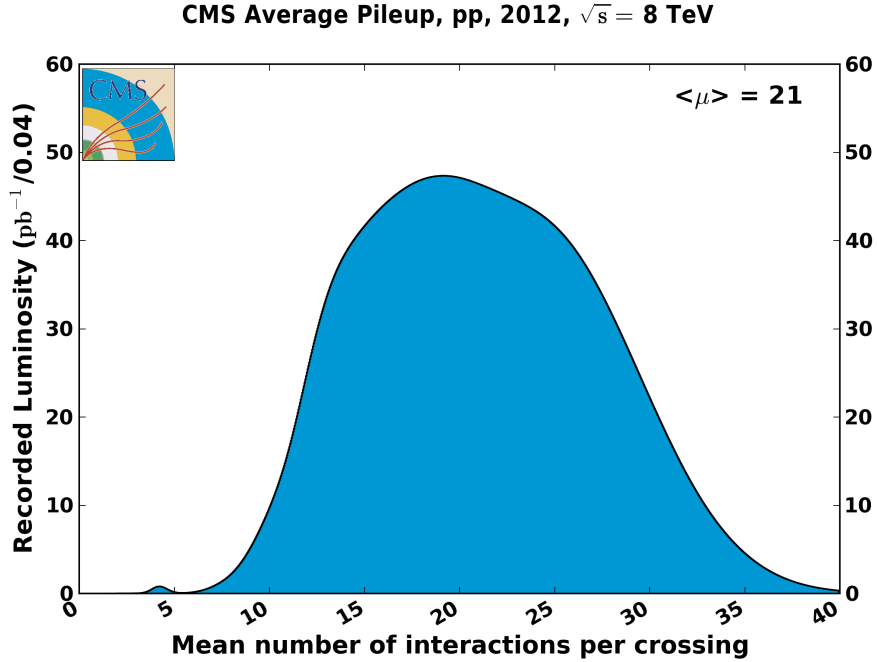


Figure 3.7: Distribution of the average pileup in CMS in 2012 [66].

### 3.1.3 Data-Taking at the LHC

The LHC first operated at a C.M. energy of 7 TeV in 2010 and 2011, and then at 8 TeV in 2012. Short heavy ion runs were performed at the end of 2011 and the beginning of 2013, after which the LHC shut down for several years. This first long shutdown (LS1) lasted until early 2015 and was intended to allow the LHC and the experiments around the ring to prepare for running at 13 TeV. The data used in this thesis corresponds to  $19.7 \text{ fb}^{-1}$  of data collected at 8 TeV in 2012, during which time there were usually about 1380 bunches colliding and 50 ns spacing between them. The LHC delivered  $23.3 \text{ fb}^{-1}$  of data to CMS and ATLAS in 2012, and out of the data recorded by CMS,  $20.6 \text{ fb}^{-1}$  was certified to be suitable for analyses using muons. The analysis only uses  $19.7 \text{ fb}^{-1}$  of data because there was a problem with the configuration of the trigger for the analysis in the beginning of the 2012 run.

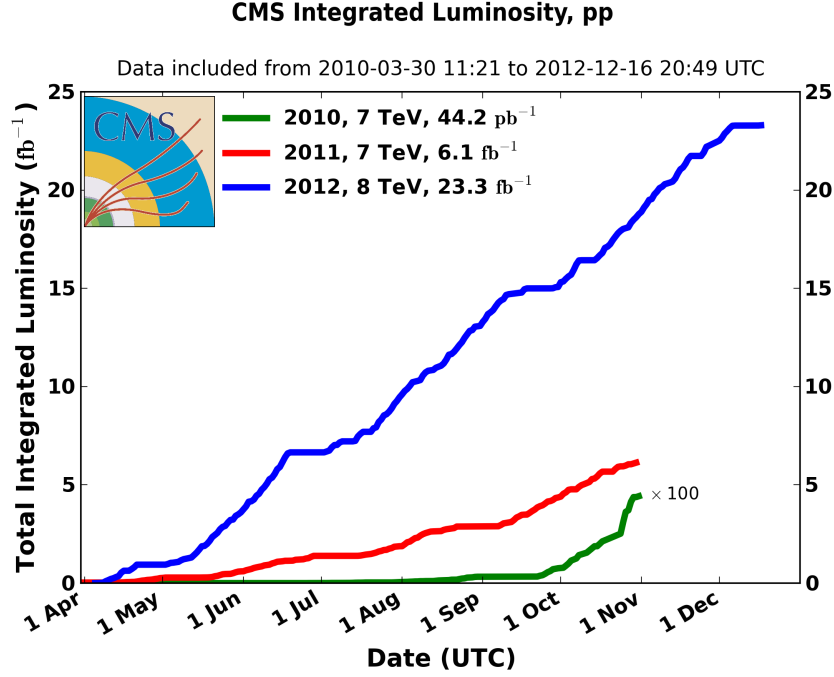


Figure 3.8: The delivered integrated luminosity at CMS for  $pp$  collisions in 2010-2012 [66].

## 3.2 The Compact Muon Solenoid Experiment (CMS)

CMS was so named for three key features of its design [1, 69–72]. First of all, it is *compact* in the sense that it has a small volume, when compared to A Toroidal LHC Apparatus (ATLAS), the other general-purpose detector at the LHC. CMS has a 15 m diameter and 21.5 m length, and it is also extremely dense, weighing 12.5k tons. Secondly, the CMS design focused on the *muon* system, optimizing the experiment to measure high energy muons. The final key feature of the CMS design is its *solenoid* magnet, which curves the tracks of charged particles within the detector, allowing for a precise measurement of the particles' momenta.

CMS began to be constructed in 1999, and was finally completely assembled in the cavern and ready for the first beams in the fall of 2008. The first 7 TeV collisions

happened in CMS in March 2010. CMS recorded  $44.2 \text{ pb}^{-1}$  of data at 7 TeV in 2010,  $6.1 \text{ fb}^{-1}$  of data at 7 TeV in 2011, and  $23.3 \text{ fb}^{-1}$  of data at 8 TeV in 2012 [66].

The CMS detector is composed of several subdetectors: the inner tracker, the electromagnetic and hadronic calorimeters, and the muon system. Particles created from the  $pp$  collisions will travel radially outward through these subdetectors, and they can be identified from the signatures they leave in the subdetectors. As previously mentioned, there is a superconducting solenoid magnet, located just outside the hadronic calorimeter, which serves to bend the trajectories of charged particles. The final components of the CMS detector are the trigger, which selects which events the experiment records, and the data acquisition (DAQ), which collects and digitizes the data. See Figs. 3.9 and 3.10 for a diagram and photograph, respectively, of CMS.

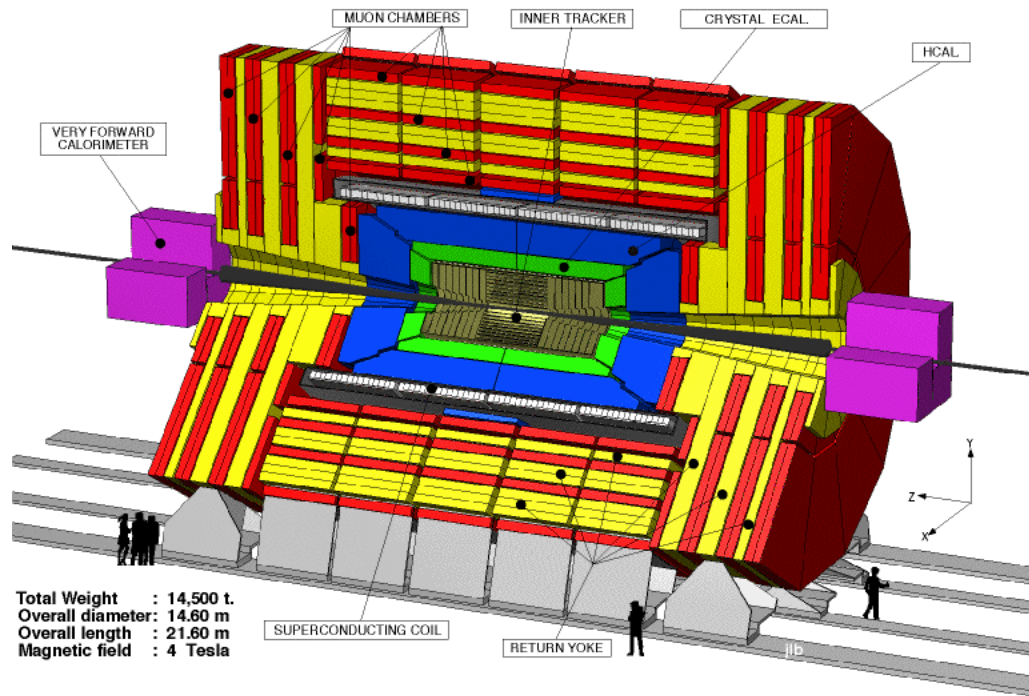


Figure 3.9: Diagram of the CMS detector.



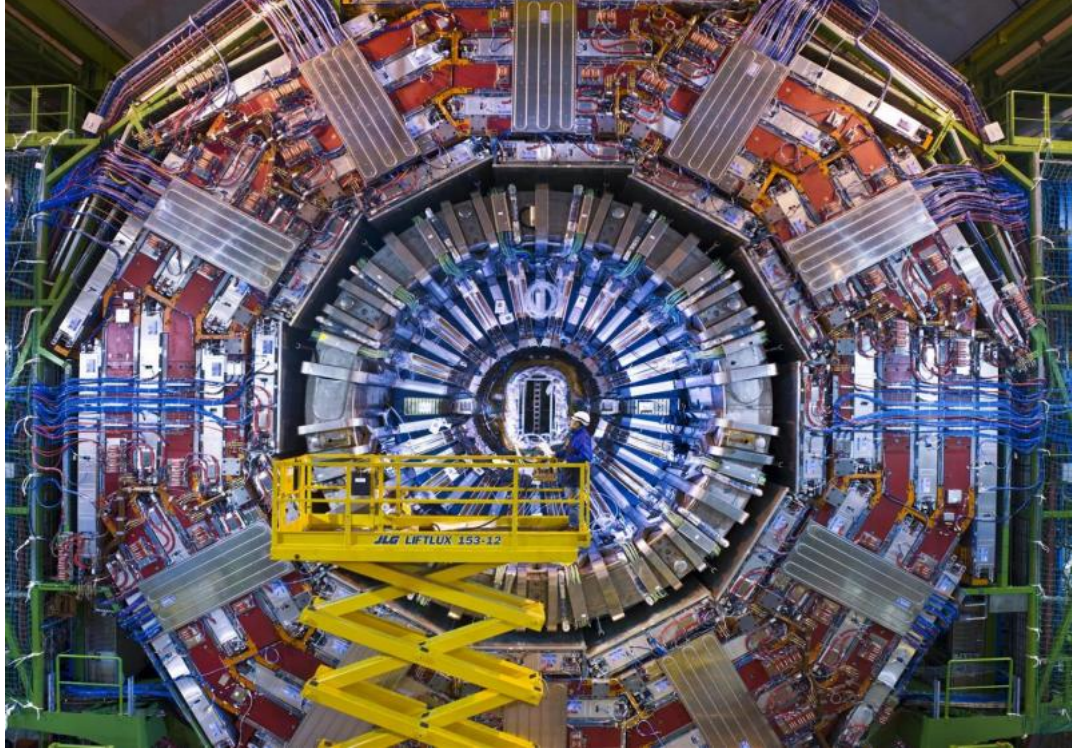


Figure 3.10: Photograph of the CMS detector.

In the next section, we will briefly cover the passage of elementary particles through matter, to understand what is happening to particles in CMS. In the rest of this chapter, we will discuss the definition of the CMS coordinate system, the superconducting magnet, and then the four subdetectors of CMS. Afterward, we will discuss the trigger and DAQ, followed by how events and objects are reconstructed in CMS.

### 3.2.1 Particle Interactions in Matter

To begin to understand how the CMS detector distinguishes different particles, we should first briefly discuss the passage of elementary particles through matter. Relativistic charged particles primarily interact with matter through inelastic collisions with atomic electrons and inelastic collisions with atomic nuclei [1–3]. Interactions with atomic electrons can result in two possibilities: excitation or ionization. An

incoming particle can excite atomic electrons to higher energy states; often, when the electrons de-excite back to the ground state, a photon is emitted, which can be detected as scintillation light. A relativistic charged particle can also ionize atomic electrons, meaning that the electrons are completely stripped from the atom. The mean rate of ionization energy loss of relativistic charged particles can be described by the Bethe equation:

$$-\left\langle \frac{dE}{dx} \right\rangle = KQ^2 \frac{Z}{A} \frac{1}{\beta^2} \left[ \frac{1}{2} \ln \frac{2m_e \beta^2 \gamma^2 T_{max}}{I_e^2} - \beta^2 - \frac{\delta(\beta\gamma)}{2} \right] \quad (3.3)$$

See Table 3.2 for the definition of the variables in this equation.

Table 3.2: The variables used in the Bethe formula [1].

Symbol	Definition	Value and/or Units
$m_e$	Electron mass	0.511 MeV
$r_e$	Classical electron radius= $\frac{e^2}{4\pi\epsilon_0 m_e}$	2.82 fm
$Q$	Charge of incident particle	
$Z$	Atomic number of absorber	
$A$	Atomic mass of absorber	g mol <sup>-1</sup>
$N_A$	Avagadro's number	$6.022 \times 10^{23}$ mol <sup>-1</sup>
$K$	$4\pi N_A r_e^2 m_e$	$K/A = 0.307 \text{ MeV g}^{-1}\text{cm}^2$ for A=1 g mol <sup>-1</sup>
$\beta$	Speed per unit $c$ of incident particle	
$\gamma$	$\frac{1}{\sqrt{1-\beta^2}}$	
$T_{max}$	Maximum kinetic energy that can be transferred to a free electron in a single collision	MeV
$I_e$	Mean excitation energy	eV
$\delta(\beta\gamma)$	Density effect correction to ionization energy loss	

Relativistic charged particles can also interact with the nuclei. If a particle interacts electromagnetically with the nucleus, a photon is usually emitted and radiation occurs. The particle undergoes bremsstrahlung electromagnetic radiation, which is the deceleration of the charged particle when deflected by the nucleus, and experi-

ences significant energy loss. A particle can also interact via the strong force with a nucleus, if it is a hadron. Hadrons interacting with the nucleus will create many quarks and antiquarks that combine in many ways to make mesons and baryons, a process known as *hadronization*.

We have discussed electromagnetic and strong interactions of particles with matter; the only force left to mention is the weak force, as gravity is extremely weak at these length scales. Neutrinos interact via the weak force, but their presence in high energy experiments can only be indirectly detected from the imbalance of momentum measured from all the particles in an event. See Section 3.2.11 for a further discussion of neutrinos and missing momentum.

We will now go on to discuss the behavior of a few specific particles in matter. The behavior of muons in matter is shown in Fig. 3.11, which depicts the rate of energy loss  $dE/dx$  as a function of momentum for muons traveling through copper. Muons will primarily lose energy in the detector from ionization, if their momentum is sufficiently low, that is, less than several hundred GeV, or they will primarily lose energy through radiation, if their momentum is greater than several hundred GeV.

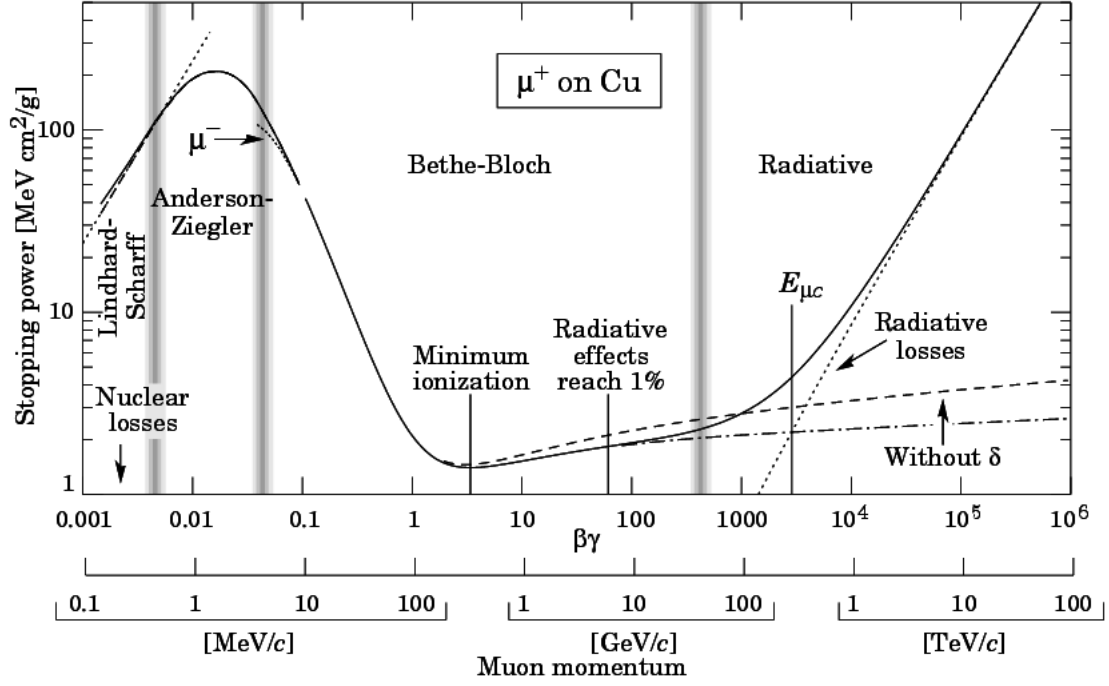


Figure 3.11: Stopping power ( $\langle -dE/dx \rangle$ ) for positive muons in copper as a function of  $\beta\gamma = p/Mc$  over nine orders of magnitude in momentum (12 orders of magnitude in kinetic energy). Solid curves indicate the total stopping power. Vertical bands indicate boundaries between different approximations [1].

The energy loss of electrons in matter is shown in Fig.3.12. Ionization dominates the electron/positron energy loss at low energies. Then, ionization rates fall off logarithmically with energy, while bremsstrahlung losses rise almost linearly and dominate above a few tens of MeV in most materials. Given that electrons traveling in CMS typically have energies above a few GeV, bremsstrahlung is by far the dominate process for electrons in CMS.

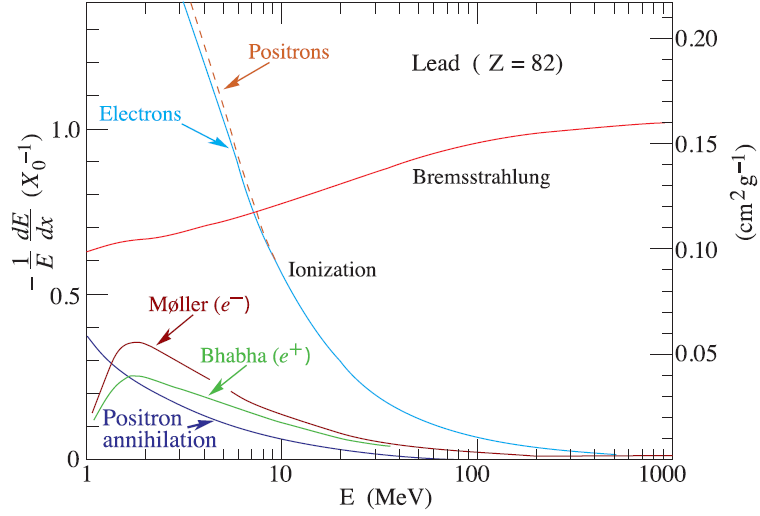


Figure 3.12: Fractional energy loss per radiation length in lead as a function of electron or positron energy. Electron (positron) scattering is considered as ionization when the energy loss per collision is below 0.255 MeV, and as Moller (Bhabha) scattering when it is above [1].

Figures 3.13 and 3.14 describe the energy loss of photons in matter. At low energies, the photoelectric effect dominates, and for photon energies of a few MeV, the Compton Effect is dominant, but  $e^+e^-$  pair production dominates as the energy increases above 1 GeV.

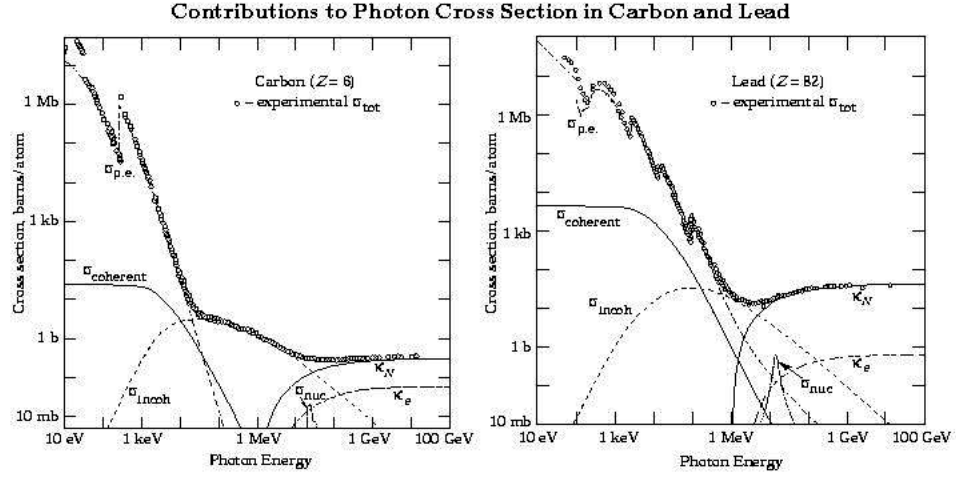


Figure 3.13: Photon total cross sections as a function of energy in carbon and lead, showing the contributions of different processes:

$\sigma_{p.e.}$  = Atomic photoelectric effect (electron ejection, photon absorption)

$\sigma_{Rayleigh}$  = Rayleigh (coherent) scattering – atom neither ionized nor excited

$\sigma_{Compton}$  = Incoherent scattering (Compton scattering off an electron)

$\kappa_{nuc}$  = Pair production, nuclear field

$\kappa_e$  = Pair production, electron field

$\sigma_{g.d.r.}$  = Photonuclear interactions, most notably the Giant Dipole Resonance. In these interactions, the target nucleus is broken up. [1]

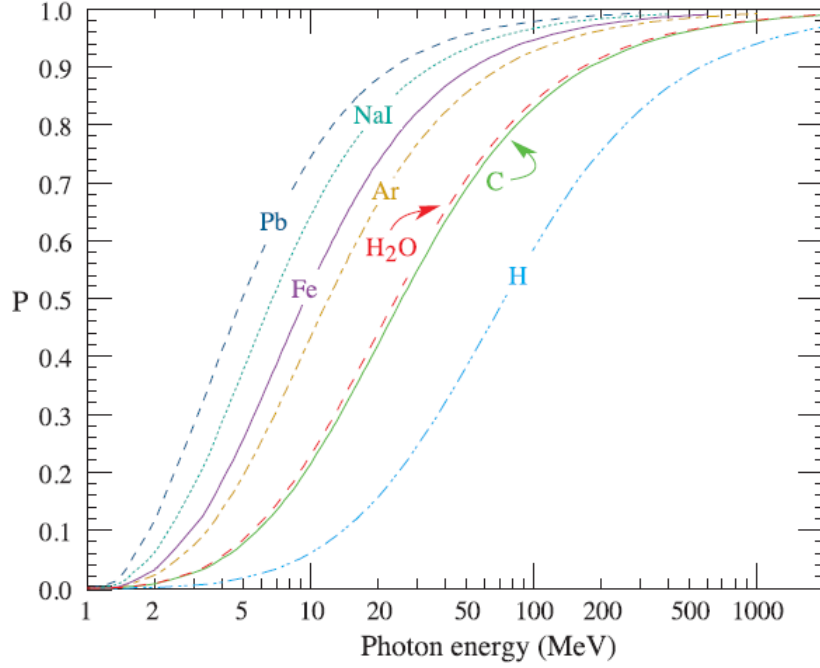


Figure 3.14: Probability that a photon interaction will result in conversion to an  $e^+e^-$  pair [1].

### 3.2.2 The Coordinate System

The CMS experiment uses a right-handed Cartesian coordinate system  $(x, y, z)$ , where the origin is at the center of the detector. The  $x$ -axis points radially inwards toward the center of the LHC ring, the  $y$ -axis points vertically upwards, and the  $z$ -axis points counter-clockwise along the beam pipe, toward the Jura Mountains. Measurements are often performed in the  $x - y$  plane, that is, the plane transverse to the beam pipe. Thus,  $E_T$  and  $p_T$  are the transverse energy and transverse momentum, respectively, and are computed from the  $x$  and  $y$  components. Spherical coordinates are also used; the azimuthal angle  $\phi$  is measured from the  $x$ -axis in the  $x - y$  plane, the polar angle  $\theta$  is measured from the  $z$ -axis, and  $r$  is the radial coordinate. The pseudorapidity  $\eta$ , defined as  $\eta = -\ln[\tan(\theta/2)]$ , is commonly used in collider physics. It approximates the true rapidity  $y = \frac{1}{2} \ln \left[ \frac{E+p_z}{E-p_z} \right]$  for finite angles, in the limit that  $m/E \rightarrow 0$ . The pseudorapidity is often used instead of the polar angle because particle production is

approximately constant as a function of  $\eta$ . Parts of the CMS detector were lowered into the experimental cavern through a hole, which is now located at negative  $z$ .

### 3.2.3 The Superconducting Magnet

One of the main features of the CMS detector is the superconducting solenoid magnet, which curves the tracks of charged particles in the detector and thus allows us to measure particle momenta. Since the momentum resolution is inversely proportional to the strength of the magnetic field, CMS chose a large superconducting solenoid magnet with a 4 T magnetic field, placed outside the tracker and calorimeters, in order to avoid particles losing energy in the solenoid before making the energy measurement. At 12.5 m long and 6 m in diameter, the solenoid is the largest of its type ever constructed and is large enough to allow the tracker and the calorimeters to be housed inside it. It has an NbTi coil, which winds around the cylinder in four layers. The solenoid operated in 2012 at 3.8 T. The return yoke of the magnet is made of 10k tons of iron and is interspersed within the layers of the muon system. Thus, there is a 2 T magnetic field between the outer radius of the solenoid and the outer radius of CMS, which bends the trajectories of muons in the opposite direction. See Fig.3.15 for a comparison of solenoids in recent high energy experiments.



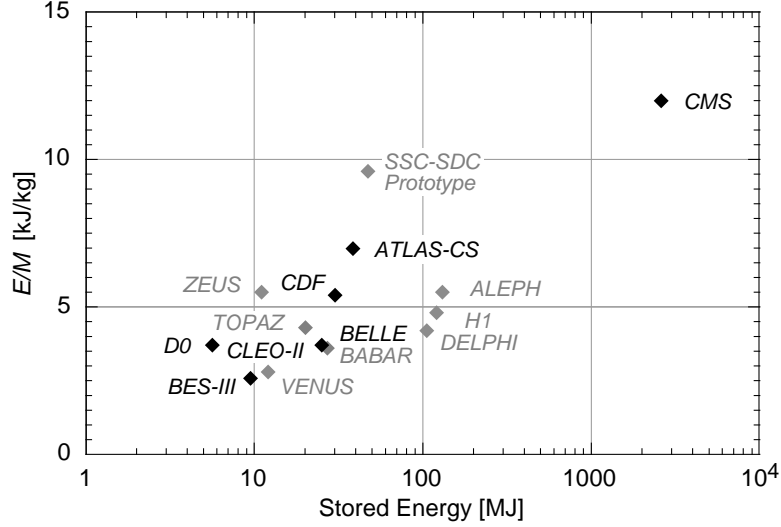


Figure 3.15: Ratio of stored energy to cold mass for major detector solenoids [1].

### 3.2.4 The Inner Tracker

The inner tracker is the first subdetector that a particle produced in the collision will encounter. It has a length of 5.8 m and a diameter of 2.5 m. The main purposes of the inner tracker are to efficiently and precisely measure the trajectories, charge, and momentum of charged particles and to reconstruct primary and secondary vertices. The tracker must be capable of identifying separate tracks for about 1000 particles per bunch crossing, at the LHC design luminosity. Therefore, it must have a short response time and high granularity. At the same time, the inner tracker must be radiation hard; the tracker constantly operates in a region of high radiation due to the high particle flux. The goal was to design a tracker that could maintain its performance in the intense radiation environment for 10 years. As a result of these requirements, the inner tracker was constructed entirely of silicon. The CMS tracker is the largest silicon tracker ever built, with about 200 m<sup>2</sup> of active silicon. The inner tracker provides coverage to  $|\eta|$  of 2.5 and reconstructs charged particles with an efficiency of more than 90%. The tracker measures particles' transverse momenta with a resolution of about 1%, for  $p_T < 100$  GeV.

Tracking detectors measure the ionization produced by the charged particle passing through the detector medium, which could be a semiconductor, such as the CMS silicon inner tracker. The ionization creates electron-hole pairs, and due to the applied electric field, the charges move toward their collection electrodes and are measured as a current. The number of charge carriers is proportional to the amount of deposited ionizing energy, which is proportional to the energy of the incident particle.

The inner tracker is comprised of a pixel detector from a radius of 4.4 cm to 10.2 cm and a silicon strip tracker that extends to 1.1 m in radius. See Fig. 3.16 for a diagram of the inner tracker. We will now discuss the two subdetectors of the inner tracker in turn.

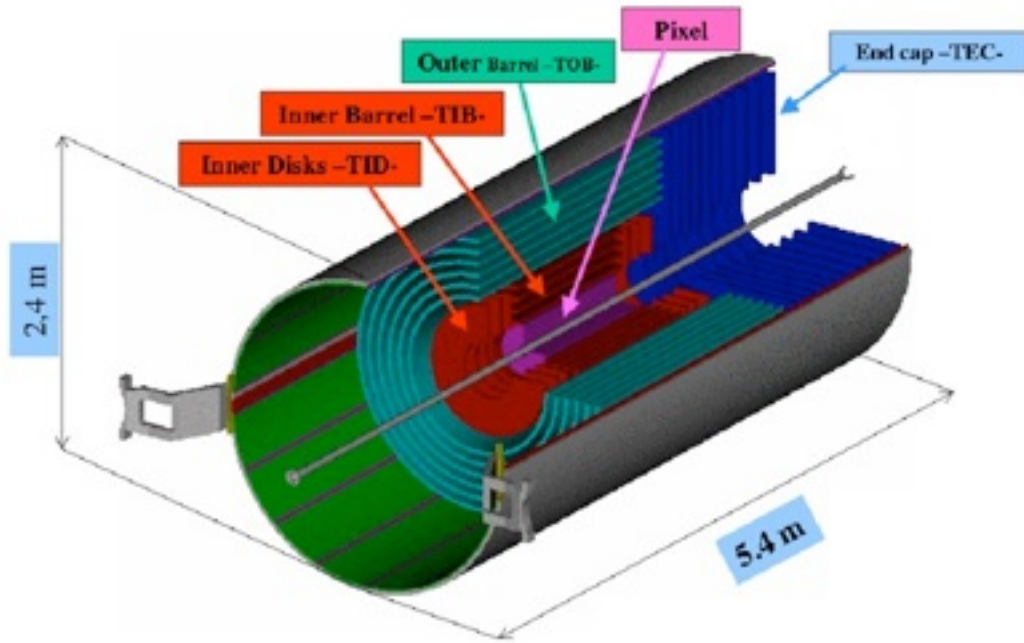


Figure 3.16: Diagram of the CMS inner tracker [71].

#### 3.2.4.1 The Pixel Detector

The pixel detector is the innermost component of the inner tracker and is located just outside the beam pipe. It is required to have a fine granularity in order to precisely

distinguish different tracks and primary and secondary vertices. Secondary vertices, in particular, can be reconstructed well, due to the small pixel cell size of  $100 \times 150 \mu\text{m}^2$ , which gives similar track resolution in both the  $r-\phi$  and  $z$  directions and makes a 3D vertex reconstruction possible.

The pixel detector consists of three barrel layers, containing 48 million pixels, and two endcap disks, containing 18 million pixels. The spatial resolution of the pixel detector is about  $20 \mu\text{m}$ . See Fig.3.17 for a diagram of the pixel detector.

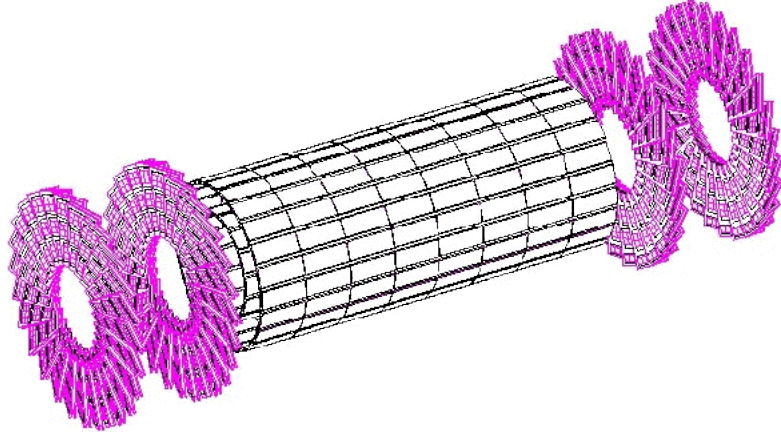


Figure 3.17: Diagram of the CMS pixel detector [71].

#### 3.2.4.2 The Silicon Strip Tracker

The silicon strip tracker sits directly outside the pixel detector. CMS was the first general purpose detector to use silicon detectors in this outer tracker region, a choice that was made in order to maximize the ability of the tracker to quickly distinguish multiple particles and yet withstand the prolonged radiation from these particles. See Fig.3.18 for a picture of the silicon strip tracker.

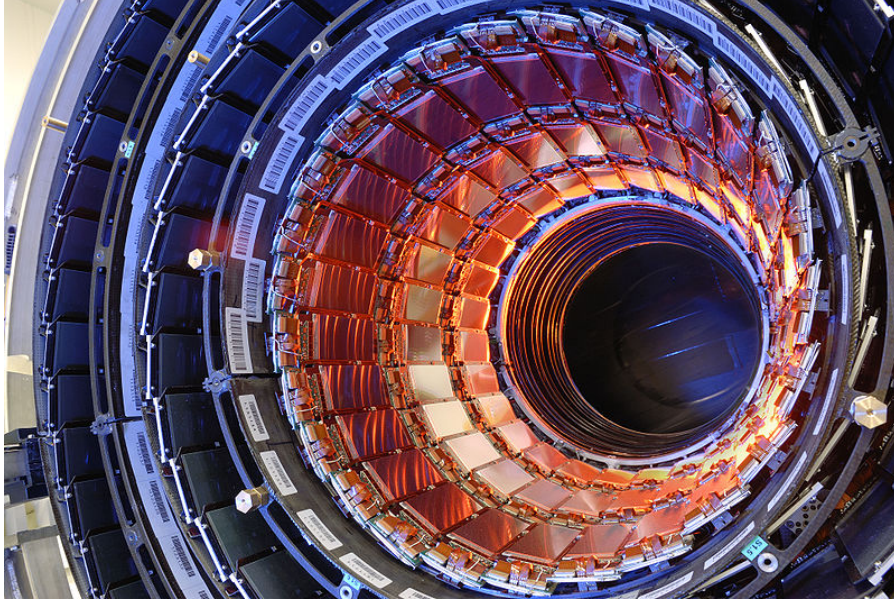


Figure 3.18: Photograph of the CMS silicon strip tracker.

The use of silicon in the strip tracker was made possible by a few key developments. First of all, sensors were made on 6 in instead of 4 in wafers, which reduced the cost per sensor and allowed the sensors to cover the necessary large area. Secondly, front-end readout chips were used with sub-micron technology, leading to a large cost savings and an improved signal-to-noise ratio. Finally, the module assembly was automated and high throughput wire bonding machines were used.

The silicon sensors are single-sided  $p - n$  silicon microstrip sensors. The base material is  $n$ -doped float zone silicon with a 1,0,0 crystal orientation: this crystal orientation was used over the more common 1,1,1 orientation because the buildup of surface charge on crystals of this orientation has been shown to be much smaller, thus causing less inter-strip capacitance increase.

### 3.2.5 The Electromagnetic Calorimeter (ECAL)

The electromagnetic calorimeter (ECAL) is situated outside the tracker. The ECAL detects the energies from the electromagnetic showers of electrons and photons. See Fig. 3.19 for a diagram of the CMS ECAL.

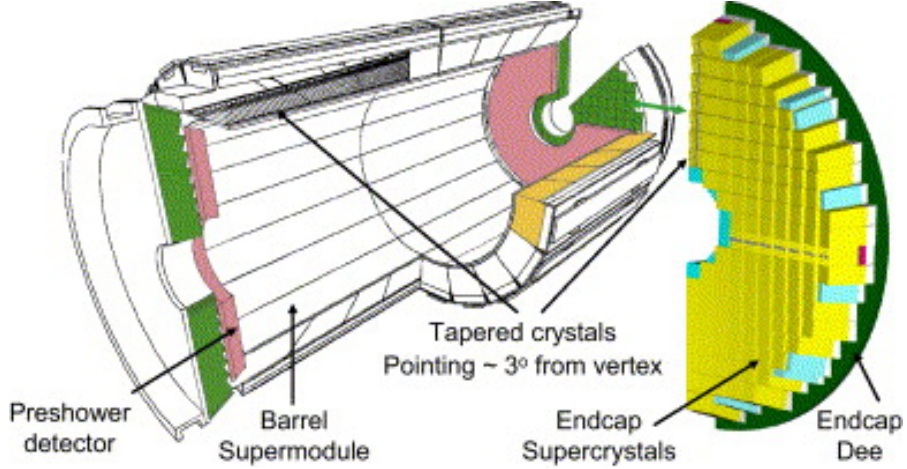


Figure 3.19: Diagram of the CMS electromagnetic calorimeter [71].

As mentioned in Section 3.2.1, electrons in high-energy experiments usually lose energy in matter through bremsstrahlung, and high-energy photons, by  $e^+e^-$  pair production. Since pair production and bremsstrahlung produce more electrons and photons with lower energy, electrons and photons create electromagnetic cascades or showers when they interact with a thick absorber. The shower continues until the energy falls below the critical energy, and then the rest of the electron or photon energy is dissipated through ionization or excitation. The characteristic amount of matter traversed by the cascade is called the radiation length  $X_0$ , which is proportional to the Molière radius  $R_M$  of the material. The Molière radius contains 90% of the electromagnetic cascade. Calorimeters detect the ionization energy from high energy particle showers, which is proportional to the energy of the incident particle.

The ECAL is a homogeneous calorimeter, meaning that its entire volume is used as the active scintillating material to detect electromagnetic signals and as the absorbing material that initiates the showers. Homogeneous calorimeters have exceptional energy resolution, but are costly, and so are usually only used to measure electromagnetic showers, which have shorter interaction lengths than hadronic showers. The ECAL is made of lead tungstate ( $\text{PbWO}_4$ ) crystals, which were chosen because of their high density ( $8.28 \text{ g/cm}^3$ ), short radiation length ( $0.89 \text{ cm}$ ), and small Molière

radius (2.2 cm). This results in a finely granulated and compact calorimeter.

The calorimeter energy resolution can be parametrized like so:

$$\left(\frac{\sigma}{E}\right)^2 = \left(\frac{S}{\sqrt{E}}\right)^2 + \left(\frac{N}{E}\right)^2 + C^2 \quad (3.4)$$

where  $S$  is the stochastic term,  $N$  is the noise term, and  $C$  is the constant term. In the CMS ECAL, this equation is:

$$\left(\frac{\sigma}{E}\right)^2 = \left(\frac{2.8\%}{\sqrt{E}}\right)^2 + \left(\frac{0.12}{E}\right)^2 + (0.30\%)^2 \quad (3.5)$$

The stochastic term is dominated here by fluctuations in the lateral shower containment, photostatics, and fluctuations in the energy in the preshower. The main contributions to the noise term are electronics, digitization, and pileup noise. The constant term is governed by non-uniformity of the longitudinal light collection, intercalibration errors, and leakage of energy from the back of the crystal. Furthermore, a resolution of 0.5% has been measured for 120 GeV electrons, which is consistent with the parameterization above.

The ECAL has two main parts: the ECAL barrel (EB) and the ECAL endcaps (EEs).

### 3.2.5.1 The ECAL Barrel

The EB covers  $|\eta| < 1.479$  and is comprised of 61200 PbWO<sub>4</sub> crystals. The crystals in the barrel have a tapered shape, slightly varying with position in  $\eta$ . The EB is 8.14 m<sup>3</sup> and weighs 67.4 T. The photodetectors in the EB are custom Hamamatsu avalanche photodiodes.

### 3.2.5.2 The ECAL Endcaps

The EEs cover  $1.479 < |\eta| < 3.0$  and are situated 315 cm from the interaction point. The 7324 crystals in each of the endcaps have the same shape, and they are grouped in  $5 \times 5$  blocks called supercrystals. The photodetectors in the EEs are custom vacuum phototriodes from National Research Institute Electron in St. Petersburg.

### 3.2.5.3 The ECAL Preshower Detector

The ECAL also contains a preshower detector (ES), which is used to identify neutral pions in the endcaps within  $1.653 < |\eta| < 2.6$ . It also helps to distinguish electrons from minimum ionizing particles and to improve the position measurement of electrons and photons. The ES is a sampling calorimeter, which means that there are two types of material in the calorimeter: the metal absorber, in which the showers are generated, and the active material, in which the signal is measured. The ES is made of lead radiators and silicon strip detectors.

## 3.2.6 The Hadronic Calorimeter (HCAL)

The hadronic calorimeter (HCAL) is placed outside the ECAL and before the solenoid magnet, and it is used to detect the energies from hadronic showers. See Fig. 3.20 for a photograph of the CMS HCAL.





Figure 3.20: Photograph of the CMS hadronic calorimeter.

Hadrons create hadronic showers through their interactions with atomic nuclei via the strong force, as discussed in Section 3.2.1. The high-energy hadron is converted to many low energy hadrons, typically pions, and the shower stops when all of the incident energy is transferred to secondary particles through ionization or nuclear processes. We define a nuclear interaction length  $\lambda_0$  similar to the electromagnetic radiation length to describe the length of the hadronic shower.  $\lambda_0$  is typically longer than  $X_0$  because nuclear interactions are less probable. For example,  $(X_0)_{\text{Pb}} = 0.56\text{cm}$  while  $(\lambda_0)_{\text{Pb}} = 17.6\text{cm}$ , and  $(X_0)_{\text{Fe}} = 1.8\text{cm}$  while  $(\lambda_0)_{\text{Fe}} = 16.8\text{cm}$ . Since hadronic showers start later and are larger, both laterally and longitudinally, than electromagnetic showers, the HCAL is thicker and placed after the ECAL.

The HCAL is a sampling calorimeter made of steel and brass absorbers sandwiched between plastic scintillators or quartz fibers. Plastic scintillators are a type of organic scintillator, which use the ionization produced by charged particles to produce photons in the blue to green wavelength regions. Plastic scintillators are commonly used in high energy experiments because they are cost-effective.

The HCAL is organized into four subdetectors: the HCAL barrel (HB), the HCAL endcaps (HEs), the HCAL outer calorimeter (HO), and the HCAL forward calorimeter



(HF). The HB, HEs, and HO use plastic scintillators and read out the signal using multichannel hybrid photodiodes. The HF, which is very forward and will receive very high particle fluxes, uses quartz fibers as the active material, in order to be very radiation-hard. Since the magnetic fields are much smaller in the HF, conventional Hamamatsu photomultiplier tubes are used to collect the signal. We will now discuss each of the four subdetectors in more detail.

The HCAL energy resolution can also be parametrized as in Equation 3.4, except without a noise term. The HB/HE energy resolution is given by:

$$\left(\frac{\sigma}{E}\right)^2 = \left(\frac{90\%}{\sqrt{E}}\right)^2 + (4.5\%)^2 \quad (3.6)$$

And the HF energy resolution is given by:

$$\left(\frac{\sigma}{E}\right)^2 = \left(\frac{172\%}{\sqrt{E}}\right)^2 + (9.0\%)^2 \quad (3.7)$$

The stochastic term is governed by statistical fluctuations and intrinsic shower fluctuations, and the constant term is governed by non-uniformity and calibration uncertainties.

### 3.2.6.1 The HCAL Barrel

The HB covers  $|\eta| < 1.3$  and is composed of 36 identical azimuthal wedges of absorber plates. Most of the absorber plates are brass, but the innermost and outermost plates are made of stainless steel for structural strength. The plastic scintillator is divided into 16  $\eta$  sectors, resulting in a segmentation of  $(\Delta\eta, \Delta\phi) = (0.087, 0.087)$ . The total HB absorber thickness at  $\eta = 0$  is  $5.82 \lambda_0$  and  $10.6 \lambda_0$  at  $|\eta| = 1.3$ .

### 3.2.6.2 The HCAL Endcaps

The HEs cover  $1.3 < |\eta| < 3.0$  and consist of brass absorbers and plastic scintillators. The absorber is arranged geometrically in staggered plates bolted together, in order to minimize the gaps between the HEs and HB. The granularity of the HEs is  $(\Delta\eta, \Delta\phi) = (0.087, 0.087)$  for  $|\eta| < 1.6$  and  $(\Delta\eta, \Delta\phi) \approx (0.17, 0.17)$  for  $|\eta| \geq 1.6$ .

### 3.2.6.3 The HCAL Outer Calorimeter

To make sure all the hadronic showers are contained in the central region, the HCAL is extended outside of the solenoid in the HO or tail-catcher region. The HO covers  $|\eta| < 1.26$  and is the first layer in the five rings of the iron yoke. The central ring has 2 layers of HO scintillators separated by a 19.5 cm thick piece of iron, since the HB absorber thickness is minimal at  $\eta = 0$ . The other four rings have a single HO layer at a radial distance of 4.07 m. The total depth of the HCAL is therefore extended to at least  $11.8 \lambda_0$ , except at the barrel-endcap boundary. Each ring of the HO has 12 identical  $\phi$  sectors, which are separated by stainless steel beams that hold the iron return yoke and the muon chambers.

### 3.2.6.4 The HCAL Forward Calorimeter

The HF is on either side of the impact parameter (IP) at  $z = \pm 11.2\text{m}$  and covers  $2.9 < |\eta| < 5.2$ . Therefore, the HF will see a very high particle flux and needs to be extremely radiation-hard. Each  $pp$  collision will deposit about 760 GeV in the HF, as compared to only 100 GeV in the rest of the detector. There are 36  $20^\circ$  azimuthal wedges in the HF, which form  $(\Delta\eta, \Delta\phi) = (0.175, 0.175)$  towers. The HF uses steel as the absorber and quartz fibers as the active material, as mentioned above.

### 3.2.7 The Muon System

The muon system is the outermost subdetector of CMS because only muons are expected to penetrate this far. The muon system is composed of several subdetectors: the Drift Tubes (DTs), the Cathode Strip Chambers (CSCs), and the Resistive Plate Chambers (RPCs). The DTs are located in the barrel only, the CSCs are only located in the endcaps, and the RPCs are located in both. A muon station generally consists of one or two layers of RPCs and a layer of either DTs or CSCs. There are four muon stations in concentric rings around the beam line, and in between each station is iron that forms the magnet return-yoke. See Figs.3.21 and 3.22 for diagrams of the muon system.

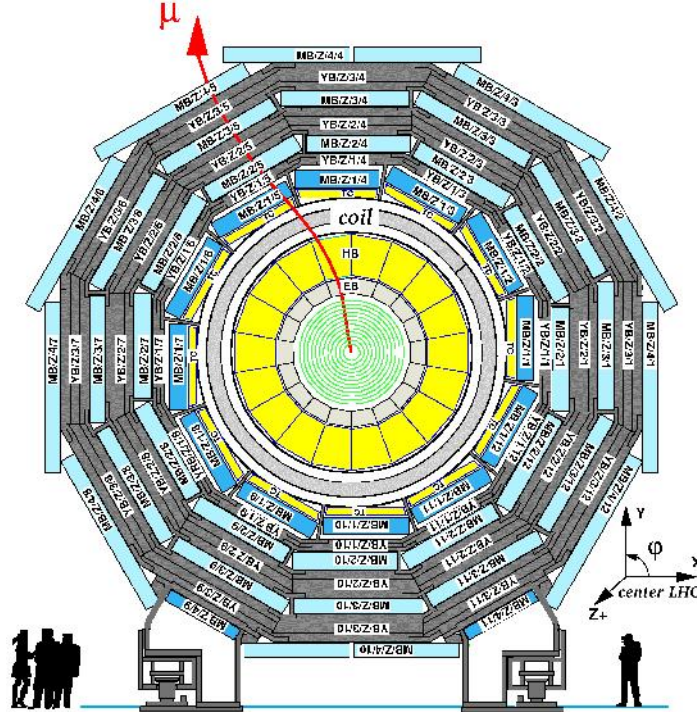


Figure 3.21: Diagram of the CMS barrel muon system [71].

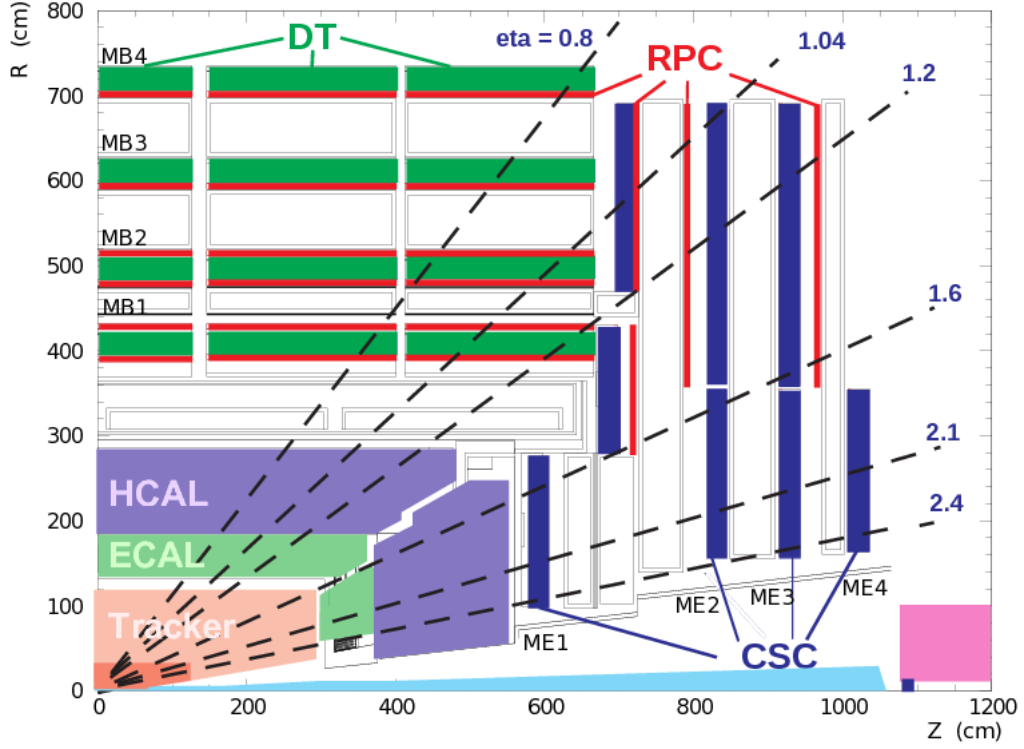


Figure 3.22: Diagram of a slice of the CMS detector. Individual DT, CSC, and RPC chambers can be seen in the muon system [71].

The CMS muon system is an iron-core spectrometer; the muon DT, CSC, and RPC stations are interspersed with the iron return-yoke of the solenoid magnet. Thus, the muon  $p_T$  is measured from the return field inside the magnetized iron. The muon  $p_T$  resolution is discussed in Section 3.2.11.2.

The three subdetectors of the muon system are gaseous tracking detectors, not unlike the inner tracker, except that the inner tracker is a solid state semiconductor tracker. Gaseous and solid state trackers are the two main types of tracking detectors commonly found in detectors at colliders. There are two types of gaseous tracking detectors: wire chambers, such as the DTs and CSCs, and wireless chambers, such as the RPCs. The wire chambers rely on ionized electrons that drift to the wire, and since the maximum drift time is 380 ns in the DTs, wire chambers are not particularly fast. However, they have a high spatial resolution; the DTs and CSCs both have a position resolution within about  $100 \mu\text{m}$  offline in the  $r - \phi$  plane per chamber.

DTs and CSCs were chosen for their high precision in determining the position of particles, while RPCs were chosen for their timing resolution. RPCs consist of two parallel plates, where one is the anode and one is the cathode; ionized electrons are attracted to the anode RPC plate, rather than the anode wire, as in the DT and CSC wire chambers. The RPCs determine the time of a muon to a precision of 1 ns at a fast rate of at least 1 kHz/cm<sup>2</sup>. Therefore, the fast RPCs are used in both the barrel and the endcaps and are critical contributors to the muon trigger.

### 3.2.7.1 The Drift Tubes

There are a total of 130 DTs in the barrel of the muon system, spread across the four muon stations and five barrel wheels and covering  $|\eta| < 0.8$ . The DTs are in the barrel because they are very sensitive to the magnetic field, which has a relatively low strength in the barrel, and have low expected rate. The three inner DT chambers are comprised of three super-layers, two measuring the  $\phi$  projection and one measuring the  $\theta$  projection. The outermost DT chamber just has two  $\phi$  projection super-layers. Each super-layer is composed of four layers of staggered drift tubes. A single super-layer provides a time resolution of a few ns.

The CMS drift tubes include a gold-plated stainless steel anode wire, which is 50  $\mu\text{m}$  in diameter. The electrode is a 50  $\mu\text{m}$  thick piece of aluminum tape glued onto some thicker mylar tape, which insulates the electrode. The cathode is also made of aluminum tape, insulated by mylar tape. The gas that becomes ionized by the muon in the tube is 85% argon (Ar) and 15% carbon dioxide (CO<sub>2</sub>). See Fig.3.23 for a diagram of a drift tube.

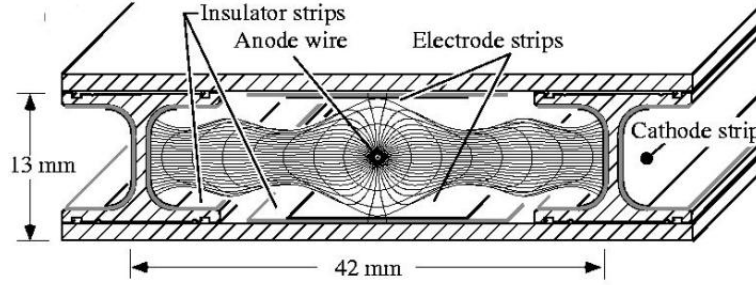


Figure 3.23: Diagram of a drift tube cell [71].

### 3.2.7.2 The Cathode Strip Chambers

The CSCs are in the endcaps only because they have short drift paths and are less sensitive to the magnetic field. Therefore, they can operate in high-rate, large magnetic field conditions, such as those found in the endcaps. There are four chambers of CSCs in each endcap, for a total of 468 CSCs. The CSCs are trapezoidal, and they overlap to provide continuous  $\phi$  coverage. The CSCs exclusively cover  $1.2 < |\eta| < 2.4$ . A muon can be detected by both DTs and CSCs in the overlap region,  $0.9 < |\eta| < 1.2$ .

A CSC is made of six anode wires and seven cathode panels. The anodes are gold-plated tungsten wires, measuring  $50\ \mu\text{m}$  in diameter. The cathodes consist of a polycarbonate honeycomb core with FR4, a fire-retardant fiberglass/epoxy material that is widely used in circuit boards, and a  $36\ \mu\text{m}$  thick layer of copper. The CSC gas is 40% Ar, 50%  $\text{CO}_2$ , and 10% carbon tetrafluoride ( $\text{CF}_4$ ).

See Fig. 3.24 for a diagram of a CSC.

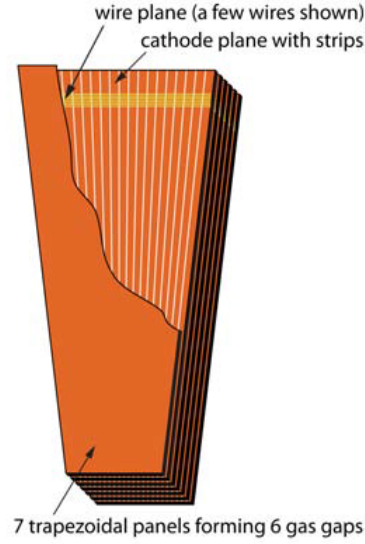


Figure 3.24: Diagram of a cathode strip chamber [71].

### 3.2.7.3 The Resistive Plate Chambers

There are six layers of rectangular RPCs in the barrel: the first two muon stations in the barrel have two layers of RPCs each, and the other two muon stations have one layer each. There are three layers of trapezoidal RPCs in each endcap. The RPCs cover  $|\eta| < 1.6$ . RPCs are fast, so they are crucial for triggering and have very a good time resolution of about 1 ns. See Fig. 3.25 for a diagram of the RPCs.

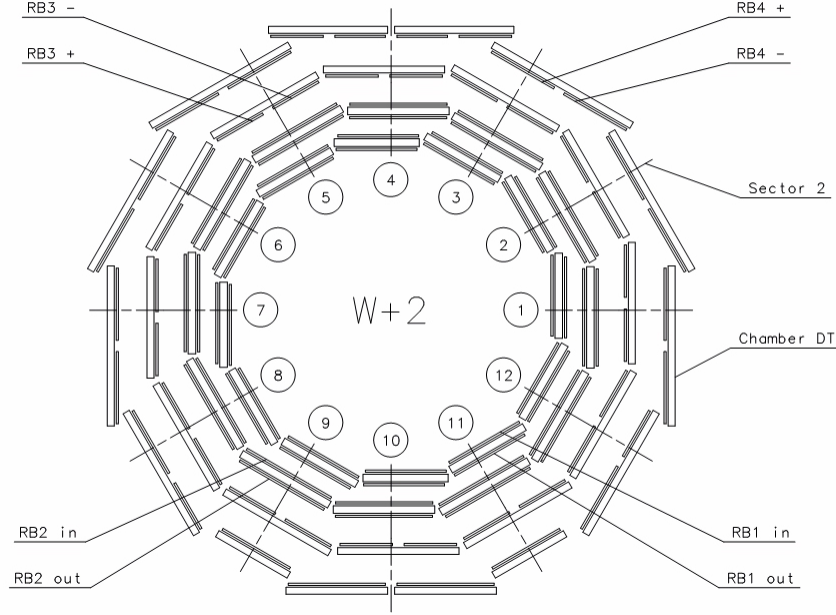


Figure 3.25: Diagram of the barrel resistive plate chambers [71].

The CMS RPCs are double-gap modules, which operate in avalanche mode with common pickup readout strips in between the gaps. So, the total signal is the sum of the two single-gap signals; this is a more efficient configuration than single-gap modules. The RPC plates are made of aluminum, and the gas between them is mostly tetrafluoroethane ( $C_2H_2F_4$ ).

### 3.2.8 The Trigger and Data Acquisition

The aim of the trigger and data acquisition (DAQ) is to select and acquire the interesting events that we would like to record. The trigger is built in several stages. At Level 1 (L1) [73], the first stage of the trigger, the event rate is quickly reduced as much as possible with fast, custom-built hardware and firmware. Then, a more detailed calculation of which events to select is made at the more time-consuming software High Level Trigger (HLT) [74]. At the design specifications, the trigger system should reduce the 40 MHz input rate from the  $pp$  collisions to about 100 kHz after the L1 trigger, and then further reduce the event rate to about a few hundred



Hertz at the HLT output. In practice in 2012, the L1 trigger rate was at about 80 kHz, and the HLT rate was at about 1 kHz, at the start of a fill. We were able to push the limits of writing the data to tape and achieve these rates by using more powerful computers than had previously been envisioned. In 2012, the maximum attained stable instantaneous luminosity was  $7.7 \times 10^{33} \text{ cm}^{-2} \text{ s}^{-1}$ , with 1380 proton bunches. The maximum achieved HLT rate in 2012 was about 1330 Hz, for the total stream A rate (see Section 3.2.8.2 for a description of streams).

There are a few trigger concepts that are used at both the L1 and the HLT. First of all, there are signal, backup, and control triggers. We typically use a signal trigger for highly interesting processes, where we want to record every event that passes some criteria. A backup trigger is like a signal trigger but with a higher  $p_T$  or  $E_T$  threshold; a backup trigger will be used in place of the signal trigger if the event rate becomes higher than anticipated. We also design control triggers to measure common background processes or to measure efficiencies. Control triggers are typically *prescaled*, which means that we write to tape only a fraction of events that pass the trigger. For example, a trigger with a prescale of 20 means that we accept one in 20 events that passes the trigger. Both L1 and HLT triggers can be prescaled. We use a set of prescale columns, or a list of different prescale values for each trigger. As the event rate naturally decreases during a fill, we typically relax the prescales on the triggers by switching to a different prescale column in order to accept more events in the prescaled triggers.

### 3.2.8.1 Level 1 Trigger

The L1 trigger consists of a muon trigger, which receives local trigger information from the RPCs, CSCs, and DTs, and a calorimeter trigger, which receives local trigger information from the HF, HCAL, and ECAL (see Fig. 3.26). The L1 trigger does not use information from the inner tracker because the tracker has complex algorithms

and huge amounts of data, while the pattern recognition algorithms of the muon system and calorimeters are much faster and simpler. Once the global calorimeter trigger and the global muon trigger make a decision on the calorimeter and muon L1 trigger objects, respectively, the information is passed to the global L1 trigger. The L1 trigger selects the four highest  $E_T$  egamma (electron or photon) objects, the four highest  $E_T$  central jets, the four highest  $E_T$  forward jets, the four highest  $E_T$  tau-jets, the four highest  $p_T$  muons, missing transverse energy (MET) (see Section 3.2.11), and the scalar sum of the jet transverse momenta ( $H_T$ ) in each event. It measures the  $p_T$ ,  $\eta$ ,  $\phi$ , and sometimes the quality for each of these objects. The L1 trigger takes a maximum of  $3.2 \mu\text{s}$  to decide whether to accept an event.

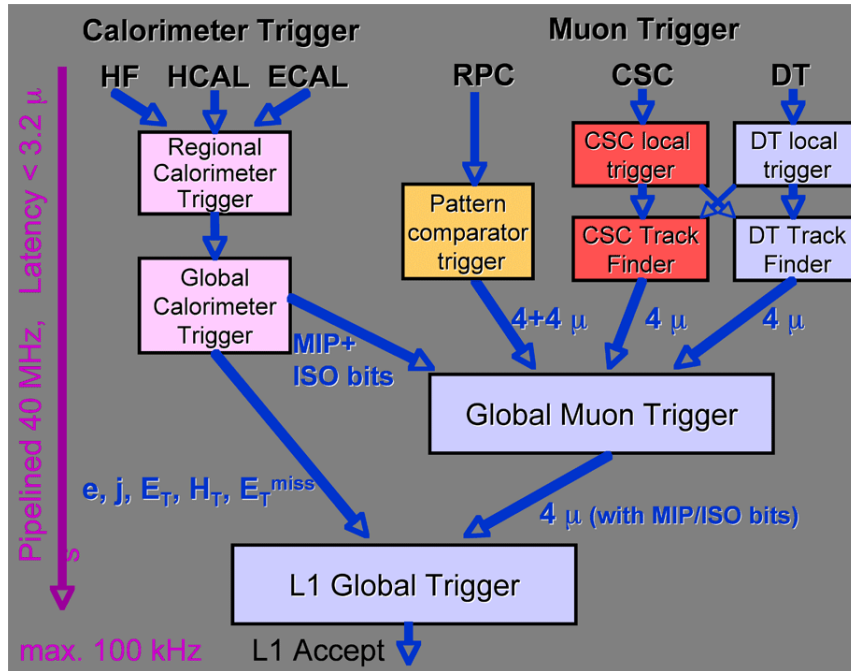


Figure 3.26: Diagram of the L1 trigger architecture [71].

The muon trigger receives input from all 3 muon subsystems, but the RPCs are crucial because they are very fast, operating at a rate of at least 1 kHz, and their time resolution of a few ns is much better than the time resolution of the DTs or CSCs. The local DT trigger forms segments, made of hits in each of the 4 muon stations, and then the regional DT trigger forms L1 trigger tracks from the segments, using look-up

tables. The regional DT trigger assigns the track  $p_T$ , position, and charge. The CSC trigger works in much the same way, with a local trigger forming segments and the regional trigger forming tracks from those segments and assigning  $p_T$ ,  $\eta$ , and  $\phi$ . The muon quality for the DTs and CSCs is based on the number of muon stations used to reconstruct the muon candidate. The DTs and CSCs both send the four highest  $p_T$  muon candidates to the global muon trigger. The RPCs are different in that they compare the pattern of hits in the detector with template patterns, corresponding to different  $p_T$  bins, and then directly send the four highest  $p_T$  muon candidates to the global muon trigger. The global muon trigger selects up to four muon candidates and passes that information to the global L1 trigger.

The calorimeter trigger logic starts with trigger primitives in the ECAL and HCAL that contain trigger tower energy sums, and additionally, the transverse size of the energy deposit in the ECAL. The ECAL and HCAL trigger primitives are sent to the regional calorimeter trigger, which sums the energies across the trigger towers to identify electrons, photons, jets and taus. The global calorimeter trigger receives the information from the regional calorimeter trigger and forms jet and electron objects using a sliding window algorithm.

The global L1 trigger receives the input from the global muon and global calorimeter triggers and decides whether an event will be accepted or rejected at L1. The global L1 trigger consists of 128 trigger bits, which are each assigned to a L1 algorithm trigger. The algorithm triggers, together with the technical trigger bits, can be programmed for different L1 trigger objects and  $p_T$  or  $E_T$  thresholds. See Ref. [75] for a complete description of the different L1 trigger menus.

### 3.2.8.2 High Level Trigger

The L1 trigger bits are the inputs or *L1 seeds* to the HLT triggers or *paths*. The HLT is purely software and is run on the online computing farm. HLT triggers are called

paths because they are entirely software: they consist of a series of “modules,” which are independent pieces of code that produce a HLT trigger object or make a decision on whether to keep the event, based on those trigger objects; that is, they filter the objects. A typical HLT path consists of a few basic components: a L1 seed, a prescale module, producers to make trigger objects, and filters to select the objects with the desired qualities.

The HLT defines different *menus*, or lists of specific paths with specific thresholds, for different maximum instantaneous luminosities. The HLT menu evolves with the instantaneous luminosity delivered by the LHC. A typical HLT menu, such as the 2012 *8e33 menu*, consisted of 450 HLT paths, 15 streams, 40 primary datasets (including the *parking* datasets), and 9 prescale columns. A *primary dataset* is defined by a list of HLT paths. All the paths in a dataset usually trigger on similar objects; for example, some common primary datasets are called SingleMu or DoubleElectron, which contain all the HLT paths triggering on at least one muon or at least two electrons, respectively. A stream is a collection of primary datasets. The main physics stream is called Stream A, but there are also other streams, such as those used for data quality monitoring or for release validation. A prescale column is a list of prescales for all the paths; the prescale for many control triggers can be set to change according to the instantaneous luminosity, thus defining the different columns. The HLT menus are created using a database called ConfDB: see [76] for the ConfDB browser and [77] for the main HLT twiki page.

The HLT uses information from the entire detector, including the inner tracker, to make a decision on whether or not to accept an event. The HLT uses the full event information and is therefore a more precise measurement than at L1. The HLT uses many tools such as isolation, b- and  $\tau$ -jet tagging, and track reconstruction and matching in order to make a precise, informed decision on each event. The HLT takes an average of about 40 ms to make a decision on an event, but it can often take much

longer.

It is important to mention the muon HLT reconstruction, since muon paths are used in the analysis presented in this thesis. The L1 muon information is passed to the HLT as L1 muon seeds. Then, a *L2 muon* is created, using only information in the muon system. The L2 muon is the analog of the offline standalone muon, which will be described in Section 3.2.11.2. The L2 muons are matched to tracks reconstructed in the inner tracker, and then *L3 muons* are created. A L3 muon is the analog of a global muon, which will also be described in Section 3.2.11.2.

The HLT must cover a wide range of different physics processes at a high efficiency. Therefore, triggers are designed to be as inclusive as possible: one main HLT path will generally serve many different analyses. However, while the signal efficiency must be maximized, the event rate must be kept as low as possible, in order to be able to save all the important information to tape. In addition, the CPU time must be kept within the available computing limits.

### 3.2.8.3 Data Acquisition

Figure 3.27 shows the CMS trigger and DAQ. The L1 decision is distributed to the frontends and readout systems. The event is built in the builder network, in two stages: the *FED-builder*, which assembles the data from the eight frontends to one super-fragment at 100 kHz, and the eight independent *DAQ slices*, which assemble the super-fragments into full events. The HLT uses the full event information to make a decision on whether or not to accept the event, and then the accepted events are stored with the computing services.

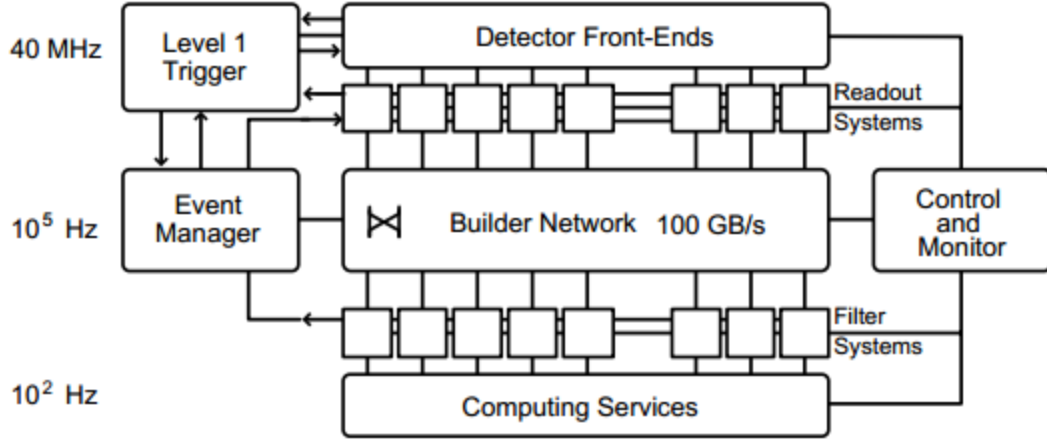


Figure 3.27: Diagram of the DAQ architecture [71].

The CMS DAQ consists of eight parallel slices, each with their own dedicated online storage system. Each slice has a 32 TB disk array, for a total of more than 250 TB of online storage. Every 93 s, a data file is closed and transferred to the CERN offline storage area, called the CERN Tier 0 (T0), which is the first place the primary datasets are assembled. Once the file is successfully transferred to the T0, it is deleted from the online storage.

### 3.2.9 The Detector Infrastructures

There are a number of miscellaneous detector systems that perform a variety of detector and safety-related services, which we will briefly describe here.

#### 3.2.9.1 Detector Powering

Considerable electrical power is needed to run CMS. Some of the most important systems needing power are the front-end electronics (FEE), the electronics racks in the counting rooms and in the site control centers, and the auxiliary services, such as cranes, ventilation and cooling stations, etc. Table 3.3 gives an overview of the power requirements for CMS.

Table 3.3: Power requirements for CMS [71].

System	Power [kW]
General site services	2200
Electronics racks	2300
Low voltage to FEEs	1000
Magnet and cryogenics	1250
Ventilation stations	1250
Surface cooling stations	4000
Underground cooling stations	1500
Total steady-state consumption	9000

### 3.2.9.2 Detector Cooling

The FEEs dissipates about 800 kW in the cavern. See Table 3.4 for the power dissipated by each system. As a result, the systems must be cooled by water at 18°C for the ECAL, HCAL, and muon system, and by perfluorohexane ( $C_6F_{14}$ ) fluid between  $-15^\circ\text{C}$  and  $-25^\circ\text{C}$  for the Preshower, Pixel, and Strip Tracker systems. Chilled water is produced at the SU5 building and then transferred to the USC55 cooling plant. From there, five independent water circuits distribute the water to the experimental cavern at 18°C.

Table 3.4: Cooling power for each CMS subsystem [71].

System	Power [kW]
Muon Endcaps	100
Muon Barrel	50
HCAL and Yoke Barrel	60
ECAL	300
Rack system	1600
Strip Track, Pixel, and Preshower	150

Cryogenics are used at the CMS site to cool the superconducting magnet to 4.7 K. The cryogenic system delivers a cooling power of 800 W (4500 W) at 4.7 K (60 K) to cool the coil’s thermal screens, and 4 g/s of liquid helium to cool the 20 kA coil

current leads. Cooling the superconducting coil down from room temperature takes three weeks.

### 3.2.9.3 Detector Cabling

The power cables and coolant, gas, and optical fibers are made to run through huge cable-chains, so that the detector can be opened and closed without disconnecting everything (see Fig.3.28). The cables are primarily HV cables, LV cables for DC power to the FEE, FEE read-out cables, optical fiber read-out cables, monitoring and control cables, general purpose power cables, and safety system cables for hard-wired signals and interlocks. CMS has some 30000 cables.

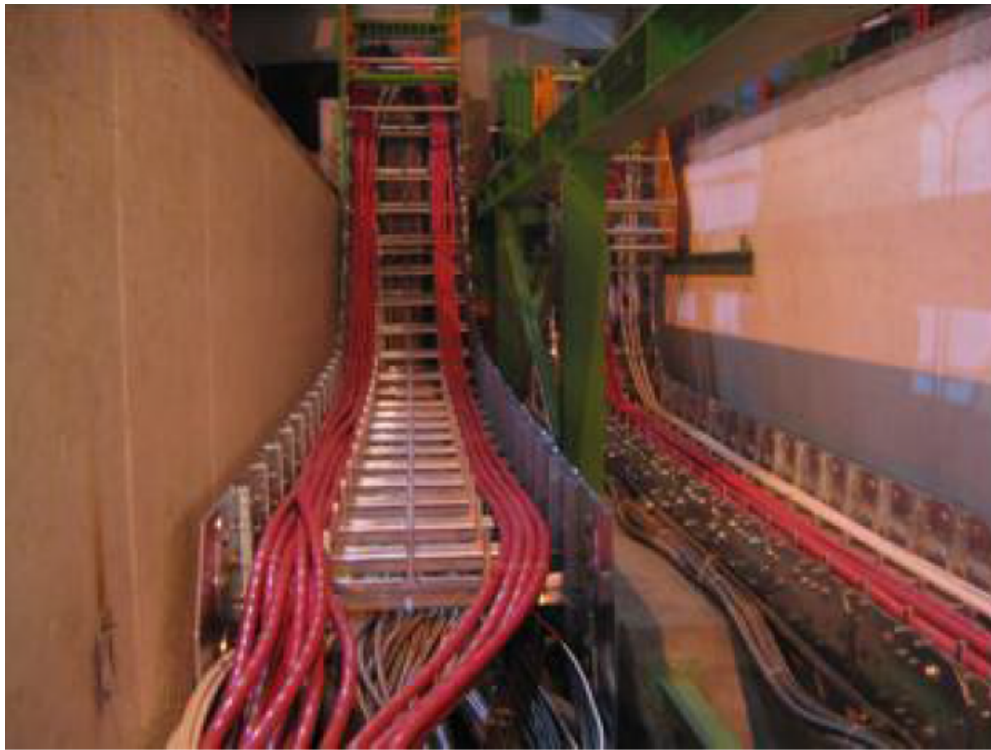


Figure 3.28: YB+2 and YE+1 cable-chains in the UXC55 basement trenches [71].

### 3.2.9.4 Detector Safety System (DSS)

The Detector Safety System (DSS) is a common development carried out by the four large LHC experiments, together with the CERN IT department. The purpose of the



DSS is to protect the detector and experimental equipment from hazards. The DSS actions are fast and coarse; for example, it will cut power to the entire cavern if smoke is detected. These actions will disrupt data taking, but will ensure that damage to the equipment is avoided.

### 3.2.9.5 Beam and Radiation Monitoring (BRM) Systems

There are several Beam and Radiation Monitoring (BRM) systems at CMS, which both monitor and protect the experiment against beam radiation. The main BRM systems are listed in Table 3.5. We will focus here on the most important BRM systems to CMS and the ones most relevant to the analysis in this thesis.

Table 3.5: The BRM systems in CMS [71]. The table is ordered from top to bottom in increasing time resolution.

System (Sensor Type)	Location Distance from IP [m]	Sampling Time	Function	Readout + Interface LHC or CMS type	Number of Sensors
Passives (TLD + Alanine)	CMS and UXC	months	Monitoring	N/A	Many
RADMON (RadFets + SRAM)	CMS and UXC	1 s	Monitoring	Standard LHC	18
BCM2L (Polycrystalline Diamond)	Behind TOTEM T2 $z = \pm 14.4\text{m}$	$40\ \mu\text{s}$	Protection	Standard LHC	24
BCM1L (Polycrystalline Diamond)	Pixel Volume $z = \pm 1.8\text{m}$	$5\ \mu\text{s}$	Protection	Standard LHC	8
BCM2F (Polycrystalline Diamond)	Behind TOTEM T2 $z = \pm 14.4\text{m}$	$\sim\text{ns}$	Monitoring	CMS Standalone	8
BSC (Scintillator Tiles)	Front of HF $z = \pm 10.9\text{m}$	$\sim\text{ns}$	Monitoring	CMS Standalone	32
BCM1F (Single Crystal Diamond)	Pixel Volume $z = \pm 1.8\text{m}$	$\sim\text{ns}$	Monitoring	CMS Standalone	8
BPTX (Button Beam Pickup)	Upstream of IP5 $z = \pm 175\text{m}$	200 ps	Monitoring	CMS Standalone	2

**BRM Protection Systems** The BRM protection systems are based on chemical vapor deposition diamond detectors, which have been used in other collider experiments and proven to be radiation hard, fast enough to match beam abort scenarios, and small enough to be inserted close to key detector components. The CMS BRM protection systems are the polycrystalline diamond Beam Conditions Monitor (BCM) systems: BCM1L, placed on either side of the IP at  $z = \pm 1.8\text{m}$ , and BCM2L, placed on either side of the IP at  $z = \pm 14.4\text{m}$ . These systems measure the rate from the pp interactions at the IP. The outer BCM2L diamonds are hidden from the beam spot and should be sensitive to beam halo. These BCM systems can generate a hardware beam abort signal, and it can be transmitted to the LHC via the Beam Interlock System, resulting in the beam being dumped within 3 orbits.

**BRM Monitoring Systems** The BRM monitoring systems, which are the BCM1F, BCM2F, Beam Scintillator Counters (BSC), and the Beam Pickup for Timing for the eXperiments (BPTX), are more precise than the protection systems described above. Like the other BCM systems, the BCM1F and BCM2F are diamond sensors, but they have readouts that are able to resolve the sub-bunch structure. The BCM1F is particularly useful because it is used to flag problematic beam conditions that result in bursts of beam loss over short periods of time, which could be very damaging to the CMS detector. This system is able to distinguish incoming and outgoing particles, based on their timing, and is therefore able to compare the rates of beam halo to particles coming from collisions. The BCM1F is sensitive to one MIP and has a timing resolution for single hits of a few ns. The BCM2F is not as sensitive as the BCM1F, but it gives additional diagnostic information about beam halo, from a position further away from the IP than the BCM1F.

The BSC system is a series of scintillator tiles that provide hit and coincidence rates. The BSC1 is located on the front of the HF and gives rate information about

the beam and can tag beam halo. The BSC1 covers about 25% of the tracker and can therefore be used to provide a minimum bias trigger, as it indicates the level of activity within the current bunch crossing. The BSC2 is located behind TOTEM T2 and can distinguish incoming and outgoing particles with a 4 ns resolution.

The final important BRM monitoring system is the BPTX, which is a beam pickup device that provides the experiment with the timing structure of the beam. It is a standard button monitor that is used elsewhere around the LHC ring to monitor the position of the beam. There are two pickup monitors for CMS, one at 175 m to the left of the IP, and one 175 m to the right. At these points, there are two beampipes, and therefore only the incoming beam is measured. The BPTX provides accurate time and phase measurements of each bunch and its intensity. The phases of all the experimental clocks can be compared to the measured phase of each bunch with a precision better than 200 ps. This also allows the  $z$ -position of the collision to be calculated from the relative phases of the BPTX measurements on opposite sides of the IP. The BPTX can also detect problems with the bunch structure and measure how much of the beam has drifted into the next RF bucket. The BPTX signal is read out using an oscilloscope and also as three technical L1 triggers. The three technical triggers provide flags as to whether a bunch in beam 1 is occupied, a bunch in beam 2 is occupied, or if both beams are occupied. If both beams are occupied, this trigger can serve as a zero bias trigger.

### 3.2.10 Computing

The CMS Software (CMSSW) is a set of tools and algorithms for event simulation and reconstruction [69, 70]. CMSSW is responsible for Monte Carlo (MC) simulation as well as for the reconstruction of real data events. We will first describe the MC simulation steps, and then describe the data formats, which are common to both MC and real data.

### 3.2.10.1 MC Event Simulation

There are two main steps in the MC event simulation: the event generation, which generates a proton collision and simulates the particles that will appear in the detector, and the detector simulation, which models how those particles will behave in the detector.

**Event Generation** Generators such as Pythia [78] and Madgraph [79] are used to produce the generator step of the MC simulation, called the GEN step. The first generator step is to simulate the hard scattering process, which is the interaction between the partons, that is, the quarks and gluons in the proton collision, that create the physics process of interest. The protons have a known momentum, but the momentum of the partons within them are constantly in flux. Therefore, MC generators use Parton Distribution Functions (PDFs), which describe the probability of partons to carry a certain momentum. PDFs are measured experimentally because current theories cannot derive them.

After the hard scatter is simulated, short lived particles are modeled. Then, the hadronization of the partons is simulated; this is called parton showering. Finally, the underlying event, which is the interaction of the soft partons from the collision, and pileup (see Section 3.1.2) are modeled.

**Detector Simulation** After the particles are produced in the generator, the detector response to these particles is modeled using GEANT [80]; this is called the SIM step. GEANT contains a detailed description of the detector, including the sensitive detectors, the sensor readout, and the dead material such as cabling and cooling components. The SIM step can either consist of the full GEANT simulation and digitization, called FullSim, or can be a faster, less CPU-intensive version, called FastSim. The energy loss of the particles, and any secondary particles, is modeled

first in the SIM step. Then, details about the magnetic field are used to produce the particle trajectories in the detector. After this, the response of subdetectors is taken into account. Then, the trigger system is emulated, and the MC data is converted to the RAW format, as is produced for real data.

### **3.2.10.2 Data Formats and Distribution**

The following reconstruction steps occur for both MC and data. The RAW data collected at the T0 is archived and reconstructed, and then sent to seven Tier 1 (T1) sites across the world, along with RAW MC simulations. The reconstructed or RECO data is a secondary and more careful reconstruction of the objects within the event, which takes more processing time than what is done at the HLT level. The RECO data is produced by applying pattern recognition and compression algorithms to the RAW data; these algorithms identify clusters and tracks, locate primary and secondary vertices, and identify particles or *high-level physics objects* based on information from several subdetectors. Secondary datasets and skims of the RECO data are then created and sent to Tier 2's and Tier 3's, where the data is kept for the common user's analysis. Analysis is typically done on Analysis Object Data (AOD) at T2s or T3s, which is a subset of the event content of the RECO data. The T0s, T1s, T2s, and T3s are connected via the Worldwide LHC Computing Grid (WLCG) or simply "the Grid." CMS users access data and MC on the Grid by using CRAB, which submits CMSSW jobs to the various data sites. See Figs. 3.29 and 3.30 for visualizations of the Grid.



Figure 3.29: WLCG sites [81]. The orange circle is the T0, the green pointers are T1s, and the blue pointers are T2s.

## LHC Data Grid Hierarchy:

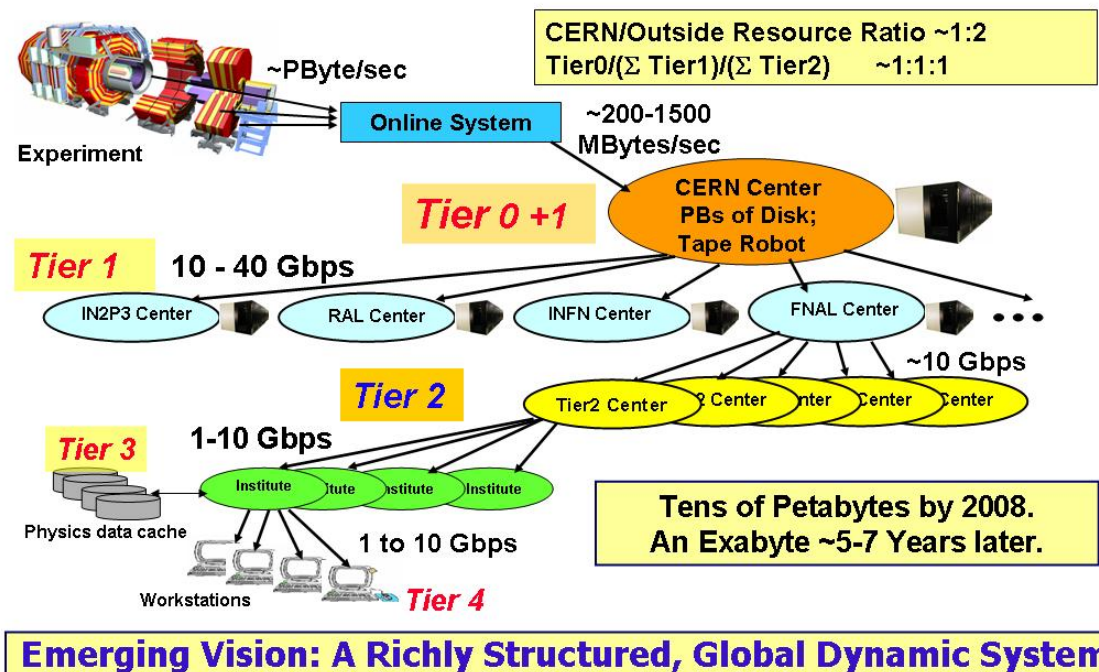


Figure 3.30: Diagram of the Grid hierarchy [82].

### 3.2.10.3 Calibration and Alignment

The detectors within CMS must be calibrated and aligned. This alignment and calibration (AlCa) is done separately for each subdetector.

The calorimeters in particular need to be calibrated carefully. The HCAL is calibrated using a radioactive source that is inserted into each tower when there are no collisions. The calorimeter deposits due to the source are measured as a function of the position of the source, and a gain calibration is computed based on an algorithm. The ECAL, on the other hand, must be calibrated using physics events because of the nature of the detector and because the level of precision needed is approximately 0.5%. Furthermore, the ECAL crystals change transparency as they become more exposed to radiation, and so the transparency of each crystal is measured every 20 minutes by injecting laser pulses and reading out the response.

Precision alignment is needed for the inner tracker and muon system. The inner tracker alignment is calculated using  $Z \rightarrow \mu\mu$  and  $W \rightarrow \mu\nu$  events collected at low luminosity. The muon system has a hardware alignment system, but with less alignment parameters than those needed for the inner tracker.

### 3.2.10.4 Data Quality Monitoring and Certification

The data is monitored and checked in order to ensure good quality. The Data Quality Monitoring (DQM) system monitors all the data from the different subsystems. The data is monitored online in the control room as well as offline, when it can be checked more thoroughly.

After the data is checked through the DQM system, the data is certified to be “good” for physics use. Each subsystem is checked to see if it performed well for each lumi section of recorded data. These checks are then combined into JavaScript Object Notation (JSON) files, which indicate if the data was marked “good” for all of the subdetectors for each lumi section. There is a “Golden” JSON file, which indicates all

of the lumi sections in which all of the subdetectors were marked “good,” and there is a “Muon” JSON file, in which the calorimeters do not need to have marked the lumi sections as “good.”

### 3.2.11 The Event and Object Reconstruction

Different elementary particles will leave different signatures in the CMS detector, and in this way, one can identify the particles resulting from a  $pp$  collision. CMS aims to be *hermetic*, meaning that all the particles produced should be detected and their positions and momenta should be well measured. If all the particles in the event can be detected, then the presence of neutrinos can be inferred: all the transverse momenta in the final state should vectorally sum to zero because the initial state should have no transverse momentum and because conservation of momentum should be upheld. If there is an imbalance of momentum, it is implied that an undetected, noninteracting neutral stable particle, such as a neutrino, was produced. This imbalance of momentum is called MET.

Figure 3.31 shows the signature of different particles in a transverse slice of the CMS detector. Charged particles will leave tracks in the tracking detectors. Particles that interact electromagnetically and are not minimum-ionizing will deposit their energy in the ECAL, while particles that interact hadronically will deposit their energy in the HCAL. As alluded to in Section 3.2.7, a muon will traverse the entire detector, making tracks in the inner tracker and muon system, as it is a charged, minimum-ionizing particle. The muon has a relatively long lifetime of  $2.2 \mu\text{s}$ , which means that if it is traveling close to the speed of light, it can travel beyond the muon system before decaying. Due to the changing direction of the magnetic field, the muon will bend one way before it passes the solenoid and bend the other way outside it. An electron will make a curved track in the inner tracker and then deposit all of its energy in the ECAL. A photon will also deposit all of its energy in the ECAL, but since it is



electrically neutral, it will leave no track in the inner tracker. A charged hadron will leave a curved track in the tracker, and then deposit all of its energy in the HCAL, while a neutral hadron will not leave a track, but deposit all of its energy in the HCAL. Quarks and gluons will hadronize in the detector, producing *jets*, which leave energy deposits in the ECAL and HCAL. In addition, heavy quarks and leptons will create secondary vertices some distance from the primary vertex, as they have longer lifetimes than many other elementary particles, and so will travel some distance before decaying. Leptons, in particular, should be measured in redundant systems, i.e. tracker and muon system for muons and tracker and ECAL for electrons, in order to have a clean identification, which is necessary since the rates of the background processes are high, relative to the rare lepton production rate.

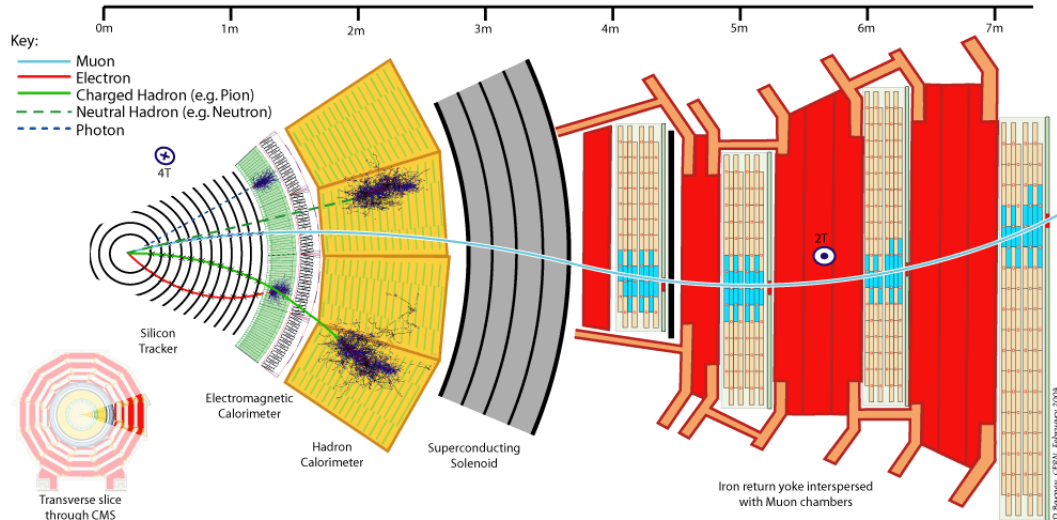


Figure 3.31: Diagram of how different particles appear in the CMS detector, in a transverse slice of the detector [68].

The CMS offline, high-level physics object reconstruction will be described in detail. The Particle Flow (PF) technique, which uses information from all the sub-detectors to reconstruct all the particles in the event, is a major theme of the CMS particle reconstruction, so it will be described in general first. The basic ingredients of PF and the way in which the particles are reconstructed will be described. Then

we will go into detail about the reconstruction of a few key physics objects in turn: muons, electrons and photons, jets, tau-leptons, and MET.

#### 3.2.11.1 Particle Flow Algorithm

PF algorithms use information from all subdetectors to reconstruct particles [83,84]. For example, instead of reconstructing a jet simply with the calorimeters, a PF jet uses redundant information from the tracker as well, resulting in much improved resolution. Furthermore, PF algorithms reconstruct all of the particles in the event, giving a global description of the event.

In order to perform PF reconstruction, there are a few requirements needed of the detector. The detector needs a large volume inner tracker in order to give highly precise and efficient tracking. A high magnetic field is necessary for good  $p_T$  resolution and to distinguish charged from neutral particles. Finally, a highly granular calorimeter, giving good energy resolution, is also necessary to distinguish charged from neutral particles.

**Basic Elements** The basic components for the PF reconstruction are tracks, ECAL and HCAL clusters, and links between the clusters and tracks. Clusters and tracks are linked together to form “blocks” with link algorithms, which draw associations between the elements and prevents double-counting of particles. The main purpose of PF is to link the information from the subdetectors, giving a global description of the particles in the event.

One of the primary ingredients in the PF algorithm is tracks. The Kalman filter algorithm is a least squares fit that forms the basis of most CMS vertex and track reconstruction algorithms [85,86]. Hits are identified in successive layers in the tracker, and combined to form *seeds*, which are the basis for the tracks. CMS has adopted an iterative tracking method in which tracks are first reconstructed using very tight

criteria. The tight selections on the tracks lead to a moderate tracking efficiency, but negligible fake rate. In the next step, the hits that were unambiguously assigned to the tracks are removed, and the selection criteria are loosened. This allows the tracking efficiency to increase and the fake rate to be kept low. The criteria are progressively loosened and the unambiguous hits removed for each iteration. The final iterations have very loose criteria placed on the primary vertex, so that secondary vertices and their resulting particles can be reconstructed. Primary vertices are identified by clustering tracks that are compatible with the beam-line; the vertex is fitted from the tracks within the cluster.

Another major component of the PF reconstruction is the calorimeter clusters. The clustering is performed separately in the barrel and endcaps of the ECAL and HCAL. The clustering algorithm starts with *cluster seeds*, which are local calorimeter cell maxima with energies above the given threshold. *Topological clusters* are formed from summing the energy from adjacent cluster seeds. The topological clusters are then the seeds of the PF calorimeter clusters.

The link algorithms associate a maximum of one tracker track, possibly several calorimeter clusters, and a maximum of one muon track, defining a single particle block. The link algorithm loops over all the tracks and clusters in the event and tries to build pairs of elements. When it tries to build a link between a track and a cluster, the algorithm proceeds by extrapolating the track from the last measured hit in the tracker. If the extrapolation is within the boundaries of the calorimeter cluster, the link is established. A link between calorimeter clusters is formed if the cluster position in the more granular calorimeter, typically the ECAL, is within the cluster envelope of the less granular calorimeter, typically the HCAL. A link between a tracker track and a muon track can also be formed: this is called a global muon and will be described in Section 3.2.11.2.

**Particle Reconstruction** For each particle block, the energy from the calorimeters can be compared with the momentum of the track. If this is done, a few categories naturally arise:

- $E_{cal} < p_{track}$
- $E_{cal} \approx p_{track}$
- $E_{cal} > p_{track}$

If the calorimeter energy is less than the track momentum, it is likely that the particle is a muon, especially if a track is created in the muon system as well as the inner tracker. Muons do not deposit much energy in the calorimeters, and so  $E_{cal}$  is likely to be small. Because of the unique signature of muons, they are the first particle to be identified in an event; in the PF algorithm, the muon block is removed from the event, and the reconstruction of the event continues. It should also be mentioned that  $E_{cal} < p_{track}$  could occur because of momentum mis-measurement or fake tracks.

If the calorimeter energy is of the same order as the track momentum, the block is probably due to a charged hadron.

The case when the calorimeter energy is larger than the track momentum is the most complicated and most typical case. If  $E_{cal} > p_{track}$ , the block could identify a charged particle, that is, either an electron or charged hadron, or a neutral particle, that is, either a photon or neutral hadron. If there is no track, the particle is neutral. If there is no track and the calorimeter energy is only in the ECAL, the block is likely to be a photon; if no track exists and the energy is only in the HCAL, the block is likely a neutral hadron. Electrons can be identified early and removed from the PF reconstruction because of their relatively short tracks and energy deposits due to bremsstrahlung radiation.

### 3.2.11.2 Muons

Muons have strong signatures in general purpose detectors like CMS, and they can usually be easily identified [84, 87–89].

The usual muon reconstruction in CMS starts with DT and/or CSC hits. For the DTs, if there are at least three hits in one super-layer, a DT segment can be formed. (Recall that there are four layers to a super-layer, and two or three super-layers per DT chamber: see Section 3.2.7.1). Then other hits from other super-layers can be included in the segment if the pattern recognition deems them to be aligned. Segments in the CSCs are formed in a similar fashion.

Seeds are then formed, which are patterns of DT and/or CSC segments. A  $p_T$  value of the seed is estimated with a parametrization of the form  $p_T = A - \frac{B}{\Delta\phi}$ , which assumes the muon originated at the primary vertex. A segment-based fit to the seeds is performed, and thus a track in the muon system is created. This muon system track is called a standalone (SA) muon track. The SA muon track can be updated at the vertex, which applies an additional bias. In 2012, a new collection called the refitted SA muon collection was introduced, which performs a refit to try to remove the bias toward the beam spot [90]. In 2014, another new collection called the displaced standalone (DSA) muon collection was introduced, which uses a cosmic seed to start the standalone muon track. See 5.3.1 for more information.

Separately, tracks in the inner tracker are created. If a SA muon track can be matched to a tracker muon track, a *global muon* is formed after a refit to all the tracker hits and muon hits is performed. A global muon is highly preferred by most analyses because the combination of information from all the subdetectors greatly improves the resolution; see Fig. 3.32 for a plot of the muon  $p_T$  resolution when using the inner tracker tracks only, the muon system only, and both systems combined. A global muon can also be labeled as a *PF muon* if its combined momentum is compatible with that determined from the tracker alone, within three standard deviations.

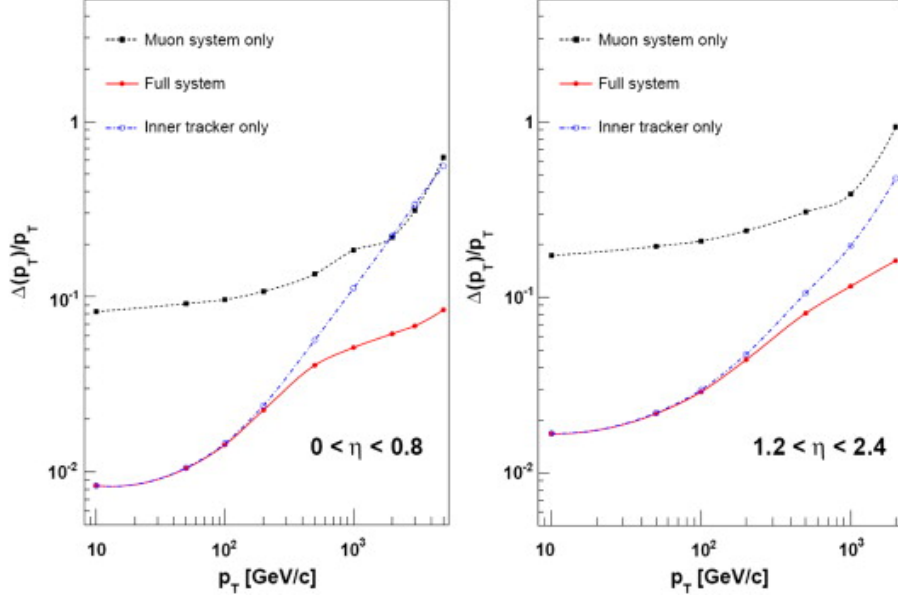


Figure 3.32: The muon  $p_T$  resolution in CMS as a function of the  $p_T$  for  $|\eta| < 0.8$  (left) and  $1.2 < |\eta| < 2.4$  (right) [71].

Additionally, a muon called a *tracker muon* is defined, which consists of a tracker track that is not matched to a full SA muon track, but to compatible signals in the calorimeter and/or a few muon segments. A tracker muon is defined for the times when a low momentum muon ( $\sim 6$  GeV) does not have enough energy to create a track in the muon system.

The typical muon reconstruction for pp collisions has been described above, but there is an additional reconstruction reserved for cosmic muons and beam halo that will be mentioned here [91]. Cosmic muons result from the showers of cosmic rays, and some penetrate the CMS detector, despite the fact that it is shielded from most cosmic rays due to the 100 m of earth above it. Furthermore, when the proton bunches travel through the beam pipe, they can create muons, which might also travel through the beam pipe and end up in the CMS detector. Since cosmic and beam halo muons do not originate at the primary vertex, they will create different types of muon tracks and deserve their own reconstruction algorithm, called the cosmic reconstruction. The cosmic reconstruction assumes the muon originated in the top

hemisphere of the detector and is traveling downwards. The cosmic muon could be reconstructed as one long muon track, nominally in both the upper and lower hemispheres, or as two separate muon tracks, allowing the possibility for only one track to be reconstructed if the cosmic muon enters or leaves the detector at an odd angle and there are insufficient hits to create a full muon track in one half of the detector. The cosmic muon reconstruction is seeded by a 10 GeV seed.

Given the different muons described above, CMS has defined several muon selections, which are commonly used in analyses [92]. A *Loose Muon*, which is a PF muon and either a global or a tracker muon, is defined for the analyses that need a very loose definition of a muon. A “Soft Muon” is a good quality tracker muon and was defined largely for the use of the B physics group. A *Tight Muon* is a global and PF muon with additional quality requirements on the number of tracker and muon hits, the  $\chi^2$  of the tracks, and the distance of closest approach to the beam line. A *High  $p_T$  Muon* is similar to the Tight Muon, except the PF muon condition is not required and other requirements are made more appropriate for high  $p_T$  muons.

The Muon POG also has recommendations for detector-based and PF-based isolation, detailed in Ref. [92].

### 3.2.11.3 Electrons and Photons

After muons are removed in the PF algorithm, electrons are the next to be identified [84, 93, 94]. Electrons will leave energy deposits in the ECAL and tracks in the inner tracker; photons will not leave tracks, since they are electrically neutral, and will simply deposit energy in the ECAL.

The reconstruction of both electrons and photons starts with *superclusters* in the ECAL. Superclusters are sums of energy deposits made from particles showering in the ECAL, which are separated only in the  $\phi$  direction. An electron will typically deposit 97% of its incident energy in a  $5 \times 5$  crystal window. If the superclusters can

be matched to track seeds from the pixel detector, then a Gaussian-Sum Filter (GSF) electron is formed; if not, then the supercluster is reconstructed as a photon. The GSF reconstruction is based on a generalized Kalman filter algorithm that accounts for the bremsstrahlung energy loss in the silicon tracker [95]. The GSF electron becomes an electron candidate if it can be significantly distinguished from a hadron. To do this, several criteria are imposed: the width of the supercluster in the  $\eta$  direction must be small, the supercluster energy must be substantial, the energy deposited in the ECAL must be much larger than that deposited in the HCAL (the “H/E” must be small), and the electron candidate must be well-separated from any muon candidate, in order to reject events where a muon leaves a track and a nearby hadron deposits significant energy in the ECAL. If these criteria are passed, the electron candidate can become a *PF electron* and is subsequently removed from the PF algorithm.

Details about how to use electrons and photons in CMS analyses can be found in Refs. [94,96].

#### 3.2.11.4 Jets

After muons and electrons are identified by the PF algorithm, the remaining particle blocks are subjected to tighter quality criteria and the calorimeter clusters are calibrated [84]. The remaining blocks are classified as either *PF photons*, *PF charged hadrons*, or *PF neutral hadrons*.

*PF jets* are formed from the PF hadrons by using the direction of the particle at the primary vertex and the anti- $k_t$  algorithm [97]. Jets are the hadronic showers of particles, created from quarks and gluons. The anti- $k_t$  algorithm and other jet-finding algorithms used in CMS proceed by merging neighboring particles if they are closer together than each individually is to the transverse plane of the beam line. This procedure continues iteratively until all of the PF hadrons have been grouped into PF jets.



For some analyses, particularly those having to do with top quarks,  $b$ -quarks, and W bosons, the identification of  $b$ -quarks, or more practically, of  $b$ -jets, can be of particular use.  $b$ -quarks are more massive (4.2 GeV) and have a longer lifetime (1.5 ps) when compared with light flavor quarks. Thus, they will typically arise from secondary vertices and can be identified by various *b-tagging* algorithms. There has been much work in CMS on  $b$ -tagging algorithms [98].

### 3.2.11.5 Taus

Tau-leptons are quite massive at 1.7 GeV, and the tau lifetime is short enough that they decay at the primary vertex [99]. Taus decay to leptons about 1/3 of the time and to one or three charged hadrons about 2/3 of the time. If the tau decays to electrons or muons, these lighter leptons will be identified, and it is difficult to identify which electrons and muons came from tau decays and which did not. Tau identification in CMS is largely concentrated on distinguishing them from decays to hadrons, which are usually charged pions.

The tau reconstruction at CMS benefits enormously from the PF algorithm. Taus are identified in general by starting with the highest  $p_T$  photon or electron in a jet, clustering all the electrons and photons in strips to capture all conversions to neutral pions, and then combining with charged hadrons to form tau candidates. Since this algorithm uses strips and charged hadrons, it is called the Hadron Plus Strips (HPS) algorithm. The strips are electromagnetic clusters with dimensions  $(\Delta\eta, \Delta\phi) = (0.05, 0.20)$ . The charged hadrons and strips are reconstructed into a narrow cone with  $\Delta R = 2.8/p_T$ , where the  $p_T$  is that of the tau and  $0.05 < \Delta R < 0.1$ . There are four possible decay modes:

- Single Hadron, where the tau candidate decayed directly to a charged hadron or in the presence of soft neutral pions
- Hadron plus One Strip, where a single charged hadron and one neutral pion

are reconstructed. The charged hadron and the strip are required to have an invariant mass compatible with the  $\rho$  meson.

- Hadron plus Two Strips, where a single charged hadron and a neutral pion are reconstructed. The pion energy must be separated on the calorimeter surface. The charged hadron and strips must also have an invariant mass compatible with the  $\rho$  meson, and the mass of the two strips must be between 50 MeV and 200 MeV.
- Three Hadrons, where three charged hadrons are reconstructed. The charge of the three hadrons must sum to 1, and they must have a mass compatible with the  $a_1$  meson.

Tau candidates must also pass isolation criteria and survive rejection of fakes from electrons and muons.

### 3.2.11.6 Missing Transverse Energy

The momentum in the transverse plane of an event should be conserved; thus, by measuring all the particles in an event, we can determine if any additional energy is needed in order to preserve the balance of momenta. If any such MET is detected, it could be indicative of the presence of neutrinos, or in some BSM theories, the presence of weakly interacting massive particles and the possible signature of dark matter.

MET in CMS is usually determined from the last step of the PF algorithm [100]. MET is the negative of absolute value of the vector sum of the transverse momenta of all the PF particles in the event:

$$\cancel{E}_T = -\left|\sum_i \vec{p}_T\right| \quad (3.8)$$

where  $i$  runs over all the PF particles in the event. MET is dependent on the efficiency of particle reconstruction and the ability to measure their momenta. MET is

sometimes also calculated in CMS using only the energies contained in the calorimeter towers and their directions relative to the center of the detector; this is called Calo MET. However, PF MET is used in the majority of CMS analyses due to its improved accuracy.

Now that we have discussed the LHC and CMS detector and we understand how the different known elementary particles are reconstructed in CMS, we can go on to discuss searches for long-lived exotic particles in the next chapter.

## Chapter 4

# EXOTIC LONG-LIVED PARTICLES

We can perform searches for exotic particles beyond the SM with the LHC and the CMS detector. We will now discuss specific BSM searches for long-lived particles (LLPs). “Long-lived” exotic particles have long lifetimes, giving them decay lengths comparable to the scale of the detector, and do not decay virtually immediately at the interaction point. Rather, they travel some distance, possibly centimeters or meters, before decaying.

Searches for LLPs are interesting, at least in part, because they need to make use of unique features of the detectors. These are not run-of-the-mill, dime-a-dozen analyses. They often have dedicated triggers, unique object reconstruction, atypical techniques and discriminating variables, or other special considerations. The objects often do not point back toward the IP, unlike particles in most other reconstructed events, and so sometimes special reconstruction algorithms must be used. Also, the important variables in the search, such as the time at which the particles are created or interact with the detectors, their velocity, or their ionization energy, are often not important for most of the other physics analyses done at these general purpose experiments. These LLP searches often have no irreducible backgrounds from SM processes, but rather, atmospheric cosmic rays, detector effects, misreconstructed

objects, and noise often are much more important sources of background.

LLPs could come with many different attributes, if they exist. They could be electrically neutral or charged; if they are charged, they could have unit, fractional, or multiple charge. It is possible that they could also have color. Furthermore, these particles could have a wide range of lifetimes. They might live long enough to decay outside the detector, or they may decay inside the detector, or they could even come to a complete stop in the detector before decaying.

This chapter will discuss LLPs beyond the SM: why we might search for them, theoretical models that predict them, how they would interact and appear in general-purpose detectors, and previous and ongoing searches for them at colliders. See Refs. [101, 102] for recent reviews and analyses of LLP searches.

## 4.1 Motivation for LLP Searches

As stated in Chapter 2, the SM is a precise theory of particles and their interactions, but it is incomplete. As a result, we should look for physics beyond the SM; there are no massive LLPs in the SM. Furthermore, the detector signatures of LLPs are extremely unique, so any evidence of these particles has a high probability of leading to a discovery.

We currently have no explanation of the dark matter observed in the universe. We have yet to find a dark matter particle, which would be a neutral, completely stable particle beyond the SM (see Section 2.2.1.3 for more on dark matter). Furthermore, cosmology may hint that a charged, LLP could exist, although it rules out absolutely stable charged massive particles, as they would be observable today [103–105]. Our present model of big bang nucleosynthesis (BBN) has difficulties in explaining the observed lithium production, but a charged LLP that decays during or after the time of BBN could resolve this disagreement [1].

Another possible phenomenon that could give rise to a LLP that could be detected at colliders is a monopole. A magnetic monopole is a hypothetical particle that is an isolated magnet with only one magnetic pole. However, all observed magnetic particles have a “North” and “South” pole; all particles have zero magnetic charge. Dirac first introduced the concept of the magnetic monopole in 1931 to explain the quantization of electric charge [106, 107]. Monopoles could be detected at colliders because they would be highly ionizing and relativistic, and could be easily distinguished from minimum ionizing particles.

## 4.2 Theoretical Models Predicting LLPs

There are many theories beyond the SM that predict the existence of massive LLPs. Section 2.3 gave an overview of BSM theories; this section will go into more detail about the specific models that predict LLPs.

### 4.2.1 Minimal Supersymmetry

The Minimal Supersymmetric Standard Model (MSSM) is the minimal extension to the SM that results in SUSY [39]. The particle content of the MSSM was actually already described when SUSY was introduced in Section 2.3.1, but it might be helpful to display the chiral and gauge supermultiplets in Tables 4.1 and 4.2, respectively.

Table 4.1: The chiral supermultiplets in the MSSM. The spin 0 fields are complex scalars, and the spin  $\frac{1}{2}$  fields are the left-handed two-component Weyl fermions [39].

Particle		Spin 0	Spin $\frac{1}{2}$	SU(3) <sub>C</sub> , SU(2) <sub>L</sub> , U(1) <sub>Y</sub>
<b>sleptons, leptons</b>	$L$	$(\tilde{\nu} \ \tilde{e}_L)$	$(\nu \ e_L)$	$(\mathbf{1}, \mathbf{2}, -\frac{1}{2})$
( $\times 3$ families)	$\bar{e}$	$\tilde{e}_R^*$	$e_R^\dagger$	$(\mathbf{1}, \mathbf{1}, 1)$
<b>squarks, quarks</b>	$Q$	$(\tilde{u}_L \ \tilde{d}_L)$	$(u_L \ d_L)$	$(\mathbf{3}, \mathbf{2}, \frac{1}{6})$
( $\times 3$ families)	$\bar{u}$	$\tilde{u}_R^*$	$u_R^\dagger$	$(\bar{\mathbf{3}}, \mathbf{1}, -\frac{2}{3})$
	$\bar{d}$	$\tilde{d}_R^*$	$d_R^\dagger$	$(\bar{\mathbf{3}}, \mathbf{1}, \frac{1}{3})$
<b>Higgs, higgsinos</b>	$H_u$	$(H_u^+ \ H_u^0)$	$(\tilde{H}_u^+ \ \tilde{H}_u^0)$	$(\mathbf{1}, \mathbf{2}, +\frac{1}{2})$
	$H_d$	$(H_d^0 \ H_d^-)$	$(\tilde{H}_d^0 \ \tilde{H}_d^-)$	$(\mathbf{1}, \mathbf{2}, -\frac{1}{2})$

Table 4.2: The gauge supermultiplets in the MSSM [39].

Particle	Spin $\frac{1}{2}$	Spin 1	SU(3) <sub>C</sub> , SU(2) <sub>L</sub> , U(1) <sub>Y</sub>
<b>gluino, gluon</b>	$\tilde{g}$	$g$	$(\mathbf{8}, \mathbf{1}, 0)$
<b>winos, W bosons</b>	$\tilde{W}^\pm, \tilde{W}^0$	$W^\pm, W^0$	$(\mathbf{1}, \mathbf{3}, 0)$
<b>bino, B boson</b>	$\tilde{B}$	$B$	$(\mathbf{1}, \mathbf{1}, 0)$

In the MSSM, the LSP is often the neutralino. The NLSP can be long-lived if the mass splitting between the NLSP and the LSP is small. If the stop is the NLSP, there are some regions of phase space where the stop can be long-lived [108]. If the mass difference between the stop and the neutralino is too small for the stop decay to a neutralino and a bottom quark to be kinematically allowed, then the stop decay will proceed via the radiative decay to a neutralino and a charm quark. This will make the stop long-lived, on the timescales of particles decaying within the detector.

## 4.2.2 Gauge Mediated Supersymmetry Breaking

Gauge mediated supersymmetry breaking (GMSB) is a SUSY model in which the supersymmetry breaking is mediated by the gauge interactions, as mentioned in Section 2.3.1 [109]. GMSB models contain three different sectors of particles: the observable sector, which contains the SM particles, two Higgs doublets, and their superpartners;

the secluded sector, which is responsible for the SUSY breaking; and the messenger sector, which contain new superfields that transform under the gauge group and couple with the goldstino superfield.

Furthermore, GMSB models are characterized by six different parameters:

- The effective mass scale of the SUSY breaking ( $\Lambda$ )
- The common messenger particle mass ( $m_m$ )
- The number of SU(5) chiral multiplets of messengers ( $N_{mes}$ )
- The tangent of the ratio of Higgs VEVs ( $\tan \beta$ )
- The sign of the Higgsino mass term ( $\text{sgn}(\mu)$ )
- The gravitino/goldstino coupling suppression factor ( $C_G$ )

GMSB models contain a light gravitino/goldstino as the lightest supersymmetric particle (LSP) [110, 111]<sup>1</sup>. The next-to-lightest supersymmetric particle (NLSP) can be either the lightest scalar tau lepton (stau) or the lightest neutralino, depending on the choice of model parameters [39, 112]. If  $N_{mes}$  is not small, the NLSP is likely to be a stau, and the GMSB models that are often referenced in LLP analyses contain a stau NLSP. Also, if the suppression factor  $C_G$  is large, the NLSP will have a long lifetime. If the stau decays to the gravitino/goldstino LSP are sufficiently suppressed, then the stau can live long enough to escape the detector [113, 114]. A lifetime of order  $1\mu\text{s}$  or more is needed in order for a LLP to escape the detector. The stau decay length is [112]:

$$L = 10 \text{ km} [\beta\gamma] \left[ \frac{F_{DSB}^{1/2}}{10^7 \text{ GeV}} \right]^4 \left[ \frac{100 \text{ GeV}}{m_{\tilde{\tau}_1}} \right]^5 \quad (4.1)$$

---

<sup>1</sup>We call it a “gravitino/goldstino” because the gravitino “eats” the goldstino, but the couplings of the goldstino are more important in determining the interactions of the particle. So there is one particle, but it is important to recognize the properties of the goldstino that is eaten by the gravitino.



where  $\beta$  is the velocity of the stau,  $\gamma$  is the usual relativistic parameter,  $F_{DSB}^{1/2}$  is the non-zero vacuum expectation value of the dynamical SUSY breaking (DSB) sector of the GMSB model, and  $m_{\tilde{\tau}_1}$  is the mass of the stau. The stau can be long-lived if  $F_{DSB}$  is on the order of  $10^7$  GeV or larger. If the stau NLSP is long-lived, then all heavier SUSY particles will first decay to a stau, which then decays to the gravitino/goldstino LSP. If SUSY with a gravitino/goldstino LSP exists in nature, the lifetime of the stau NLSP should be of order one year or more in order to avoid complications with the structure formation and BBN in the early universe.

### 4.2.3 Anomaly Mediated Supersymmetry Breaking

As mentioned in Section 2.3.1, anomaly mediated supersymmetry breaking (AMSB) is a SUSY model where the SUSY breaking is mediated by gravity [39, 115–119]. The gauge supermultiplets are confined to the observable MSSM plane, and the supergravity effects occur in the secluded plane. These models are called AMSB models because the SUSY breaking is transmitted to the observable sector via the super-Weyl anomaly.

The minimal AMSB model is characterized by four parameters:

- The auxiliary mass ( $m_{aux}$ ), which sets the overall SUSY breaking scale
- The common scalar mass ( $m_0$ )
- The tangent of the ratio of Higgs VEVs ( $\tan\beta$ )
- The sign of the Higgsino mass term ( $\text{sgn}(\mu)$ )

AMSB models can often have charginos as the NLSP and neutralinos as the LSP. If the mass difference between the chargino and the neutralino is small, that is, less than about 150 MeV, then there is little kinematic phase space available for the chargino to decay to the neutralino, and as a result, the chargino can be long-lived, with a lifetime of about 10 ns or more.

#### 4.2.4 Split Supersymmetry

Split SUSY is a model in which SUSY is broken near the unification scale [120,121]. This results in the supersymmetric squarks and sleptons being very heavy ( $> 1$  TeV), while the gauginos remain relatively light and account for the unification of the gauge couplings. The gluino is the only colored particle at this low mass scale, and it can only decay through  $t$ -channel exchanges of a virtual squark. Since the squarks are very massive, this decay will be suppressed and thus, the gluino can have a long lifetime, possibly up to 100 s. Gluinos will form  $R$ -hadrons; the specifics of this process will be discussed in Section 4.3.2.

#### 4.2.5 $R$ -Parity Violating Supersymmetry

Many SUSY models conserve  $R$ -parity, which allows the conservation of baryon ( $B$ ) and lepton ( $L$ ) numbers and guarantees the stability of the LSP, making it a natural dark matter candidate [122]. However, there are also many SUSY models that violate  $R$ -parity: we call these models  $R$ -parity violating (RPV) SUSY models. Although RPV SUSY models would necessarily violate  $B$  and  $L$  and the LSP would be allowed to decay to SM particles, the phenomenological difficulties could be overcome if the RPV interactions are small. Furthermore, RPV interactions could be desired because they could provide a source of the Majorana masses for neutrinos and/or an explanation of the baryon-antibaryon asymmetry in the universe.

In these RPV SUSY models, the LSP would be slightly long-lived due to the small RPV couplings, with decay lengths between about 1 mm and 1 m. These slightly LLPs are predicted by several RPV SUSY models, including those discussed in [122,123].

### 4.2.6 Models with Multiply or Fractionally Charged Particles

There are several BSM theories that give rise to particles with charge  $Q$  not equal to  $e$ , namely, multiply charged massive particles (mchamps) or fractionally charged massive particles (fchamps) [124]. These types of particles could be created by a modified Drell-Yan production of long-lived lepton-like fermions. Because their charge is not equal to  $e$ , they are neutral under  $SU(3)_C$  and  $SU(2)_L$ , and therefore only couple to the photon and  $Z$  boson via  $U(1)$ .

### 4.2.7 Supersymmetric Left-Right Model

Some BSM theories extend the SM Higgs sector to include new Higgs doublets or triplets containing doubly charged Higgs bosons ( $H^{\pm\pm}$ ), thereby including additional symmetries. One such model is the Supersymmetric Left-Right model, which introduces a right-handed version of the weak interaction where the gauge symmetry is spontaneously broken at a high mass scale [125]. This model predicts light neutrino masses by the seesaw mechanism, which is consistent with neutrino oscillation observations [19].

The  $H^{\pm\pm}$  often decays to two same-sign charged leptons. Since the  $H^{\pm\pm}$  is pair produced, the decay is  $H^{++}H^{--} \rightarrow l^+l^+l^-l^-$ . In this process, the quantity  $B$  minus  $L$  is conserved, but  $L$  is not conserved;  $B$  is the baryon number and  $L$  is the lepton number. Therefore, this is a lepton number violating model in which the  $H^{\pm\pm}$  has a nearly zero coupling ( $h_{ll'}$ ) to electrons and muons and a long lifetime. The CDF collaboration performed searches for doubly charged Higgs: a search for a prompt  $H^{\pm\pm}$  in the  $ee$ ,  $e\mu$ , and  $\mu\mu$  decay channels, and a search for a long-lived  $H^{\pm\pm}$  with  $c\tau > 3\text{m}$  [126, 127].

Another Supersymmetric Left-Right model with lepton number violating decays

of the Higgs boson, which results in heavy neutrinos and LLPs is given in [128].

### 4.2.8 Hidden Valley Models

As discussed in Section 2.3.4, Hidden Valley models propose new particles in a hidden sector of phase space; these particles could be long-lived and have displaced vertices [54, 55].

In particular, Ref. [129] proposes a model in which the Higgs boson decays to two neutral LLPs ( $H \rightarrow XX$ ). Each  $X$  particle could decay to two oppositely signed leptons, which would come from a displaced vertex. Each pair of leptons would form a narrow resonance in the dilepton mass spectrum.

Furthermore, there are other Hidden Valley models in which a non-SM Higgs boson decays to hidden fermions, which in turn decay to either a dark photon and a lighter hidden fermion or to a lighter hidden fermion and a hidden scalar, which then decays to pairs of dark photons [130, 131]. The dark photons can then decay to “lepton-jets”, which are collimated jet-like structures containing pairs of electrons and/or muons and/or charged pions. These lepton-jets can be produced far from the IP.

### 4.2.9 Untracked Signals of SUSY

Some additional models will give rise to appearing or kinked tracks [132]. An appearing track is a track that starts in the middle of the tracker or a calorimeter and is produced when a long-lived neutral particle travels for some distance before decaying to a charged particle and another soft charged particle with low momentum. A *kinked track* is a track with a large bend in it, which is made when a long-lived charged particle decays to another charged particle and either a soft charged particle or a neutral particle.

The SUSY models discussed in Ref. [132] that give rise to appearing or kinked

tracks involve slowly decaying charged Higgsinos that are lighter than neutral Higgsinos. However, other models could easily give rise to kinked tracks, as any slow-moving, charged particle could decay to other charged particles and thereby produce kinks. Some of these models involve a stop LSP with RPV coupling [132], a long-lived slepton NLSP [133], a wino NLSP [134], and a weakly interacting axino LSP [135]. Similar models might produce appearing tracks.

#### 4.2.10 Magnetic Monopoles

Magnetic monopoles were first introduced by Dirac in 1931 [106, 107]. Dirac showed that if monopoles exist, electric and magnetic charge must be quantized. If you have an electric charge  $q_e$  and a magnetic monopole with magnetic charge  $q_m$ , you can find that the total angular momentum stored in the fields  $\vec{L}$  is [101, 136]:

$$\frac{\mu_0}{4\pi} q_e q_m \quad (4.2)$$

Since quantum mechanical angular momentum comes in half-integer units of  $\hbar$ , we have:

$$\frac{\mu_0}{4\pi} q_e q_m = \frac{n\hbar}{2} \quad (4.3)$$

where  $n$  is an integer. If  $q_e = e$  and  $n = 1$ , we have:

$$q_m = \frac{\hbar c}{2e} \approx \frac{137}{2} e \quad (4.4)$$

And so the Dirac monopole has a charge of  $137e/2$ .

Monopoles have also been developed in the context of other theoretical models. Monopoles have been shown to arise as topological defects of space-time in GUTs [137, 138]. However, this would give rise to super heavy monopoles, with masses between  $10^{15}$  and  $10^{16}$  GeV. Intermediate mass monopoles, with masses between  $10^7$

and  $10^{14}$  GeV, arise through other symmetry-breaking scenarios [139, 140]. Gauge monopoles from electroweak symmetry breaking or another mechanism could give monopole masses such that they could be discovered at the LHC [141–144].

## 4.3 LLP Interactions in Matter

Now that we have an idea of the theory behind LLPs, we can start to think about how they will look in the detector. Before describing the different types of detector signatures of LLPs, we should first discuss the basic ways that LLPs interact in matter. As discussed in Section 3.2.1, particles can interact with atomic electrons or atomic nuclei. For LLPs, interactions with atomic electrons typically give rise to ionization, and interactions with atomic nuclei typically give rise to hadronization, if the LLP has color [101]. A few details of LLP ionization and hadronization will be discussed here.

### 4.3.1 Ionization of Electrically and Magnetically Charged LLPs

The typical electromagnetic interaction of LLPs with matter is ionization. The ionization energy loss of electrically charged LLPs can be described by the Bethe equation

$$-\left\langle \frac{dE}{dx} \right\rangle = KQ^2 \frac{Z}{A} \frac{1}{\beta^2} \left[ \frac{1}{2} \ln \frac{2m_e c^2 \beta^2 \gamma^2 T_{max}}{I_e^2} - \beta^2 - \frac{\delta(\beta\gamma)}{2} \right] \quad (4.5)$$

This is the very same formula as was discussed in Section 3.2.1. Lepton-like LLPs, such as the gravitino/goldstino or stau in GMSB, the charginos or neutralinos in AMSB, and multiply-charged particles, will interact in the detector through ionization.

Magnetically charged LLPs, that is, magnetic monopoles, would also lose en-

ergy through ionization [145–147]. Since Dirac monopoles have a magnetic charge of  $137e/2$ , their ionization energy loss would be several thousand times greater than that of a particle with charge  $e$ . In fact, the ionization energy loss of a monopole could be so great that it could cause the monopole to become stopped in the inner tracker. The ionization energy loss of monopoles has been shown to follow a similar form as the Bethe equation, except for the multiplicative factor of  $1/\beta^2$ . The stopping power of a monopole of strength  $g$  is given by:

$$-\left\langle \frac{dE}{dx} \right\rangle = KQ^2 \frac{Zg^2}{A} \left[ \frac{1}{2} \ln \frac{2m_e \beta^2 \gamma^2 T_{max}}{I_m^2} - \frac{1}{2} - \frac{\delta(\beta\gamma)}{2} + \frac{K(|g|)}{2} - B(|g|) \right] \quad (4.6)$$

See Table 4.3 for the definitions and values of the additional variables in this formula. Inspection of Equations 4.5 and 4.6 shows that the ratio of the stopping power of a Dirac monopole of unit magnetic charge to that of a unit electrically charged particle is about  $4700\beta^2$ .

Table 4.3: The variables used in the modified Bethe formula for monopoles [1]. The variables listed here are those besides the ones listed in Table 3.2.

Symbol	Definition	Value and/or Units
$I_m$	Mean excitation energy for monopoles	eV
$K( g )$	Correction term	0.406 for $g = 1$ 0.346 for $g = 2$
$B( g )$	Correction term	0.248 for $g = 1$ 0.672 for $g = 2$

We can also discuss the range of the ionization loss of monopoles, given by:

$$R = \int_0^E \frac{dE}{dE/dx} = M \int_0^\gamma \frac{d\gamma}{dE/dx(\beta\gamma)} \quad (4.7)$$

Figure 4.1 shows the stopping power for Dirac monopoles in aluminum as a function of their speed  $\beta$ , on the left. It can be seen from this figure that as the monopole

slows down, the ionization becomes less dense, in contrast to electrically charged particles (see Fig. 4.4). On the right, this figure shows the range normalized to the mass of Dirac monopoles, as a function of  $\beta\gamma = p/M$ . Monopoles give a very striking ionization signature in matter.

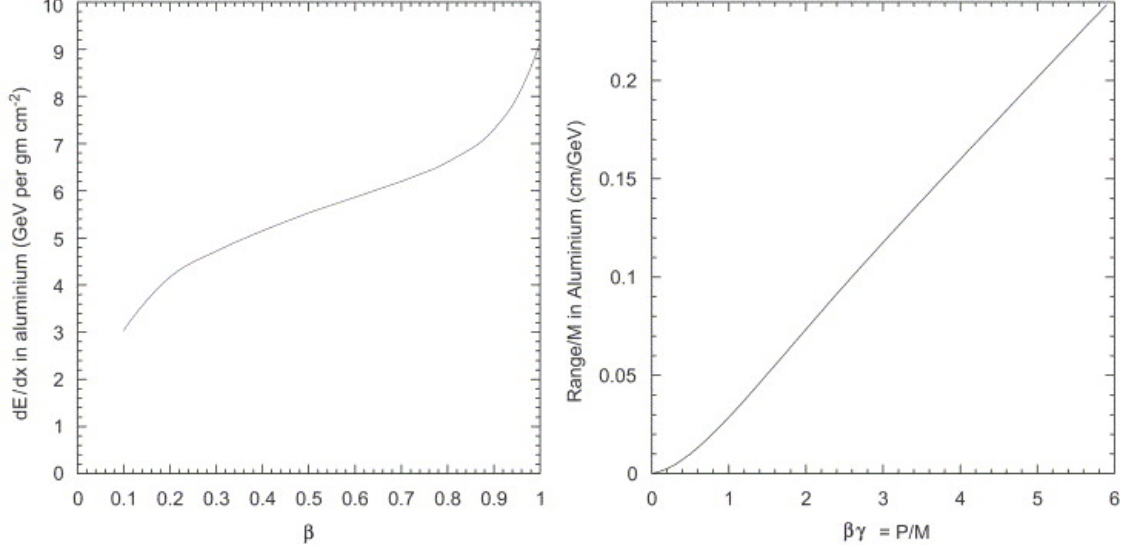


Figure 4.1: Stopping power ( $\langle -dE/dx \rangle$ ) for Dirac monopoles in aluminum as a function of  $\beta$  (left). The ratio of range to mass for Dirac monopoles in aluminum as a function of  $\beta\gamma = p/M$ , calculated from the stopping power (right) [101].

### 4.3.2 Hadronization of LLPs

Colored LLPs will interact with atomic nuclei of the detector material and undergo hadronization, picking up a light quark or gluon degrees of freedom. They could become either mesons or baryons; collectively, they are called *R*-hadrons, a name borrowed from SUSY that refers to the non-trivial *R*-parity of such hadrons. *R*-hadrons can be charged or electrically neutral, and as they traverse the detector, they can continue to hadronize and possibly change their charge [148, 149]. *R*-hadrons may not hadronize significantly, allowing them to traverse the detector and possibly reach even the muon system. On the other hand, significant hadronization may result in the *R*-hadrons coming to a stop in the detector. Colored LLPs, such as the gluinos



in Split SUSY or the stops in MSSM, will form  $R$ -hadrons.  $R$ -hadrons are typically modeled in Pythia and Herwig. For more information, see Ref. [101] and citations therein.

## 4.4 Detector Signatures of LLPs

Long-lived exotic particles can have a wide range of signatures. Some might pass through the detector, possibly all the way, with a strange signature. For example, they could have highly ionizing tracks, or low ionizing tracks. There are other LLPs that could have lifetimes such that they would decay in the detector. These particles could have displaced vertices, decay to non-pointing objects, or display kinked tracks in the detector. There are still other particles that could be so heavy that they actually come to a complete stop in the detector and decay sometime later.

### 4.4.1 Signature of Particles that Pass Through the Detector

We will first discuss the signature of LLPs that could pass all the way through the detector before decaying. This type of LLP has been called a Heavy Stable Charged Particle (HSCP), Massive Charged Particle (MCHAMP or CHAMP), Charged Massive Stable Particle (CMSP), or Charged Massive Long-Lived Particle (CMLLP) in the literature, but all these names refer to the same type of particle. We will stick with the CMLLP name here. These particles are electrically charged, have mass on the order of at least 100 GeV, and are long-lived in the sense that they would not decay within the detector. As they pass through the entire detector, they appear like muons, which are the only known charged particles that penetrate the entire detector (see Fig. 4.2 for a diagram of how different particles behave in the detector).

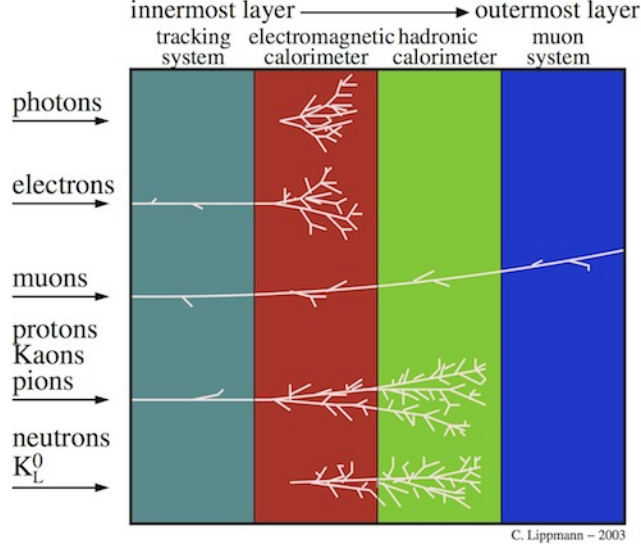


Figure 4.2: Diagram of the behavior of different particles in general-purpose particle experiments.

However, CMLLPs could be distinguished from SM muons by their speed and ionization energy loss per unit length ( $dE/dx$ ) [101]. Because CMLLPs are more massive than muons, they would move slower and ionize more heavily in the detector. However, the CMLLP ionization energy loss would be small compared to its kinetic energy. CMLLPs have high  $p_T$  due to their large mass, and so the CMLLPs could traverse the entire detector. Beam-produced muons, especially the high  $p_T$  ones that the experiment will trigger on, will be highly relativistic in the detector and travel near the speed of light. CMLLPs, on the other hand, would not be relativistic and would have a speed significantly less than  $c$ , due to their large mass. The speed of the muon or CMLLP could be measured from the time-of-flight (TOF) in the muon system, that is, how long it takes to traverse the detector. See Fig. 4.3 for a distribution of the speed, at the generator level, for simulated CMLLPs (staus, in this case) and  $Z \rightarrow \mu\mu$  events, from a D0 study.

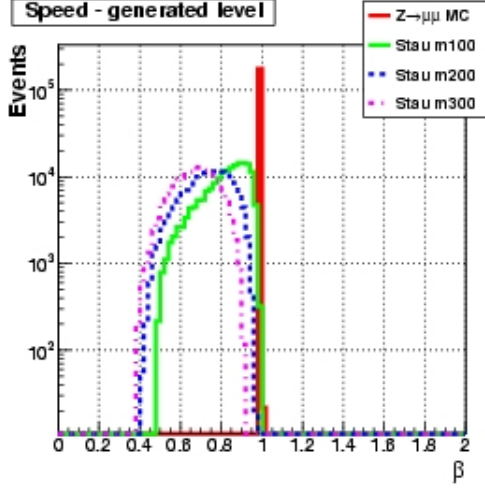


Figure 4.3: The speed distribution for MC at the generator level for three mass points of CMLLPs (stau samples 100, 200, and 300 GeV) and standard model muons from Z decays [150].

Furthermore, one can differentiate between muons and CMLLPs by the energy loss of the particle in the detector. As described in Section 3.2.1, muons will primarily lose energy in the detector from ionization, if their momentum is sufficiently low, that is, less than several hundred GeV, or they will primarily lose energy through radiation, if their momentum is greater than several hundred GeV [1]. Fig. 4.4, which shows the rate of energy loss  $dE/dx$  as a function of momentum for muons traveling through copper, was already shown in Section 3.2.1, but is reproduced here for convenience. Since  $\langle dE/dx \rangle \propto 1/\beta^2$ , where  $\beta$  is the speed per unit  $c$  of the particle, a CMLLP would deposit significantly more energy than a minimum ionizing muon, since a CMLLP would have  $\beta < 1$  and a muon has  $\beta = 1$ , if the detector resolution is ignored. However, if the muon has sufficiently large momentum, radiative effects begin to dominate over ionization, and the muon's  $dE/dx$  increases more rapidly, as can be seen in Fig. 4.4. As a result,  $dE/dx$  becomes a less powerful discriminator between CMLLPs and muons, since many muons in the detector will not be minimum ionizing. A particle's  $dE/dx$  could be measured in several subdetectors, but it is often measured in the tracker in CMLLP searches.

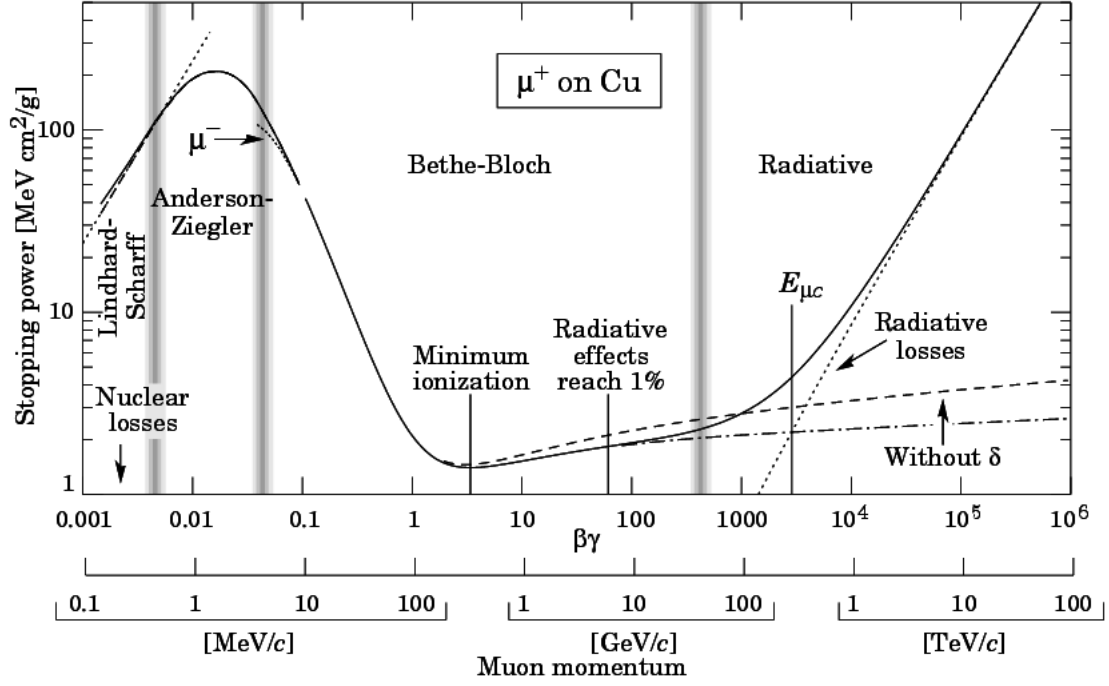


Figure 4.4: Stopping power ( $\langle -dE/dx \rangle$ ) for positive muons in copper as a function of  $\beta\gamma = p/Mc$  over nine orders of magnitude in momentum (12 orders of magnitude in kinetic energy). Solid curves indicate the total stopping power. Vertical bands indicate boundaries between different approximations [1].

The speed and  $dE/dx$  are the two main variables that can be exploited to distinguish CMLLPs from SM muons. However, there are several effects of CMLLPs that could lead to a few different signatures, each of which could be specifically searched for at colliders. First of all, a CMLLP may change its charge while interacting with the detector material. A CMLLP could be produced as charged and become neutral after interacting with the detector material, in which case, one might search for a charged particle in the inner tracker only, or a CMLLP could be produced as neutral and become charged after interacting with the detector material, in which case, one might search for a charged particle in the muon system only. The models and details of hadronization were discussed in Section 4.3.2.

Another property that could produce a different CMLLP signature is that the CMLLP could be multiply ( $Q > e$ ) or fractionally ( $Q < e$ ) charged [124]. Since  $dE/dx$

scales as the square of the charge (see Equation 3.3), multiply charged particles would have significantly greater  $dE/dx$ , while fractionally charged particles would have significantly smaller  $dE/dx$ . Searches for multiply or fractionally charged particles are complicated by the fact that the detector’s track reconstruction typically assumes  $Q = 1$  for determining  $p_T$ , meaning that the  $p_T$  of multiply (fractionally) charged tracks is underestimated (overestimated) by a factor of  $1/Q$ . Figure 4.5 shows how  $dE/dx$  can be used to distinguish CMLLP signals from backgrounds; it shows  $I_h$ , a measure of  $dE/dx$ , as a function of  $p$  for SM muons, singly, fractionally, and multiply charged CMLLP candidates in CMS data and MC.

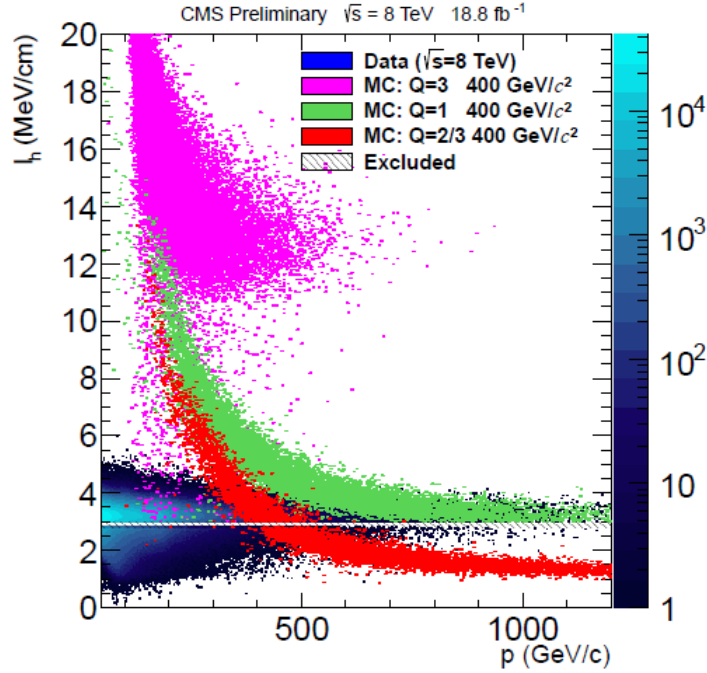


Figure 4.5: The distribution of  $I_h$ , a measure of  $dE/dx$ , as a function of  $p$  for data, singly, fractionally, and multiply charged CMLLP candidates from a CMS study [151].

#### 4.4.2 Signature of Particles that Decay in the Detector

A variety of different searches can be done for LLPs that decay somewhere within the detector [152]. For example, a neutral LLP could travel a few centimeters into the tracker before decaying, giving the signature of tracks that appear to emanate

not from the primary vertex. Searches can be performed for displaced vertices that give rise to displaced leptons, displaced jets, or non-pointing photons. In addition, a charged LLP could decay in the tracker to another charged particle and possibly a neutral particle, which would appear as a track with a “kink” in it, possibly with a large MET. A charged LLP could also decay to neutral particle(s) and low- $p_T$  pions that are not reconstructed, thereby exhibiting a “disappearing” track.

Many searches for displaced vertices focus on long-lived neutral particles that decay to two oppositely signed leptons, thereby forming a narrow resonance in the dilepton mass spectrum. Some SM processes such as  $t\bar{t}$  and  $Z \rightarrow l^+l^-$  that also decay to dileptons could be background for this search. Much of this background, however, can be rejected by requiring a large transverse decay length and/or transverse impact parameter. For neutral LLPs that decay to jets, the only significant background is multijet events, and again, making requirements on the transverse decay length and related variables can largely reduce this background.

A long-lived neutral particle could also decay to photons and MET. For this decay channel, several detector signatures could be exploited. First of all, a search could make use of timing variables in the ECAL to identify late-arriving photons. A photon that reached the ECAL significantly after the majority of prompt photons would be evidence for a LLP. In addition, one could search for photons that are converted to  $e^+e^-$  pairs, as this would signify new physics.

Searches for kinks and disappearing tracks have a few backgrounds such as hadrons that interact in the inner tracker, electrons or muons that fail to satisfy their identification criteria, and low- $p_T$  particles whose  $p_T$  is mismeasured. One can largely distinguish the signal from these backgrounds by requiring significant  $p_T$ .

### 4.4.3 Signature of Particles that Stop in the Detector

Other LLPs could be sufficiently massive, slow moving, and ionizing that they come to a complete stop somewhere in the detector and then decay seconds, days, or weeks later. If the LLP is colored, it will hadronize as it traverses the detector, creating a  $R$ -hadron, which will eventually stop in the detector [153–157]. These stopped particles can produce daughter particles when there are gaps in the beam or when there are no beams in the accelerator at all. Dedicated triggers are needed to detect particles when there are gaps in the beam. Searches have been performed for stopped particles that give rise to calorimeter deposits and for those that give rise to muons. Since the detector should be relatively quiet when there are no collisions, we can search for the decays of stopped particles with little SM background. In fact, the primary backgrounds for a search for stopped particles are simply cosmic rays, beam halo, and instrumental noise. See Fig. 4.6 for an illustration of how a stopped particle and some of the backgrounds would look in the detector.

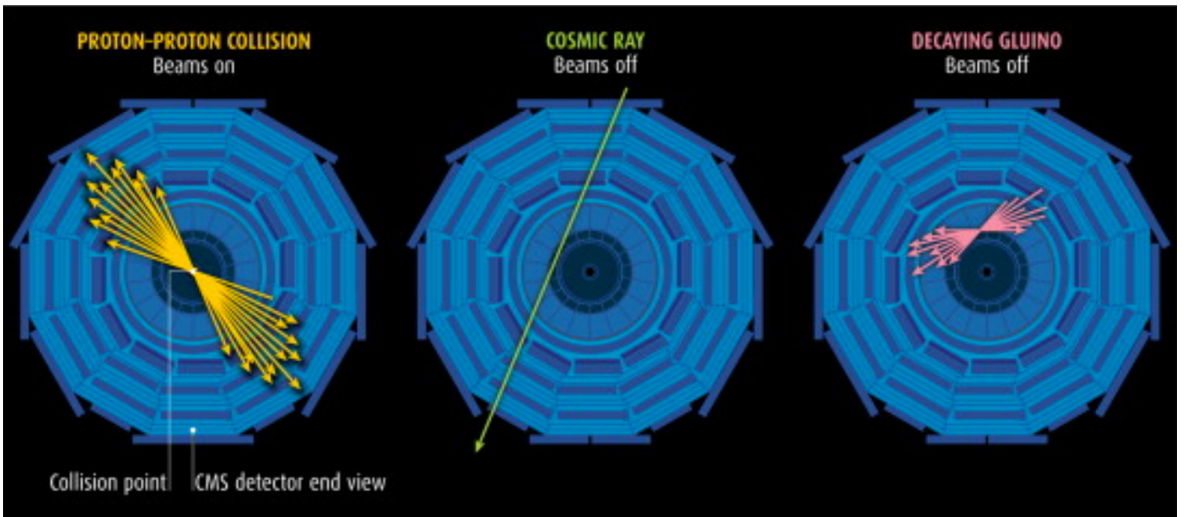


Figure 4.6: Illustration of the experimental signature of a stopped LLP and some of the principle backgrounds for this search.

An important background for a search for stopped particles is cosmic rays. Cosmic rays are particles, unusually consisting of atomic nuclei, that typically originate

outside the solar system [1]. They can create showers of secondary particles in Earth's atmosphere, and although most are stopped from reaching the CMS detector since it is about 100 m underground, some can penetrate that far. Cosmic rays that reach the CMS detector will typically be reconstructed as muons that enter the detector from the top and penetrate either partway or completely through the detector to the bottom. Furthermore, cosmic muons will in general not arrive in time with the bunch crossings. If a search is performed for stopped particles that give calorimeter deposits when they decay, cosmic ray muons can be largely rejected by vetoing on activity in the muon system. If the analysis searches for decays to muons, however, a more sophisticated cosmic rejection is needed. In this case, one might reject cosmic muons by observing the direction of the muon track; most cosmic muons will travel from the top of the detector to the bottom, while stopped particles will give rise to muons that move from the inside to the outside of the detector. The direction of a muon track can be determined from the times associated with the muon hits.

Another source of background for stopped particle searches is beam halo. Beam halo is a transverse halo of particles that forms around the narrow, focused proton beam [158]. The particles in this halo can interact with the beam pipe, creating unwanted radioactivity. Some of these particles can even make it inside the detector. The peak beam halo rate should occur in time with filled proton bunches, and so vetoing on bunch crossings at the trigger level should reject much of the beam halo in searches for stopped particles. Dedicated L1 beam halo triggers have been created, so these can also be vetoed on at the trigger level. In addition, stopped particle searches can reject beam halo offline by rejecting events containing muon segments in the endcaps. Beam halo should largely travel in the  $z$ -direction and will therefore likely have a large  $\eta$  value.

A final background to stopped particle searches is instrumental noise. Noise is typically due to random fluctuations of electrons in the readout electronics and de-



tector material. Noise is rejected in analyses that search for calorimeter deposits by using typical HCAL noise-reduction algorithms and by requiring good quality jets. Noise is rejected in analyses that search for muons by requiring a good quality muon track, with hits in several muon chambers.

#### 4.4.4 Signature of Monopoles

As mentioned in Section 4.3.1, the ionization energy loss of Dirac monopoles would be several thousand times greater than that of a particle with charge  $e$  [101]. Thus, monopoles would give a striking  $dE/dx$  signature. Searches for monopoles at colliders usually look for high  $dE/dx$  tracks in the inner tracker. Furthermore, Dirac monopoles will produce parabolic tracks that are curved in the  $r - z$  plane due to the magnetic field within the detector, and parabolic tracks can be searched for in the inner tracker.

Monopoles could also produce a narrow ECAL cluster. Monopoles would not shower much in the calorimeters, as they would deposit their energy in a single cell, and then drift along the magnetic field. However, this would often make them look like ECAL spikes, and so this source of noise is a background for collider searches for monopoles. Most searches would benefit from a relaxed ECAL spike cleaning.

The  $dE/dx$  of the monopoles could be so large that they end up coming to a stop in the beam pipe or around the IP. Stopped monopoles would become bound to the nuclei of the atoms of the detector material. This would create a strongly divergent magnetic field, which would create a residual persistent current if the material is passed through a superconducting coil. A Superconducting Quantum Interference Device (SQUID) can be used to measure this current (see Fig. 4.7).

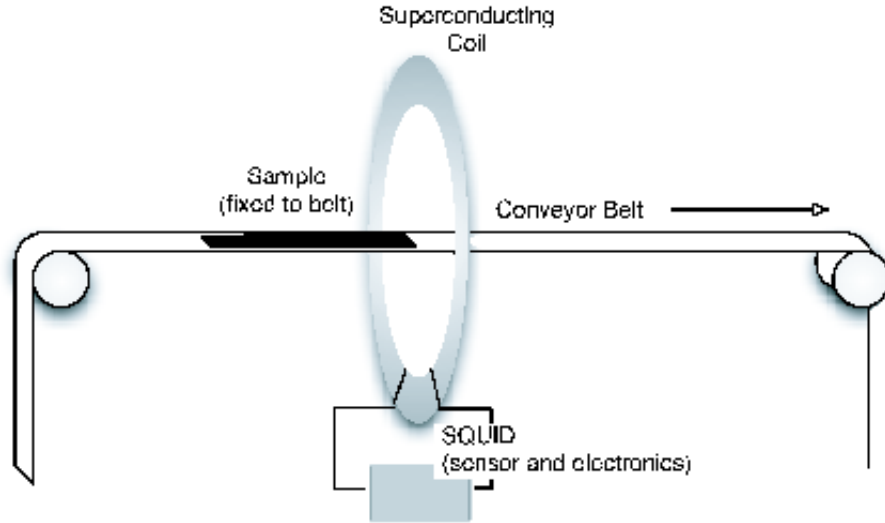


Figure 4.7: Diagram of the SQUID apparatus used at HERA [159]. The conveyor belt traveled in small steps until the sample was passed completely through the coil. At each step, the current in the superconducting coil was read.

## 4.5 Previous and Present Searches for LLPs

Searches for LLPs beyond those in the SM have been an active area of research for some time, and the field continues to thrive. And not all searches are performed at particle colliders. The hunt for dark matter, for example, has been conducted with direct detection searches, typically involving a Time Projection Chamber, a large amount of a noble gas and/or liquid, and a laboratory deep underground, and with indirect detection searches, either using astronomical experiments or particle colliders. That being said, we will focus on searches that have been performed at particle colliders for CMLLPs, displaced vertices, stopped particles, weird tracks, and monopoles, in turn. Furthermore, we will focus on searches that have been performed fairly recently, namely, at the Tevatron and the LHC, although we will mention some searches at LEP and HERA. The recent ATLAS LLP searches have been summarized in Ref. [160], and the recent CMS LLP searches have been summarized in Ref. [161].

### 4.5.1 Previous and Present Searches for CMLLPs

There have been many searches for CMLLPs at colliders. Several searches have been conducted at LEP [162–165], HERA [166], and the Tevatron [167–171], including the D0 search described in Appendix A. The most restrictive limits to date on long-lived charginos are given in Ref. [171]: D0 excluded gaugino-like charginos below 278 GeV and higgsino-like charginos below 244 GeV, at 95% confidence level (CL). Even more restrictive limits, albeit on different models, have come from the LHC [151, 172–182]. The most restrictive limits are from CMS, where gluinos below 1322 GeV and stops below 935 GeV are excluded for the cloud interaction model, and staus, including cascade decays, are excluded below 500 GeV. Fractionally and multiply charged particles with  $|Q| = e/3, 2e/3, 1e, 2e, 3e, 4e, 5e, 6e, 7e$  and  $8e$  are excluded with masses below 200, 480, 574, 685, 752, 793, 796, 781, 757, and 715 GeV, respectively [151]. CMS and ATLAS have both pursued many different models and detector signatures of CMLLPs, including searches for fractionally and multiply charged particles. Both ATLAS and CMS exploit TOF and  $dE/dx$  measurements as much as possible. The latest CMLLP paper from CMS, which uses data from 2011 and 2012 at  $\sqrt{s} = 7$  and 8 TeV, gives the details of five sub-analyses: a tracker-only search, a muon-only search, a tracker plus muon search, a multiply charged particle search, and a fractionally charged particle search. CMS has also presented a reinterpretation for their 2011 and 2012 results in the pSSM and other BSM scenarios [183]. See Ref. [184] for recent results from phenomenologists about the prospects of CMLLP searches at future colliders.

### 4.5.2 Previous and Present Searches for Displaced Vertices

There have been several searches for displaced vertices.

BaBar [185], D0 [186, 187], ATLAS [188–193], and CMS [194, 195] have performed searches for displaced leptons. The most restrictive limits from CMS, using 2012

data at  $\sqrt{s} = 8$  TeV, are on Higgs bosons that decay to a pair of long-lived neutral  $X$  bosons, which decay to dileptons ( $e^+e^-$  or  $\mu^+\mu^-$ ); the 95% CL cross section limits are between 0.1 and 5 fb for  $X$  bosons with lifetimes between 0.01 and 100 cm. The limits from CMS on a pair of squarks that decay to a long-lived neutralino, which decays to  $e^+e^-\nu$  or  $\mu^+\mu^-\nu$ , are between 2 and 5 fb for neutralino lifetimes between 0.1 and 100 cm and squark masses above 350 GeV. CMS has also started a search for displaced muons using only the muon system, in order to expand their sensitivity to LLPs with a transverse impact parameter greater than 40 cm [196].

There have been several searches for displaced jets, including CDF and D0 searches for metastable particles decaying to b-quark jets [197, 198], an LHCb search [199], the ATLAS searches mentioned above [188–190, 192], and a CMS analysis [200]. The CMS search uses 2012 data at  $\sqrt{s} = 8$  TeV and looks for Higgs bosons that decay to long-lived neutral  $X$  bosons. For Higgs boson masses between 400 and 1000 GeV,  $X$  boson masses between 50 and 350 GeV, and  $X$  boson lifetimes between 0.1 and 200 cm, the upper limits are typically 0.3 to 100 fb. These are the most stringent limits to date in this channel.

There has been a search for displaced lepton-jets at ATLAS [201]. They use the 2012,  $\sqrt{s} = 8$  TeV data set to put limits on non-prompt lepton-jet models. Assuming the SM gluon fusion production cross section for a 125 GeV Higgs boson, they find its branching ratio to hidden-sector photons to be below 10%, at 95% CL, for a hidden photon in the  $14 \text{ mm} \leq c\tau \leq 140 \text{ mm}$  range for the  $H \rightarrow 2\gamma_d + X$  model and in the  $15 \text{ mm} \leq c\tau \leq 260 \text{ mm}$  range for the  $H \rightarrow 4\gamma_d + X$  model.

A few searches for displaced photons have been performed. CDF performed a search using MET [202], and CMS performed searches using converted photons and MET [203, 204]. All other searches for photons in some SUSY scenario have been with prompt photons. Currently, a search is being performed at CMS for displaced photons using ECAL time measurements [205], and another search using photon

conversions [206]. The most stringent limits on displaced photons use 2011 data at  $\sqrt{s} = 7$  TeV; CMS excludes neutralinos with masses below 220 GeV, for lifetimes of 500 mm [204].

There have also been searches for RPV SUSY, such as one search that looks for slightly displaced, pair-produced stops [207]. This search has been performed at CMS with 2012 data at  $\sqrt{s} = 8$  TeV, and it looks for an electron and a muon in the final state, which are displaced transversely from the LHC luminous region. No excess is observed above the estimated number of background events for displacements up to 2 cm. For a lifetime of 2 cm, stops masses are excluded up to 790 GeV.

### 4.5.3 Previous and Present Searches for Weird Tracks

ATLAS has conducted a few searches for disappearing tracks [208, 209]. CMS is currently performing a search for disappearing tracks using 2012 data at  $\sqrt{s} = 8$  TeV [210]. The benchmark signal process for this search is AMSB where there is a small mass splitting between the lightest chargino and neutralino, and the chargino decays to a neutralino and a soft pion, which will not be reconstructed. If the chargino decays within the tracker volume, a disappearing track will be produced. The most stringent limits are from the CMS search, which for a mean lifetime of 1 ns, charginos with masses below 443 GeV at 95% CL are excluded.

A search for kinked tracks in the CMS tracker is also in progress. This search uses a coNLSP SUSY model in which mass degenerate selectrons and smuons decay to their SM counterparts and a nearly massless gravitino. The tracks of the mother NLSP (selectron or smuon) and of the daughter particle (electron or muon) create the kinked track that could be observed.

#### 4.5.4 Previous and Present Searches for Stopped Particles

Previous searches for stopped particles have often been referred to as “stopped gluino” searches because the benchmark signal was typically provided by various gluino models. However, these searches have been more recently expanded to the signals associated with other models, such as stops. Many of these searches have used signatures of calorimeter energy appearing when there are no collisions, but some searches, including the one described in this thesis, have been expanded to search for other objects, such as muons, detected in the absence of collisions.

Several stopped gluino searches have been reported from Tevatron experiments: a D0 search [211] and a reinterpretation of CDF results [212]. Other searches for stopped particles have come from LHC experiments [213–215]. The most restrictive limits come from CMS, based on 2012 data corresponding to 281 hours of trigger live time: assuming the cloud model of  $R$ -hadron interactions, gluinos with masses below 1000 GeV and stops with masses below 525 GeV are excluded for lifetimes between 1  $\mu$ s and 1000 s [216]. All of the above searches use signatures of out-of-time calorimeter deposits, but the analysis described in this thesis is a search for stopped particles that decay to muons.

#### 4.5.5 Previous and Present Searches for Monopoles

Searches for monopoles have been performed at LEP [217], HERA [159], and the Tevatron [218–220]. CDF performed a search using 35.7  $\text{pb}^{-1}$  of data and a custom trigger for highly ionizing particles. They set cross section limits greater than 0.2 pb for masses between 200 and 700 GeV. The other two Tevatron searches were performed by the E882 experiment, which used the SQUID technique at CDF and D0. Upper limits on the production cross section of monopoles with charge  $q_m$ ,  $2q_m$ ,  $3q_m$ , and  $6q_m$  were found to be 0.6, 0.2, 0.07, and 0.02 pb, respectively, at 90% CL, when taking the isotropic case.

The current CMS search for monopoles looks for highly ionizing tracks in the tracker, meaning many saturated hits, and a confined energy deposit in the calorimeter [221]. This analysis searches for massive Dirac-like monopoles. The ATLAS search is similar, and sets cross section limits between 1 and 100 fb for masses between 200 and 2500 GeV [222]. The current status of searches for monopoles is summarized in Ref. [223].

Now that we have introduced LLPs, we can describe the search for delayed muons, which is the main analysis in this thesis.

# Chapter 5

## A SEARCH FOR DELAYED MUONS

This chapter describes the main analysis performed for this thesis, which is a search for LLPs that stop in the detector and decay to muons. This was the first time this analysis was ever performed. The analysis uses  $19.7 \text{ fb}^{-1}$  of 8 TeV data collected by CMS in 2012, during a search interval of 293 hours of trigger livetime.

### 5.1 Introduction and Motivation

As described in the previous chapter, massive LLPs do not exist in the SM, and so any sign of them would be an indication of new physics. There are many BSM theories that predict LLPs, including split SUSY, hidden valley scenarios, GUT theories, and various SUSY models. Furthermore, our present model of BBN does not explain the observed Li level of production, but the presence of a massive, LLP would affect the light element abundances [1].

LLPs could be sufficiently massive that they would lose sufficient energy through ionization or hadronization, depending on the type of particle, that they would come to rest inside the detector material [153–157]. These stopped particles could then



decay seconds, days, or weeks after the bunch crossing. These decays could occur when there are no collisions and the detector is relatively quiet; the observation of such decays would be a clear sign of new physics. The major background to such a search would be cosmic rays that survive the 100 m trip through the earth to the CMS detector. Furthermore, decays to leptons are key flags of heavy particle production, and the presence of leptons that are delayed with respect to the bunch crossing may signal new physics.

We present here the first search for LLPs that come to a stop in the detector and decay to muons sometime after the bunch crossing. This search is somewhat similar to the CMS Search for Stopped Particles (EXO-12-036) [216], and in fact builds upon the MC simulation and trigger framework, but it searches for decays to real muons instead of calorimeter deposits. As a result, many of the analysis challenges are quite different. This search was designed to cover some of the parameter space so far unexplored by the CMS long-lived exotica program.

Analyses were performed at CMS and ATLAS that search for stopped  $R$ -hadrons [213–216]. The most restrictive of these is from CMS, using  $18.6 \text{ fb}^{-1}$  of 8 TeV data, corresponding to 281 hours of trigger livetime, which excludes gluinos with masses below 1000 GeV and top squarks with masses below 525 GeV [216]. In addition, other analyses have searched for long-lived heavy particles that pass through the detector [151, 172–183]. The most restrictive limits on mchamps with  $|Q| = 2e$  exclude masses below 685 GeV [151].

We use the data and MC simulation samples described in Section 5.2, and in particular, we use the custom trigger described in Section 5.2.1. We perform the search by following the strategy and techniques outlined in Section 5.3. The search samples are reduced by applying the offline selection criteria, as described in Section 5.4. We model the background as described in Section 5.5. The systematic uncertainties are described in Section 5.6, and the results are explained in Section 5.7. Since we observe

no significant excess, we place cross section and mass limits on the signals we explore. The main twiki page for this analysis is Ref. [224].

## 5.2 Data and Monte Carlo Samples

### 5.2.1 Trigger

We collected data during 8 TeV proton-proton collisions of the LHC in 2012 with specially designed triggers at L1 and the HLT.

The L1 and HLT triggers used for this analysis veto on the bunch crossing, in order to search for the signal when there are no prompt SM backgrounds. The triggers select events with at least one muon, so that we might be sensitive to decays of stopped long-lived particles that produce only one muon in the final state. As a result of the veto on the bunch crossing and the selection of at least one muon, the triggers for this analysis predominantly select cosmic muons. Since the rate of cosmic muons reaching the detector is small, namely, approximately 500 Hz, we can keep the  $p_T$  thresholds low and maintain a trigger rate within our allowed budget. Low  $p_T$  thresholds in the trigger, namely 6 GeV at L1 and 20 GeV at the HLT, allow us to be sensitive to stopped long-lived particles of about 100 GeV.

The L1 trigger for this analysis is L1\_SingleMu6\_NotBptxOR, which requires at least one L1 muon with a  $p_T$  of at least 6 GeV. The L1 muon  $p_T$  cut at 6 GeV was chosen to maintain a L1 trigger rate of about 30 Hz (see below). Furthermore, this “NotBptxOR” trigger collects data only when the Beam Pickup for Timing for the experiments (BPTX) signal is false for both beams. (The logic is NOT (BPTX\_plus.v0 OR BPTX\_minus.v0).) Thus, at L1, our trigger vetoes on the presence of colliding bunches. See Section 3.2.9.5 for more on the BPTX system.

The main signal HLT path developed specifically for this analysis is HLT\_L2Mu20\_NoVertex\_2Cha\_NoBPTX3BX\_NoHalo. This trigger requires at

least one L2 muon that is not updated at the vertex with a  $p_T$  of at least 20 GeV. The L2 muon  $p_T$  cut at 20 GeV was chosen to keep the HLT rate less than 5 Hz. The HLT path also requires at least 2 DT or CSC chambers with any number of hits, which was implemented to select good quality muons with many hits over multiple chambers. It also vetoes events in which the L1\_SingleMuBeamHalo trigger fires, thereby reducing the number of beam halo events collected. Furthermore, if a BPTX coincidence is seen within  $\pm 1$  potential bunch crossing bucket (BX) of the event, the event is excluded. Thus, at the HLT, our trigger also vetoes on one BX on either side of the bunch crossing. We also implemented a number of control and backup triggers for this search; the full list of triggers is given in Table 5.1.

Table 5.1: Delayed muon triggers during Run2012C and Run2012D. In Run2012A and Run2012B, the signal and backup triggers did not have the requirement of at least 2 DT or CSC chambers with any number of hits (the “2Cha” requirement).

HLT Path	L1 Seed	Type
HLT_L2Mu20_eta2p1_NoVertex	L1_SingleMu16er	Control
HLT_L2Mu10_NoVertex_NoBPTX3BX_NoHalo	L1_SingleMu6_NotBptxOR	Control
HLT_L2Mu20_NoVertex_2Cha_NoBPTX3BX_NoHalo	L1_SingleMu6_NotBptxOR	Signal
HLT_L2Mu30_NoVertex_2Cha_NoBPTX3BX_NoHalo	L1_SingleMu6_NotBptxOR	Backup

The trigger rates for L1\_SingleMu6\_NotBptxOR and HLT\_L2Mu20\_NoVertex\_2Cha\_NoBPTX3BX\_NoHalo during run 208307 and the instantaneous luminosity recorded by CMS for this fill (fill 3347) are shown in Fig. 5.1. For this long run that spanned 11.5 hours, the rate of these triggers is constant at about 32 Hz and 3.5 Hz, respectively, while the instantaneous luminosity dropped by a factor of greater than 2.5.

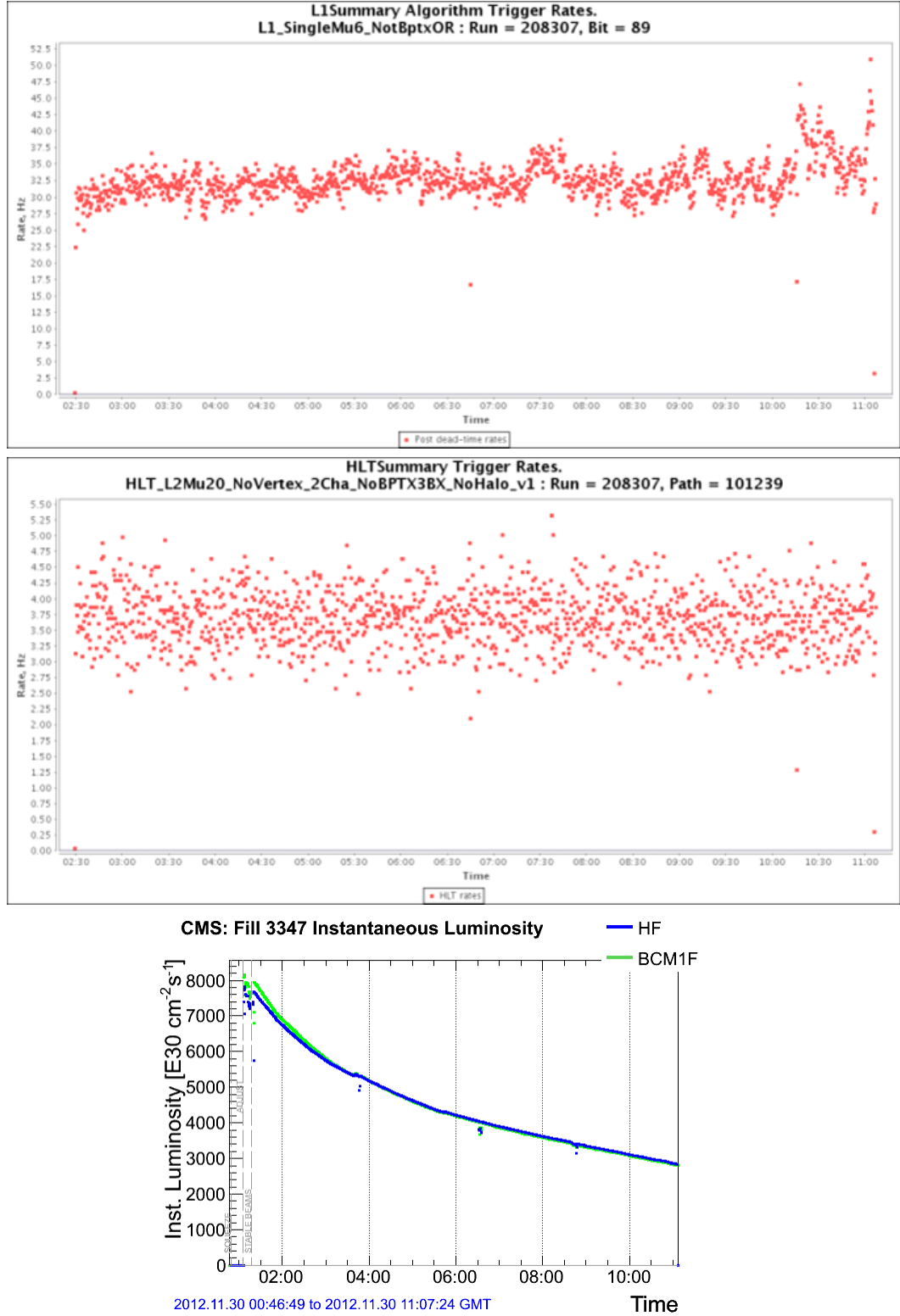


Figure 5.1: The WBM plots showing the trigger rate for L1\_SingleMu6\_NotBptxOR (top) and HLT\_L2Mu20\_NoVertex\_2Cha\_NoBPTX3BX\_NoHalo (middle) and the instantaneous luminosity (bottom) during run 208307 [225].

The trigger rate for HLT\_L2Mu20\_NoVertex\_2Cha\_NoBPTX3BX\_NoHalo and the instantaneous luminosity at the start of a fill as a function of the number of colliding bunches is shown in Fig. 5.2. As can be seen in this plot, the trigger rate is highly dependent on the number of colliding bunches, rather than on any beam-related parameters. As the number of bunches increases, there is less time available to the trigger to take data, so its rate decreases. The dominant sample collected by the trigger is “cosmic muons”, that is, muons from cosmic rays, and so the rate versus the number of bunches is linear and decreasing. On the other hand, the instantaneous luminosity at the start of the fill, and therefore the rate of “prompt” triggers that collect data in time with the bunch crossing, increases with the number of bunches.

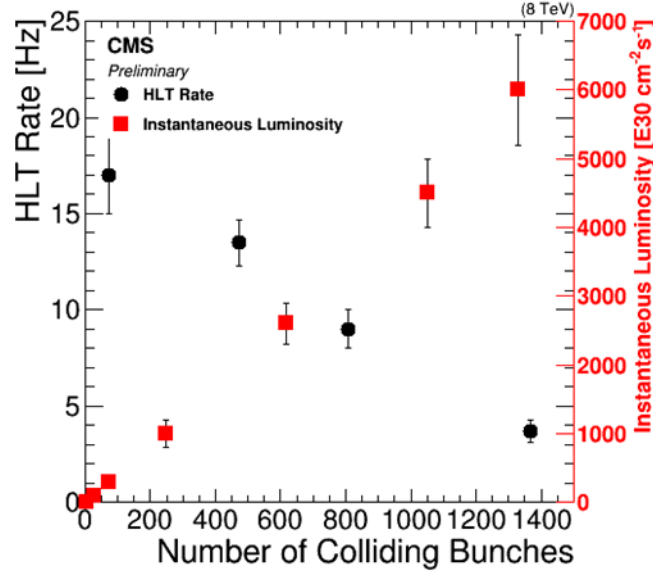


Figure 5.2: The trigger rate for HLT\_L2Mu20\_NoVertex\_2Cha\_NoBPTX3BX\_NoHalo and the instantaneous luminosity at the start of a fill as a function of the number of colliding bunches, based on early 2012 data.

The turn-on curve for HLT\_L2Mu20\_NoVertex\_2Cha\_NoBPTX3BX\_NoHalo is plotted in Fig. 5.3. The events in both the numerator and denominator were events that passed the prescaled muon NoBPTX control triggers, which had a 10 GeV L2 muon  $p_T$  cut, from Run2012C with the muon JSON file. Only the highest  $p_T$  muon is considered in the numerator and denominator. We require that the Displaced

Standalone (DSA) muon track must have at least 3 DT chambers with valid hits, at least 2 RPC hits, at least 8 DT DOF, and 0 CSC hits, in order to pass the preselection criteria. (See Section 5.3.1 for more about DSA muon tracks and Section 5.4 for the selection criteria.) The additional requirement for the numerator is that the event passes the signal trigger, which had a  $p_T$  cut of 20 GeV. The trigger is 80% efficient at a DSA track  $p_T$  of 30 GeV.

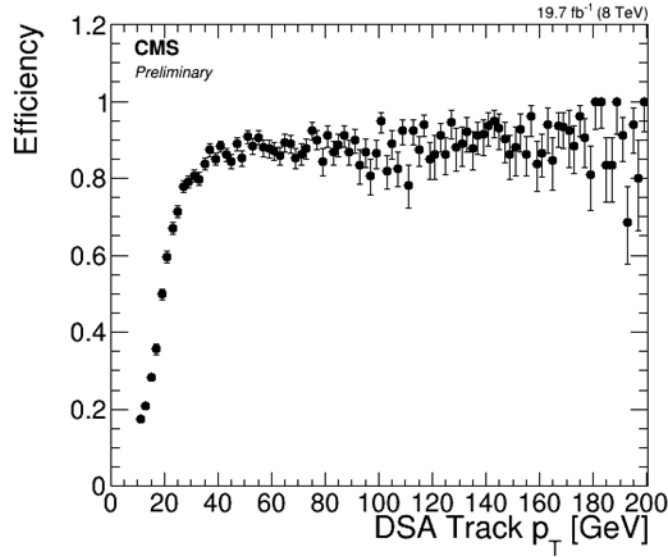


Figure 5.3: Turn-on curve for HLT\_L2Mu20\_NoVertex\_2Cha\_NoBPTX3BX\_NoHalo in Run2012C data passing the prescaled control trigger.

## 5.2.2 Data Samples

### 5.2.2.1 Search Sample

This search is performed with data taken between May and December 2012, during which  $19.7 \text{ fb}^{-1}$  of 8 TeV data was collected by CMS and approved for analyses using muons. The RAW datasets analyzed are listed in Table 5.2. They were reconstructed in 72X, in order to take advantage of the DSA muon track collection (see Section 5.3.1). The recoed datasets are listed in Table 5.3. Run2012A is excluded due to a problem with the trigger configuration during this time; the HLT path mistakenly vetoed on a double muon L1 seed, rather than on the L1 beam halo seed.

Table 5.2: RECO data samples.

---

/NoBPTX/Run2012B-v1/RAW
/NoBPTX/Run2012C-v1/RAW
/NoBPTX/Run2012D-v1/RAW

---

Table 5.3: RECO data samples.

---

/NoBPTX/jalimena-Reco_NoBPTX_Run2012B_period1_723patch1-4e26b46248715cfa5a8f6edd
/NoBPTX/jalimena-Reco_NoBPTX_Run2012B_period2_723patch1-4e26b46248715cfa5a8f6edd
/NoBPTX/jalimena-Reco_NoBPTX_Run2012C_723patch1-4e26b46248715cfa5a8f6eddd101
/NoBPTX/jalimena-Reco_NoBPTX_Run2012D_723patch1-4e26b46248715cfa5a8f6eddd101

---

We used the official Muon JSON file for this analysis, namely:

```
/afs/cern.ch/cms/CAF/CMSCOMM/COMM_DQM/certification/Collisions12/8TeV/Reprocess
Cert_190456-208686_8TeV_22Jan2013ReReco_Collisions12_JSON_MuonPhys.txt
```

Because our trigger vetoes on the bunch crossing and  $\pm 1$  BX, it is important to compute how often the trigger is live, in other words, the livetime fraction, and then the effective luminosity of the search. The LHC bunch filling scheme was described in Section 3.1.1; the LHC filling scheme is reproduced in Fig. 5.4 for convenience. The beam is arranged in an irregular pattern of batches, with 72 bunches of protons per batch and each bunch spaced 25 ns away from the next, which is the nominal spacing. At 50 ns and with the maximum number of bunches, the LHC bunch structure was very similar to what is shown in Fig. 5.4, except for having 36 bunches in the PS, that is, 36 bunches per batch, rather than 72. A collision occurred every other BX, except between batches and during the abort gap. Because our trigger vetoes on  $\pm 1$  BX, that means that every BX bucket in each batch of protons is unavailable to the trigger. We only collect data in the spaces between batches, including the 3  $\mu s$  abort gap. Since there is a total of 3564 possible buckets per orbit, the livetime fraction (LF) is:

$$\text{LF} = \frac{3564 - N_{\text{Unavailable BX}}}{3564} \quad (5.1)$$

where  $N_{UnavailableBX}$  is the number of unavailable BXs per orbit. Table 5.4 shows the livetime fraction for each of the LHC filling schemes used in 2012 at 50 ns spacing. Also see [226]<sup>1</sup>.

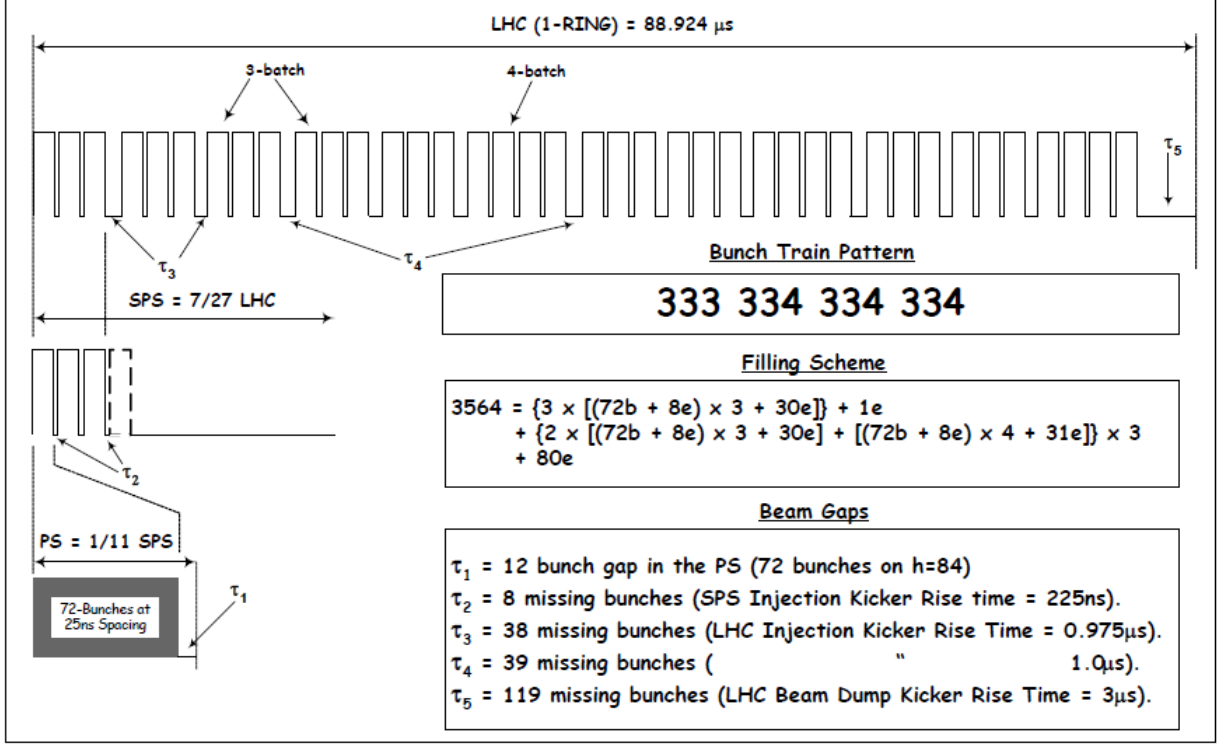


Figure 5.4: Diagram of the LHC bunch filling scheme, at 25 ns and with 3564 total bunches (2808 colliding) [63]. See also [64, 65] for updates.

<sup>1</sup>At 50 ns spacing,  $N_{UnavailableBX}$  is approximately twice the number of collisions per orbit because in each batch of protons, every other bucket is filled. The trigger vetoes  $\pm 1$  BX, so that means that every bucket in each batch of protons is unavailable to the trigger, especially when the maximum number of colliding bunches at 50 ns, 1380 bunches, is used. Interestingly, at 25 ns spacing and 2800 bunches per orbit, we actually expect about the same amount of trigger livetime. At 25 ns, every bucket is filled in each batch, so again, every bucket in each batch of protons is unavailable to the trigger. However, now  $N_{UnavailableBX}$  is simply equal to the number of collisions per orbit. Thus, with this back-of-the-envelope calculation, LF is 0.21 for 25 ns and 2800 bunches and 0.23 for 50 ns and 1380 bunches. If actually only achieve 2500 bunches at 25 ns in 2015, LF will be 0.30. Notice that this is an approximate calculation, and the more careful calculation of the trigger livetime reported in Table 5.4 is less because of factors such as lost time in between bunch trains.



Table 5.4: The trigger livetime fraction for each of the LHC filling schemes used in 2012..

Filling scheme	Number of Collisions Per Orbit	Approximate $N_{UnavailableBX}$	LF
50ns_78b_72_0_48_36bpi3inj	72	144	0.94
50ns_456b_447_0_431_72bpi12inj	447	894	0.68
50ns_474b_465_0_452_72bpi12inj	465	930	0.71
50ns_480b_471_0_461_72bpi12inj	471	942	0.71
50ns_840b_801_0_804_108bpi13inj	801	1602	0.49
50ns_840b_807_0_816_108bpi12inj	807	1614	0.49
50ns_852b_807_0_816_108bpi13inj	807	1614	0.48
50ns_1374_1368_0_1262_144bpi12inj	1368	2736	0.20
50ns_1380b_1377_0_1274_144bpi12inj	1377	2754	0.20

Figure 5.5 shows the BX distribution for events passing HLT\_L2Mu20\_NoVertex\_2Cha\_NoBPTX3BX\_NoHalo. This trigger takes most of its data during the gaps between batches in the bunch structure and the abort gap. The 11 major gaps between batches and the abort gap can clearly be seen on this plot as the 12 major spikes in the distribution.

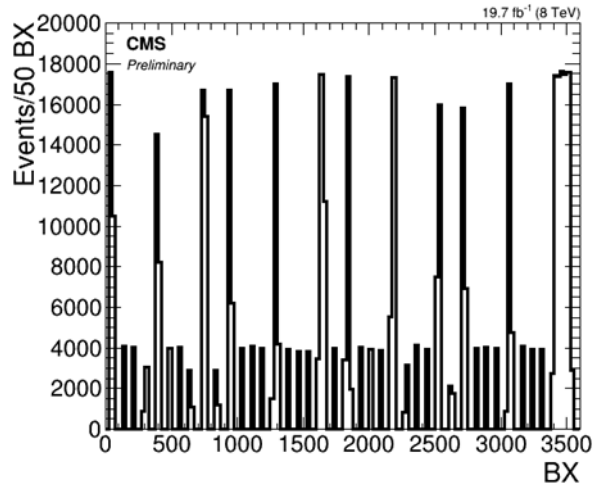


Figure 5.5: BX distribution for events passing HLT\_L2Mu20\_NoVertex\_2Cha\_NoBPTX3BX\_NoHalo. This trigger takes most of its data during the gaps between batches in the bunch structure and the abort gap. The 11 major gaps between batches and the abort gap can clearly be seen on this plot as the 12 major spikes in the distribution.

### 5.2.2.2 Cosmic Muon Background Sample

The background from muons coming from cosmic rays was modeled with cosmic ray data from the end of the 2012 pp run. Although these data were used to determine how the background would appear, they were not actually used in the background prediction (see Section 5.5). These data were collected when collisions were not occurring, but the CMS detector was operational. In particular, triggering at L1 was enabled for both the upper and lower hemispheres, as is done for normal pp collision data-taking; in the typical cosmic runs, only the bottom half of the detector is used to trigger. These data were collected with a special trigger key, `l1_hlt_cosmics_allphi/v1`, and the signal trigger used for this search was included in the HLT menu used to take these data (`/cdaq/special/Interfill/2012/v6.2/HLT/V1`). The JSON file for this configuration, which shows the runs and lumi sections used, is shown below:

```
{"208593": [[1, 245]], "208628": [[1, 5]], "208635": [[1, 9]],  
"208636": [[1, 17]], "208651": [[1, 128]], "208655": [[1, 34]],  
"208660": [[1, 89]], "208663": [[1, 24]], "208664": [[1, 11]],  
"208666": [[1, 30]]}
```

## 5.2.3 Signal Samples

### 5.2.3.1 Models

We investigated five different possible signals, over a range of masses and lifetimes. These are stops, gluinos, `mchamps/H±±`, `ppstaus`, and `gmstaus`. However, in the end, only the `mchamps` were used in the full analysis. `Mchamps` were chosen because of their high stopping efficiency and because `mchamps` with  $Q = 2e$  give two generated muons in the final state. The work done on the other samples, including the possible reweighting of the `mchamp` sample to `H±±`, is presented here for completeness.

Long-lived stops and gluinos were generated in the context of Split SUSY [120,121].

Stops and gluinos would form  $R$ -hadrons in the detector, interacting via the strong force and hadronizing with quarks, as discussed in Section 4.3.2. Split SUSY was described in Section 4.2.4.

The rest of the models are more lepton-like. The mchamps with  $Q = 2e$  behave like a doubly charged Higgs ( $H^{\pm\pm}$ ) [125–127]. The mchamps are modified Drell-Yan production of long-lived lepton-like fermions. In this scenario, new massive spin-1/2 particles have arbitrary electric charge and are neutral under  $SU(3)_C$  and  $SU(2)_L$ , and therefore couple only to the photon and the Z boson [124]. Multiply (and fractionally) charged particle models were discussed in Section 4.2.6, and Supersymmetric Left-Right Models, containing doubly charged Higgs, were discussed in Section 4.2.7. The other type of lepton-like LLP is a stau, generated in the context of the minimal gauge mediated SUSY model (mGMSB) [109]. Staus can be produced through direct pair production (ppstau) or through production of heavier SUSY particles that decay to staus (gmstau). GMSB was discussed in Section 4.2.2. These lepton-like models primarily interact with the detector material through ionization, as discussed in Section 4.3.1.

### 5.2.3.2 Signal Generation

There are three major steps in the signal generation process. In Stage 1, a LLP for each kind of signal is generated with PYTHIA [78, 227] and propagated through the detector with GEANT4 v9.2 [228, 229]. Some fraction of these are sufficiently slow-moving to come to a stop in the detector material. Thus, the Stage 1 determines the LLP’s stopping efficiency. For the strongly interacting LLPs, the hadronization is done via the PYRAD subroutine, resulting in the  $R$ -hadron. Then, in Stage 2, the parent LLP or  $R$ -hadron is forced to decay at the stopping position defined in Stage 1 (via appropriate channels) to muons. Thus, Stage 2 determines the reconstruction efficiency. Finally, Stage 3 is a pseudo-experiment MC simulation used to

estimate the probability for stopped particle decays to occur when the detector is sensitive, that is, when the detector is on but there are no collisions occurring. In other words, the Stage 1 and 2 MC simulation determine how the signal will look in the detector, and Stage 3 determines when it will occur. The signal MC simulation is much the same as the Stopped Particle search [216], except in Stage 2, the stopped particles are forced to decay to muons.

It is possible for one or more than one particle per interaction to stop in the detector. In models of lepton-like particles that are pair produced, that is, the mchamps and the pair-produced staus, it is possible for one or both LLPs in each interaction to stop in the detector. For the staus produced in cascades, a small fraction of the time ( $<0.01\%$ ) even a third LLP could stop in the detector. For the strongly interacting LLPs, it is possible for one or more  $R$ -hadron to stop in the detector.

Furthermore, if there is more than one stopped particle per interaction, it is unlikely that they both will stop and decay close in time with each other, if the lifetime of the stopped particle is long. Given that the time window associated with a triggered event is on the order of 100 ns, and the lifetimes this analysis is sensitive to are longer than that, we will assume that every decay of a stopped particle is triggered separately. In other words, the decay of each stopped particle will be in a separate event. Therefore, in the Stage 2 MC simulation, if a second or third particle is stopped in the detector, the additional particle's decay is put in a new event.

**Stage 1 Generation** The Stage 1 GEN-SIM samples used are listed in Table 5.5. The stops and gluinos are produced for masses between 300 and 1500 GeV using PYTHIA v8.153 with the default tune 4C. The mchamps are simulated with PYTHIA v6.426 with the Z2 tune, for masses between 100 and 1000 GeV. We use the  $Q = 2e$  scenario in order to best represent  $H^{\pm\pm}$ . The staus are produced using the SPS7 slope [230], which has the stau as the NLSP. The particle mass spectrum and the

decay table are produced with ISASUGRA v7.69 [231]. The mGMSB parameter  $\Lambda$  is varied from 31 TeV to 160 TeV, with fixed parameters  $N_{mes} = 3$ ,  $\tan\beta = 10$ ,  $\mu > 0$ ,  $C_G = 10000$ , and  $M_{mes}/\Lambda = 2$  (see Section 4.2.2 for an explanation of these parameters). The large value of  $C_G$  results in a long-lived stau, and the range of  $\Lambda$  values gives a stau mass between 100 and 494 GeV. The produced SUSY mass spectrum is fed to PYTHIA v6.426 with the Z2 tune.

Table 5.5: Stage 1 GEN-SIM signal samples. These samples were produced privately in order to avoid the feature for the stopped mchamp anti-particles. The mchamps have “Tune\*2star” in the sample name because a typo was made, and some of the samples were called “TuneT2star” instead of “TuneZ2star” by mistake.

---

/HSCPstop_M-*_Tune4C_8TeV-pythia8/jalimena-stage1_stop*_710-*/USER
/HSCPgluino_M-*_Tune4C_8TeV-pythia8/jalimena-stage1_gluino*_710-*/USER
/HSCPMchamp6_M-*_Tune*2star_8TeV-pythia6/jalimena-stage1_mchamp*_710-*/USER
/HSCPgmstau_M-*_TuneZ2star_8TeV-pythia6/jalimena-stage1_gmstau*_710-*/USER
/HSCPppstau_M-*_TuneZ2star_8TeV-pythia6/jalimena-stage1_ppstau*_710-*/USER

---

The Stage 1 MC simulation was originally the same as what was centrally produced for the HSCP analyses [232]. However, a feature, which affects only the lepton-like LLPs (mchamps and staus), was discovered in the code that is used to find and save the stopped particles [233]. In Ref. [234], the anti-particles were erroneously not considered, to determine if they had stopped in the detector. This one line of code was fixed and was available as of CMSSW\_7\_5\_0\_pre1 and backported to 71X as early as CMSSW\_7\_1\_15, so that the 13 TeV HSCP signal samples would have this fix. We also took this opportunity to add the mass, `pdgId`, and charge of the stopped particles to the code and to the Stage 1. The 8 TeV Stage 1 MC simulation was remade privately with this change and these additional variables were added to CMSSW\_7\_1\_0 (see Table 5.5).

**Stage 2 Generation** Stage 2 MC simulation is privately produced in a fashion similar to what is done in the Stopped Particle analysis [216], except that the particles are forced to decay to muons wherever possible and an additional event is created for

the decay of the second stopped particle, if it exists, as described above. The Stage 2 samples, which were produced in CMSSW\_7\_1\_0, are listed in Table 5.6. The corresponding RECO samples, which were produced in CMSSW\_7\_2\_5, are listed in Table 5.7. Only the mchamps were remade, since we determined that the 8 TeV analysis should focus on this one important signal sample.

Table 5.6: Stage 2 signal samples.

---

/HSCPMchamp6_M-*_Tune*2star_8TeV-pythia6/jalimena-stage2_mchamp*_separateEvents_
--

---

Table 5.7: Stage 2 RECO signal samples.

---

/HSCPMchamp6_M-*_TuneZ2star_8TeV-pythia6/jalimena-reco_mchamp*_separateEvents_
--

---

The generation of the final state muon depends on the type of stopped particle:

- The stop decays to a top and a neutralino, and then the top decays to a W boson and a  $b$  quark. The W boson is then forced to decay to a muon and a neutrino.
- The gluino decays to a gluon and a neutralino. Then the gluon interacts further, and muons are obtained in the final state via charmed meson decays (61%), bottom meson decays (21%), tau decays (11%), and bottom, charmed, strange baryons, J/Psi, and light mesons (7%).
- The mchamps with  $Q = 2e$  decay directly to two same-sign, back-to-back muons, as this is a lepton number violating model. The mchamp is assigned to be the tau prime particle (PDG Id 17), and the PYTHIA card file must be changed to change the charge of the tau prime:

KCHG(17,1)=-6

- The staus decay to a tau and a light gravitino. The PYTHIA card file must read:

IMSS(11)=1

in order to turn on decays to gravitinos. Then the tau is forced to decay to a muon, a muon antineutrino, and a tau neutrino.

The recipe to produce the MC simulation for this analysis is detailed in Ref. [235], with additional notes in Ref. [236].

**Stage 3 Generation** The Stage 3 pseudo-experiment MC simulation is much the same as described in Ref. [226]. The input to the Stage 3 MC simulation is the final signal acceptance after all the selection criteria have been applied, which is multiplied by the production cross section, instantaneous luminosity, and running time to determine the total number of detectable decays. Then the simulation determines when these decays could take place. A random lifetime is drawn from an exponential distribution with a time constant equal to the proper lifetime. The simulation determines the runs and lumi sections analyzed from the muon JSON file, when BX vetoes are applied, the different bunch structures during the 2012 run, etc., and it computes an “effective luminosity” for each lifetime considered. Since the timestamp information is available for each lumi considered, the luminosity model is constructed for the entire year of data-taking, allowing a stopped particle to be produced in one fill and decay during another. For lifetimes shorter than one orbit, we search within a time-window of 1.3 times the lifetime, which is optimized for sensitivity to that lifetime. This restriction avoids the addition of backgrounds, which are assumed to be constant in time, for time intervals during which the signal will have already decayed. The pseudo-experiment MC simulation performs similar steps for the background events and observed data events. The results of the Stage 3 MC simulation and counting experiment are shown in Section 5.7.

### 5.2.3.3 Stopping Probability

The likelihood that a LLP will stop in the detector is calculated by the Stage 1 MC simulation.

Figure 5.6 shows how the stopping efficiency of the mchamps changes, once the Stage 1 stopped particle feature mentioned above was fixed. The stopping efficiency is plotted as a function of the mass of the generated mchamp. Before the Stage 1 was adjusted to include the stopped anti-particles, the stopping efficiency was represented by the black circles; that is, only the negatively charged mchamps ( $\tilde{\text{HIP6}}$ ) were considered. The red squares represent the stopping efficiency after the Stage 1 bug was fixed and the positively charged mchamps ( $\text{anti-}\tilde{\text{HIP6}}$ ) were recovered. Then, if we assume that each stopped particle decays in a separate event and allow for this in the Stage 2 MC simulation, we obtain the stopping efficiency shown by the blue triangles.



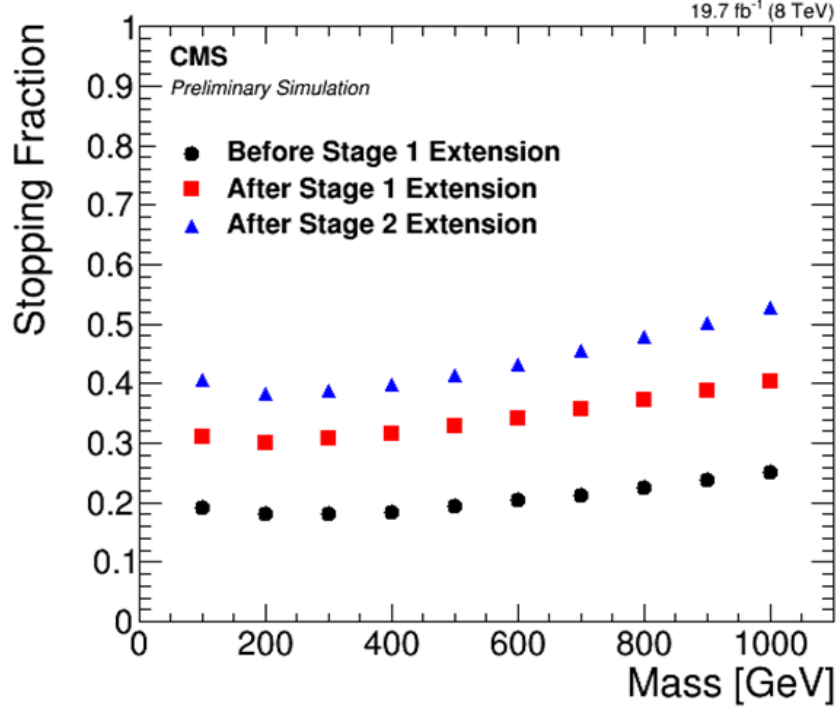


Figure 5.6: The fraction of stopped particle decays per mchamp pair production, as a function of mchamp mass. The black points correspond to the stopping efficiency before the Stage 1 MC simulation change, the red squares show the stopping efficiency after the bug fix, and the blue triangles correspond to the stopping efficiency if we assume every stopped particle decays in a different triggered event.

It is also worth mentioning that there is a slight asymmetry in the charge of the stopped mchamps. If there are two stopped mchamps in an interaction, one will be positive and one will be negative, since they are produced in opposite sign pairs. However, if there is only one stopped mchamp, 55% of the time it will be positive, and 45% of the time it will be negative. This charge asymmetry is constant as a function of mchamp mass. This charge asymmetry in the stopping power of heavy charged particles is expected, as shown by the Born expansion of the Bethe stopping power [1, 237].

Figure 5.7 shows the stopping efficiency as a function of mass for each of the possible signal samples. The top left plot shows the efficiency before the bug fix, and the top right plot shows the efficiency after the bug fix (the graphs are the same for

the stop and gluinos, as the bug and the fix only affect the lepton-like HSCPs). In both of these plots, the stopping efficiency for at least one particle to stop in the detector is plotted. The bottom plot shows the maximum stopping efficiency after the bug fix, assuming every stopped particle decays in a different event.

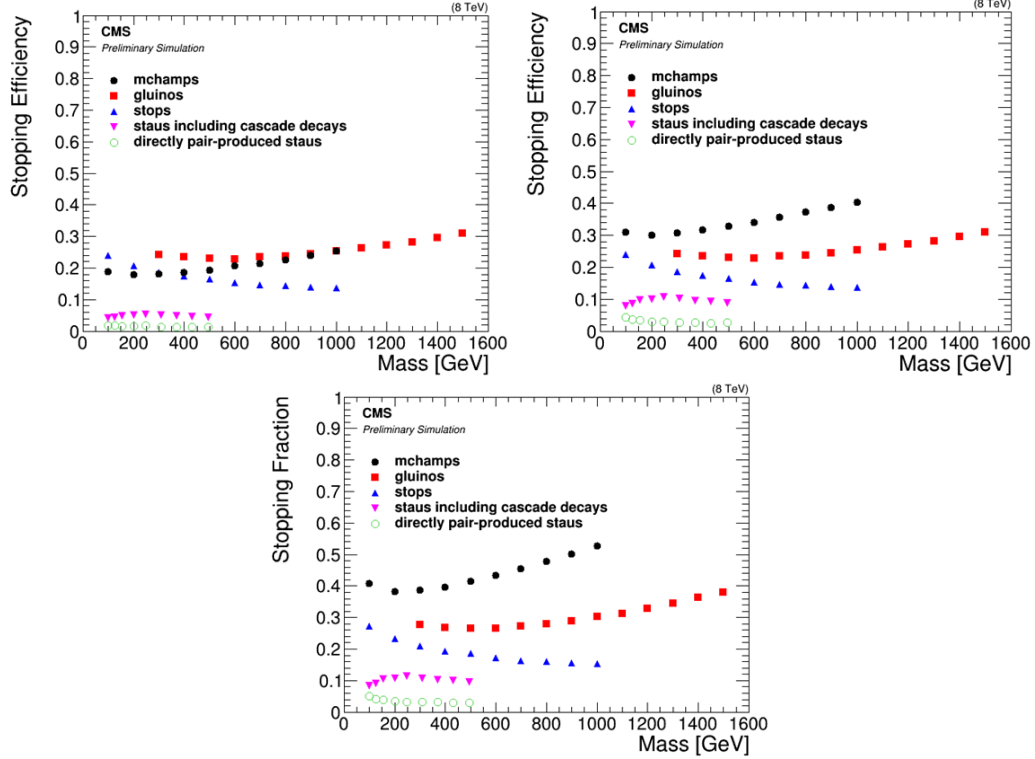


Figure 5.7: The stopping efficiency as a function of mass for each of the possible signal samples. The top left plot shows the efficiency before the bug fix, and the top right plot shows the efficiency after the bug fix. In both of these plots, the stopping efficiency for at least one particle to stop in the detector is plotted. The bottom plot shows the maximum stopping efficiency after the bug fix, assuming every stopped particle decays in a different event.

With the bug fix, and especially when considering the maximum possible stopping efficiency, the mchamps give the highest stopping probability because they have twice the electron charge. The  $R$ -hadrons from the stops and gluinos are the next most likely to stop in the detector. The staus have the lowest stopping efficiency, as lepton-like particles with the electron charge will interact with the detector material the least. The staus produced in cascade (GMSB staus) are more likely to stop in the detector

than those that are directly pair produced (PP staus) because they have a softer  $\beta$  distribution for each mass point.

The following figures were all made after the bug fix. Figure 5.8 shows the stopped particle distribution in  $x$  and  $y$  for each signal sample, with a LLP mass of  $\sim 500$  GeV. Fig. 5.9 shows the fraction of stopped events by detector region, for one mass point from each signal. The majority of the LLPs that stop in the detector are found in the muon and HCAL barrel.

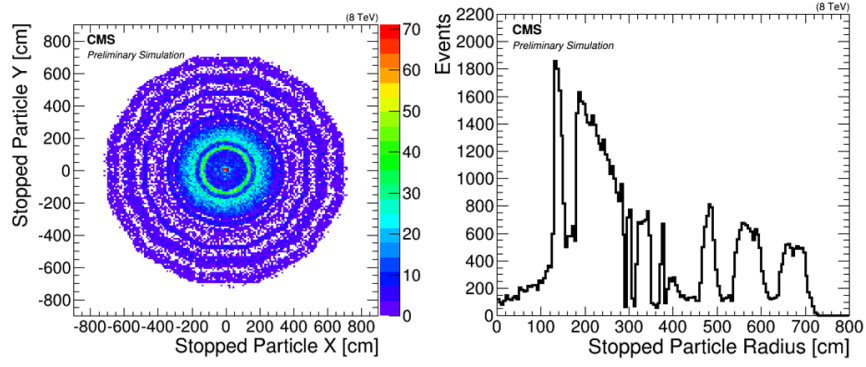


Figure 5.8: Stopping positions for 500 GeV mchamps. The  $y$  stopping coordinate as a function of the  $x$  stopping coordinate (left), and the radial  $r$  stopping coordinate (right). For the left plot, the colors indicate the number of events in each bin. These plots exclude the particles that stop in the cavern walls.

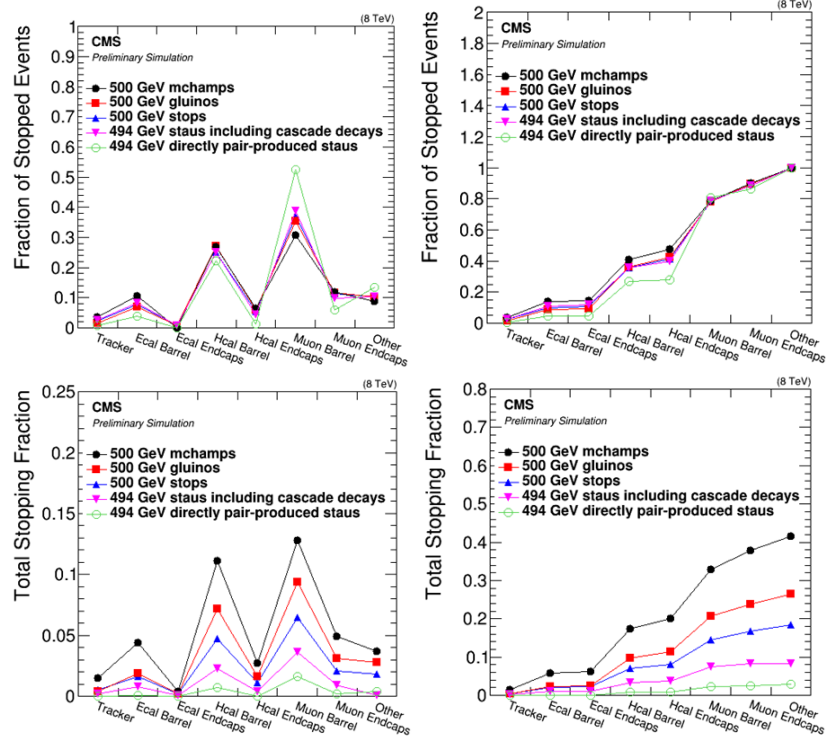


Figure 5.9: Fraction of events that stop in each detector region, for one mass point for all signal samples. The top row shows the events that stop in each region of the detector out of the events that stop, while the bottom row shows the events that stop out of all the events generated. The two plots on the left show the stopping fraction in each region, while the two plots on the right show the cumulative fraction in each region. The bin labeled “Other” includes LLPs that stop in the cavern walls.

#### 5.2.3.4 Event Weight for Doubly Charged Higgs

The mchamps with  $Q = 2e$  were an available HSCP sample that was used to model the doubly charged Higgs. In order to set limits on doubly charged Higgs, the mchamp sample can be reweighted to match the doubly charged Higgs at the generator level. This reweighting will have a direct effect on the stopping probability and position.

Figures 5.10 and 5.11 show the generator level kinematic distributions of 500 GeV mchamps compared with 500 GeV doubly charged Higgs. The mchamp sample is the Stage 1 MC simulation, and we consider all the events generated, regardless of whether the mchamp stopped in the detector. The doubly charged Higgs sample is:

/HPlusPlusHMinusMinusHTo4L\_M-500\_8TeV-pythia6/Summer12\_DR53X-PU\_S10\_START53\_V7C

The positively charged mchamp or doubly charged Higgs is plotted in Fig. 5.10, while the negatively charged mchamp or doubly charged Higgs is plotted in Fig. 5.11. Figure 5.12 shows the correlation between the  $p_T$  of the positively charged mchamp or doubly charged Higgs and the negatively charged one.

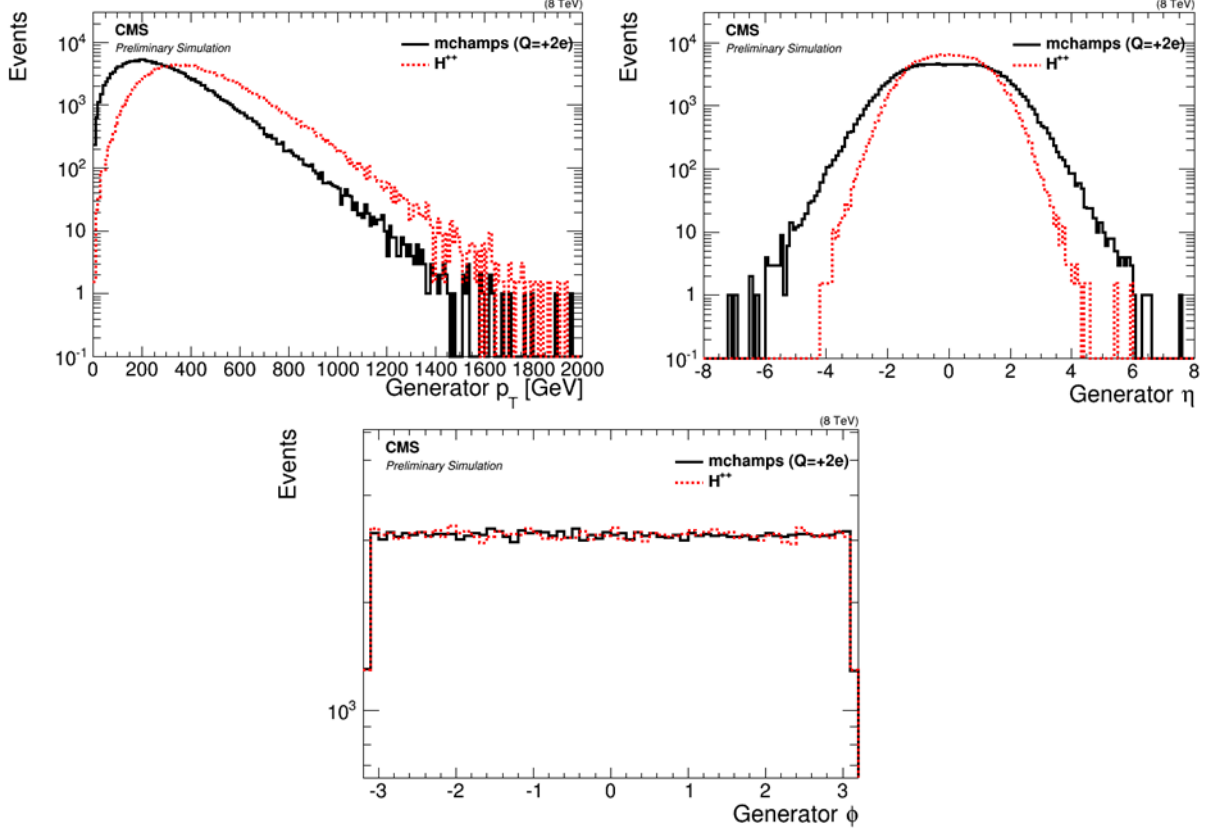


Figure 5.10: Distributions of  $p_T$ ,  $\eta$ , and  $\phi$  at the generator level for the positively charged 500 GeV mchamps and the positively charged 500 GeV doubly charged Higgs. The histograms are normalized to the same number of events.

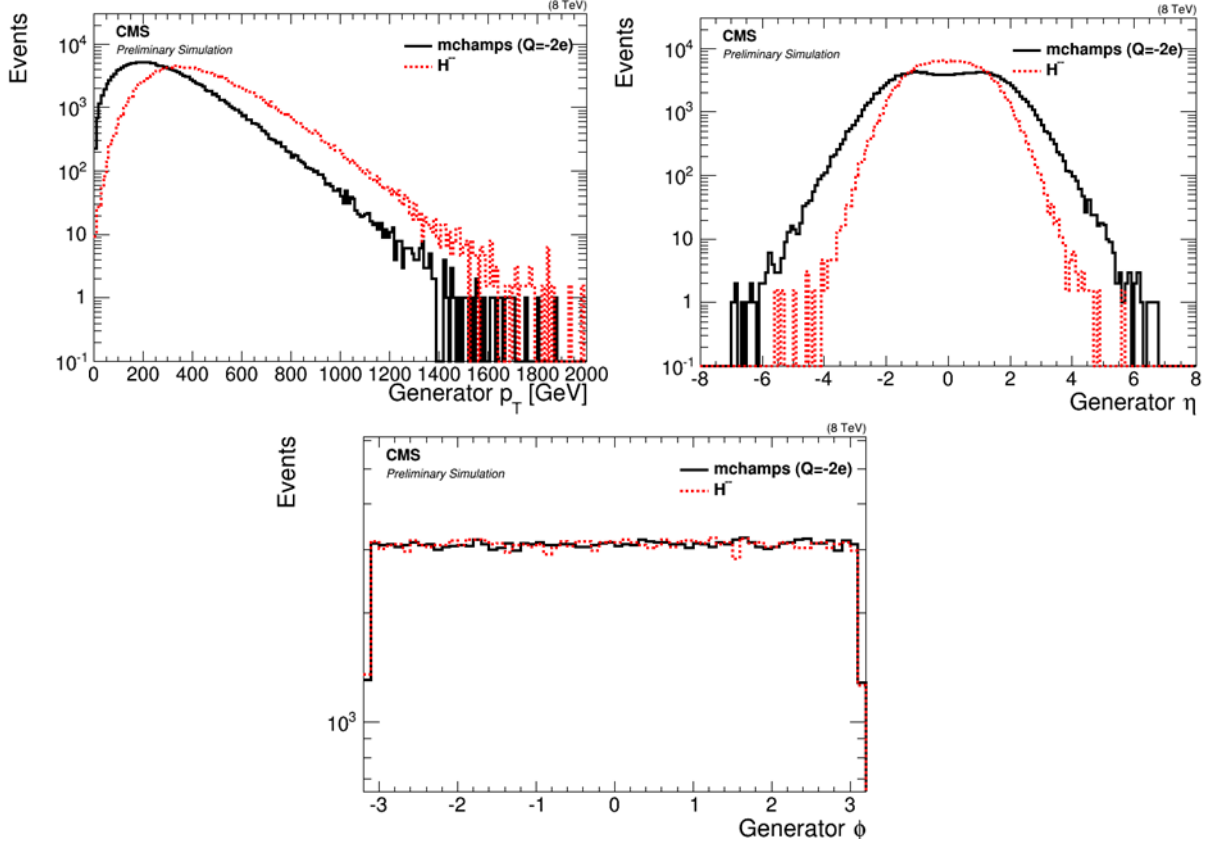


Figure 5.11: Distributions of  $p_T$ ,  $\eta$ , and  $\phi$  at the generator level for the negatively charged 500 GeV mchamps and the negatively charged 500 GeV doubly charged Higgs. The histograms are normalized to the same number of events.

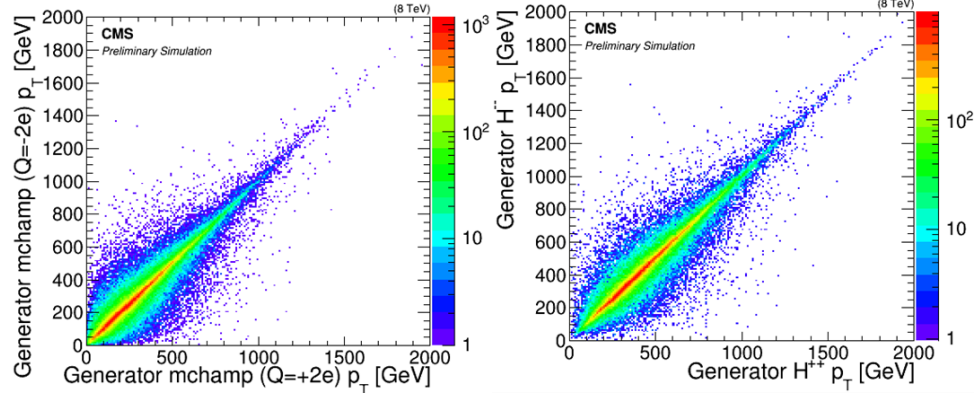


Figure 5.12: Distributions of the positively charged versus the negatively charged 500 GeV mchamps  $p_T$  (left) and of the positively charged versus negatively charged 500 GeV doubly charged Higgs  $p_T$  (right), at the generator level. The colors indicate the numbers of events in each bin.

The reweighting is done based on the 2D plot of the mchamp and doubly charged

Higgs  $p_T$ . The event weight is derived from the ratio of the doubly charged Higgs plot content to the mchamp one, on a bin-by-bin basis. This event weight is then applied to each mchamp event. Figures 5.13, 5.14, and 5.15 show the generator level kinematics after the 2D  $p_T$  reweighting. After reweighting, the mchamp and doubly charged Higgs are in good agreement for every kinematic variable.

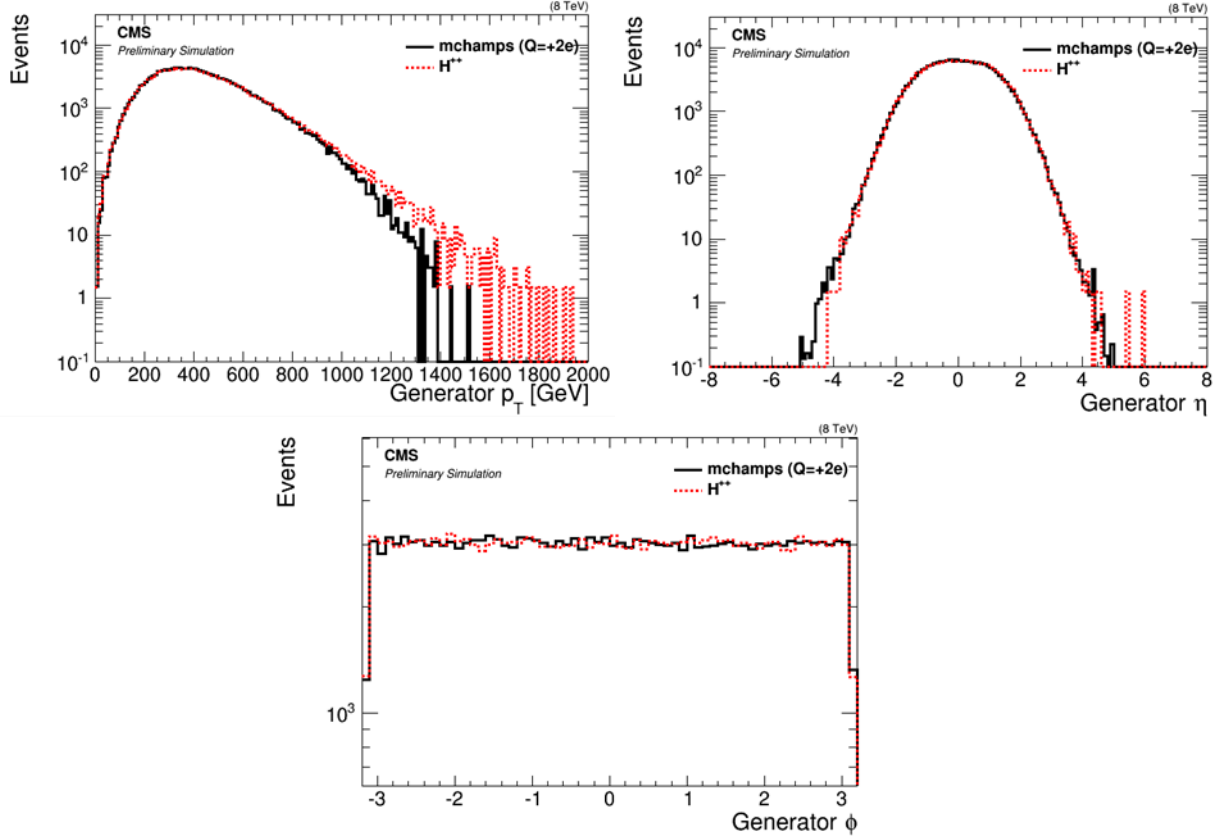


Figure 5.13: Distributions of  $p_T$ ,  $\eta$ , and  $\phi$  at the generator level for the positively charged 500 GeV mchamps and the positively charged 500 GeV doubly charged Higgs, after the reweighting.

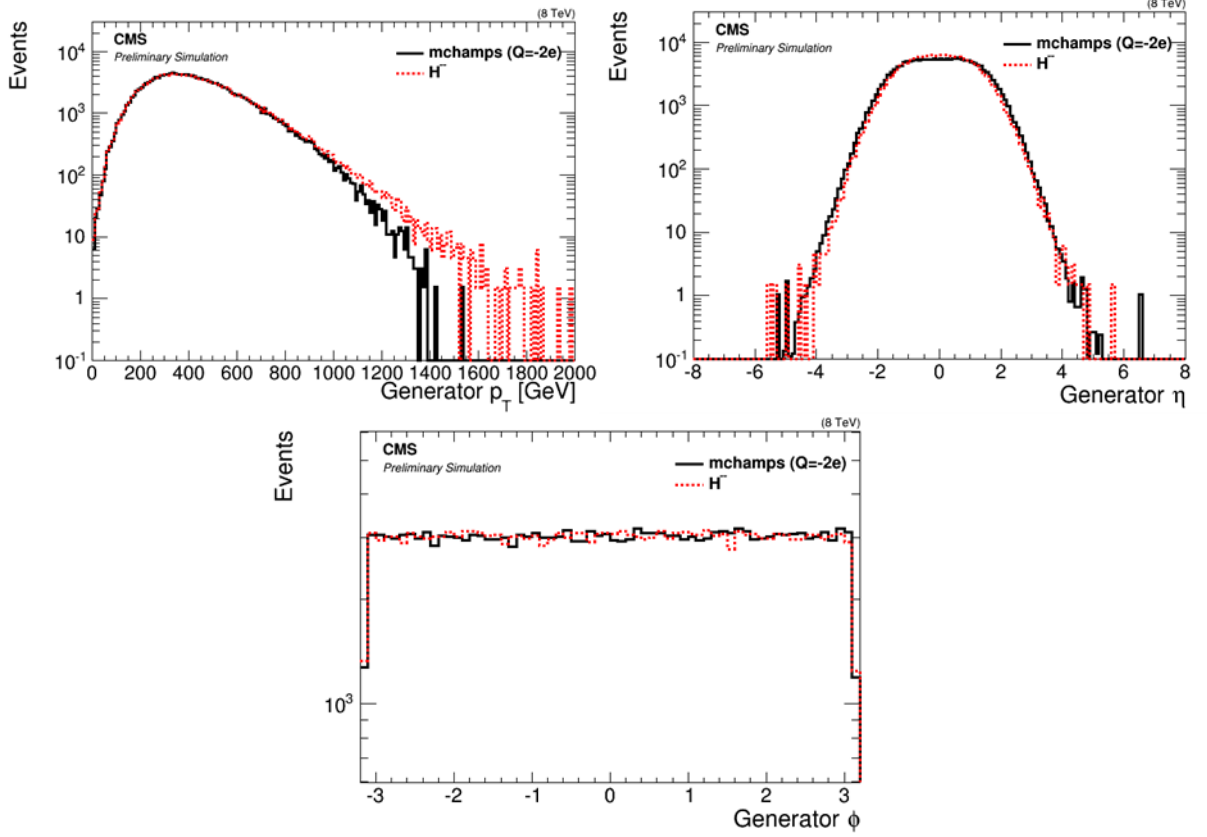


Figure 5.14: Distributions of  $p_T$ ,  $\eta$ , and  $\phi$  at the generator level for the negatively charged 500 GeV mchamps and the negatively charged 500 GeV doubly charged Higgs, after the reweighting.

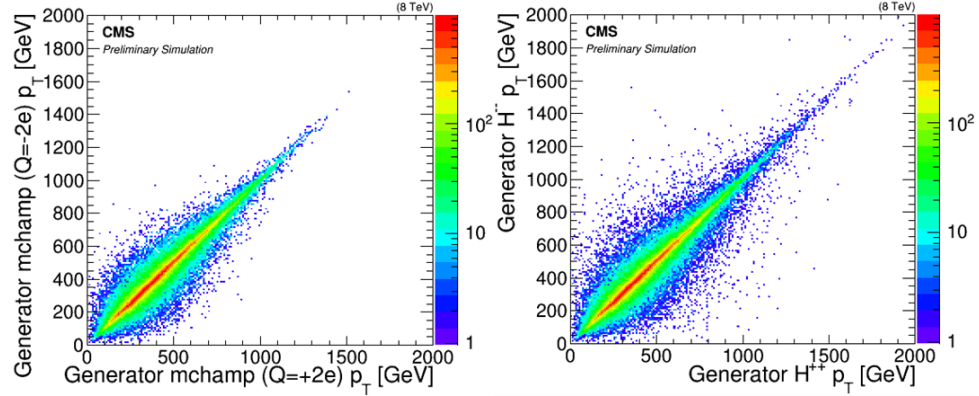


Figure 5.15: Distributions of the positively charged versus the negatively charged 500 GeV mchamps  $p_T$  (left) and of the positively charged versus negatively charged 500 GeV doubly charged Higgs  $p_T$  (right), at the generator level, after the reweighting. The colors indicate the numbers of events in each bin.



### 5.2.4 Cosmic Muon MC Simulation Sample

A cosmic muon MC simulation was used for cross checks. The sample,

`/Cosmics/jalimena-CosmicMC_PPreco_Plus125_RECO_723patch1-5416f02f2f84c038ddd1f9`

was made in CMSSW\_7\_2\_3\_patch1 and used the standard cosmic muon MC simulation python config file [238], except that the generator level timing distribution was adjusted to match that of the cosmic data sample, which was dependent on the trigger configuration.

## 5.3 Analysis Strategy and Techniques

To search for stopped LLPs that decay to muons, we trigger on muons that are out-of-time with respect to the bunch crossing. We model the signal with a MC simulation of LLPs that are stopped throughout the detector, and decay to muons. We identify background sources: muons from cosmic rays, noise, and beam halo. These cosmic muons are modeled with data and studied carefully, while noise and beam halo backgrounds are negligible after the full selection criteria and can be ignored. We use the muon time-of-flight (TOF) information from the DTs and RPCs to distinguish the background cosmic muons from signal. We also use the  $p$  or  $p_T$  measurement of the muons to aid in the identification of the background. The TOF variables are the most discriminating, but the  $p$  is an independent variable that is also useful. These key variables are described below.

### 5.3.1 Displaced Standalone Muon $p_T$

Because the cosmic muon momentum spectrum is steeply falling [1] and a massive LLP will decay to high  $p_T$  particles, the muon  $p_T$  can be used to discriminate between the high  $p_T$  muons from the signal and those from the cosmic muon background (see Fig. 5.16).

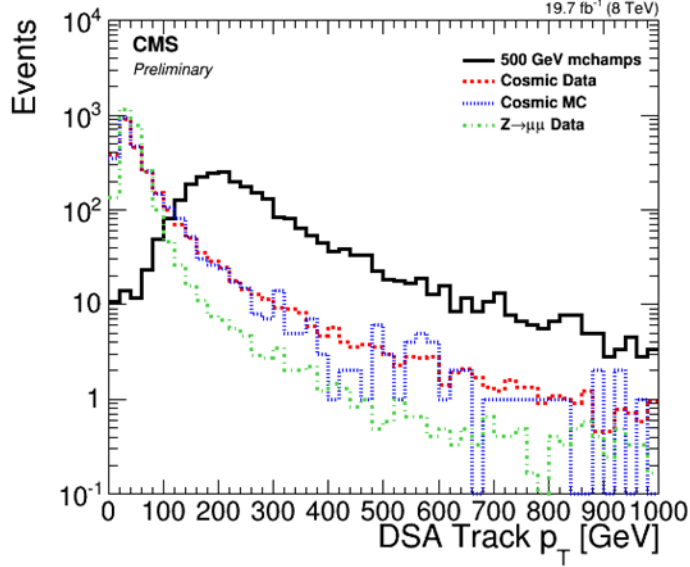


Figure 5.16: DSA muon  $p_T$  for 500 GeV mchamps,  $Z \rightarrow \mu\mu$  data, cosmic muon MC simulation, and cosmic muon data. Events must pass the trigger and the preselection. The highest  $p_T$  DSA track is plotted. The "DSA muon track"  $p_T$  shown is that after the revised reconstruction described in the text. The histograms are normalized to the same number of events.

However, we observed a problem with the SA muon  $p_T$  in CMSSW\_5\_3\_X. We noticed that the  $p_T$  from highly displaced SA muons was reconstructed anomalously lower than the generator muon  $p_T$ ; indeed, the SA muon  $p_T$  was not correlated with the generator muon  $p_T$ . This is easiest to see and test with the mchamp signal sample. Since the mchamp comes to a stop in the detector and then decays to two back-to-back muons, the generator muon  $p_T$  is sharply peaked at half the mass of the mchamp, and falls off to lower  $p_T$  if the muon undergoes bremsstrahlung radiation (see Fig. 5.17). However, the SA muon  $p_T$ , for events with good quality muons, was much lower than the generator muon  $p_T$ . The SA muon  $p_T$  distribution was anomalously low for the typical SA muon reconstruction, the refitted SA muon reconstruction, and the SA cosmic muon reconstruction (see Fig. 5.18).

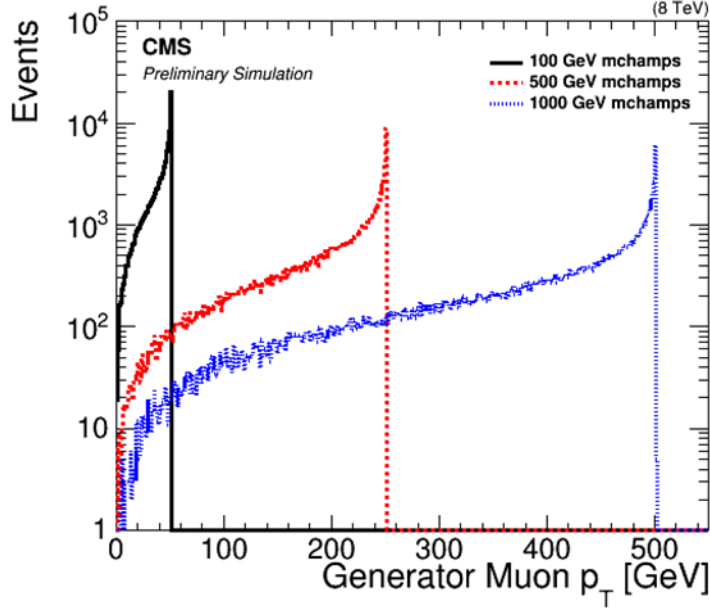


Figure 5.17: Generator muon  $p_T$  distribution for mchamps with masses of 100 GeV, 500 GeV, and 1000 GeV. No selection criteria have been applied. The histograms are normalized to the same number of events.

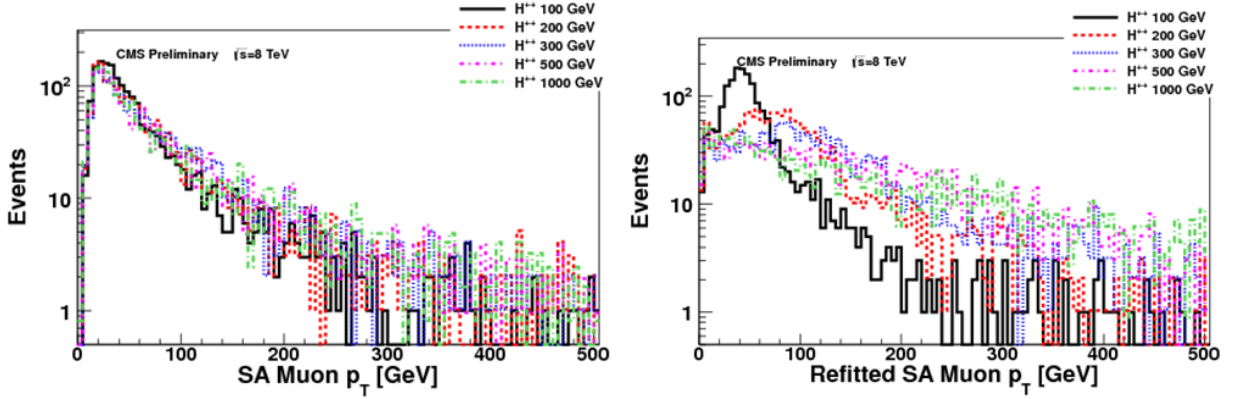


Figure 5.18: Reconstructed muon  $p_T$  distribution in 53X for mchamps with masses of 100 GeV, 200 GeV, 300 GeV, 500 GeV, and 1000 GeV. SA muon  $p_T$  (left) and RSA muon  $p_T$  (right). The histograms are normalized to the same number of events.

We explored different options in the latest release, such as combining parts of the cosmic muon and standard SA reconstruction, in a way that would be beneficial for delayed and displaced muons. We found that the optimal configuration was a SA reconstruction consisting of a cosmic muon seed in which the segments are not forced to point downwards [239], together with the SA trajectory builder [240] (see

Fig. 5.19). The regular muon segments designed for collisions were used as inputs to the seeds and to the trajectory builder, and the refitting of the SA track was not necessary. This new “DSA muons” track is not updated at the vertex. Furthermore, imposing quality criteria on these DSA muons, e.g. requiring at least 2 DT chambers with valid hits, brings the reconstructed muon  $p_T$  distribution even closer to that of the generator muon.

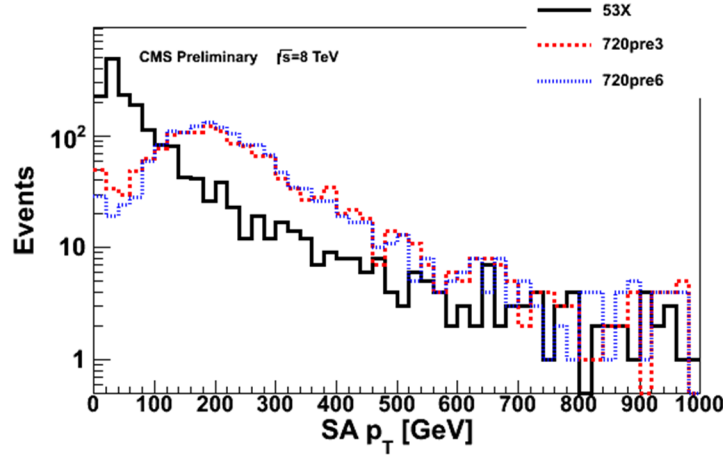


Figure 5.19: SA muon  $p_T$  distribution in 53X and 72X for mchamps with a mass of 500 GeV, which predominantly decay to two generator muons with a  $p_T$  of 250 GeV each. The black histogram shows the default SA muon  $p_T$  distribution in 53X, and the blue histogram shows the DSA muon  $p_T$ , as reconstructed in CMSSW\_7\_2\_0\_pre6. The blue histogram is the final version of the  $p_T$  distribution, whereas the red histogram shows an intermediate step, before the reconstruction was finalized. The histograms are normalized to the same number of events.

The DSA track reconstruction algorithm also makes use of a number of improvements in the muon reconstruction after CMSSW\_5\_3\_X, which was the version of the CMS software recommended to analyze 2012 data. The analysis was updated to be performed in CMSSW\_7\_2\_X to make use of:

- The latest (2015) version of the mean timer for the DT local reconstruction, which handles out-of-time muons in an appropriate way
- The latest local DT uncertainties

Figure 5.20 shows the resolution in  $p_T$  (left) and in  $q/p_T$  (right) of the different SA reconstruction algorithms for mchamps with a mass of 500 GeV, compared with a sample of prompt muons from a particle gun, with momentum of 250 GeV. The magenta line is the “standard” SA reconstruction not updated at the vertex for 500 GeV mchamps, and if this is compared to the green line, for the DSA track reconstruction of 500 GeV mchamps, the large improvement in the resolution can be seen. In the plot on the left, the magenta line is asymmetric because the generator  $p_T$  is high but the “standard” SA reconstruction gives an anomalously low  $p_T$ , thus indicating how poor the  $p_T$  resolution is for the “standard” SA reconstruction of very displaced muons. The DSA track reconstruction (green line) is still asymmetric, but the resolution for this reconstruction algorithm is much improved with respect to that of the “standard” SA reconstruction, for very displaced muons. The plot on the right has been approved for conferences. See Ref. [241, 242] for more information.

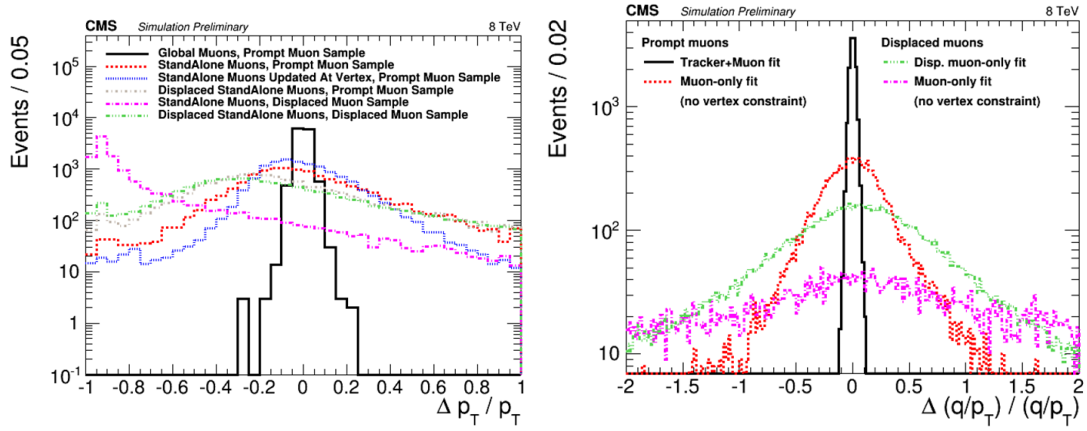


Figure 5.20:  $p_T$  resolution (left) and charge divided by  $p_T$  resolution (right) for different muon reconstruction algorithms, for prompt and displaced muon samples. The prompt muon sample is a particle gun of generator muons with  $p = 250$  GeV. The displaced muon sample is 500 GeV mchamps, which decay to 2 back-to-back muons, each with  $p = 250$  GeV. The SA tracks have at least 2 DT chambers with valid hits. The global muon, shown in black, must also be a SA muon with at least 2 DT chambers. The TuneP charge and  $p_T$  are plotted for the global muon. The SA tracks are matched to the generator muon within a cone of  $\Delta R < 0.5$ . The histograms are normalized to the same number of events.

The signal MC simulation and data were re-recoed with these improvements in

72X, and this custom SA reconstruction was made available as an explicit option in CMSSW in CMSSW\_7\_2\_0\_pre6 [243].

The data events obtained in 2012 were reconstructed at L1 and the HLT with this poor measurement of the L1 and L2 muon  $p_T$ . As will be discussed in Section 5.4.1, the L2 muon  $p_T$  threshold combined with the systematically low reconstructed muon  $p_T$  resulted in an anomalously low trigger acceptance. We improved the  $p_T$  resolution at L1 and HLT for 2015 (see Section 5.9).

### 5.3.2 DT Time of Flight

A reasonably accurate measurement of the time-of-flight of muons can be obtained using timing measurements in the DTs.  $\beta^{-1}$ , which is defined as  $c/v$  and is therefore directly proportional to the TOF, is the main timing variable used in this analysis. The standard  $\beta^{-1}$  measurement, as used by the HSCP search, is a calculation of the TOF of the muon from the IP to the DT chambers. However, in this analysis, we instead use  $\beta_{Free}^{-1}$ , which is determined by a fit to the times and positions of the DT hits, without a constraint to the beam spot.  $\beta_{Free}^{-1}$  and all of the associated timing variables discussed in this analysis use only the DTs to compute the measurements.

$\beta_{Free}^{-1}$  gives us the direction of the muon, that is, whether it is incoming toward the beam spot or outgoing from the beam spot. Outgoing muons should have a positive  $\beta_{Free}^{-1}$  and incoming muons should have a negative  $\beta_{Free}^{-1}$ . As a result, this  $\beta_{Free}^{-1}$  measurement can distinguish the cosmic muon background from the muons from the signal in the upper hemisphere. See Fig. 5.21 for a schematic diagram of  $\beta_{Free}^{-1}$  for cosmic muons and muons from the signal. Cosmic muons will predominantly be incoming in the upper hemisphere and outgoing in the lower hemisphere, as they come in from the top of the detector and continue to move downwards. The signal, on the other hand, will be outgoing in both hemispheres.

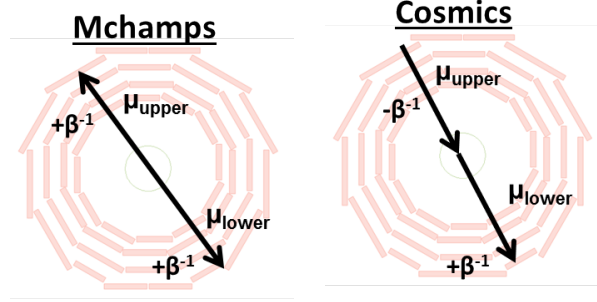


Figure 5.21: A diagram showing the direction and thus, the sign of  $\beta^{-1}$ , of muons coming from signal (left) and cosmic muon background (right).

$\beta_{Free}^{-1}$  is plotted in Fig. 5.22. Cosmic muons have two peaks in  $\beta_{Free}^{-1}$ : one peak at -1, which corresponds to the incoming muon in the upper hemisphere, and one peak at +1, which corresponds to the outgoing muon in the lower hemisphere. Muons from the signal have only one peak at a  $\beta_{Free}^{-1}$  value of +1, as these muons are always outgoing. As can be seen from the figure, the cosmic muons  $\beta_{Free}^{-1}$  distribution is broader than that of  $Z \rightarrow \mu\mu$  data or the signal MC simulation. Furthermore, the  $\beta_{Free}^{-1}$  distribution has the same shape in  $Z \rightarrow \mu\mu$  data and the signal MC simulation. The distributions of  $\beta_{Free}^{-1}$  for cosmic muons and signal muons are plotted for upper and lower hemisphere muons in Fig. 5.23. The resolution of  $\beta_{Free}^{-1}$ , which was found by fitting the signal to a Gaussian distribution, is 0.4. This is the first time  $\beta_{Free}^{-1}$  is used in a CMS physics analysis.

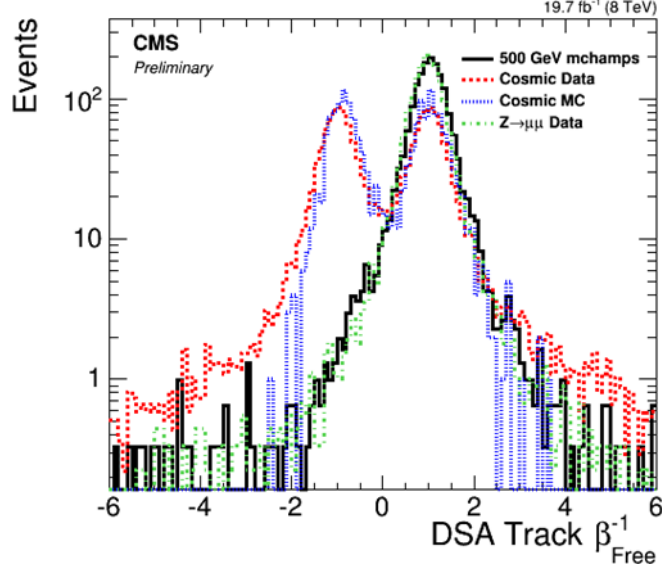


Figure 5.22: DSA track  $\beta_{Free}^{-1}$  for 500 GeV mchamps,  $Z \rightarrow \mu\mu$  data, cosmic muon MC simulation, and cosmic muon data. Events must pass the trigger and the preselection (see Section 5.4.2), and there must be at least one DSA track in the upper hemisphere and at least one in the lower hemisphere. The highest  $p_T$  DSA track in the upper hemisphere and the highest  $p_T$  DSA track in the lower hemisphere are plotted. The histograms are normalized to the same number of events.

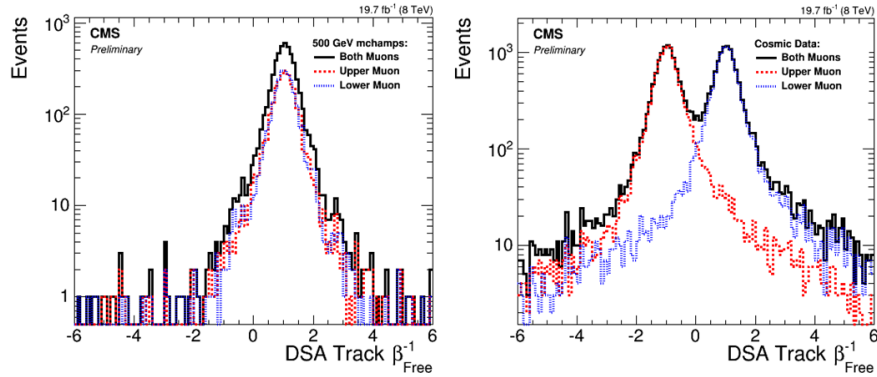


Figure 5.23: The  $\beta_{Free}^{-1}$  distribution for 500 GeV mchamps and cosmic muon data. Events must pass the trigger and the preselection (see Section 5.4.2), and there must be at least one DSA track in the upper hemisphere and at least one in the lower hemisphere. The highest  $p_T$  DSA track in the upper hemisphere (red), the highest  $p_T$  DSA track in the lower hemisphere (blue), and their sum (black) are plotted.



### 5.3.3 RPC BX Assignments

The RPCs are very fast, with a timing resolution of about 1 ns, and so we would like to take advantage of their timing measurement for this analysis. However, this fast timing information is mostly used in the trigger, and then only some information is saved at the RECO level in a compressed form. For each of the six layers of the RPCs, the muon is given a BX assignment. A typical prompt muon created at the IP will have each of its RPC BX assignments be zero; thus, its RPC BX pattern will be 0,0,0,0,0,0, if all the RPC layers gave good BX measurements. The BX assignments of cosmic muons are especially useful in the upper hemisphere of the detector, as the incoming cosmic muons will typically be assigned negative and decreasing BX values. For example, a typical upper hemisphere cosmic muon BX pattern will be -1,-1,-2,-2, for the RPC layers ranging from the innermost to the outermost. For our signal, the RPC BX assignments will typically each be zero (e.g. 0,0,0,0) or positive and a constant values (e.g. 1,1,1,1). See Fig. 5.24 for a schematic diagram of the BX assignments for cosmic muons and muons from the signal. Furthermore, see Fig. 5.25 for the distribution of BX assignment patterns in signal and background and Fig. 5.26 for the BX assignment patterns of the upper and lower hemisphere muons.

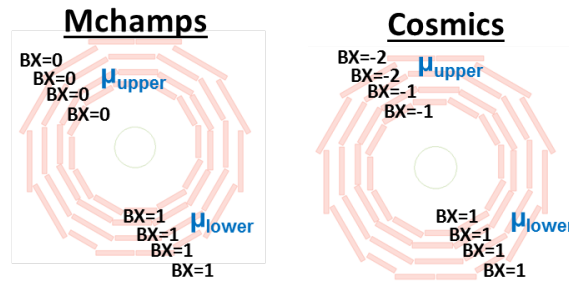


Figure 5.24: A diagram showing the RPC BX assignments of muons coming from signal (left) and cosmic muon background (right).

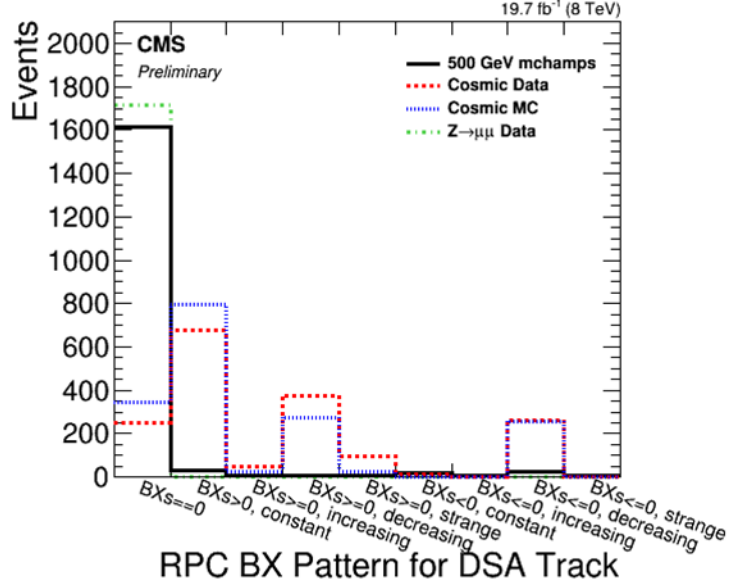


Figure 5.25: DSA muon RPC BX pattern for 500 GeV mchamps,  $Z \rightarrow \mu\mu$  data, cosmic muon MC simulation, and cosmic muon data. Events must pass the trigger and the preselection (see Section 5.4.2), and there must be at least one DSA track in the upper hemisphere and at least one in the lower hemisphere. The highest  $p_T$  DSA track in the upper hemisphere and the highest  $p_T$  DSA track in the lower hemisphere are plotted. The histograms are normalized to the same number of events.

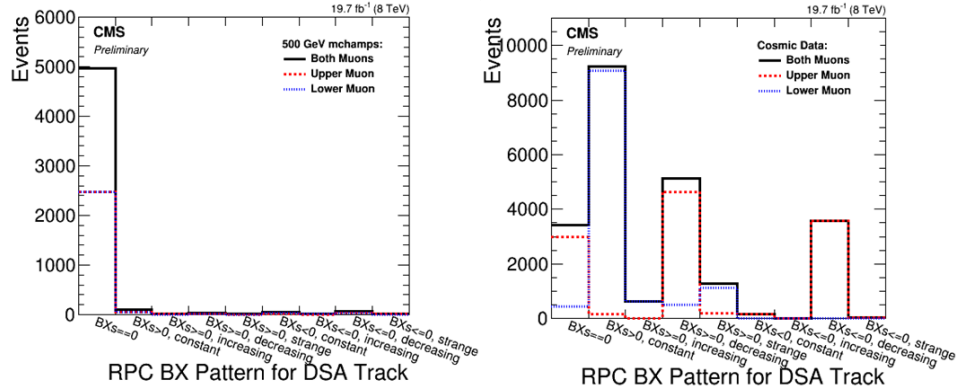


Figure 5.26: The RPC BX pattern for 500 GeV mchamps and cosmic muon data. Events must pass the preselection (see Section 5.4.2), and there must be at least one DSA track in the upper hemisphere and at least one in the lower hemisphere. The highest  $p_T$  DSA track in the upper hemisphere (red), the highest  $p_T$  DSA track in the lower hemisphere (blue), and their sum (black) are plotted.

## 5.4 Event Selection

Events are selected from the RECO data and the signal MC simulation samples discussed above. The LLP generated by the signal MC simulation is required to stop in the detector, and in particular, to not stop in the cavern walls. There must also be at least one generator muon with status 1, which means it is a final state PYTHIA particle. The data and MC simulation events must pass the trigger, pass the offline BX veto, and have at least one DSA muon track.

### 5.4.1 Trigger and Reconstruction Efficiency

The trigger efficiency and the efficiency to reconstruct at least one DSA track are both shown in Fig. 5.27.

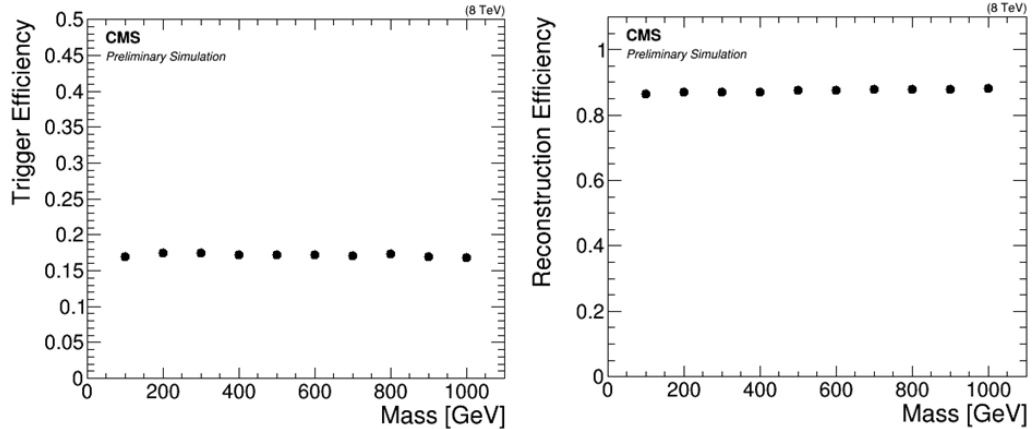


Figure 5.27: The signal HLT path efficiency (left) and reconstruction efficiency (right) as a function of mchamp mass. The trigger efficiency is defined as the number of events passing the signal trigger divided by the number of events with at least 1 reconstructed DSA track. The reconstruction efficiency is defined as the number of events with at least 1 DSA track divided by the number of stopped particle decays, excluding those in the cavern walls. The L2 muon reconstruction was similar to the standard offline SA muon track reconstruction, and thus gave a similarly incorrect  $p_T$  measurement.

The trigger efficiency is about 17% for all mchamp masses. The trigger efficiency is low primarily because the standalone muon  $p_T$  bias discussed in Section 5.3.1 was

present in the 2012 trigger, in both the L1 and HLT measurements of the muon  $p_T$ . Thus, the L2 muon momentum for muons from mchamps was anomalously low, and thus many mchamp events failed the 20 GeV  $p_T$  threshold at the HLT. The momentum measurement used in the trigger for 2015 has been improved; see Section 5.9 for more details.

The DSA track reconstruction performs reasonably well, reconstructing at least 1 DSA track for about 87% of the stopped particle decays, excluding those that stop in the cavern walls. It is most difficult to reconstruct a DSA track when the mchamp stops in the muon system. If the mchamp stops in the middle of the iron, the resulting muon(s) might only cross a few muon chambers and therefore not produce a good track, or the muon could move largely along the iron, rather than through the DT or RPC chambers.

### 5.4.2 Preselection Criteria

We first developed a preselection criteria to select a sample of events with reasonably good quality muons, in order to study the background and signal. In order to pass the preselection criteria, a DSA muon track must have:

- $p_T > 10$  GeV, to reject some background but still have enough low  $p_T$  events to study the cosmic muon background (see Section 5.3.1 for a description of the DSA  $p_T$  measurement)
- $> 1$  DT chambers with valid hits, to ensure a good quality DSA muon track and to reject noise
- $> 1$  valid RPC hits, to ensure a good RPC BX assignment measurement
- $> 7$  TOF number of degrees of freedom (DOF), that is,  $> 7$  DT hits with good timing measurements, to ensure a good DT timing measurement (see Section 5.3.2 for a description of the DT TOF variables)

- $\beta_{Free}^{-1} \chi^2$ -fit error  $< 10.0$ , to ensure a good DT timing measurement
- 0 valid CSC hits, to reduce beam halo and restrict the search to the barrel

There must also be less than 6 DSA tracks per event to reduce the cosmic muon background when several cosmic muons are triggered concurrently.

### 5.4.3 Signal and Background Comparison

Plots of the important reconstructed object variables are shown in Figs. 5.28, 5.29, and 5.30. The variables are plotted for 500 GeV mchamps,  $Z \rightarrow \mu\mu$  data, cosmic muon data, and cosmic muon MC simulation. Thus, we can see the important variables that distinguish signal from background and also compare cosmic muon data and cosmic muon MC simulation.

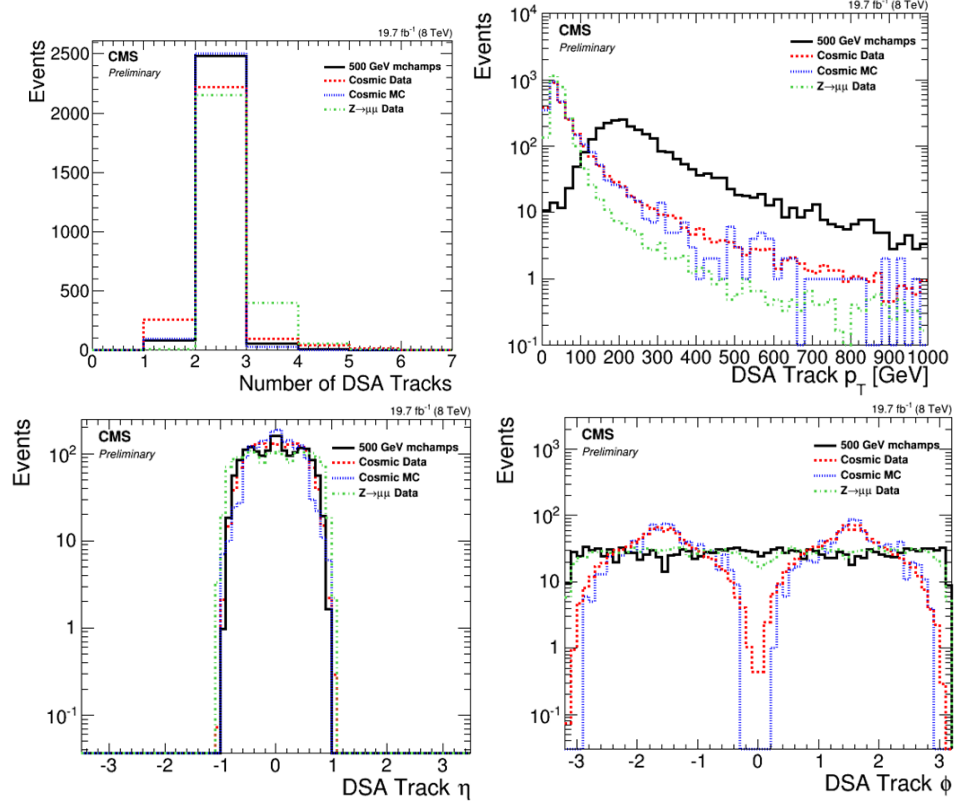


Figure 5.28: Number of DSA tracks, DSA track  $p_T$ , DSA track  $\eta$ , and DSA track  $\phi$ , for 500 GeV mchamps,  $Z \rightarrow \mu\mu$  data, cosmic muon MC simulation, and cosmic muon data. Events must pass the preselection. The highest  $p_T$  DSA track is plotted for the number of DSA tracks and the  $p_T$  distributions. The highest  $p_T$  DSA track in the upper hemisphere and the highest  $p_T$  DSA track in the lower hemisphere are plotted for the  $\eta$  and  $\phi$  distributions. The histograms are normalized to the same number of events.

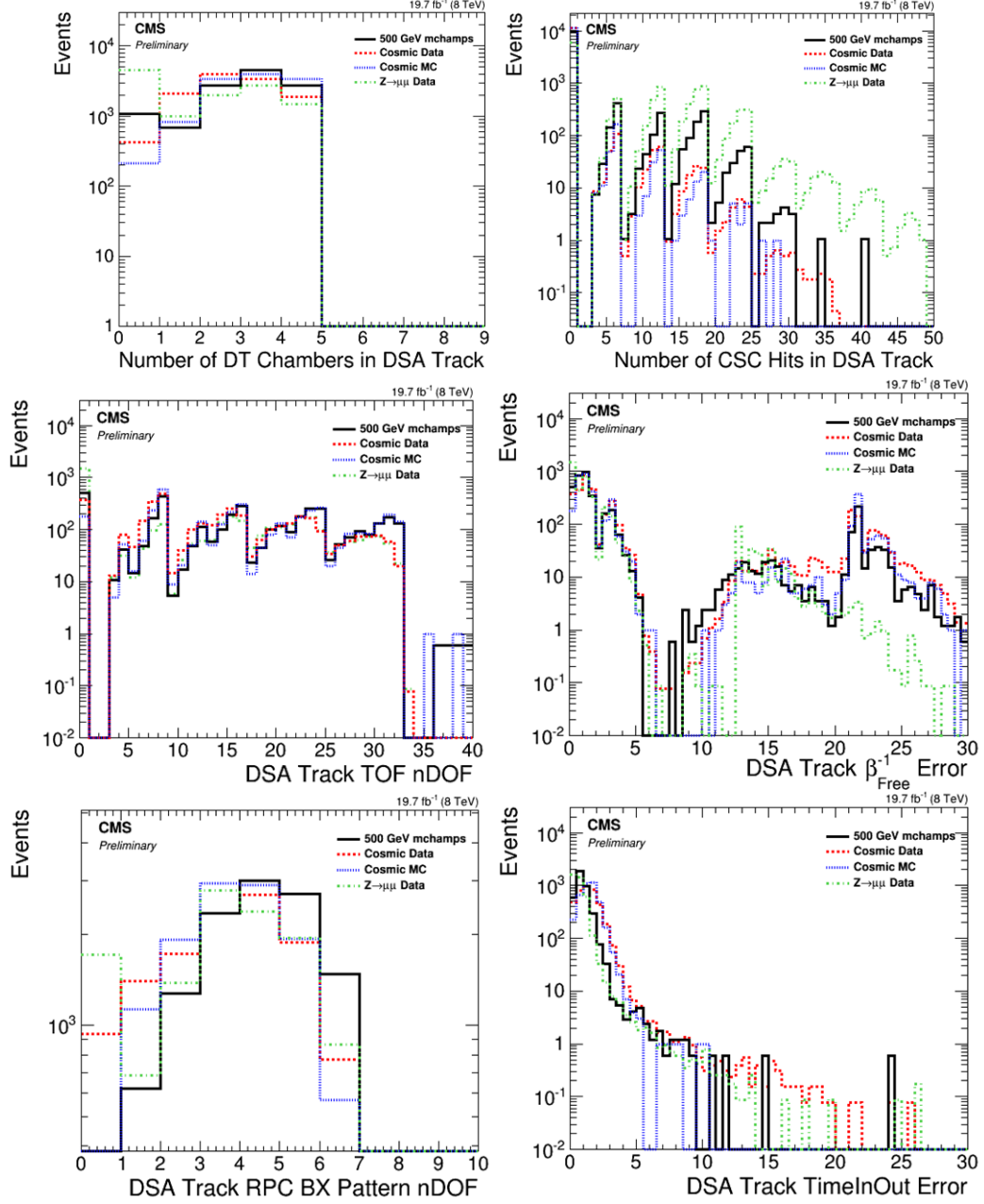


Figure 5.29: Number of DT chambers with valid hits, number of valid CSC hits, number of degrees of freedom for the DT TOF calculation,  $\beta_{Free}^{-1}$  error, number of RPC hits with good BX measurements, and TimeInOut error for the highest  $p_T$  DSA track, for 500 GeV mchamps,  $Z\rightarrow\mu\mu$  data, cosmic muon MC simulation, and cosmic muon data. Events must pass the trigger and the DSA track  $p_T > 10$  GeV cut from the preselection. The histograms are normalized to the same number of events.

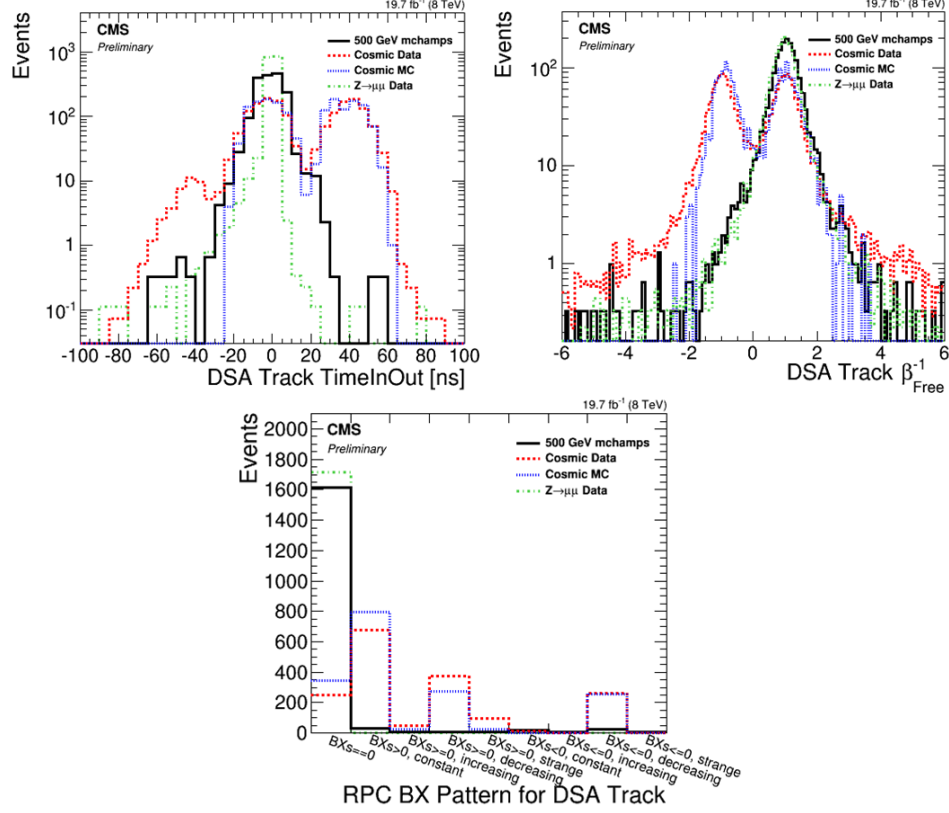


Figure 5.30: DSA track TimeInOut,  $\beta_{Free}^{-1}$ , and the RPC BX pattern, for 500 GeV mchamps,  $Z \rightarrow \mu\mu$  data, cosmic muon MC simulation, and cosmic muon data. Events must pass the preselection, and there must be at least one DSA track in the upper hemisphere and at least one in the lower hemisphere. The highest  $p_T$  DSA track in the upper hemisphere and the highest  $p_T$  DSA track in the lower hemisphere are plotted. The histograms are normalized to the same number of events.

Figure 5.28 shows the main kinematic variables. The top left plot shows that, predominantly, both muons are reconstructed for both the mchamp signal and the cosmic muon background. The top right plot shows the cosmic muons have a falling  $p_T$  spectrum, while muons from the signal have high  $p_T$ , so this variable can be used to discriminate signal from background (also see Section 5.3.1). The bottom two plots show that the background and signal are similarly central, but the signal is isotropically distributed in the  $\phi$  direction while the cosmic muon background is peaked at  $\phi = \pm\pi$  because the cosmic muons predominantly go straight through the detector from top to bottom.



Figure 5.29 shows the muon quality variables and variables related to the accuracy of the timing measurements. There is not a strong difference between signal and background in these plots, except for the number of DT chambers, number of DOF in the RPC BX pattern, and TimeInOut error, where the signal is slightly more accurate than the background. DSA muon tracks can have a maximum of four DT chambers with valid hits (top left plot), since there are four muon stations. Both signal and background are central and so they predominantly have 0 hits in the endcap CSCs (top right plot). The TOF number of DOF plot (middle left) shows the number of DT hits with good timing measurements, which come from the DT layers in the  $r - \phi$  direction. There are four DT chambers, each with two  $r - \phi$  superlayers comprised of four DT layers, for a maximum of 32 possible DT time measurements. The  $\beta_{Free}^{-1}$  error distribution (middle right) has two major peaks due to the TOF number of DOF distribution. The maximum number of DOF in the RPC BX pattern (bottom left plot) is six, due to the six RPC layers in the barrel. The error in the TimeInOut measurement is small for the muons from mchamps because both muons are outgoing, while this error is slightly larger for cosmic muons because the upper hemisphere cosmic muon is incoming and the lower hemisphere cosmic muon is outgoing.

Figure 5.30 shows the three main timing variables, which distinguish signal from background. The TimeInOut plot (top left) shows one peak centered at 0 ns for the outgoing muons from the mchamp signal, while there are two major peaks for cosmic muons: one at 0 ns for the outgoing lower hemisphere cosmic muon and one at  $\sim 50$  ns for the incoming upper hemisphere cosmic muon (see Section 5.4.4 for more details). Similarly, the  $\beta_{Free}^{-1}$  plot (top right) shows a separation between outgoing muons from the signal centered at  $\beta_{Free}^{-1} = +1$  and cosmic muons, which have the outgoing lower hemisphere muon centered at  $\beta_{Free}^{-1} = +1$  and the incoming upper hemisphere muon centered at  $\beta_{Free}^{-1} = -1$  (also see Section 5.3.2). The RPC BX pattern plot (bottom) shows that muons from the signal predominantly have each BX assigned to 0, while

cosmic muons more often have other BX patterns (also see Section 5.3.3).

In addition, plots of the timing variables are shown in another way in Figs. 5.31, 5.32, and 5.33. In these distributions, we have selected events that pass the preselection criteria, and we have plotted the upper hemisphere muon and the lower hemisphere muon for each timing variable. Thus, we can see how the timing distributions are different depending on whether the muon is in the upper hemisphere or the lower hemisphere and whether we consider background or signal.

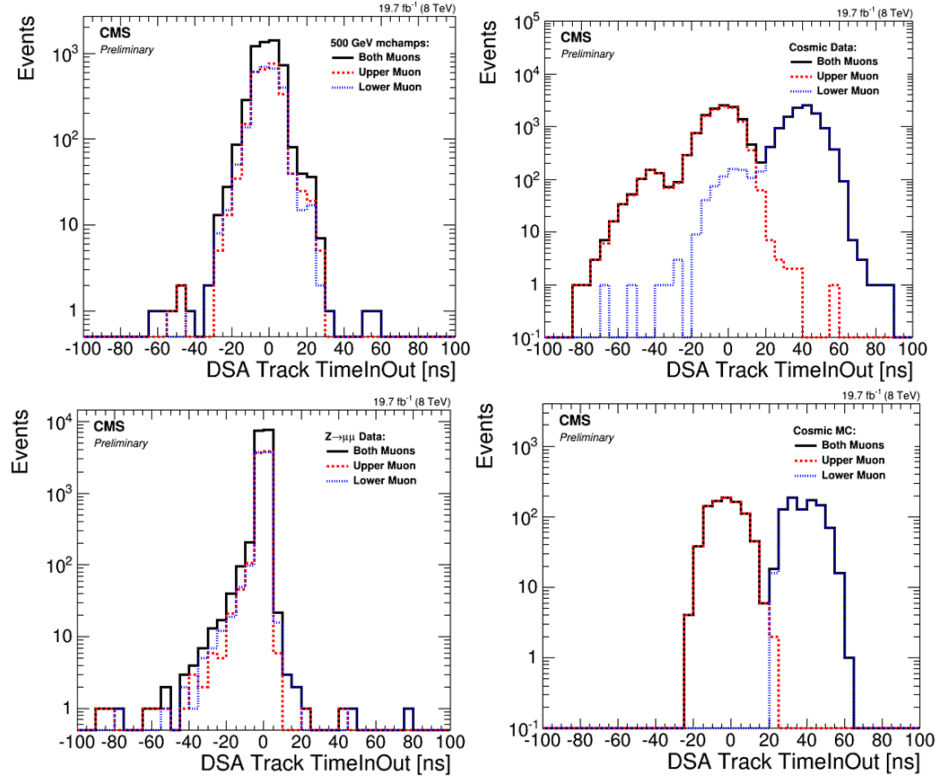


Figure 5.31: The TimeInOut distribution for 500 GeV mchamps (top left),  $Z \rightarrow \mu\mu$  data (bottom left), cosmic muon data (top right), and cosmic muon MC simulation (bottom right). Events must pass the preselection, and there must be at least one DSA track in the upper hemisphere and at least one in the lower hemisphere. The highest  $p_T$  DSA track in the upper hemisphere (red), the highest  $p_T$  DSA track in the lower hemisphere (blue), and their sum (black) are plotted.

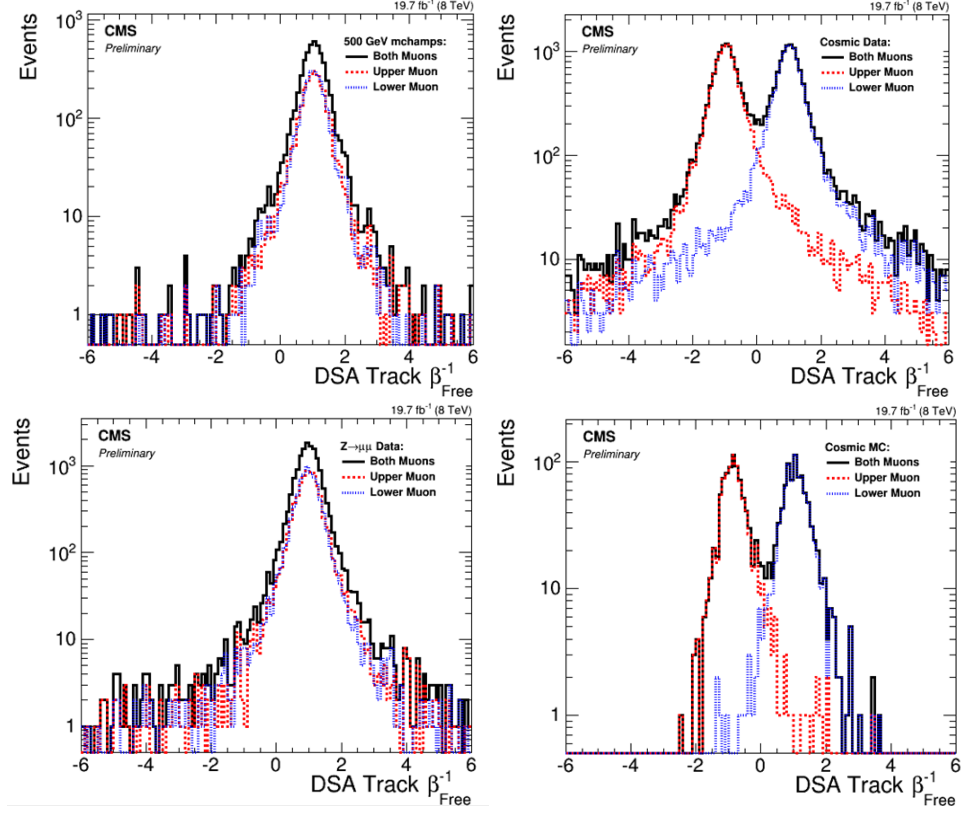


Figure 5.32: The  $\beta_{Free}^{-1}$  distribution for 500 GeV mchamps (top left),  $Z \rightarrow \mu\mu$  data (bottom left), cosmic muon data (top right), and cosmic muon MC simulation (bottom right). Events must pass the preselection, and there must be at least one DSA track in the upper hemisphere and at least one in the lower hemisphere. The highest  $p_T$  DSA track in the upper hemisphere (red), the highest  $p_T$  DSA track in the lower hemisphere (blue), and their sum (black) are plotted.

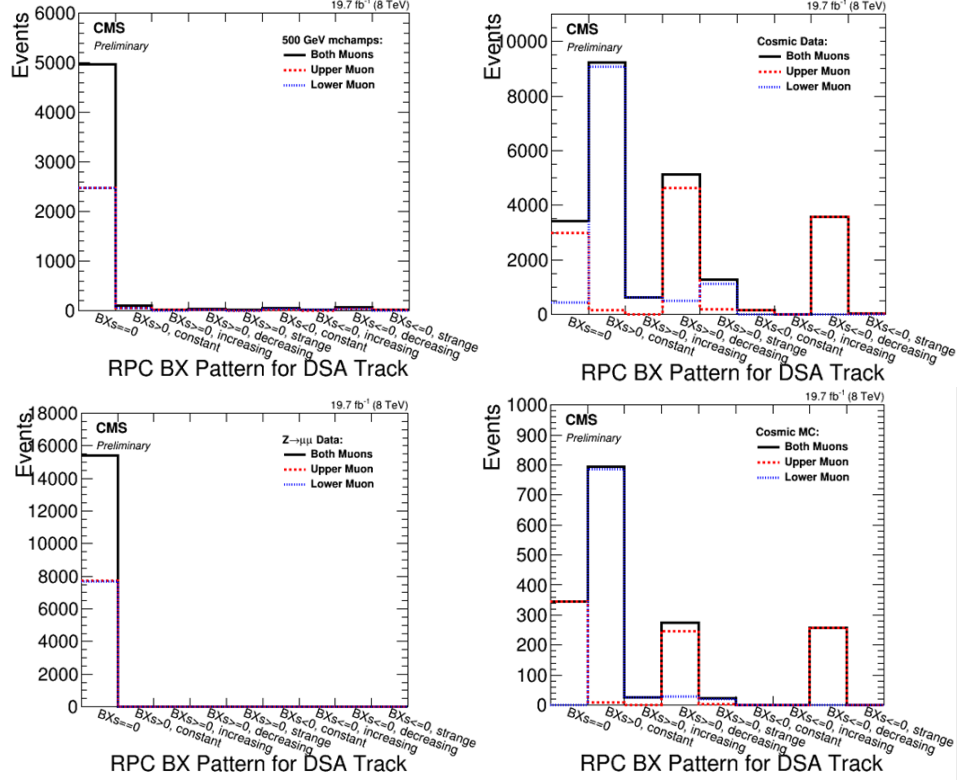


Figure 5.33: The RPC BX pattern for 500 GeV mchamps (top left),  $Z \rightarrow \mu\mu$  data (bottom left), cosmic muon data (top right), and cosmic muon MC simulation (bottom right). Events must pass the preselection, and there must be at least one DSA track in the upper hemisphere and at least one in the lower hemisphere. The highest  $p_T$  DSA track in the upper hemisphere (red), the highest  $p_T$  DSA track in the lower hemisphere (blue), and their sum (black) are plotted.

#### 5.4.4 Cosmic Muon TOF

A few points about the TOF of cosmic muons should be discussed. The cosmic muon data TimeInOut distribution (Fig. 5.31) can be understood if one considers the trigger configuration. During typical cosmic runs, only the bottom half of the detector is configured to trigger, while during normal pp running, both hemispheres are used to trigger. As stated in Section 5.2.2.2, we asked for a few cosmic runs at the end of 2012 to be configured as they are during pp running, namely, triggering on both hemispheres, so we could easily compare our cosmic run data with cosmic muons taken with our trigger during normal pp running. The cosmic muon data in

these plots are data from these special cosmic runs.

In the cosmic muon data TimeInOut distribution, the major peaks are when the upper hemisphere muon is found at a time of  $\sim 0$  ns, and when the lower hemisphere muon is found at  $\sim 50$  ns. This corresponds to the situation when the upper hemisphere muon is triggered, and thus given a time of 0 ns, and the lower hemisphere muon arrives  $\sim 50$  ns later.

The two early shoulders in the cosmic muon data TimeInOut distributions, at -50 ns for the upper hemisphere muon and at 0 ns for the lower hemisphere muon, can be explained by a lower hemisphere muon being triggered when the upper hemisphere muon was missed by the trigger. Thus, the time of the lower hemisphere muon is 0 ns. Since this variable shows the offline reconstruction, we can see that offline, the missing upper hemisphere muon was recovered, and it was found about 50 ns earlier than the lower hemisphere muon, that is, at about -50 ns.

These conclusions about the TimeInOut distribution can be seen clearly when one plots the TimeInOut for the upper hemisphere muon as a function of that of the lower hemisphere muon (see Fig. 5.34).

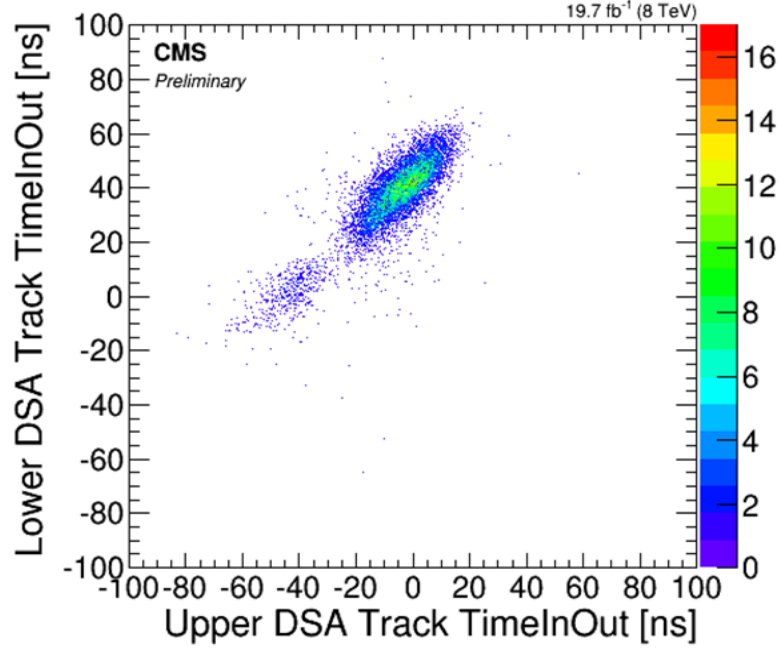


Figure 5.34: A scatter plot of the TimeInOut distribution for the lower hemisphere muon as a function of that of the upper hemisphere muon, for cosmic muon data. Events must pass the preselection, and there must be at least one DSA track in the upper hemisphere and at least one in the lower hemisphere. The highest  $p_T$  DSA track in the upper hemisphere and the highest  $p_T$  DSA track in the lower hemisphere are plotted. The colors indicate the numbers of events in each bin.

However, all of these different TimeInOut considerations are irrelevant for the  $\beta_{Free}^{-1}$  distribution. As can be seen in Fig. 5.32,  $\beta_{Free}^{-1}$  has only two peaks in cosmic data, corresponding to incoming or outgoing cosmic muons. Regardless of whether an upper hemisphere cosmic muon had a TimeInOut of -50 ns or 0 ns, its  $\beta_{Free}^{-1}$  is -1, on average. Similarly, a lower hemisphere cosmic muon has a mean  $\beta_{Free}^{-1}$  of +1, regardless of whether its TimeInOut is 0 ns or 50 ns. See Fig. 5.35 for more details.

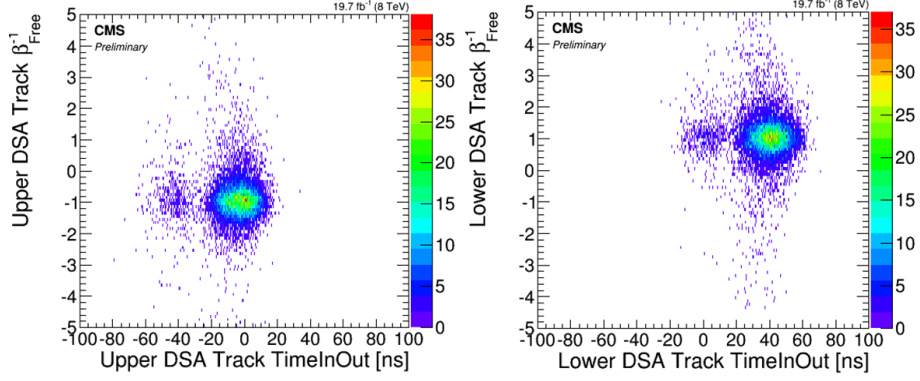


Figure 5.35: A scatter plot of  $\beta_{Free}^{-1}$  as a function of TimeInOut for cosmic muon data in the upper hemisphere (left) and in the lower hemisphere (right). Events must pass the preselection, and there must be at least one DSA track in the upper hemisphere and at least one in the lower hemisphere. The highest  $p_T$  DSA track in the upper hemisphere and the highest  $p_T$  DSA track in the lower hemisphere are plotted. The colors indicate the numbers of events in each bin.

A further question one can ask is whether the TOF measurements for a cosmic muon from a dedicated cosmic run and for a cosmic muon observed during pp collisions are equivalent. Figure 5.36 compares cosmic muon events from cosmic runs with cosmic muon events from collision data that pass the prescaled control trigger, which has a 10 GeV  $p_T$  cut at the HLT, but the same NoBPTX condition as the signal trigger. Indeed, the TimeInOut distribution (Fig. 5.36 left) is different for these two samples because the timing measurements are synchronized to the LHC clock during collisions, but the LHC clock is not used during dedicated cosmic runs, where the cosmic muon starts the time measurement. However, the  $\beta_{Free}^{-1}$  distribution (Fig. 5.36 right) is in much better agreement, especially in the analysis signal region ( $\beta_{Free}^{-1} > 0$ ). Therefore, the shift in the TimeInOut distribution does not have a significant impact on the  $\beta_{Free}^{-1}$  distribution.

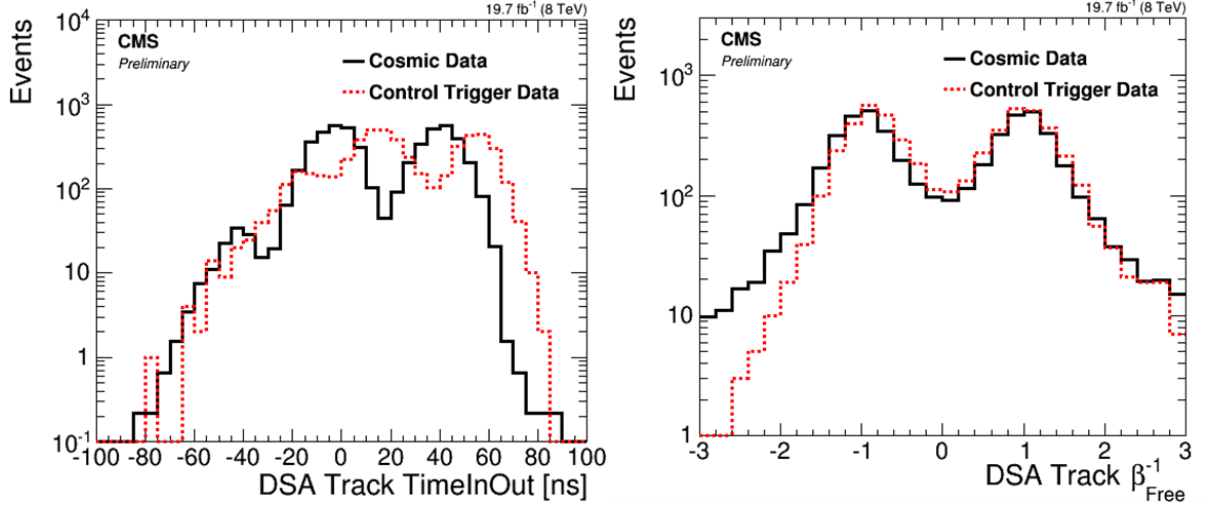


Figure 5.36: DSA track TimeInOut and  $\beta_{Free}^{-1}$  for cosmic muon data and collision data passing the prescaled control trigger. Events must pass the preselection, and there must be at least one DSA track in the upper hemisphere and at least one in the lower hemisphere. The highest  $p_T$  DSA track in the upper hemisphere and the highest  $p_T$  DSA track in the lower hemisphere are plotted. The histograms are normalized to the same number of events.

#### 5.4.5 Final Selection Criteria

After the preselection criteria are applied, the final selection criteria are applied. The final selection criteria were chosen to reject the background while maintaining a high signal acceptance. The final selection chooses events that have at least one good DSA track in the upper hemisphere and at least one good DSA track in the lower hemisphere. In order to pass this criteria, both the upper and lower hemisphere DSA tracks must have:

- $p_T > 30$  GeV, so both are in the plateau of the trigger turn-on curve (see Section 5.2.1 for the trigger turn-on curve)
- $> 2$  DT chambers with valid hits, to ensure each is a good quality DSA muon track and to reject noise
- $> 2$  RPC hits, to ensure each has a good RPC BX assignment measurement



- RPC BX assignments that are each 0 or each positive and constant, to distinguish a signal muon from cosmic ray background muon (see Section 5.3.3 for a description of the RPC BX assignments)
- Time measured at the IP, assuming the muon is outgoing ( $\text{TimeInOut} > -10.0$  ns, to reduce the cosmic muon background
- Error in  $\text{TimeInOut} < 2.0$  ns, to reduce the cosmic muon background
- the same charge, to reduce the cosmic muon background

The lower hemisphere DSA track must then also have:

- TOF direction = 1
- $\beta_{Free}^{-1} > 0.0$

The ABCD method, which estimates the background (see Section 5.5), then places tighter cuts on the  $p$  and  $\beta_{Free}^{-1}$  of the upper hemisphere muon. All of these selection criteria were developed while the analysis was kept blinded, meaning that we did not look at the data in the signal region, which is defined by positive  $\beta_{Free}^{-1}$  and large  $p$ .

The acceptance tables for data, cosmic muon all-phi data, and signal MC simulation are shown in Tables 5.8 and 5.9. Although the stopping efficiency is higher for higher mchamp masses than lower masses, decreases in many of the final selection criteria bring the overall efficiency to be about the same for all the mchamp masses. The last row in the signal acceptance table shows the upper bound on the signal acceptance, before running the pseudo-experiment simulation. Using this signal acceptance, the theoretical cross section, and the integrated luminosity, we can obtain an upper bound on the number of signal events, namely, 44 events for 100 GeV mchamps, 0.24 events for 500 GeV mchamps, and 0.0029 events for 1000 GeV mchamps.

Table 5.8: Cumulative selection cut efficiencies for collision data and cosmic muon data events. Note that in the last row, a cut of  $p > 60$  GeV on the upper hemisphere DSA track is shown, but this cut varies for each mchamp mass considered.

Selection Criteria	Run 2012B,C, D Collision Data		Cosmic Muon Data	
	Number of Events	Fraction of Events	Number of Events	Fraction of Events
Total (all triggers)	22373395	1.000	450682	1.000
At least one DSA track	21097157	0.943	427220	0.948
Pass trigger	20844859	0.932	328611	0.729
Preselection n DSA tracks $< 6$	20723801	0.926	327367	0.726
Preselection $p_T > 10$ GeV	18500958	0.827	260006	0.577
Preselection $> 1$ DT chambers with valid hits	16171663	0.723	215298	0.478
Preselection $> 1$ valid RPC hits	14979542	0.670	202272	0.449
Preselection $> 7$ TOF nDOF	4300323	0.192	41369	0.092
Preselection $\beta_{Free}^{-1}$ error $< 10.0$	3782992	0.169	35333	0.078
Preselection valid CSC hits $==0$	3711420	0.166	34853	0.077
At least 2 DSA tracks	858302	0.038	10332	0.023
At least 1 upper and 1 lower DSA track, each with:	853804	0.038	10290	0.023
$p_T > 30$ GeV	482721	0.021	5825	0.013
$> 2$ DT chambers with valid hits	253837	0.011	3288	0.0073
$> 2$ valid RPC hits	235384	0.011	3154	0.0070
RPC BXs $==0$ or BXs $>0$ and constant	30312	0.0014	520	0.0012
TimeInOut $> -10.0$ ns	27137	0.0012	444	0.00099
TimeInOut Error $< 2.0$ ns	17981	0.00080	302	0.00067
Same charge	735	0.00003	10	0.00002
DT TOF direction = 1, for lower DSA track	716	0.00003	10	0.00002
$\beta_{Free}^{-1} > 0.0$ , for lower DSA track (Events in regions A, B, C and D)	716	0.00003	10	0.00002
$\beta_{Free}^{-1} > 0.5$ , for upper DSA track (Events in regions C and D)	40	0.000002	0	0.0
$p > 60$ GeV, for upper DSA track (Events in region D)	30	0.000001	0	0.0

Table 5.9: Cumulative selection cut efficiencies (fraction of events) for 100 GeV, 500 GeV, and 1000 GeV mchamps. Note that in the last row, the  $p_T$  cut on the upper hemisphere DSA track varies for each mchamp mass considered.

Selection Criteria	100 GeV mchamp	500 GeV mchamp	1000 GeV mchamp
Total generated	1.000	1.000	1.000
Maximum stop in detector	0.407	0.414	0.527
Not in cavern walls	0.371	0.379	0.483
At least one status 1 gen muon	0.371	0.379	0.483
At least one DSA track	0.321	0.331	0.426
Pass trigger	0.055	0.057	0.072
Preselection n DSA tracks < 6	0.055	0.057	0.072
Preselection $p_T > 10$ GeV	0.054	0.057	0.071
Preselection > 1 DT chambers with valid hits	0.050	0.051	0.064
Preselection > 1 valid RPC hits	0.049	0.050	0.063
Preselection > 7 TOF nDOF	0.030	0.031	0.039
Preselection $\beta_{Free}^{-1}$ error < 10.0	0.027	0.027	0.034
Preselection valid CSC hits ==0	0.026	0.026	0.033
At least 2 DSA tracks	0.013	0.014	0.017
At least 1 upper and 1 lower DSA track, each with:	0.013	0.014	0.017
$p_T > 30$ GeV	0.011	0.013	0.016
> 2 DT chambers with valid hits	0.0087	0.0089	0.011
> 2 valid RPC hits	0.0080	0.0081	0.010
RPC BXs==0 or BXs>0 and constant	0.0077	0.0076	0.0092
TimeInOut > -10.0 ns	0.0071	0.0070	0.0083
TimeInOut Error < 2.0 ns	0.0069	0.0068	0.0081
Same charge	0.0069	0.0065	0.0069
DT TOF direction = 1, for lower DSA track	0.0068	0.0065	0.0068
$\beta_{Free}^{-1} > 0.0$ , for lower DSA track (Events in regions A, B, C and D)	0.0068	0.0065	0.0068
$\beta_{Free}^{-1} > 0.5$ , for upper DSA track (Events in regions C and D)	0.0065	0.0059	0.0063
$p > 60$ GeV, 110 GeV, 200 GeV, respectively, for upper DSA track (Events in region D)	0.0012	0.0054	0.0058

## 5.5 Background Modeling

### 5.5.1 ABCD Method

The background is estimated using the ABCD method, with the upper hemisphere DSA track  $\beta_{Free}^{-1}$  and  $p$  as the two variables providing the most separation between the background (cosmic muons) and the signal.  $\beta_{Free}^{-1}$  and  $p$  are independent, as shown below. For muons in the upper hemisphere, most of the cosmic muon background has  $\beta_{Free}^{-1} < 0$  and low  $p$ , while the signal has  $\beta_{Free}^{-1} > 0$  and high  $p$ . If a cosmic muon has  $\beta_{Free}^{-1} > 0$  and low  $p$  in the upper hemisphere, its  $\beta_{Free}^{-1}$  is mismeasured. If a cosmic muon has  $\beta_{Free}^{-1} < 0$  and high  $p$  in the upper hemisphere, its  $p$  could be genuine or mismeasured. Figure 5.37 shows a schematic of the different regions defined by the  $\beta_{Free}^{-1}$  and  $p$ , and the expected background and signal in each. Given that  $\beta_{Free}^{-1}$  and  $p$  are independent, the ratio of the number of background events in region B to the number of such events in region A should be equal to the ratio of the number in region D to the number in region C. Equivalently, the ratio of the numbers in regions C and A should be equal to the ratio of the numbers in regions D and B. Using the number of background events found in regions A, B, and C, the background in region D, which is where signal events would collect, can be estimated. The number of background events in D should be approximately  $BC/A$ , and thus the number of observed signal events is  $D - BC/A$ . Therefore, the ABCD method provides a way to use regions with negligible signal to estimate the number of observed signal events, assuming the variables being used are uncorrelated.

	Low $p$	High $p$
$\beta_{Free}^{-1} > 0$	<b>C</b> A few cosmics (mis-measured $\beta^{-1}$ )	<b>D</b> Cosmics and <b>Signal</b>
$\beta_{Free}^{-1} < 0$	<b>A</b> Cosmics	<b>B</b> A few cosmics (mis-measured $p$ and high $p$ )

Figure 5.37: Schematic of the ABCD regions for the background estimation.

### 5.5.2 Choice of Momentum Variable for Background Estimation

It is clear that we need to use the  $\beta_{Free}^{-1}$  of the upper hemisphere DSA muon track in the ABCD method, but we have some freedom to choose the exact momentum variable. The  $p$  of both the upper and lower hemisphere DSA tracks should be equally good at discriminating between cosmic muons and muons from the signal. Furthermore, it is not obvious a priori whether  $p$  or  $p_T$  would give better separation between cosmic muons and signal muons.

We computed the  $S/\sqrt{(S+B)}$  curves of the upper hemisphere DSA muon track  $p$  (the “upper  $p$ ”), of the average  $p$  of the upper and lower hemisphere DSA tracks (the “average  $p$ ”), and of whichever  $p$  of the two was a greater value (the “highest  $p$ ”). See Fig. 5.38 for these  $S/\sqrt{(S+B)}$  curves. Then we did the same for the DSA track  $p_T$ , that is, the “upper  $p_T$ ,” the “average  $p_T$ ,” and the “highest  $p_T$ ” (see Fig. 5.39). The  $S/\sqrt{(S+B)}$  curves of the  $p$  variables are consistently slightly greater than those of the  $p_T$  variables, and so we can conclude that  $p$  is slightly better at discriminating cosmic muons from signal muons than  $p_T$ . Furthermore, although the highest and average  $p$  or  $p_T$  have higher  $S/\sqrt{(S+B)}$  curves than the upper  $p$  or  $p_T$ , the highest and average  $p$  and  $p_T$  have zero background events at low values of  $p$  and  $p_T$ . To

avoid this problem, we choose the upper hemisphere DSA muon track  $p$  to use in the ABCD method.

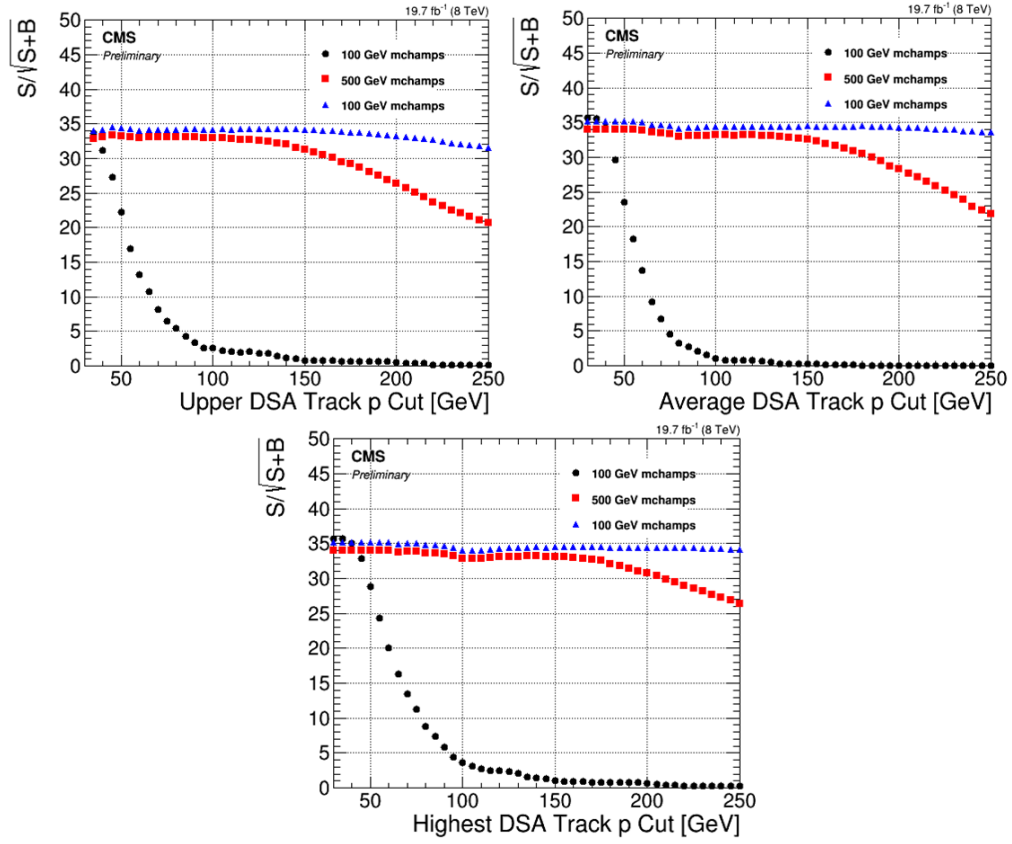


Figure 5.38:  $S/\sqrt{(S+B)}$  as a function of the upper hemisphere  $p$  (top left), the average  $p$  (top right), and the highest  $p$  (bottom), for three mchamps masses.

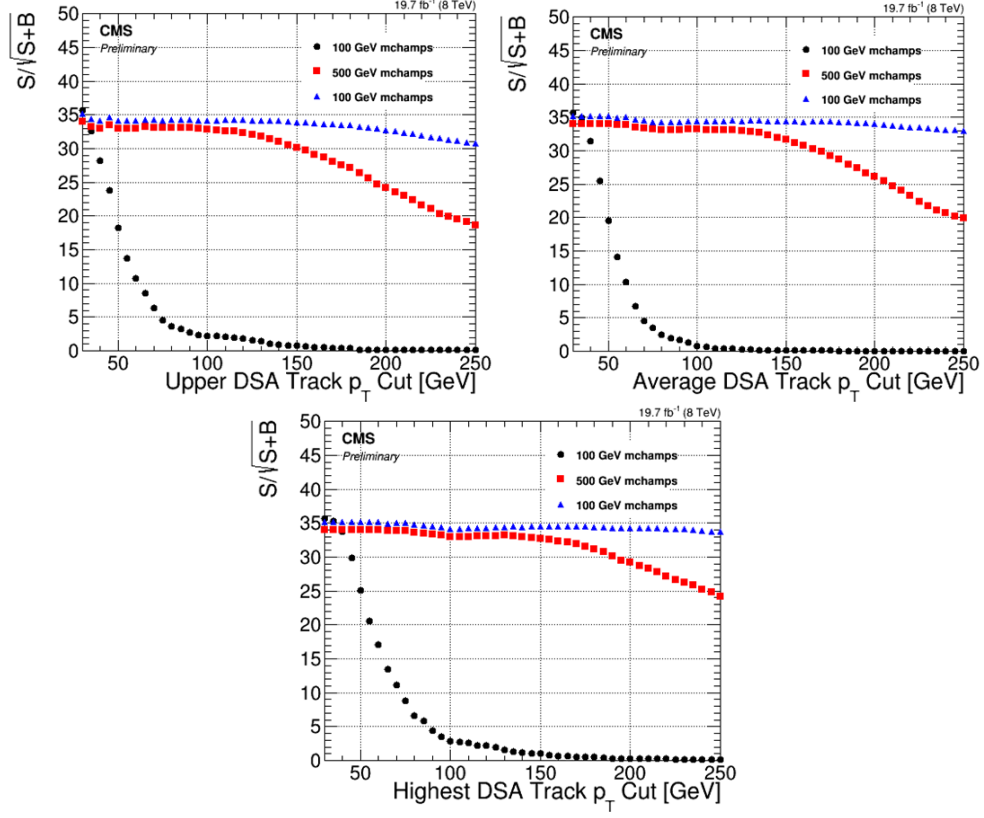


Figure 5.39:  $S/\sqrt{(S+B)}$  as a function of the upper hemisphere  $p_T$  (top left), the average  $p_T$  (top right), and the highest  $p_T$  (bottom), for three mchamp masses.

### 5.5.3 Choice of $\beta_{Free}^{-1}$ and $p$ Cuts

The cut values for  $\beta_{Free}^{-1}$  and  $p$  should be chosen to maximize the signal and minimize the background in region D. The  $\beta_{Free}^{-1}$  distribution does not vary among the different mchamp mass points (see Fig. 5.40 left), so one value of  $\beta_{Free}^{-1}$  was chosen for all masses.  $\beta_{Free}^{-1} = 0.5$  was chosen to define the boundary because this value gave the lowest upper cross section expected limits. This choice of  $\beta_{Free}^{-1}$  cut is also in the plateau of the  $S/\sqrt{(S+B)}$  curve (see Fig. 5.41), and so it gives a stable result for small variations in  $\beta_{Free}^{-1}$ .

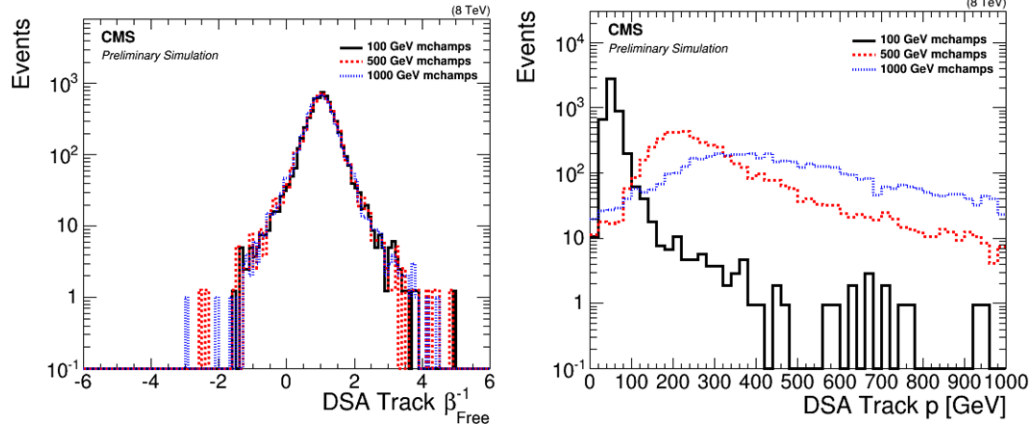


Figure 5.40: DSA track  $\beta_{Free}^{-1}$  (left) and  $p$  (right) for 100, 500, and 1000 GeV mchamps. Events must pass the trigger and the preselection. The highest  $p_T$  DSA track is plotted. The histograms are normalized to the same number of events.

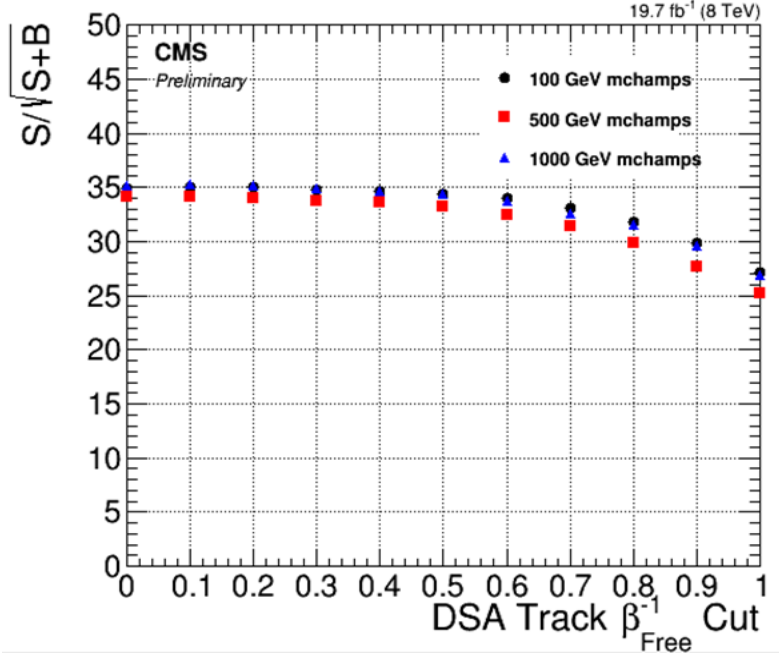


Figure 5.41:  $S/\sqrt{(S+B)}$  as a function of  $\beta_{Free}^{-1}$  for three mchamp masses.

On the other hand, the  $p$  distribution varies greatly among the different mchamp masses (see Fig. 5.40 right), and so different  $p$  cut values were chosen to optimize the separation between signal and background, for each signal mass. Figure 5.42 shows  $S/\sqrt{(S+B)}$  as a function of  $p$  for different mchamp masses. The  $p$  cut values were chosen to be in the plateau of each of these curves. The choices of  $p$  cuts will be listed



in Table 5.12, which will appear in the Results section.

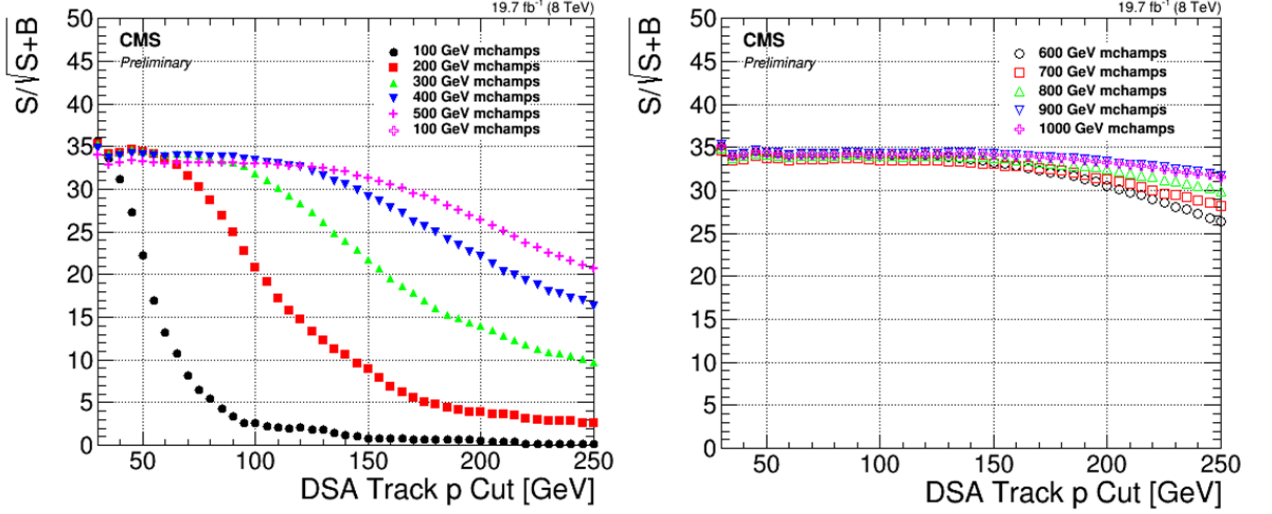


Figure 5.42:  $S/\sqrt{(S+B)}$  as a function of  $p$  for all mchamp masses. Masses 100 to 500 GeV are on the left, and masses 600 to 1000 GeV are on the right.

Besides providing the lowest expected limits and being on the plateau of the  $S/\sqrt{(S+B)}$  curve, the other criterion considered for choosing the cut values for  $\beta_{Free}^{-1}$  and  $p$  was that each control region in the background estimation was required to contain at least 10 events, in order to have sufficient statistics in each control region.

#### 5.5.4 Background Closure Test

Figure 5.43 shows a scatter plot of  $\beta_{Free}^{-1}$  as a function of  $p$  for 500 GeV mchamp events and for cosmic muon data. The A, B, C, and D regions are defined by the  $\beta_{Free}^{-1} = 0.5$  and  $p = 100$  GeV lines. A test was performed on the cosmic muon data to see how well  $BC/A$  agrees with D. Table 5.10 shows the number of events in each region. For this definition of the regions,  $BC/A = 12.4 \pm 2.5$  events, as compared with  $9 \pm 3$  events in region D; the two values agree within uncertainties. Furthermore, additional tests have been done with other choices for values of  $\beta_{Free}^{-1}$  and  $p$  to define the A, B, C, and D regions, and in these additional test,  $BC/A$  agrees with D within

uncertainties. Therefore, we can infer that  $\beta_{Free}^{-1}$  and  $p$  are uncorrelated, and we can consider this background estimation method validated. As discussed in Section 5.6, a possible small correlation is treated as a systematic uncertainty.

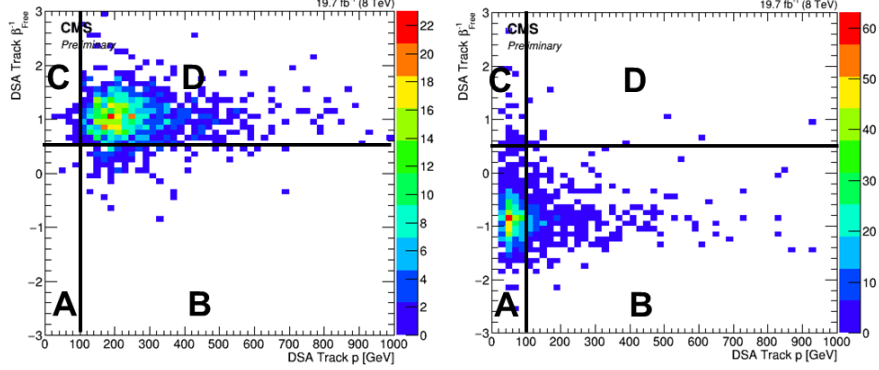


Figure 5.43: A scatter plot of the DSA track  $\beta_{Free}^{-1}$  as a function of  $p$  for 500 GeV mchamps (left) and cosmic muon data (right). The events must pass all of the selection criteria except the charge and RPC BX assignments cut (in order to have a sufficient number of events for the closure test). The A, B, C, and D regions are the different regions for the background estimation, defined here by the black lines at  $\beta_{Free}^{-1} = 0.5$  and  $p = 100$  GeV. The signal is concentrated in region D, while the background is concentrated in region A. The colors indicate the numbers of events in each bin.

Table 5.10: Number of events in each region in Figure 5.43 for cosmic muon data.

Region	Number of Events
A	$1009 \pm 31.8$
B	$464 \pm 21.5$
C	$27 \pm 5.2$
D	$9 \pm 3$

### 5.5.5 Background Estimation

The background is estimated using the collision data events that pass all the selection criteria shown in Table 5.8. Figure 5.44 shows a scatter plot of  $\beta_{Free}^{-1}$  as a function of  $p$  for 500 GeV mchamp events and for the full Run2012 collision data. The background estimate is different for the different mchamp mass points because the choice of the minimum  $p$  cut varies for the different mass points. The background estimate, that

is,  $BC/A$  from collision data events, is described in Section 5.7.

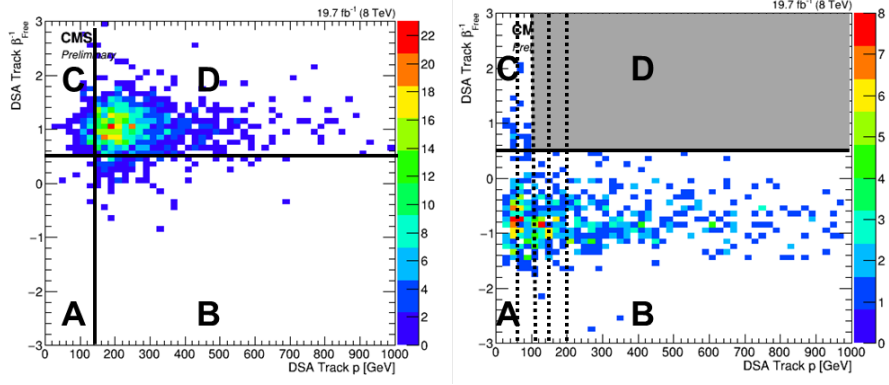


Figure 5.44: A scatter plot of the DSA track  $\beta_{Free}^{-1}$  as a function of  $p$  for 500 GeV mcham events (left) and for Run2012 collision data (right). The events must pass all of the selection criteria. The A, B, C, and D regions are the different regions for the background estimation, shown here by the black lines at  $\beta_{Free}^{-1} = 0.5$  and  $p = 60, 100, 150, \text{ and } 200$  GeV. The signal is concentrated in region D, while the background is concentrated in region A. Region D is blinded for the background estimation. The colors indicate the numbers of events in each bin.

### 5.5.6 Other Backgrounds

We looked in the final sample for evidence of other backgrounds, namely, beam halo, up-scattering cosmic muons, and noise.

Beam halo or up-scattering cosmic muons could be characterized by muons that are outgoing in the upper hemisphere. Since this would also characterize muons from the signal, beam halo or up-scattering cosmic muons might be identified if they also have a lower hemisphere muon that is incoming. However, we did not observe a significant number of these events in cosmic muon data (see Fig. 5.45), and in fact, events with incoming lower hemisphere muons are rejected by the selection criteria.

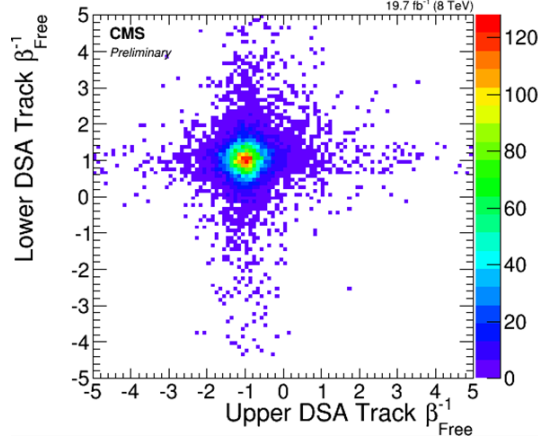


Figure 5.45: A scatter plot of the  $\beta_{Free}^{-1}$  distribution for the lower hemisphere muon as a function of that of the upper hemisphere muon for cosmic muon data. Events must pass the preselection, and there must be at least one DSA track in the upper hemisphere and at least one in the lower hemisphere. The highest  $p_T$  DSA track in the upper hemisphere and the highest  $p_T$  DSA track in the lower hemisphere are plotted. Up-scattering cosmic muons or beam halo would be characterized by a negative lower hemisphere  $\beta_{Free}^{-1}$  and a positive upper hemisphere  $\beta_{Free}^{-1}$ . The colors indicate the numbers of events in each bin.

Beam halo could also be characterized by a large number of CSC segments in the event, which are not necessarily associated with a DSA track. However, we did not find many events in cosmic muon data, from collisions or dedicated cosmic runs, with a large number of CSC segments (see Fig. 5.46). In fact, these distributions agree fairly well with that of signal, and so if we placed criteria to limit the number of CSC segments, we would reduce a significant fraction of the signal as well. Furthermore, we looked at cosmic muons, from both cosmic runs and collision data, that pass all of the selection criteria, including the final  $p$  and  $\beta_{Free}^{-1}$  cuts, and all of them had exactly 0 CSC segments.

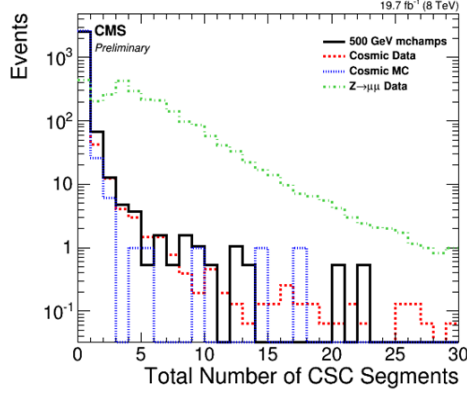


Figure 5.46: Number of CSC segments in the event for 500 GeV mchamps, cosmic muon data, cosmic muons from collision events passing the prescaled control trigger, and  $Z \rightarrow \mu\mu$  data. Events must pass the trigger and the preselection. The histograms are normalized to the same number of events.

Noise is rejected by requiring a large number of DT and RPC chambers and a large number of DT hits with good TOF measurements.

We conclude that there is no significant amount of other backgrounds in the final sample of events.

## 5.6 Systematic Uncertainties

The luminosity is estimated within 2.6% [244].

We considered the systematic uncertainty associated with the MC simulation modeling of the key variables,  $p_T$  and  $\beta_{Free}^{-1}$ . We compared these two distributions in cosmic muon data and cosmic muon MC simulation (see Fig. 5.47). We found no evidence of a systematic difference in the  $p_T$  distribution, but a small systematic shift in the  $\beta_{Free}^{-1}$  distribution. We fit the two peaks in  $\beta_{Free}^{-1}$  with gaussian distributions, and observed the differences in the fits between data and MC simulation in the signal region ( $\beta_{Free}^{-1} > 0$ ). Since the  $\sigma$  of the cosmic muon MC simulation fit in the signal region was smaller than that of the cosmic muon data, the cosmic muon data was already more conservative. Therefore, we only focused shifting the mean of the MC

simulation distribution. We shifted the  $\beta_{Free}^{-1}$  distribution in signal by subtracting 0.05 from each value of  $\beta_{Free}^{-1}$ , since 0.05 is the difference in the gaussian means of the cosmic muon MC simulation and cosmic muon data, and then recalculated the signal yields. The signal yields changed by 2%, and thus, we take 2% as the systematic uncertainty in the MC simulation modeling of  $\beta_{Free}^{-1}$ .

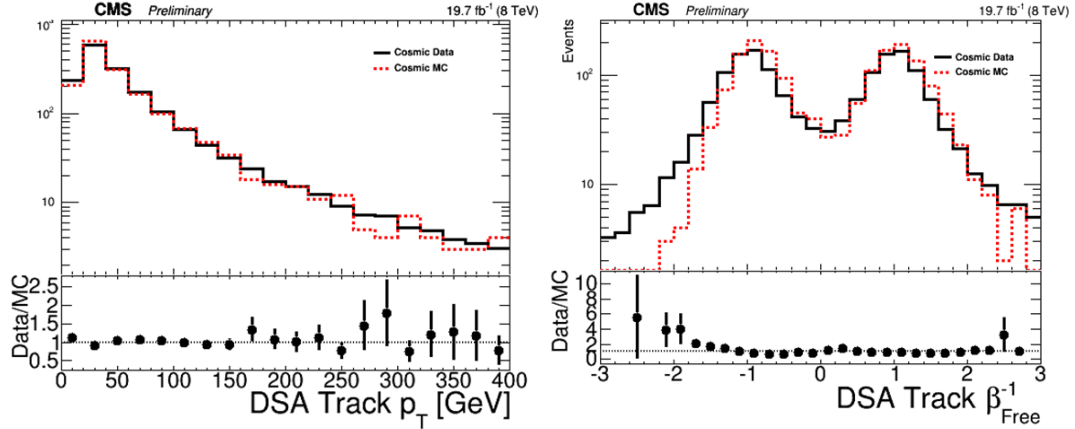


Figure 5.47: The DSA track  $p_T$  (left) and  $\beta_{Free}^{-1}$  (right) for cosmic muon data and cosmic muon MC simulation. Events must pass the preselection, and there must be at least one DSA track in the upper hemisphere and at least one in the lower hemisphere. The highest  $p_T$  DSA track in the upper hemisphere and the highest  $p_T$  DSA track in the lower hemisphere are plotted. The histograms are normalized to the same number of events.

There can also be a systematic uncertainty associated with the trigger acceptance. Figure 5.48 shows the trigger turn-on curve for data and cosmic muon MC simulation. The plateaus were each fitted with a horizontal line. The data was found to plateau at an efficiency of  $0.884 \pm 0.004$ , and the MC simulation was found to plateau at an efficiency of  $0.918 \pm 0.007$ . Since the plateau of the cosmic muon MC simulation is more ideal than that of the data by about 4%, we take 4% as the systematic uncertainty in the trigger acceptance.

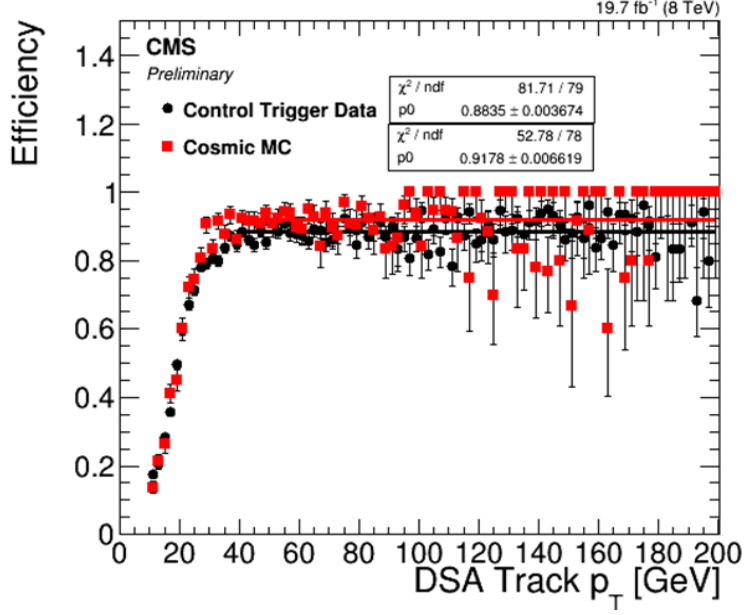


Figure 5.48: Turn-on curve for HLT\_L2Mu20\_NoVertex\_2Cha\_NoBPTX3BX\_NoHalo in Run2012C data passing the prescaled control trigger and in cosmic MC simulation. The cosmic MC simulation events were also required to pass the prescaled control trigger.

The systematic uncertainties described above are all applied to the signal MC simulation. In addition, there can be a systematic uncertainty in the background estimation, due to any possible correlation between  $\beta_{Free}^{-1}$  and  $p$  in the background sample. The systematic uncertainty in the ABCD method is evaluated by further dividing the A, B, and C control regions with stricter selection criteria on  $\beta_{Free}^{-1}$  and  $p$ . The sub-ABC regions are then used in calculating  $BC/A$ , and then these estimates of the background are compared with the nominal one in order to determine the systematic uncertainty. Several different sub-ABC regions were tried, and the choice giving the largest deviation from the nominal background prediction was when the A and C regions were divided with an additional cut in  $p$  at 60 GeV, giving left and right sub-A regions and left and right sub-C regions. The full B region, defined by  $\beta_{Free}^{-1} < 0.5$  and  $p > 110$  GeV, was used. The left sub-A region was defined by  $\beta_{Free}^{-1} < 0.5$  and  $p < 60$  GeV, while the right sub-A region was defined by  $\beta_{Free}^{-1} < 0.5$  and  $60 < p < 110$  GeV. The left sub-C region was defined by  $\beta_{Free}^{-1} > 0.5$  and

$p < 60$  GeV, and the right sub-C region was defined by  $\beta_{Free}^{-1} > 0.5$  and  $60 < p < 110$  GeV. These sub-regions gave a background prediction that deviated from the nominal prediction by an average of 20%, and so this value is used as the systematic uncertainty in the background prediction.

The systematic uncertainties are summarized in Table 5.11.

Table 5.11: Systematic uncertainties.

Systematic Uncertainty	Background	Signal
Luminosity	-	2.6%
$\beta_{Free}^{-1}$ Mis-modeling	-	2%
Trigger Acceptance	-	4%
Background Estimation	20%	-

## 5.7 Results

Using the ABCD method, we can compare the data observed in region D with the background predicted in region D. Figure 5.49 shows the  $p$  and  $\beta_{Free}^{-1}$  distributions for the Run2012 collision data in region D, the background predicted in region D, both of which have been optimized for the 500 GeV mchamp case, and the 500 GeV mchamp signal in region D. The background events predicted in region D in the  $p$  plot are the events in region B, normalized by  $C/A$ , while the background predicted in region D in the  $\beta_{Free}^{-1}$  plot consists of the events in region C, normalized by  $B/A$ . The 500 GeV mchamps are the signal events in region D, normalized to the predicted number of signal events. Figure 5.50 shows a scatter plot of these two variables, for data events that pass all of the selection criteria except except the final  $p$  and  $\beta_{Free}^{-1}$  selections in the ABCD method.



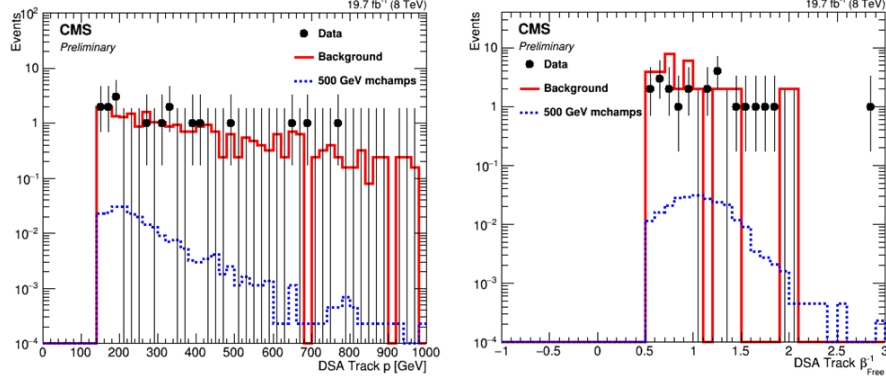


Figure 5.49:  $p$  and  $\beta_{Free}^{-1}$  distributions for the Run2012 collision data in region D, the background predicted in region D, both of which have been optimized for the 500 GeV mchamp case, and the 500 GeV mchamp signal in region D. The background events predicted in region D in the  $p$  plot are the events in region B, normalized by C/A, while the background predicted in region D in the  $\beta_{Free}^{-1}$  plot consists of the events in region C, normalized by B/A. The 500 GeV mchamps are the signal events in region D, normalized to the predicted number of signal events.

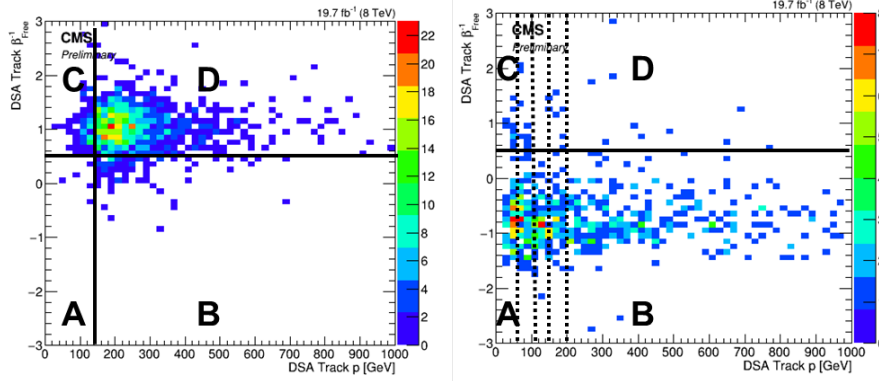


Figure 5.50: A scatter plot of the DSA track  $\beta_{Free}^{-1}$  as a function of  $p$  for 500 GeV mchamp events (left) and for Run2012 collision data (right). The events must pass all of the selection criteria. The A, B, C, and D regions are the different regions for the background estimation, shown here by the black lines at  $\beta_{Free}^{-1} = 0.5$  and  $p = 60, 100, 150,$  and  $200$  GeV. The signal is concentrated in region D, while the background is concentrated in region A. The colors indicate the numbers of events in each bin.

Table 5.12 shows the signal acceptance and the numbers of expected and observed events, for each mchamp mass. The  $p$  cut in the ABCD method is optimized for each mchamp mass (see Section 5.5.3), and so the numbers of expected background and observed events also vary with mchamp mass. These values represent the maximum

signal, background, and data that can be measured before considering the lifetime of the stopped particle.

Table 5.12: Signal acceptance, number of expected background events, and number of observed events for each mchamp mass. The  $p$  cut in the ABCD method is optimized for each mchamp mass, and so the numbers of expected background and observed events also vary with mchamp mass.

Mchamp Mass [GeV]	$p$ Cut for ABCD Method [GeV]	Signal Acceptance	Expected Background	Observed Events
100	60	0.0012	$76 \pm 24$ (stat.) $\pm 15$ (sys.)	30
200	60	0.0060	$76 \pm 24 \pm 15$	30
300	80	0.0060	$60 \pm 18 \pm 12$	26
400	110	0.0058	$54 \pm 13 \pm 11$	22
500	140	0.0054	$36 \pm 8 \pm 7$	22
600	150	0.0058	$34 \pm 8 \pm 7$	21
700	170	0.0055	$33 \pm 8 \pm 7$	19
800	170	0.0058	$33 \pm 8 \pm 7$	19
900	200	0.0058	$32 \pm 7 \pm 6$	15
1000	200	0.0058	$32 \pm 7 \pm 6$	15

Event displays for three of the 15 data events that have  $p > 200$  GeV and  $\beta_{Free}^{-1} > 0.5$  are in Figs. 5.51, 5.52, and 5.53.

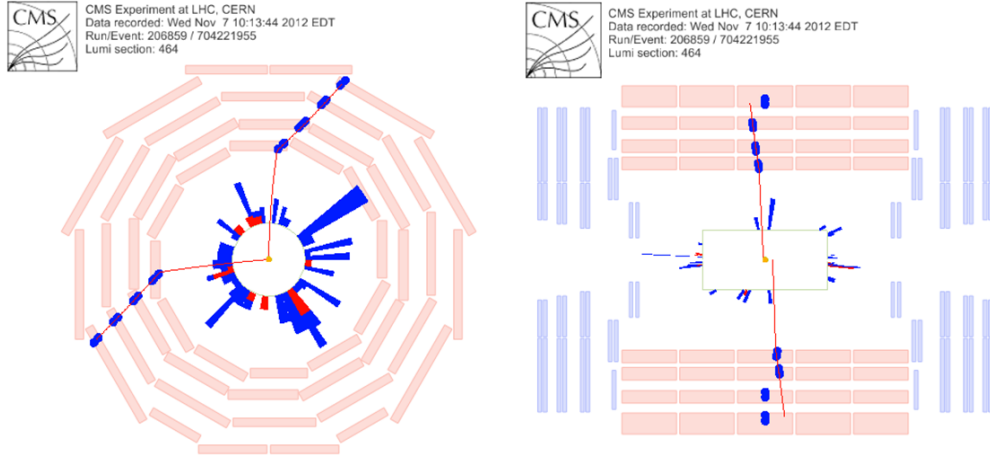


Figure 5.51: Event display of a data event (run 206859, event 704221955) passing all selection criteria, including  $p > 200$  GeV and  $\beta_{Free}^{-1} > 0.5$ . The  $\phi$  view is on the left and the  $\rho$ - $z$  view is on the right.

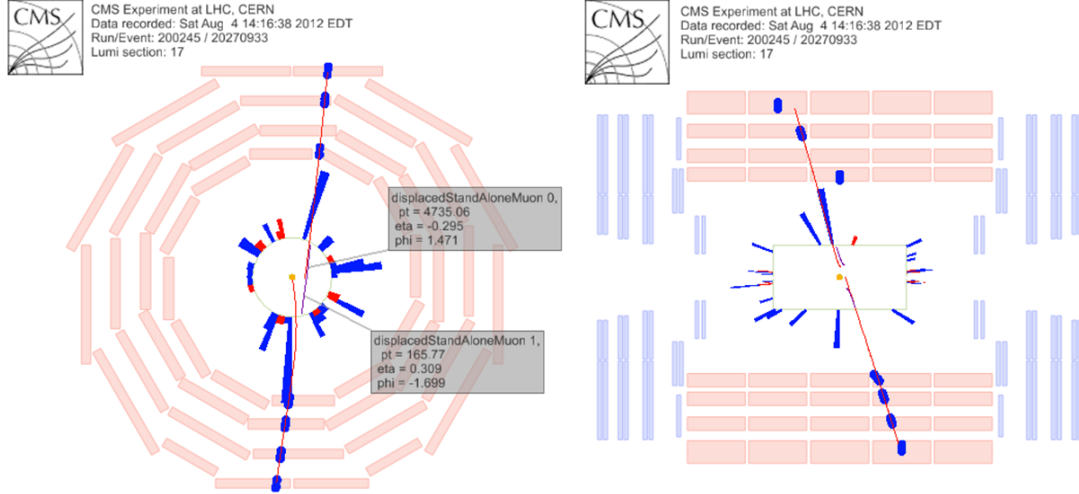


Figure 5.52: Event display of a data event (run 200245, event 20270933) passing all selection criteria, including  $p > 200$  GeV and  $\beta_{Free}^{-1} > 0.5$ . The  $\phi$  view is on the left and the  $\rho$ - $z$  view is on the right.

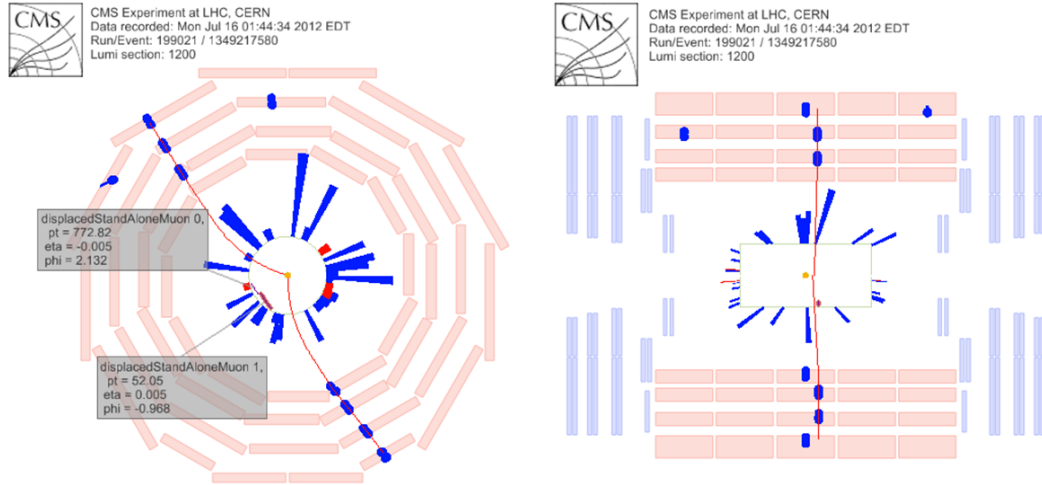


Figure 5.53: Event display of a data event (run 199021, event 1349217580) passing all selection criteria, including  $p > 200$  GeV and  $\beta_{Free}^{-1} > 0.5$ . The  $\phi$  view is on the left and the  $\rho$ - $z$  view is on the right.

We were sensitive to 293 hours ( $1.056 \times 10^6$  seconds) of trigger livetime during the 2012 run, as determined by the pseudo-experiment Stage 3 MC simulation, using the muon JSON file. The maximum effective luminosity is about  $4 \text{ fb}^{-1}$ , which is reasonable when considering the integrated luminosity of  $19.7 \text{ fb}^{-1}$  and the livetime

fraction of 0.23, which is the livetime fraction for the most common bunch spacing in 2012 (see the last row of Table 5.4).

We perform a counting experiment in bins of mchamp lifetime from 200 ns to  $10^7$ s. Table 5.13 shows the results of the counting experiment for different lifetimes, for 100, 500, and 1000 GeV mchamps. Recall from Section 5.2.3.2 that for lifetimes shorter than one LHC orbit of  $89\ \mu\text{s}$ , we search within a time-window of 1.3 times the lifetime, to avoid the addition of backgrounds for time intervals during which the signal will have already decayed to unobservable levels. Thus, for lifetimes smaller than 1 orbit, both the number of observed events and the expected background depend on the time-window considered, which is a fraction of the total trigger livetime. Similarly, the effective luminosity is smaller than  $4\ \text{fb}^{-1}$  for short lifetimes. However, for lifetimes bigger than a single orbit, the trigger livetime, the expected background, and the number of observed events are independent of the lifetime. The effective luminosity decreases with lifetime after the lifetimes are longer than 1 LHC fill.

The data shows no excess over background, and so we set upper limits on the signal production cross section using a hybrid  $\text{CL}_\text{S}$  method [245, 246] to incorporate the systematic uncertainties [247]. The 95% CL limits on the cross section as a function of lifetime for the 100, 500, and 1000 GeV mchamp cases are shown in Fig. 5.54. The detection sensitivity and the cross section limit are degraded for very small lifetimes, since any muons detected within two bunch crossings are vetoed. The limit curve is then flat for lifetimes greater than one orbit, since the numbers of observed and background events are constant. Finally, the sensitivity and effective luminosity are degraded for lifetimes larger than an LHC fill.

Table 5.13: Counting experiment results for different lifetimes, for 100, 500, and 1000 GeV mchamps.

Lifetime [s]	$L_{eff}$ [ $\text{fb}^{-1}$ ]	Livetime [s]	Expected Background (100 GeV mchamps)	Observed Events (100 GeV mchamps)	Expected Background (500 GeV mchamps)	Observed Events (500 GeV mchamps)	Expected Background (1000 GeV mchamps)	Observed Events (1000 GeV mchamps)
$10^{-7}$	0.536	$2.089 \times 10^5$	$15 \pm 3$ (stat.) $\pm 3$ (sys.)	4	$7 \pm 2$ (stat.) $\pm 1$ (sys.)	3	$6 \pm 1$ (stat.) $\pm 1$ (sys.)	1
$10^{-6}$	2.993	$8.758 \times 10^5$	$63 \pm 13 \pm 13$	22	$30 \pm 6 \pm 6$	17	$27 \pm 5 \pm 5$	11
$10^{-5}$	4.060	$1.037 \times 10^6$	$74 \pm 15 \pm 15$	30	$35 \pm 7 \pm 7$	22	$32 \pm 6 \pm 6$	15
$10^{-4}$	4.152	$1.056 \times 10^6$	$76 \pm 24 \pm 15$	30	$36 \pm 8 \pm 7$	22	$32 \pm 7 \pm 6$	15
1	4.152	$1.056 \times 10^6$	$76 \pm 24 \pm 15$	30	$36 \pm 8 \pm 7$	22	$32 \pm 7 \pm 6$	15
$10^3$	4.026	$1.056 \times 10^6$	$76 \pm 24 \pm 15$	30	$36 \pm 8 \pm 7$	22	$32 \pm 7 \pm 6$	15
$10^4$	3.114	$1.056 \times 10^6$	$76 \pm 24 \pm 15$	30	$36 \pm 8 \pm 7$	22	$32 \pm 7 \pm 6$	15
$10^5$	1.797	$1.056 \times 10^6$	$76 \pm 24 \pm 15$	30	$36 \pm 8 \pm 7$	22	$32 \pm 7 \pm 6$	15
$10^6$	1.234	$1.056 \times 10^6$	$76 \pm 24 \pm 15$	30	$36 \pm 8 \pm 7$	22	$32 \pm 7 \pm 6$	15

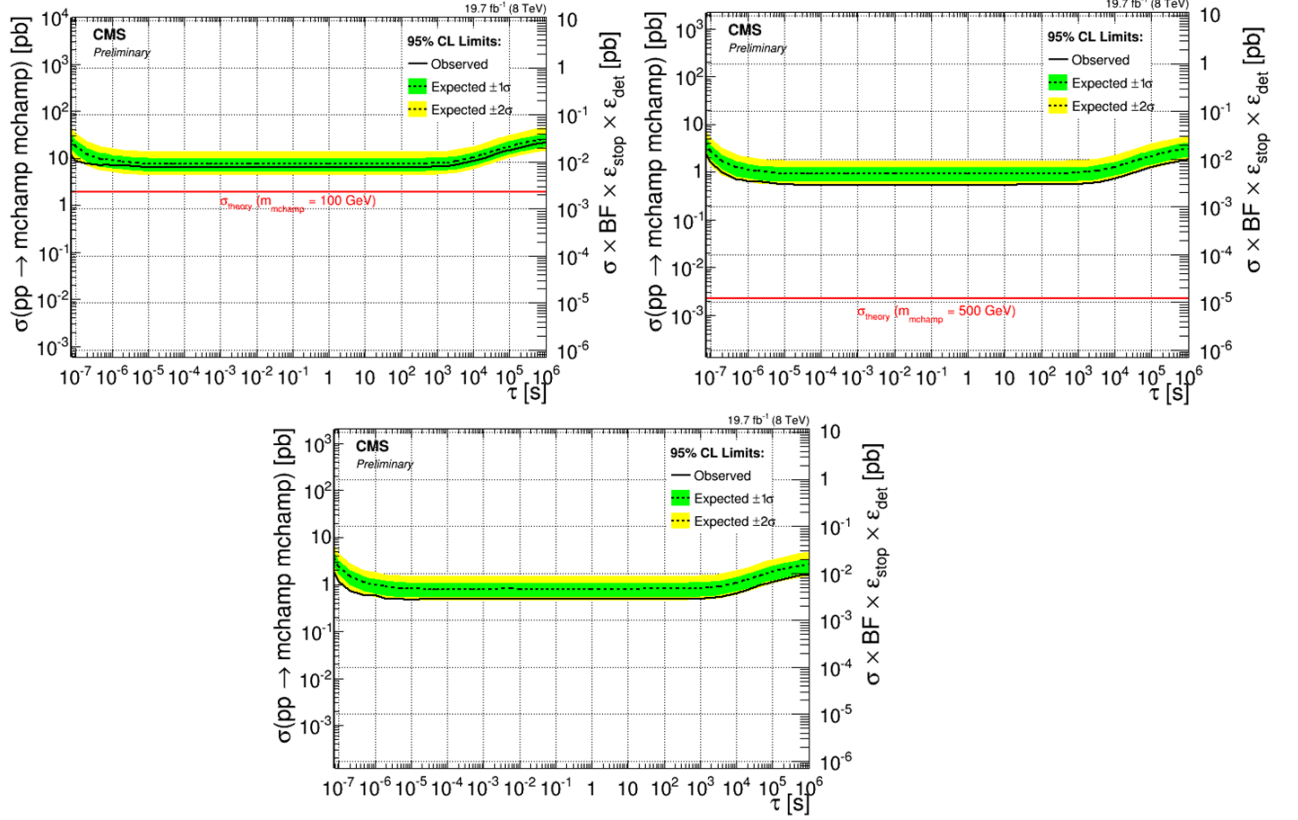


Figure 5.54: 95% CL cross section limits as a function of lifetime, for 100 (top left), 500 (top right), and 1000 (bottom) GeV mchamps. The observed limits are shown in the solid black line, the expected limits are shown in the dotted black line, the expected  $1\sigma$  and  $2\sigma$  bands are shown in green and yellow, respectively, and the theoretical cross sections are shown in the red line. The theoretical cross section for 1000 GeV mchamps is below the range of the plot.

The 95% CL limits on the cross section as a function of mchamp mass, for a lifetime of 1 sec, are shown in Table 5.14 and Fig. 5.55. These are the first limits for stopped particles that decay to muons, and they are also the first limits on lepton-like multiply charged particles that stop in the detector. Furthermore, this is the first time  $\beta_{Free}^{-1}$  is being used in a CMS physics analysis, and it is the first time a muon trigger that vetoes on the bunch crossing has been used.

Table 5.14: LO cross sections and cross section limits for mchamps with a lifetime of 1 sec.

Mass [GeV]	LO Cross-Section [pb]	95% CL Limit [pb]	Expected Limit $\pm 1\sigma$ [pb]
100	1.880	6.36	$7.58^{+2.44}_{-2.35}$
200	0.1402	1.27	$1.52^{+0.49}_{-0.47}$
300	0.02622	1.01	$1.25^{+0.41}_{-0.40}$
400	0.006968	0.930	$1.18^{+0.39}_{-0.38}$
500	0.002257	0.536	$0.925^{+0.312}_{-0.302}$
600	0.0008183	0.483	$0.834^{+0.282}_{-0.286}$
700	0.0003228	0.482	$0.851^{+0.289}_{-0.287}$
800	0.0001333	0.457	$0.807^{+0.274}_{-0.272}$
900	0.00005764	0.484	$0.805^{+0.274}_{-0.271}$
1000	0.00002540	0.484	$0.805^{+0.274}_{-0.271}$

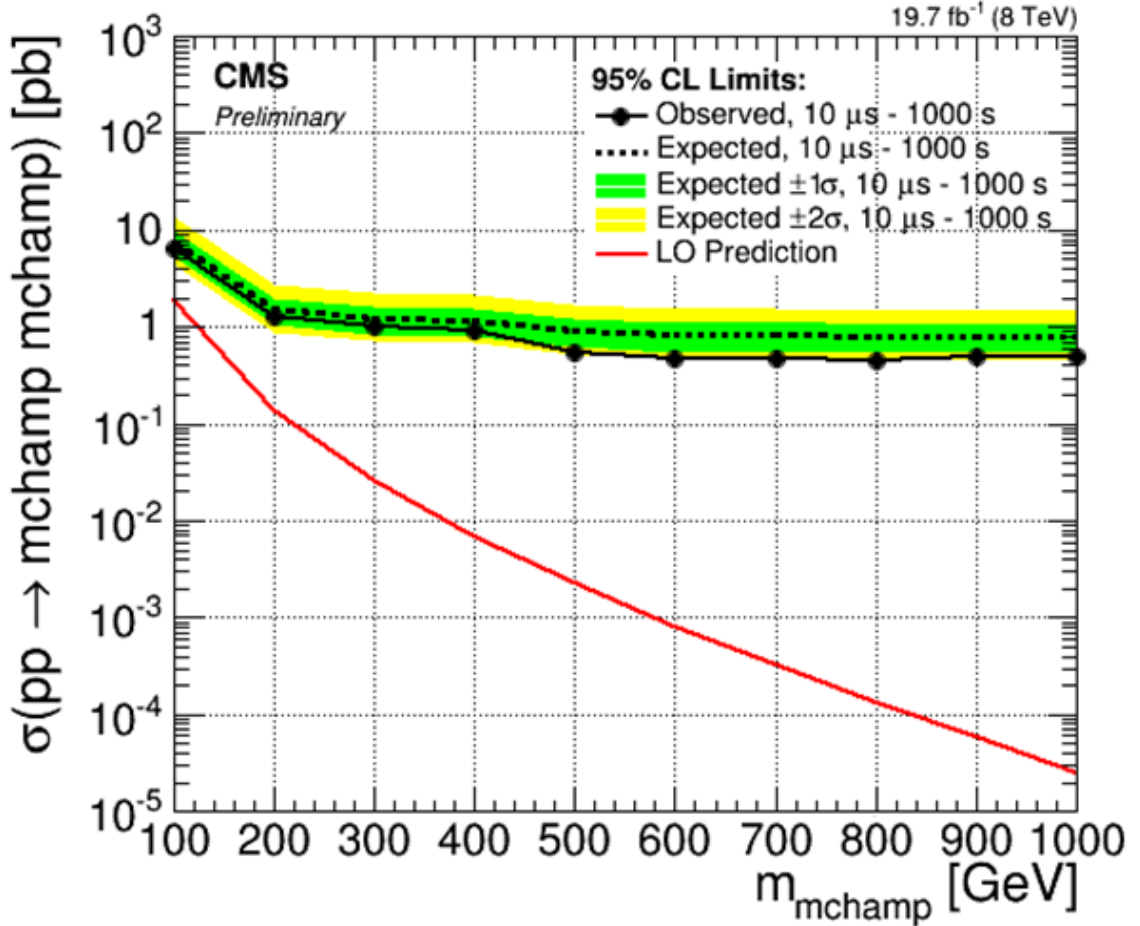


Figure 5.55: 95% CL cross section limits as a function of mchamp mass, for a lifetime of 1 sec. The observed limits are shown in the solid black points, the expected limits are shown in the dotted black line, the expected  $1\sigma$  and  $2\sigma$  bands are shown in green and yellow, respectively, and the theoretical cross sections are shown in the red line.

## 5.8 Results with at Least One Upper Hemisphere DSA Track

There are several ways in which we can modify the analysis, in order to present results that cover different model scenarios. For example, the analysis described above requires at least one upper hemisphere DSA track and at least one lower hemisphere DSA track. This choice is appropriate because the model we consider contains an mchamp that decays to two back-to-back muons, and it provides the strongest result because much more of the cosmic muon background can be rejected if two good muons are required instead of just one. However, we can also present the results if we require at least one upper hemisphere DSA track and make no requirements on any lower hemisphere DSA tracks in the event. As a minimum, an upper hemisphere DSA track is needed in order to distinguish the outgoing muons from the signal and the incoming muons from the cosmic muon background. This scenario gives higher expected cross section limits as a function of mchamp mass than the main analysis, because the background of the one upper hemisphere DSA track scenario is significantly larger than that of the main analysis, while the signal acceptance is only marginally larger. Results with this selection are important because they expand the scope of the search to models in which the decay of the stopped particle results in only one muon plus, for example, a neutrino or two (see Section 5.2.3.2 for specific examples).

For the one upper hemisphere DSA track selection, we use the same preselection criteria as described in Section 5.4.2 but modify the rest of the selection criteria. For the final selection, we require an upper hemisphere DSA track with:

- $p_T > 30$  GeV
- $> 2$  DT chambers with valid hits
- $> 2$  RPC hits



- RPC BX assignments that are all 0 or all positive and constant
- TimeInOut  $> -10.0$  ns
- Error in TimeInOut  $< 2.0$  ns

Then the same criteria on the  $p_T$  and  $\beta_{Free}^{-1}$  of the upper hemisphere muon are applied in the ABCD method. This is the same criteria as was applied for the main analysis, except it is now only applied to the upper hemisphere DSA track, and any requirements for both DSA tracks or the lower hemisphere DSA track are dropped.

The acceptance tables for the one upper hemisphere DSA track selection for data, cosmic muon all-phi data, and signal MC simulation are shown in Tables 5.15 and 5.16. The preselection is the same as in Tables 5.8 and 5.9.

Table 5.15: Cumulative selection cut efficiencies for the one upper hemisphere DSA track selection, for collision data and cosmic muon data events. Note that in the last row, a cut of  $p > 60$  GeV on the upper hemisphere DSA track is shown, but this cut varies for each mchamp mass considered.

Selection Criteria	Run 2012B,C, D Collision Data		Cosmic Muon Data	
	Number of Events	Fraction of Events	Number of Events	Fraction of Events
At least 1 upper DSA track	2468358	0.11	23518	0.052
with:				
$p_T > 30$ GeV	1635496	0.073	15415	0.034
$> 2$ DT chambers with valid hits	1191727	0.053	11845	0.026
$> 2$ valid RPC hits	1161856	0.052	11549	0.026
RPC BXs==0 or BXs>0 and constant	264458	0.012	2885	0.0064
TimeInOut $> -10.0$ ns	252296	0.011	2416	0.0054
TimeInOut Error $< 2.0$ ns	169892	0.0076	1641	0.0036
(Events in regions A,B,C, and D)				
$\beta_{Free}^{-1} > 0.5$ (Events in regions C and D)	5274	0.00024	37	0.000082
$p > 60$ GeV (Events in region D)	2619	0.00012	18	0.000040

Table 5.16: Cumulative selection cut efficiencies (fraction of events) for the one upper hemisphere DSA track selection, for 100 GeV, 500 GeV, and 1000 GeV mchamps. Note that in the last row, the  $p_T$  cut on the upper hemisphere DSA track varies for each mchamp mass considered.

Selection Criteria	100 GeV mchamp	500 GeV mchamp	1000 GeV mchamp
At least 1 upper DSA track with:	0.019	0.020	0.025
$p_T > 30$ GeV	0.018	0.019	0.024
> 2 DT chambers with valid hits	0.016	0.016	0.019
> 2 valid RPC hits	0.015	0.015	0.019
RPC BXs==0 or BXs>0 and constant	0.014	0.015	0.018
TimeInOut > -10.0 ns	0.014	0.014	0.017
TimeInOut Error < 2.0 ns (Events in regions A,B,C, and D)	0.013	0.014	0.016
$\beta_{Free}^{-1} > 0.5$ (Events in regions C and D)	0.012	0.013	0.015
$p > 60$ GeV, 110 GeV, 200 GeV, respectively (Events in region D)	0.0023	0.012	0.014

As before, the ABCD method is used to predict the background. The same selection on the  $p_T$  and  $\beta_{Free}^{-1}$  as in the main analysis are applied. Figure 5.56 shows the  $p$  and  $\beta_{Free}^{-1}$  distributions for the one upper hemisphere DSA track selection, for data, which are the events passing all of the selection criteria, including the final  $p$  and  $\beta_{Free}^{-1}$  selections for the 500 GeV mchamp case, for background, which is the events in the A, B, and C control regions, normalized to the background prediction for the 500 GeV mchamp case, and for 500 GeV mchamps, which are normalized to the predicted number of signal events. Figure 5.57 shows a scatter plot of these two variables for the one upper hemisphere DSA track selection, for data events that pass all of the selection criteria except except the final  $p$  and  $\beta_{Free}^{-1}$  selections in the ABCD method.

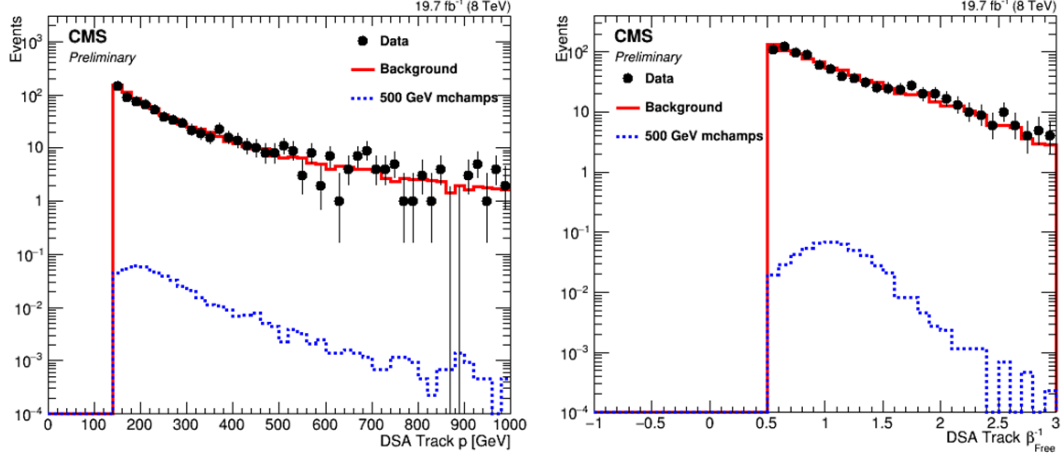


Figure 5.56:  $p$  and  $\beta_{Free}^{-1}$  distributions for the one upper hemisphere DSA track selection, for Run2012 collision data, which are the events passing all of the selection criteria, including the final  $p$  and  $\beta_{Free}^{-1}$  selections for the 500 GeV mchamp case, for background, which is the events in the A, B, and C control regions, normalized to the background prediction for the 500 GeV mchamp case, and for 500 GeV mchamps, which are normalized to the predicted number of signal events.

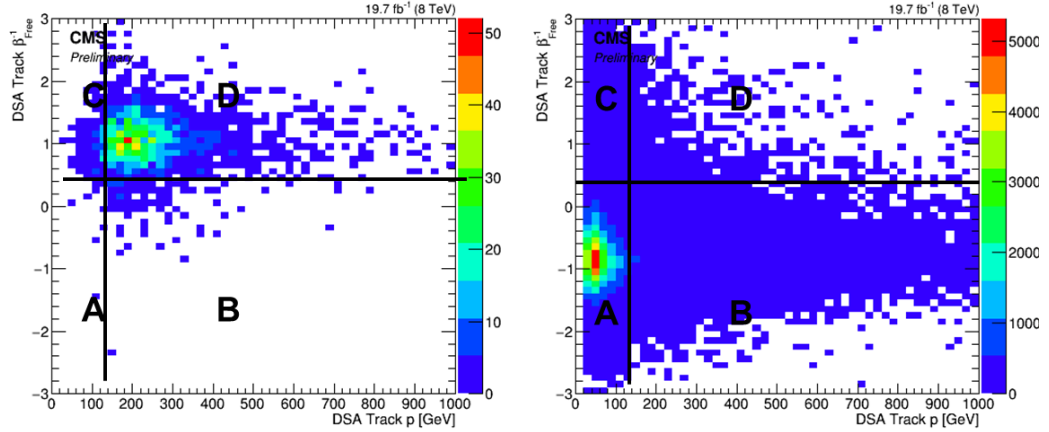


Figure 5.57: A scatter plot of the DSA track  $\beta_{Free}^{-1}$  as a function of  $p$  for the one upper hemisphere DSA track selection, for 500 GeV mchamp events (left) and for Run2012 collision data (right). The A, B, C, and D regions define the different regions for the background estimation. The signal is concentrated in region D, while the background is concentrated in region A. The colors indicate the numbers of events in each bin.

Table 5.17 shows the signal acceptance and the numbers of expected and observed events for the one upper hemisphere DSA track selection, for each mchamp mass. The  $p$  selections in the ABCD method are the same as in the main analysis. These values

represent the maximum signal, background, and data that can be measured before considering the lifetime of the stopped particle.

Table 5.17: Signal acceptance, number of expected background events, and number of observed events for the one upper hemisphere DSA track selection, for each mchamp mass. The  $p$  selections in the ABCD method are the same as in the main analysis.

Mchamp Mass [GeV]	$p$ Cut for ABCD Method [GeV]	Signal Acceptance	Expected Background	Observed Events
100	60	0.0023	$2810 \pm 57$	2620
200	60	0.012	$2810 \pm 57$	2620
300	80	0.012	$1930 \pm 34$	1810
400	110	0.012	$1240 \pm 21$	1200
500	140	0.012	$877 \pm 14$	822
600	150	0.012	$794 \pm 13$	813
700	170	0.012	$648 \pm 11$	695
800	170	0.013	$648 \pm 11$	695
900	200	0.014	$526 \pm 9$	571
1000	200	0.014	$526 \pm 9$	571

Again, no excess of data is observed. We set  $CL_S$  cross section limits at 95% CL, and the same systematic uncertainties as in Table 5.11 are used. The 95% CL limits on the cross section as a function of mchamp mass for a lifetime of 1 sec, for the one upper hemisphere DSA track selection, are shown in Table 5.18 and Fig. 5.58. If this table and figure are compared with Table 5.14 and Fig. 5.55, one can see that the one upper hemisphere DSA track selection gives cross section limits that are about an order of magnitude higher than the main result.

Table 5.18: LO cross-sections and cross-section limits for the one upper hemisphere DSA track selection, for mchamps with a lifetime of 1 sec.

Mass [GeV]	LO Cross-Section [pb]	95% CL Limit [pb]	Expected Limit $\pm 1\sigma$ [pb]
100	1.880	110	$123^{+31}_{-29}$
200	0.1402	21.7	$24.3^{+6.1}_{-5.8}$
300	0.02622	14.7	$16.6^{+4.6}_{-4.1}$
400	0.006968	10.1	$11.1^{+3.2}_{-2.8}$
500	0.002257	7.53	$7.90^{+2.28}_{-2.08}$
600	0.0008183	6.50	$6.65^{+1.92}_{-1.76}$
700	0.0003228	5.84	$5.54^{+1.60}_{-1.48}$
800	0.0001333	5.32	$5.05^{+1.46}_{-1.35}$
900	0.00005764	4.36	$4.06^{+1.18}_{-1.10}$
1000	0.00002540	4.26	$3.97^{+1.16}_{-1.07}$

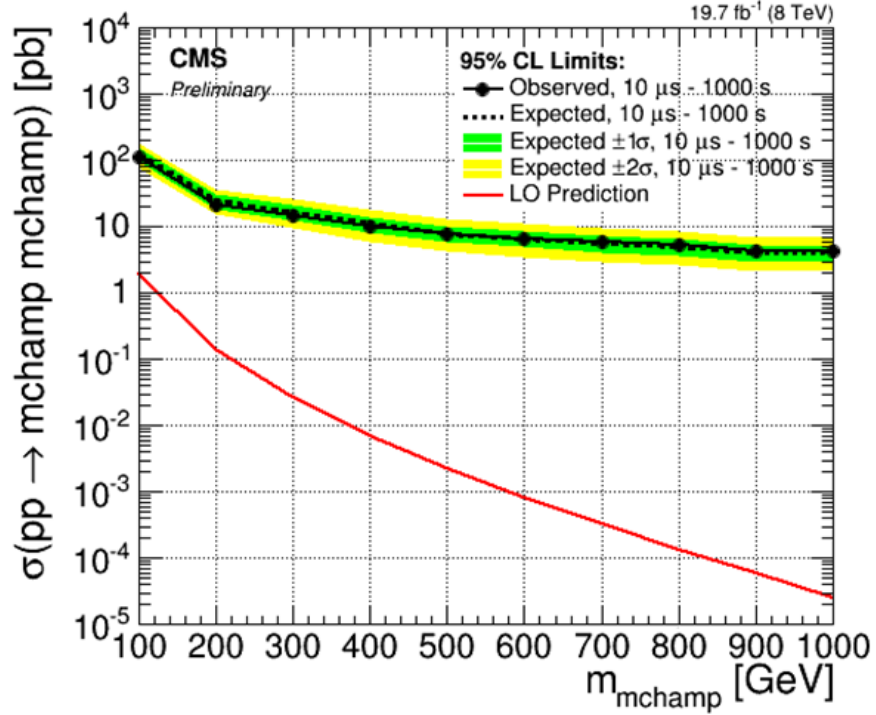


Figure 5.58: 95% CL cross section limits as a function of mchamp mass for a lifetime of 1 sec, for the one upper hemisphere DSA track selection. The observed limits are shown in the solid black points, the expected limits are shown in the dotted black line, the expected  $1\sigma$  and  $2\sigma$  bands are shown in green and yellow, respectively, and the theoretical cross sections are shown in the red line.

## 5.9 Preparation for 13 TeV

The LHC has begun operating at  $\sqrt{s} = 13$  TeV in 2015, and it will eventually operate at the design C.M. energy of 14 TeV. This search could be repeated with data from the higher energy regime, which would increase the search sensitivity and discovery potential. As preparation for the 13 TeV run in 2015, several aspects of the analysis were investigated.

The most crucial matter for any analysis to prepare early is the trigger associated with the physics of interest. As discussed in Section 5.2, our NoBPTX trigger depends strongly on the number of colliding bunches, and not on beam parameters. Indeed, the largest background contribution is from cosmic muons, which should have a constant rate. As discussed earlier, we expect about the same trigger livetime at 25 ns spacing and 2800 colliding bunches as we had with 50 ns spacing and 1380 colliding bunches. Thus, we can expect the trigger to have about the same rate in 2015 as it had in 2012. Our design for the 2015 trigger was similar to the 2012 trigger, but with several very important changes. This trigger has already taken data in 2015.

Despite the fact that the bandwidth available for this trigger is the same in the 2012 and 2015 runs, we were able to improve the trigger significantly. Figure 5.59 shows the acceptance of different cuts applied at the HLT, for data and a 500 GeV mchamp signal at 8 TeV, relative to the 2012 control trigger (first bin, with a L2 muon  $p_T$  of 10 GeV). Each subsequent bin shows possible selection criteria that could be made at the HLT. The bin labeled “original\_pt20,Cha2” is the configuration of the signal trigger in 2012: the L2 muon  $p_T$  threshold was 20 GeV and at least 2 DT or CSC chambers with any hits were required. As can be seen in the figure, the trigger rate in data can be decreased while the signal acceptance can be increased, relative to the 2012 signal trigger, if we instead require at least 3 stations with any hits (the bin labeled “pt20,St3”). Thus, a signal trigger with a L2 muon  $p_T$  threshold of 20 GeV and at least 3 stations was the initial 2015 proposal. The relative signal acceptance

goes from 0.65 to 0.7, while the relative rate goes from 0.85 to 0.57, comparing the 2012 signal trigger with the initial 2015 signal trigger proposal.

After this initial proposal was accepted, the DSA muon track collection was finalized for offline, and then we began to bring these offline improvements to the HLT. While the mean timer and the cosmic muon seeding would, in principle, be beneficial to several long-lived analyses using displaced muons, we did not observe any improvement at the trigger level for those custom triggers, except in the muon NoBPTX triggers for this search. As a result, the mean timer and cosmic muon seeding were introduced at the HLT only for the muon NoBPTX paths, at this time.

The effect of the mean timer and the cosmic muon seeding in L2 muons passing the muon NoBPTX signal trigger was checked for the mchamp signal (see Fig. 5.60). As with the offline improvement, the improvement in the L2 muon  $p_T$  distribution is substantial.

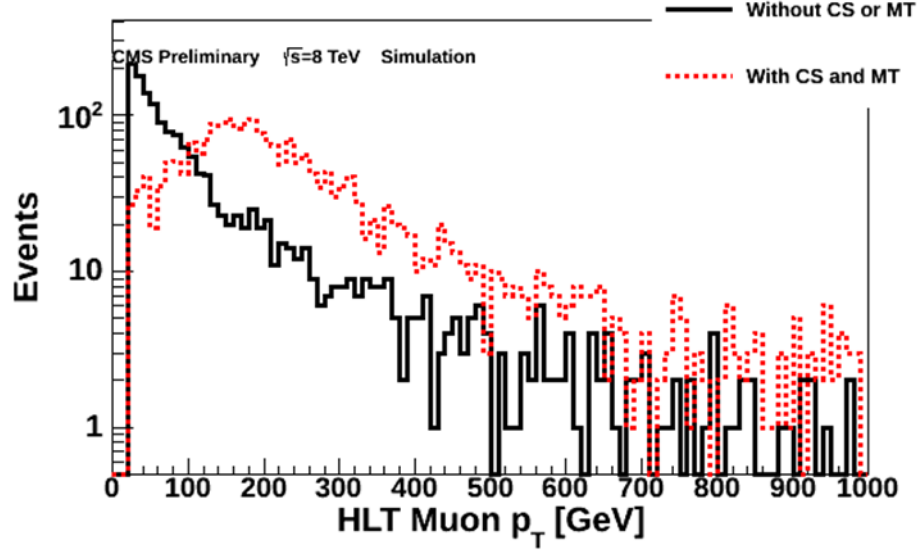


Figure 5.60: The L2 muon  $p_T$  distribution in 72X for mchamps with a mass of 500 GeV. The black histogram shows the default L2 muon  $p_T$  distribution, and the red histogram shows the L2 muon  $p_T$  distribution with the meantimer and the cosmic muon seeding. The histograms are normalized to the same number of events.

The mean timer and cosmic muon seeding improve the bias in the L2 muon  $p_T$

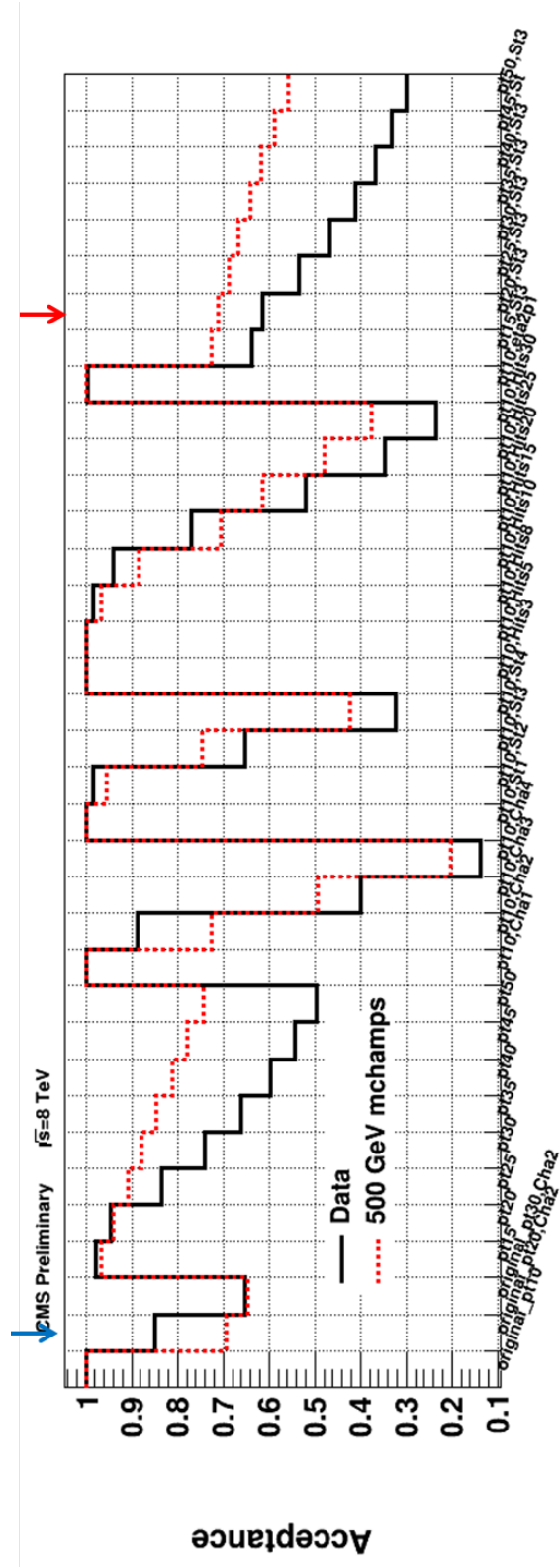


Figure 5.59: Acceptance of different cuts applied at the HLT, for data and a 500 GeV mchamp signal at 8 TeV, relative to the control trigger. The bin labeled “original\_pt20,Cha2” and pointed out with a blue arrow corresponds to the settings for the 2012 signal trigger. The bin labeled “pt20\_St3” and pointed with a red arrow corresponds to the settings for the 2015 signal trigger proposal.



from the Delayed Muons signal, but what about at L1? Unfortunately, a bias in the L1 muon  $p_T$  was also observed, which reflects the known L1 muon bias toward the beam spot (see Fig. 5.61). However, the L1 muon  $p_T$  bias can be circumvented by reducing the L1 muon  $p_T$  cut to 0 GeV. This is possible because the rate from L1\_SingleMuOpen\_NotBptxOR is only expected to be about 100 Hz. The cosmic muon rate in CMS is no more than about 400 Hz; L1\_SingleMuOpen was only 400 Hz in cosmic runs in 2012. The L1 muon quality assignment is kept loose, that is, the same L1 muon quality of L1\_SingleMuOpen, as tighter quality cuts at L1 would only bias the muon more toward the beam spot. The effect of using a 0 GeV  $p_T$  L1 muon seed and the meantimer and the cosmic muon seeding at the HLT is shown in Fig. 5.62.

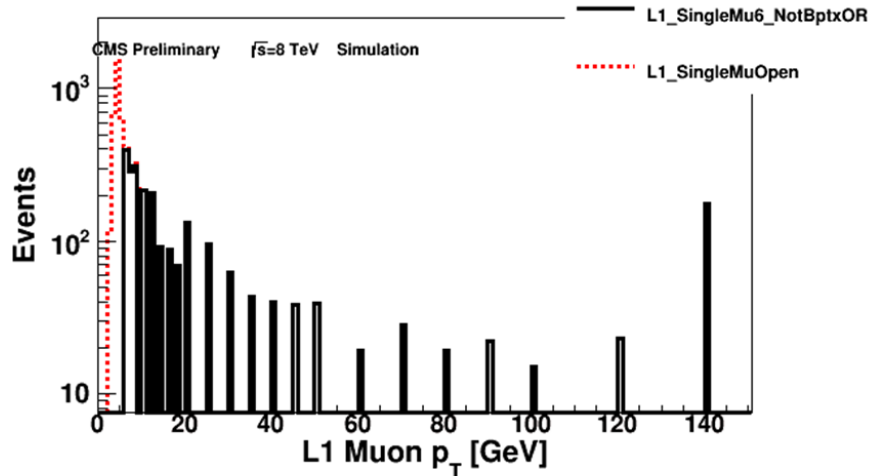


Figure 5.61: The L1 muon  $p_T$  distribution in 72X for mchamps with a mass of 500 GeV. The black histogram shows the events that pass L1\_SingleMu6\_NotBptxOR, and the red histogram shows the events that pass L1\_SingleMuOpen. Most of the signal is biased towards low  $p_T$  bins by the poor L1 reconstruction of displaced muons. The last bin at  $p_T = 140$  GeV includes all muons with  $p_T$  greater than 140 GeV. The histograms are normalized to the same number of events.

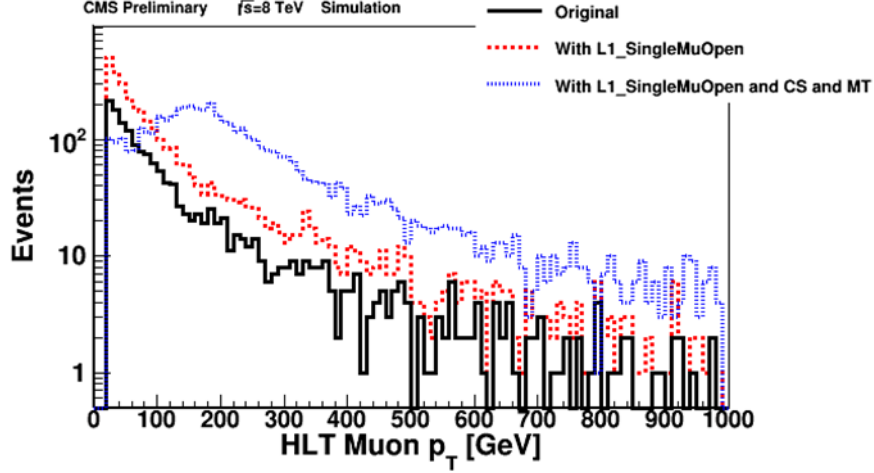


Figure 5.62: The L2 muon  $p_T$  distribution in 72X for mchamps with a mass of 500 GeV. The black histogram shows the default L2 muon  $p_T$  distribution, the red histogram shows the L2 muon  $p_T$  distribution with L1\_SingleMuOpen as the L1 seed, and the blue histogram shows the L2 muon  $p_T$  distribution with the meantimer and the cosmic muon seeding and L1\_SingleMuOpen as the L1 seed. The histograms are normalized to the same number of events.

In addition to bringing the HLT  $p_T$  distribution closer to the generator muon one, these changes also increase the signal acceptance at the HLT. Table 5.19 shows the relative improvement for each change at L1 and the HLT. The combination of all of the changes results in three times the original signal acceptance.

Table 5.19: Relative improvement for each change at L1 and HLT. The combination of all of the changes results in three times the original signal acceptance.

Configuration	Number of events passed HLT	Ratio (with improvement/ original)
Original	1623	-
With meantimer	1699	1.05
With cosmic muon seeding	2270	1.40
With meantimer and cosmic muon seeding	2342	1.44
With L1_SingleMuOpen as the L1 seed	3404	2.10
With meantimer, cosmic muon seeding, and L1_SingleMuOpen as the L1 seed	5227	3.22

The mean timer and the cosmic muon seeding at L2 increase the HLT rate,

and L1\_SingleMuOpen\_NotBptxOR increases the L1 rate. Since the L2 muon  $p_T$  measurement could now be trusted more, we increase the L2 muon  $p_T$  cut in order to keep the HLT rate low. The full and final 2015 proposal, including signal, backup, and control triggers, is shown in Table 5.20. All paths are seeded by L1\_SingleMuOpen\_NotBptxOR, expected to run at 100 Hz in 2015. This proposal was accepted into the 2015 trigger menu. The first HLT menu with these changes was /dev/CMSSW\_7\_3\_0/HLT/V102. See Ref. [248] for more information.

Table 5.20: Delayed muon triggers for 2015. All paths are seeded by L1\_SingleMuOpen\_NotBptxOR.

HLT Path	Expected Rate [Hz]	Type
HLT_L2Mu10_NoVertex_NoBPTX	0.2 (prescaled)	Control
HLT_L2Mu10_NoVertex_NoBPTX3BX_NoHalo	0.2 (prescaled)	Control
HLT_L2Mu35_NoVertex_3Sta_NoBPTX3BX_NoHalo	5	Signal
HLT_L2Mu40_NoVertex_3Sta_NoBPTX3BX_NoHalo	3.5	Backup

Figure 5.63 compares the signal 2012 HLT path rate with the rate of the 2015 HLT path, as a function of the number of colliding bunches.

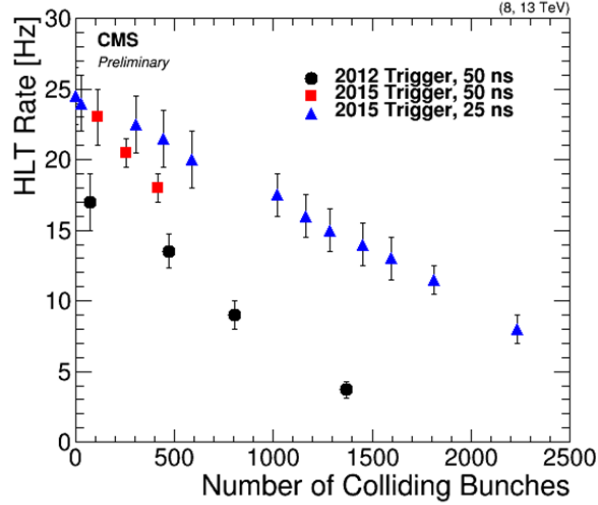


Figure 5.63: The rate of the signal HLT path in 2012 and 2015, as a function of the number of colliding bunches. The trigger rate during the two years is significantly different because the trigger changed significantly during this time, at L1 and at the HLT. There is little difference in the rate due to the change from 50 to 25 ns in bunch spacing because the trigger livetime does not change drastically between these two spacings (see the discussion in Section 5.2.2.1).

In addition to the trigger, other preparations are underway for 2015. The Stage 1 signal MC simulation at 13 TeV is being produced centrally in PYTHIA6 and PYTHIA8, in a similar fashion as to what was done for 8 TeV. The Stage 2 will be produced privately again in 2015.

The event content of AOD was also extended to include the DT and CSC segments, the RPC hits, and other variables necessary for the HSCP search. This will make it easier to perform the analysis with 2015 data, as the full RECO will not be available for analysis.

# Chapter 6

## SUMMARY

A search for delayed muons produced in pp collisions at  $\sqrt{s} = 8$  TeV was performed at CMS with  $19.7 \text{ fb}^{-1}$  of data. This search looked for LLPs that stopped in the CMS detector and subsequently decayed to muons. These stopped particles were looked for when there were no collisions in the detector, namely, during gaps between LHC beam crossings.

No evidence of signal was found and 95% CL cross section upper limits were set between 6.4 and 0.46 pb for mchamps of mass between 100 and 1000 GeV, assuming a lifetime of 1 sec. Cross section limits were also set for each mchamp mass as a function of lifetime, for lifetimes between 100 ns and 10 days. This main result requires at least one upper hemisphere and at least one lower hemisphere muon in each event. If instead only one upper hemisphere muon was required, the cross section limits are degraded by about an order of magnitude. These are the first limits for stopped particles that decay to muons, and they are also the first limits for lepton-like multiply charged particles that stop in the detector. Furthermore, this is the first time  $\beta_{Free}^{-1}$  was used in a CMS physics analysis, and it is the first time a muon trigger that vetoes on the bunch crossing was used.

# Appendix A

## A SEARCH FOR CHARGED MASSIVE LONG-LIVED PARTICLES AT D0

Another search for long-lived exotic particles, besides the principle search described in this thesis, was performed at the D0 Experiment, which was at the Fermilab Tevatron Collider outside Chicago, Illinois. This analysis at D0 searched for charged massive long-lived particles (CMLLPs), which are high  $p_T$  particles predicted by theories beyond the SM. CMLLPs resemble slow, massive, long-lived muons in the detector, and they penetrate the entire detector before decaying. CMLLPs can be distinguished from SM muons with time-of-flight (TOF) and ionization energy loss ( $dE/dx$ ) measurements. While the main CMS analysis in this thesis searched for long-lived particles that *decay* to muons, the D0 analysis described here searched for long-lived particles that actually *appear* as muons, but with TOF and  $dE/dx$  measurements inconsistent with SM muons.

This search for CMLLPs used  $5.2 \text{ fb}^{-1}$  of RunIIb data and looked for events with one or more long-lived particle. We then selected the most energetic apparent

muon for study. We called this analysis the “Single CMLLP Analysis”, and it was published in PRL [170]. At the same time, another search for a pair of CMLLPs (the “Pair Analysis”), which required exactly two apparent muons per event, was performed with the same data sample. Both of these analyses are documented in a D0Note [249]. An earlier search for a pair of CMLLPs [250, 251], based on  $1.1 \text{ fb}^{-1}$  of RunIIa data, was published in PRL [169]. These three analyses were combined and more thoroughly explained in a PRD article [171]. The statistical method of the combination was discussed in [252]. The single CMLLP analysis will be described in detail here, but it is worth noting that all three analyses exist, have points in common, and are described fully in the PRD publication. There has also been an even earlier version of this search at D0 [253, 254], not to mention several CDF analyses [167, 168], and continuing searches at CMS [179–181] and ATLAS [172–176] at the LHC.

## A.1 Motivation and Signal Samples

### A.1.1 Motivation and Models

While the analysis was generally model-independent, we obtained results with several SUSY models that could create a CMLLP. Although cosmological observations place severe limits on absolutely stable massive particles [103–105], these limits do not rule out the long-lived particles predicted by these SUSY models, which could have a lifetime somewhat longer than the time it takes them to traverse the detector. In particular, our present model of big bang nucleosynthesis (BBN) does not explain the observed Li abundance. One possible solution may be the existence of a CMLLP which decays during or after the time of BBN [1].

Various supersymmetric models predict either the lightest chargino or the lightest scalar tau lepton ( $\text{stau}$ ) to be a CMLLP. All Gauge Mediated Supersymmetry Breaking (GMSB) models contain a light gravitino/goldstino as the lightest supersymmetric

particle (LSP) [110, 111]. The next-to-lightest supersymmetric particle (NLSP) can be either the lightest scalar tau lepton (stau) or the lightest neutralino, depending on the choice of model parameters [39, 112]. The GMSB model employed in this analysis was a model with a stau NLSP. If the stau decays to the gravitino/goldstino are sufficiently suppressed, which can happen because the effective coupling to the gravitino/goldstino is a free parameter in the model, then the stau can live long enough to escape the detector as a candidate CMLLP [113, 114]. If the stau NLSP is long-lived, then all heavier SUSY particles will first decay to a stau, which then decays to the gravitino/goldstino LSP [255].

Another model explored in this analysis predicts a light chargino that can have a lifetime long enough to escape the detector. The lifetime of the lightest chargino can be long if the mass difference between the lightest chargino and the lightest neutralino is less than about 150 MeV [115, 118], which can occur in Anomaly Mediated Supersymmetry Breaking (AMSB) or in models that do not have gaugino mass unification. There are two general cases explored in this analysis: one where the chargino is mostly higgsino, and the other where the chargino is mostly gaugino. These two cases are treated separately in this analysis.

There are some SUSY models that predict top squark NLSPs and gravitino LSPs where top squarks are long-lived. The top squarks hadronize into both charged and neutral mesons and baryons, which also live long enough to be CMLLP candidates [109]. Furthermore, the Hidden Valley models predict GMSB-like scenarios where the top squark acts like the LSP and does not decay. In these models, the top squark hadronizes into charged and neutral hadrons that escape the detector, making them good CMLLP candidates [54, 55]. In general, any SUSY scenario where the top squark is the lightest colored particle, which occurs in models with mass unification and heavy gluinos, can have a top squark CMLLP. Any colored CMLLP will have additional complications of hadronization and charge exchange during nuclear interactions [256].



### A.1.2 Signal Generation

For each of the four models considered (staus, top squarks, and two varieties of charginos), we simulated direct pair-production of the CMLLPs, without including cascade decays. That is, we generated exactly two stable CMLLPs in each signal event. For the stau candidate CMLLPs, which are predicted by a specific GMSB model, the parameters are well-defined, so the definition of cascade decay chains was straightforward. For this model, we generated additional samples of events with one or more CMLLPs, derived from the expected combination of direct production and cascade decays.

PYTHIA 6.409 [78] was used to generate the CMLLPs. Samples were generated from within PYTHIA for three different models: a GMSB model with a long-lived stau NLSP, a SUSY model with a long-lived higgsino-like chargino, and a SUSY model with a long-lived gaugino-like chargino. The long-lived top squarks were generated and hadronized by linking external code to PYTHIA 6.409. The top squark production code [257] is applicable to any SUSY model that features a long-lived top squark.

For each of the models, mass points were generated with a CMLLP mass of 100, 150, 200, 250 and 300 GeV. A total of 50,000 events were generated for each model and mass point. Additionally, for the model with long-lived top squarks, we generated 50,000 event samples at CMLLP masses of 350 and 400 GeV.

The D0 full detector GEANT simulation (D0GSTAR) [80] was employed to simulate the detector response for Monte Carlo (MC) samples. The detector geometry information was described in D0GSTAR, which provided the position and hit information of the scintillation counters.

### A.1.3 Detection of Top Squarks

As explained in our D0Note on the top squark detection probabilities [256], only 60% of top squark hadrons will be charged after initial hadronization [101]. We checked this

number by counting the number of charged and neutral top squark states produced by PYTHIA. After initial hadronization, top squark hadrons can undergo charge flipping as they pass through material. Furthermore, the top squark hadrons will have different charge survival efficiencies depending on whether they are top squarks or anti-top squarks. After the numerous interactions in the detector material, all top squark hadrons are baryons, and out of the three possible final states, two are charged. Thus, a top squark hadron will have a  $2/3$  probability of being charged after scattering. On the other hand, anti-top squark hadrons are all mesons after scattering, and so they will have a  $1/2$  probability of being charged [148, 149, 258]. As can be seen in Fig. A.1, the top squarks and anti-top squarks must be charged at three locations while passing through the detector: at production, after the calorimeter, and after the muon toroid. Therefore, the probability of a top squark being charged at all three locations is  $0.6$  (at production)  $\times 0.67$  (at the end of the calorimeter)  $\times 0.67$  (at the end of the muon toroid)  $= 0.27$ . Likewise, the probability of an anti-top squark being charged at all three locations is  $0.6 \times 0.5 \times 0.5 = 0.15$ .

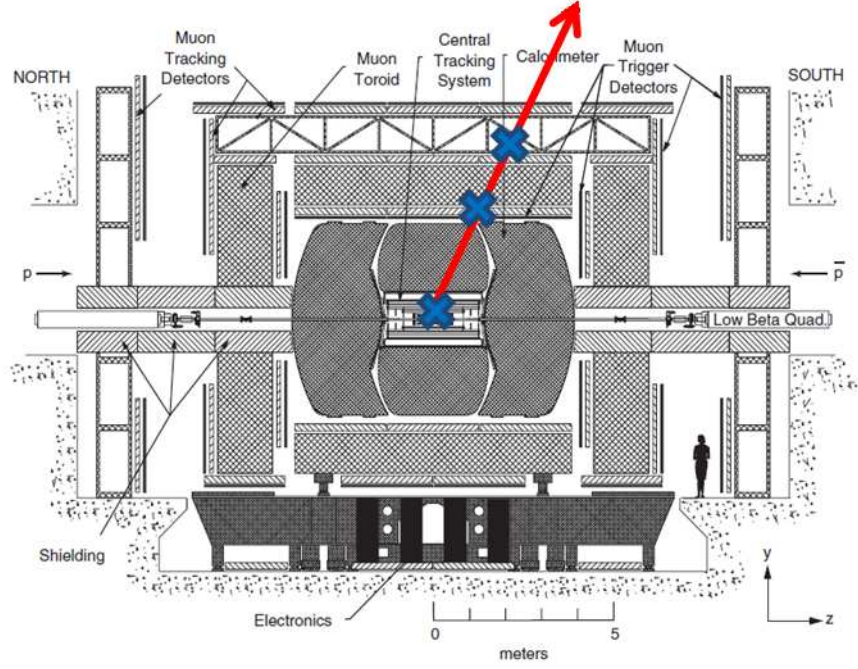


Figure A.1: Diagram of the D0 detector showing the locations (blue crosses) where a top squark hadron must be measured as charged to be selected as a CMLLP candidate.

For the single CMLLP analysis, either the top squark or the anti-top squark could be charged, or both could be charged. In that case, the probability of at least one particle being charged in all three locations was  $0.27 \times (1-0.15) + 0.15 \times (1-0.27) + 0.27 \times 0.15 = 0.38$ , or 38%. This was the charge survival probability used for the single CMLLP analysis.

After obtaining limits with the charge survival probabilities listed above, we also considered limits in the extreme case that there is no charge flipping in the detector. However, the 60% of top squarks that are charged after initial hadronization must still be taken into account. For the single CMLLP analysis, one or both particles could be charged at production. In this case, the charge survival probability was  $2 \times 0.6 \times (1-0.6) + 0.6 \times 0.6 = 0.84$ , or 84%, for the single CMLLP analysis, when there was no charge flipping. The charge survival probability was applied as an additional factor when the top squark MC is normalized to the expected number of events.

## A.2 The D0 Experiment at the Tevatron Collider

This search for CMLLPs was performed using the D0 Experiment, which was a general-purpose particle detector that ran at the Fermilab Tevatron Collider. Since the D0 detector and the CMS detector are similar in many ways and the CMS detector was described in detail in Chapter 3, this section will be brief and focus on the differences between the two experiments and on the subsystems that were the most important for the CMLLP search.

### A.2.1 The Tevatron and the D0 Detector

The D0 Experiment was a general-purpose detector that measured the properties of particles produced from proton-antiproton elastic collisions in the Tevatron, which operated at a center-of-mass energy of 1.96 TeV [259]. The Tevatron accelerated 36 proton and 36 antiproton bunches around a ring that is 6.28 km in circumference, colliding them at various points around the ring. The bunches collided every 396 ns. D0 and CDF were the two general-purpose collider detectors located along the Tevatron ring, while it operated from 1985 to 2011. See Fig. A.2 for a diagram of the Tevatron.

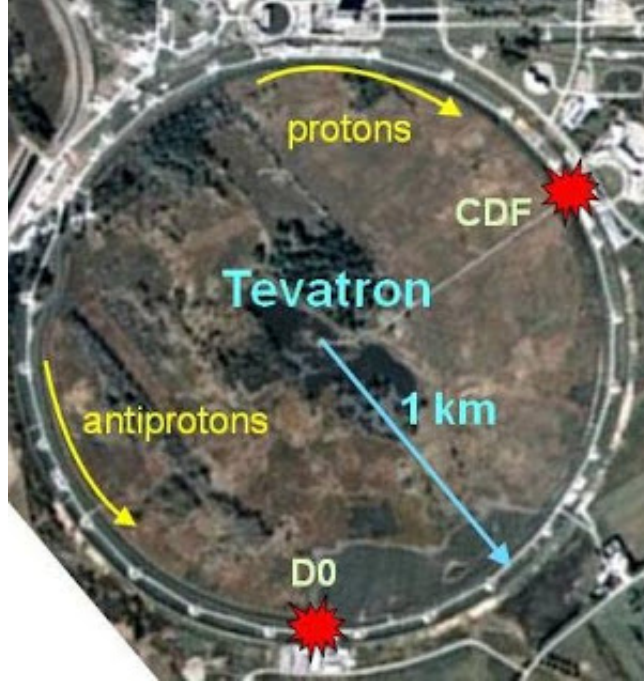


Figure A.2: A diagram of the Fermilab Tevatron.

The D0 detector was proposed in 1983, and its construction was completed in 1992. The D0 experiment had two major run periods: Run I, from 1992 to 1996, when the Tevatron operated at 1.8 TeV and had 3500 ns between bunch crossings, and Run II, from 2001 to 2011, when the Tevatron operated at 1.96 TeV and had 296 ns between bunch crossings. During Run I, D0 collected about  $120 \text{ pb}^{-1}$  of data, and then the detector was upgraded for Run II. About  $10 \text{ fb}^{-1}$  were recorded by D0 in Run II [260]. Like the CMS experiment, the D0 detector was comprised of several concentric subdetectors: the central tracker, the electromagnetic and hadronic calorimeters, and the muon system [261]. These systems will be described here, and then the D0 trigger, and in particular, the trigger used for the CMLLP analysis, will be explained. See Fig. A.3 for a picture of D0.



Figure A.3: A picture of the D0 detector.

### A.2.2 The Central Tracker

The innermost D0 subdetector was the central tracker. The central tracking system determined a particle's trajectory, charge, and momentum, using a 2 T solenoid magnet that encased the tracking system. The central tracker consisted of the Silicon Microstrip Tracker (SMT) and the Central Fiber Tracker (CFT). The two tracking subdetectors pinpointed the primary interaction vertex with a resolution of about  $35\ \mu\text{m}$ . Both subdetectors provided tracking information to the trigger. See Fig. A.4 for a diagram of the tracker.

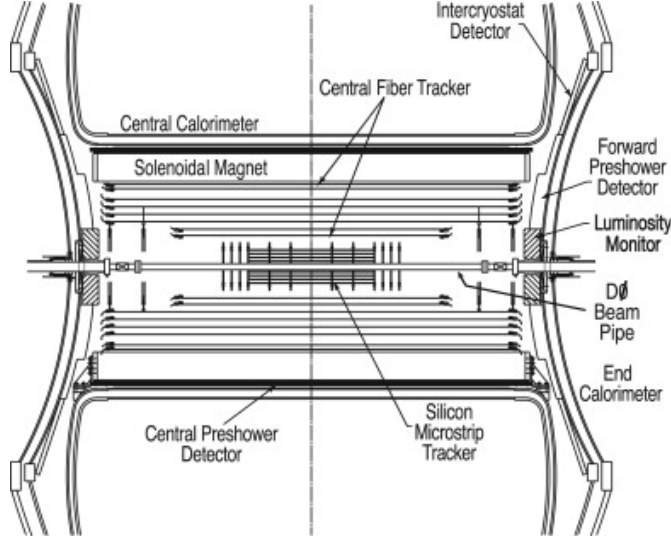


Figure A.4: A diagram of the D0 central tracking system.

The SMT provided triggering and vertexing for the detected particles. The SMT was comprised of six barrels and 12 “F-disks” in the central region, and four “H-disks” in the forward regions, two to each side. Each barrel had four silicon readout layers. The F-disks were double-sided wedge detectors, and the H-disks were large-diameter disks, which provided tracking at high  $|\eta|$ . The SMT provided triggering information at Level 2 (L2) and Level 3 (L3), which was particularly useful for identifying displaced vertices from  $b$  quark decays. It is from the SMT that the CMLLP analysis obtained the ionization energy loss, or  $dE/dx$ , measurement. The  $dE/dx$  was an important variable used in the analysis because muons are minimum ionizing particles, while CMLLPs are highly ionizing.

The CFT, which spanned the radial space between 20 and 52 cm as measured from the center of the detector, consisted of scintillating fibers that were on eight concentric cylinders. The CFT provided fast tracking to the first trigger level (L1), as well as slower information reaching the L2 and L3 of the trigger.

### A.2.3 The Calorimeter

Surrounding the central tracker was the calorimeter. The electromagnetic calorimeter detected the energies from the showers of particles that interact electromagnetically, such as photons and electrons, while the hadronic calorimeter detected the energies from the showers of particles that interact due to the strong force, such as protons, neutrons, pions, and kaons. The D0 calorimeter consisted of a barrel and two endcap sampling calorimeters, which were primarily uranium and liquid argon. The central calorimeter (CC) covered  $|\eta| \leq 1$ , while the two endcap calorimeters, ECN (north) and ECS (south), extended the coverage to  $|\eta| = 4$ . Each calorimeter section was comprised of the electromagnetic section, which was closest to the tracker, followed by fine and coarse hadronic sections. See Fig. A.5 for a diagram of the calorimeter.

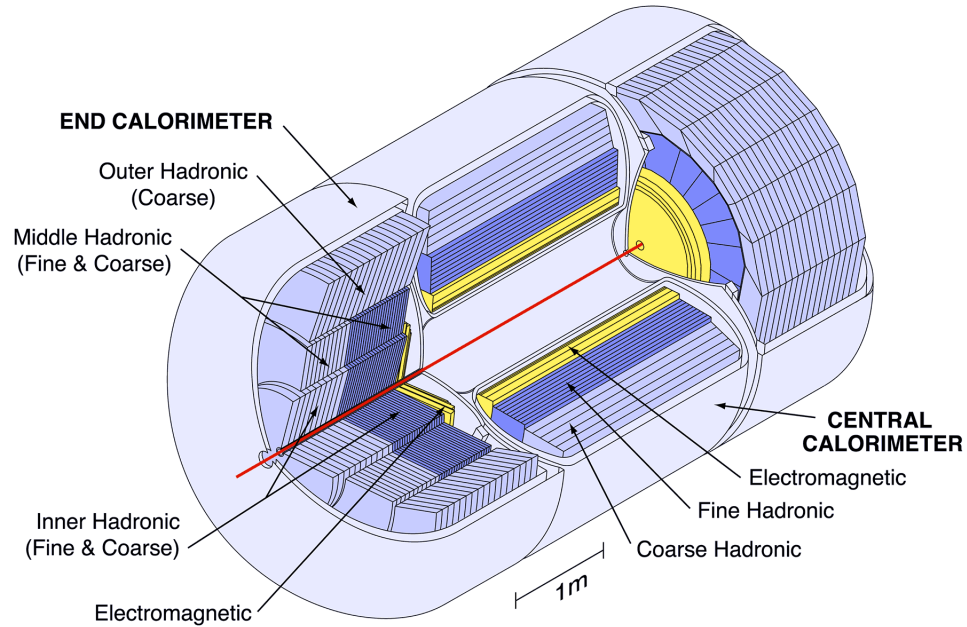


Figure A.5: A diagram of the D0 calorimeter.

### A.2.4 The Muon System

The outermost subdetector of D0 was the muon system. The muon system paid attention to muons, the only known particle from a collision that should penetrate this



far from the center of the detector and could be directly detected. The muon system was composed of the central muon system, which used the original proportional drift tubes (PDTs) from Run I and provided coverage to  $|\eta| = 1$ , and the forward muon system, which was completely new in Run II, used mini drift tubes (MDTs) instead of PDTs, and extended the coverage to  $|\eta| = 2$ . The muon system had three layers: the A, B, and C layers, with a 1.8 T toroid between the A and B layers. (Unlike the CMS muon system, where the magnetic field is produced by the return field of the solenoid, the magnetic field in the D0 muon system was produced by the iron toroid.) The muon system used wires for muon tracking and scintillators for muon triggering. See Fig. A.6 for a picture of the D0 muon system.

The CMLLP analysis made use of the scintillator hits in all three layers, if they existed. The scintillator hit times, and the distance from the production vertex to that scintillator hit, allowed us to compute independent TOF and speed (or  $\beta$ ) measurements for up to three possible layers. Particles traveling at the speed of light were calibrated to arrive at 0 ns, while CMLLPs arrive at late times.



Figure A.6: A picture of the D0 muon system.

### A.2.5 The Trigger

Unlike CMS’s two stage trigger, that is, the L1 and the HLT, the D0 trigger was comprised of the more traditional three level trigger.

The D0 L1 trigger was a hardware system that reduced the 2.5 MHz input rate to about 2 kHz. The Level 1 (L1) trigger, which consisted of 128 trigger bits, was made up of the calorimeter trigger, the central track trigger, the muon trigger, and the forward proton detector trigger. The trigger framework combined the information from all the subsystems of the L1 trigger and decided whether the event would be accepted at L1. The Level 2 (L2) reduced the event rate further to 1 kHz and began to form physical objects. Then, the Level 3 (L3) processor farm performed more complex algorithms on the data and reduced the acceptance rate to about 100 Hz. The data that passed the L3 trigger were written to tape for further analysis offline.

CMLLPs would appear as muons in the detector, and we applied our analysis to events associated with triggers indicating the presence of one or more muons. Because the speed was such an important variable in this analysis, we required triggers with the “tight” scintillator condition to select events with hits in both the A layer and the B or C layer of scintillation counters, in order to maximize the number of independent speed measurements. The details of triggering for this analysis can be found in [262], and are briefly summarized here.

The acceptance of slow-moving particles in the muon trigger system was limited by the length of trigger gates used in the L1 muon trigger. The effect of these trigger gates was much more pronounced for a dimuon trigger, where both slow-moving particles must arrive within the trigger gate, as compared to single muon triggers, where only one of the two slow-moving particles must arrive within the trigger gate. This effect can be seen in Fig. A.7. A single muon trigger is much more efficient for the slow-moving signal than a dimuon trigger, whether looking at just the trigger gate effect, or if also including the trigger efficiency for speed-of-light muons. As the mass

of the slow moving particle increases, and the speed therefore decreases, the effect of the L1 trigger gates becomes more pronounced.

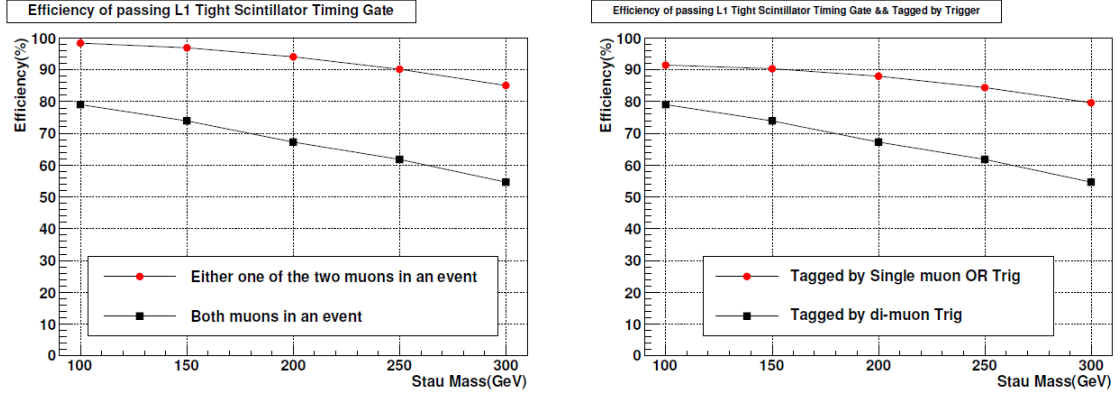


Figure A.7: The efficiency for staus to pass the L1 muon trigger gates. There are always two staus in the event, and the two lines show the efficiency for either both, or for only one, of the two staus to be within the trigger gate. The plot on the left only includes the effect of the trigger gate, while the plot on the right includes the effect of the trigger gate and the efficiency of the single muon triggers. We assume that the efficiency of the dimuon trigger is 100%.

Since the experiment was able to trigger much more efficiently on single slow-moving particles than on pairs of slow moving particles, the events used in this analysis were required to pass an “OR” of single muon triggers. There was, however, a complication with using the standard D0 single muon OR trigger suite in this analysis. In the trigger lists used to collect all RunIIb data, a scintillator timing cut was applied at the L2 of the muon trigger system to reduce rates, by reducing out-of-time backgrounds. However, this L2 timing requirement was very inefficient for our slow-moving signal.

The single muon triggers implemented in the trigger lists used to collect RunIIb data used an “OR” of several different terms at L2. One of the terms was a muon term that required a timing cut, while there was another term involving central tracking at L2, which did not involve a timing cut. To properly utilize these L2 tracking terms for data events, the trigger matching code was modified to require that events pass the L2 tracking term that was implemented in the trigger list used to collect

that particular event. Trigger efficiencies were also measured in data, using the same framework used to measure the official single muon OR trigger efficiencies, explicitly requiring the relevant L2 tracking trigger term, instead of the OR of the L2 muon and the L2 tracking term. These trigger efficiencies were then applied to the simulated events as trigger weights. There was a small, but unavoidable, reduction in the trigger efficiency as measured on prompt muons that resulted from explicitly requiring the L2 tracking term.

## A.3 Analysis Strategy and Techniques

Within the D0 detector, CMLLPs would appear to have the same properties as muons, except they would be more massive, slower, and highly-ionizing. CMLLPs would have a mass about three orders of magnitude heavier than SM muons, which have a mass of 0.106 GeV. Typical muons in the detector travel at about the speed of light, while the speed of CMLLPs would be considerably less, more on the order of  $0.5c$ . Furthermore, CMLLPs ionize heavily because they move slowly, while SM muons are minimum-ionizing particles.

We exploited these two variables in the analysis, as well as their combination, as the speed and  $dE/dx$  were highly anti-correlated for signal, and not for background. See Section A.6 for a further discussion of the relationship between these two key variables, and how it was used in this analysis.

### A.3.1 Time-of-Flight Measurement

One of the most important variables in this analysis was the TOF of the apparent muon. We measured the TOF to the A, B, and C layers of the muon system, for each layer where there were hits for the given muon, and using the distance from the vertex to the scintillator hit, we could determine independent speed (or  $\beta = v/c$ )

measurements for each layer. We then computed a weighted average of the speeds from different layers. CMLLPs would have a slow  $\beta$ , while SM muons have  $\beta = 1$ . See Fig. A.8 for the average  $\beta$  distribution for data, background (largely SM muons), and signal CMLLPs. For background and data, the distribution is somewhat broad around  $\beta = 1$  due to the imperfect detector resolution.

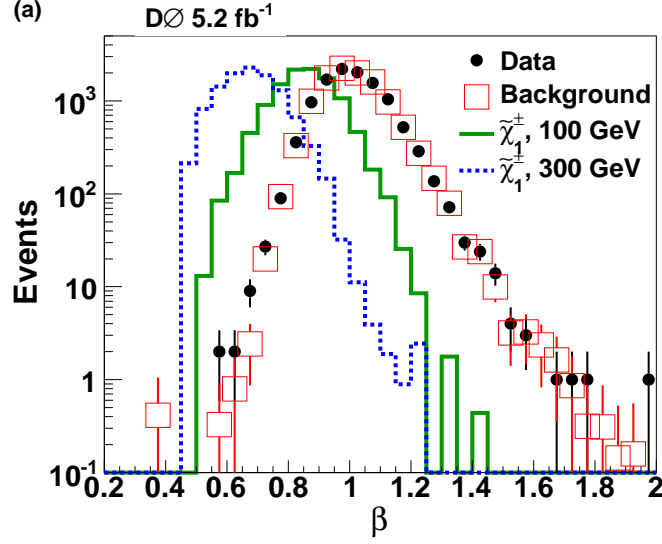


Figure A.8: The speed distribution for data, background, and signal (100 and 300 GeV gaugino-like charginos). The histograms were normalized to have the same number of events.

The TOF was calculated from the muon scintillation counter hit information (the region, layer, octant of the detector, time, and position). The muon scintillator timing electronics were adjusted for each channel, with the goal that speed-of-light particles from the interaction region collisions registered an averaged digitized time of 0 ns. In reality, the digitized time from SM muons was Gaussian distributed; the width of the Gaussian gave us the timing resolution, as measured for each region and layer of the detector, which can be seen in Table A.1.

Table A.1: The measured muon scintillator timing resolutions.

Scintillator	Timing Resolution [ns]
Forward A Layer	2.165
Forward B Layer	2.296
Forward C Layer	2.405
Central A Layer	2.065
Central B Layer Sides	2.274
Central B Layer Bottom	3.110
Central C Layer Top and Sides	3.775
Central C Layer Bottom	2.379

The D0 muon system employed several timing gates at L1, which were relevant for this analysis. The first of these were the timing readout gates, which were asymmetric gates of 100 ns, with a typical muon traveling at the speed of light recording a time of 0 ns. Since these gates were asymmetric, they allowed slow-moving apparent muons to be recorded, thus allowing for our signal CMLLPs. The second set of timing gates were the L1 muon trigger gates, which were symmetric electronic gates set in each layer of the scintillators. The readout and trigger gates are given in Table A.2.

Table A.2: The muon scintillator readout and trigger gates.

Scintillator	Readout Gate [ns]	L1 Trigger Gate [ns]
All Forward Layers	[-15, 85]	[-15, 15]
Central A Layer	[-12, 88]	[-12, 12]
Central B Layer Sides	[-42, 58]	[-42, 42]
Central B Layer Bottom	[-25, 75]	[-25, 25]
Central C Layer Top and Sides	[-23, 77]	[-23, 23]
Central C Layer Bottom	[-30, 70]	[-30, 30]

We will briefly define the TOF variables and show how they were calculated. The first variable was the speed (in units of  $c$ ) or  $\beta$ , which was a weighted average of the speeds found from each scintillator hit for a given muon. The speed from a single scintillator hit was:

$$\beta_i = \frac{d_i}{ct_i} \quad (\text{A.1})$$

where  $d_i$  was the distance from the production place of the muon to the position of the scintillator hit and  $t_i$  was the digitized time of the hit plus the time  $t_c$  it takes a speed-of-light particle to reach the scintillator counter ( $t_c = \frac{d_i}{c}$ ). The production place was assumed to be at  $x = y = 0$ , and the  $z$ -coordinate was taken to be the  $z$ -component of the point of closest approach to the beam line. The error in the speed for a single scintillator hit was:

$$\sigma_i = \beta_i \frac{\sigma_t}{t_i} \quad (\text{A.2})$$

where  $\sigma_t$  was the scintillator resolution for the relevant region of the muon system, as listed in Table A.1.

Then, the average weighted speed ( $\beta$ ) was:

$$\beta = \sigma^2 \sum_i \frac{\beta_i}{\sigma_i^2} \quad (\text{A.3})$$

where  $\sigma$  was the error in the weighted average speed, defined by:

$$\frac{1}{\sigma^2} = \sum_i \frac{1}{\sigma_i^2} \quad (\text{A.4})$$

Thus, a speed measurement from a particular scintillator hit was given more weight in the average speed if it was more accurate.

It should be noted that we explicitly required that there was at least an A layer and either a B or C layer hit, which is in keeping with the quality of the muons selected for this analysis, when performing the average speed calculation and all the calculations that follow. Therefore,  $i$  was at least 2.

The speed  $\chi^2$  (per degree of freedom) was defined as:

$$\chi^2 = \frac{1}{i-1} \sum_i \frac{(\beta - \beta_i)^2}{\sigma_i^2} \quad (\text{A.5})$$

The speed  $\chi^2$  was based on the average speed, the speed from each scintillator hit, and the error in the speed from each scintillator hit; it was then normalized by the number of degrees of freedom. As we discussed in [150], we developed an algorithm based on this speed  $\chi^2$  to eliminate spurious inclusion of random hits in the speed calculation. Some hits were not consistent with the other hits for a given muon, which resulted in a high speed  $\chi^2$ . It was important to remove these spurious hits because they tended to give slow speeds, which could resemble our slow-moving signal.

We also defined a variable called the speed significance as:

$$\frac{1 - \beta}{\sigma} \quad (\text{A.6})$$

which is based on the average speed and the error in the average speed.

A complete discussion of the TOF, the timing corrections, smearing, and algorithms we applied, and the related timing variables for this analysis can be found in [150].

### A.3.2 $dE/dx$ Measurement

In addition to the long TOF, a large ionization energy loss  $dE/dx$  was a distinguishing characteristic of the candidate CMLLPs.  $dE/dx$  varies roughly as  $1/\beta^2$  for CMLLPs, while the rise in  $dE/dx$  at high  $\beta$  is logarithmic. As shown in Fig. A.9, the  $dE/dx$  between SM muons and CMLLPs is well separated.



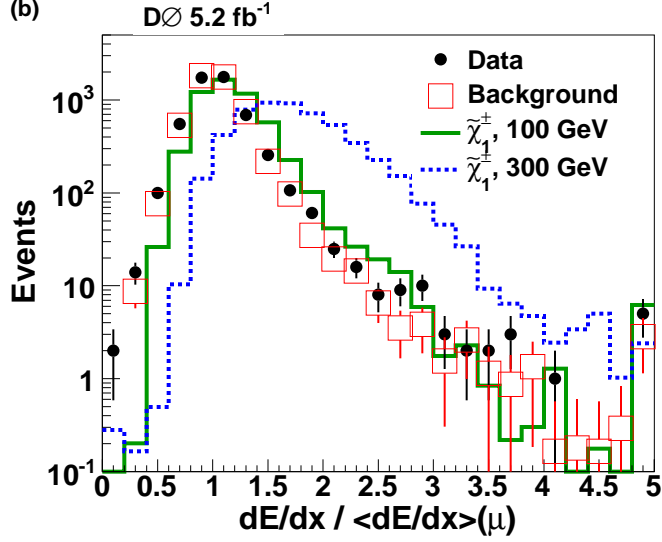


Figure A.9: The  $dE/dx$  distribution for data, background, and signal (100 and 300 GeV gaugino-like charginos). The histograms were normalized to have the same number of events. We have adjusted the scale of the  $dE/dx$  measurements so that the  $dE/dx$  of muons from  $Z \rightarrow \mu\mu$  events peak at 1.

The measurement of  $dE/dx$  was best made in the central tracking system, where ionization is sampled multiple times per track. We used the  $dE/dx$  as measured in the SMT because it could be associated with a specific track and thus could easily be corrected for the track inclination and because the associated electronics allowed for a large range in digitized values. The SMT  $dE/dx$  was a calibrated average over the SMT clusters and was corrected for the particle path in the barrels or disks to reduce the strong angular dependence. The  $dE/dx$  was determined from the energy deposits and the path length in the SMT layers. It was derived from the pulse height values of the SMT hits used in the track fit. The algorithm excluded SMT clusters with the highest 20%  $dE/dx$  values, in order to minimize the contribution of data from the Landau tails.

As discussed in [263], this analysis required a constant average  $dE/dx$  over the time period in which the data were collected, in order to have a baseline value for the  $dE/dx$  of SM muons. However, the  $dE/dx$  as a function of delivered integrated luminosity

was not constant, due to the radiation in the silicon, which resulted in a roughly linear decline, and also due to SMT upgrades in the online software, which resulted in abrupt jumps in the distribution. In order to provide a constant average  $dE/dx$ , we recalibrated every  $dE/dx$  value, dividing the value given for the particle by the mean muon  $dE/dx$  values from  $Z \rightarrow \mu\mu$  events, at the integrated luminosity for that store. See Fig.A.10 for the mean  $dE/dx$  in data before and after this recalibration was applied. We adjusted the MC similarly, normalizing the  $dE/dx$  values by the mean of the muon  $dE/dx$  from  $Z \rightarrow \mu\mu$  events.

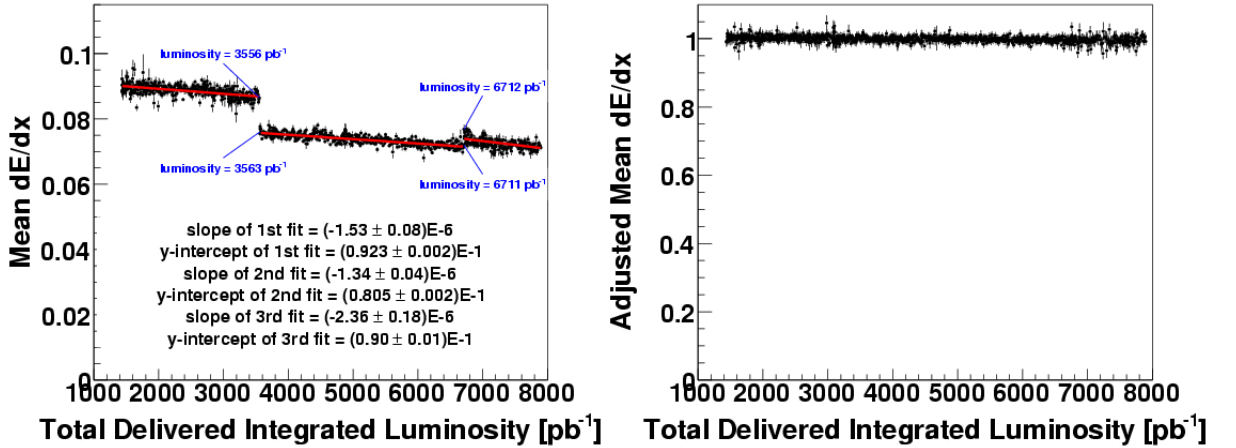


Figure A.10: The mean  $dE/dx$  as a function of delivered integrated luminosity, before (left) and after (right) the adjustment. The “1st fit” is for luminosities between 1800 and 3556 pb<sup>-1</sup>, the “2nd fit” is for luminosities between 3563 and 6711 pb<sup>-1</sup>, and the “3rd fit” is for luminosities between 6712 and 7900 pb<sup>-1</sup>.

We also introduced a variable called the  $dE/dx$  significance, much like the speed significance discussed in the previous section, in order to relate the  $dE/dx$  measurement to its error, which would depend on the number of individual measurements taken, that is, the number of SMT hits. The  $dE/dx$  significance was defined as:

$$\frac{dE/dx - 1}{RMS(N_c)} \quad (A.7)$$

where  $RMS(N_c)$  is the root mean squared of the distribution of adjusted  $dE/dx$ , for

the given number of SMT hits  $N_c$ , for  $Z \rightarrow \mu\mu$  data.

A complete discussion of the  $dE/dx$ , the corrections and smearing we applied, and the related variables for this analysis can be found in [263].

## A.4 Event Selection

Now that we have introduced the analysis strategy, we can discuss the selection of events used in the single CMLLP search. The D0 p20 MUinclusive skim, a common data sample used by many analyses in D0 that has at least one reconstructed muon per event, was re-skimmed by the CMLLP group in order to include the muon scintillator hit information. The “p20” term refers to the fact that the data was reconstructed with the p20 release of the D0 packages; it corresponds to the RunIIB data taking period, of which  $5.2 \text{ fb}^{-1}$  of data was used in this analysis. At the time of this re-skim, a cut of  $p_T > 20 \text{ GeV}$  was applied to reduce the large dataset. Then, for the single CMLLP search, an initial Muon Selector was applied to select events where at least one muon has a  $p_T > 60 \text{ GeV}$ , which was added to help reduce the large background in the single CMLLP study. The choice of 60 GeV was optimized for the single CMLLP search. The events selected for the single CMLLP search must have at least one muon, and then the muons are sorted by their  $p_T$ . The highest  $p_T$  muon must satisfy the:

- Single muon trigger without the L2 tight scintillator timing cut (see [262])
- `mediumnseg3NCV` muon identification
- `trackmedium` track quality
- `NPtight` isolation
- $|\text{det } \eta| < 1.6$

which are fully described in [264].

The highest  $p_T$  muon must pass the cosmic cuts that were applied for one muon:

- The muon's Distance of Closest Approach (DCA) to the beam line must be less than 0.2 cm.
- The muon's C-layer time minus the A-layer time must be greater than -10 ns.

In addition, more cosmic cuts were applied if there are exactly two muons in the event. If there were exactly two muons, an event was rejected if any of the following conditions were true:

- The DCA of either muon was larger than 0.2 cm.
- The absolute value of the difference in A-layer times of the two muons was larger than 10 ns. (See Fig. A.11 (b) for this distribution in  $Z \rightarrow \mu\mu$  and cosmic data.)
- The C-layer time minus the A-layer time for either muon was less than -10 ns. (See Fig. A.11 (a) for this distribution in  $Z \rightarrow \mu\mu$  and cosmic data.)
- The pseudo-acolinearity  $\Delta\alpha = |\Delta\phi + \Delta\theta - 2\pi| < 0.05$ , to reject cosmic ray events that appear as two muons essentially back-to-back.

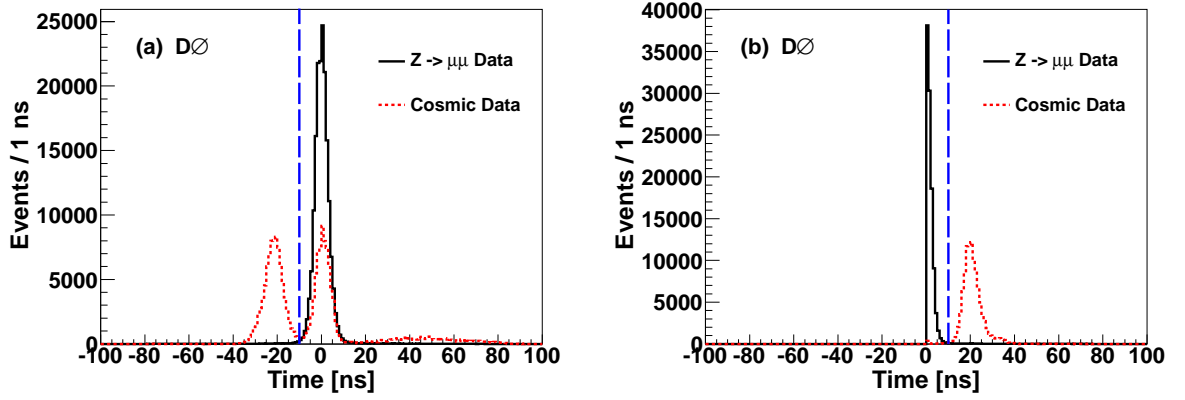


Figure A.11: (a) Distribution of the difference between the A-layer and C-layer times for a single muon. There are two cosmic ray peaks for the two possible directions, away from or towards the  $p\bar{p}$  collision vertex. (b) Distribution of the absolute value of the difference between the A-layer times of the two muons in the event. The times shown in these plots are centered at zero for  $\beta = 1$  particles. This cosmic ray data was collected when there was no  $p$  or  $\bar{p}$  beam in the Tevatron collider. The selection requirement on the time difference is shown with a blue vertical line. The histograms have been normalized to the same number of events.

Furthermore, additional cuts were applied to the highest  $p_T$  muon:

- $|z_{\text{AtPca}}| < 40$  cm (z-coordinate of the DCA)
- $p_T \geq 60$  GeV
- $\beta < 1.0$
- Speed  $\chi^2/\text{dof} < 2$
- Matching  $\chi^2 \leq 100$

More details about the speed and speed  $\chi^2$  variables can be found in [150]. The matching  $\chi^2$  describes the agreement between the local muon system track and the central track. A cleanup cut of 100 was applied to remove events in which the local muon has been matched to the wrong central track.

The background was modeled with data, so to create separate data and background samples, a transverse mass ( $M_T = \sqrt{(p_T + \cancel{E}_T)^2 - (p_x + \cancel{E}_x)^2 - (p_y + \cancel{E}_y)^2}$ )

cut was applied. Most of the background in this sample was  $W \rightarrow \mu\nu$  events, so events with  $M_T < 200$  GeV were selected as the “background” sample, as is done in the  $W$  mass group to select  $W$  events. Events with  $M_T > 200$  GeV were selected as the “data” sample. See Fig. A.12 for a plot of  $M_T$  for the single muon events and 100, 200, and 300 GeV higgsino-like charginos. The single muon events sample has all of the selection criteria described above except the transverse mass cut, which separates the “data” from “background” samples. The charginos have all the selection criteria except the  $M_T > 200$  GeV cut.

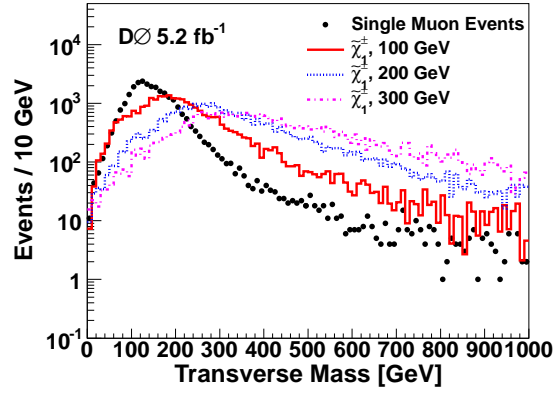


Figure A.12: The transverse mass distribution for single muon events and 100, 200, and 300 GeV higgsino-like charginos. The single muon events sample has all of the selection criteria described above except the transverse mass cut, which separates the “data” from “background” samples. The charginos have all the selection criteria except the  $M_T > 200$  GeV cut. The histograms have been normalized to the same number of events.

The speed  $\chi^2$  distribution was not modeled perfectly in MC (see Fig. A.13, comparing the distributions for  $Z \rightarrow \mu\mu$  data and MC). The MC distribution was broader than that of data, and thus the speed  $\chi^2$  cut over-reduced the signal acceptance. As a result, we applied an additional event weight to the signal to correct for this over-reduction. The event weight was based on the ratio of  $Z \rightarrow \mu\mu$  data to MC for each bin in the speed  $\chi^2$  distribution. The event weight was applied in a final step to the signal MC. One can observe from the tables below that the overall signal acceptance

was 4-7% higher, due to this speed  $\chi^2$  correction.

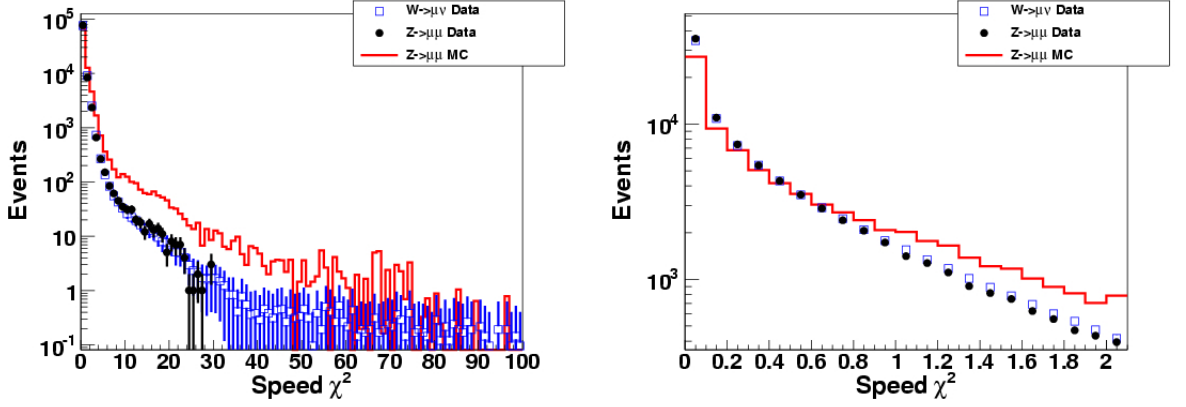


Figure A.13: The speed  $\chi^2$  distribution for  $W \rightarrow \mu\nu$  data,  $Z \rightarrow \mu\mu$  data, and  $Z \rightarrow \mu\mu$  MC, for the leading muon in each event. The plot on the right is the same as on the left, but zoomed in between speed  $\chi^2$  values of 0 and 2. (The single CMLLP analysis only accepts events with the leading muon's speed  $\chi^2 < 2.0$ .) The histograms have been normalized to the same number of events.

The acceptance tables for data (including the background sample) and signal MC are shown in Tables A.3 - A.7. In these tables, please note that “good beta” means that the speed calculation has explicitly required an A and either a B or C layer scintillator hit and that the speed  $\chi^2$  minimizing algorithm has been performed (see [150] for more details). “Good  $dE/dx$ ” means that  $dE/dx > 0$ , and there are at least 3 SMT clusters for that muon's  $dE/dx$  value.

Table A.3: Selection cut efficiencies for data events.

Cut	Number of Events Passing Cut	
After initial Muon Selector	345173	
Remove bad runs and lbns	314711	
Event quality	304791	
$ \text{detector } \eta  < 1.6$	290511	
Calorimeter isolation < 2.50 GeV	156869	
Track isolation < 2.50 GeV	141008	
Trigger Matching	79983	
Difference in A and C layer times	79308	
Timing for 2 muons	79096	
Acolinearity < 0.05 for 2 muons	79076	
$ \text{zAtPca}  < 40 \text{ cm}$	70464	
Good beta and good $dE/dx$	57532	
$p_T > 60 \text{ GeV}$	56466	
Speed < 1.0	30336	
Speed $\chi^2 < 2$	27876	
Matching $\chi^2 \leq 100$	27740	
	Background( $M_T < 200$ GeV)	Data ( $M_T > 200$ GeV)
$M_T$	22368	5374



Table A.4: Selection cut efficiencies for stau MC events.

Cut	Percent of Stau Events Passing Each Cut				
	100 GeV	150 GeV	200 GeV	250 GeV	300 GeV
Initial	100.0	100.0	100.0	100.0	100.0
Lumi reweighting	98.9	97.1	97.4	97.3	97.7
Beam weight	98.8	96.7	97.3	97.1	97.7
Remove bad runs and lbns	91.0	88.6	88.9	88.8	89.5
Event quality	87.2	84.8	85.1	84.9	85.6
$ \text{detector } \eta  < 2.0$	81.0	78.8	79.4	79.0	79.6
Medium quality	75.4	73.9	74.7	74.1	74.5
Number of layers $\geq 3$	72.9	71.6	72.5	71.7	72.2
Matched with central track	70.6	69.4	70.2	69.6	70.0
Track fit chi-square $< 4.00$	69.5	68.5	69.4	68.7	69.1
DCA $< 0.02$ for nSMT $> 0$ and DCA $< 0.2$ for nSMT $= 0$	68.9	67.9	68.9	68.1	68.5
N muons $\geq 1$	68.9	67.9	68.9	68.1	68.5
$ \text{detector } \eta  < 1.6$	66.0	66.0	67.2	66.8	67.2
Calorimeter isolation $< 2.50$ GeV	60.8	61.1	62.2	61.7	62.2
Track isolation $< 2.50$ GeV	59.1	59.5	60.6	60.2	60.8
muon_id_corr	56.2	56.4	57.3	56.9	57.3
muon_track_corr	49.5	49.4	50.0	49.5	49.8
muon_track_corr_lumi	49.8	49.7	50.3	49.8	50.1
muon_deltaR_corr	50.6	50.5	51.1	50.6	50.8
muon_iso_corr	49.3	49.2	49.7	49.2	49.5
Trigger Probability	31.5	31.2	31.4	31.0	31.0
Difference in A and C layer times	28.1	26.5	25.7	27.8	26.5
Timing for 2 muons	27.9	26.2	25.3	27.3	26.1
Acolinearity $< 0.05$ for 2 muons	27.8	26.1	25.1	27.1	25.8
$ \text{zAtPca}  < 40$ cm	25.9	24.2	23.3	25.1	24.0
Good beta and good $dE/dx$	21.3	18.7	17.0	17.2	14.9
$p_T > 60$ GeV	19.5	18.5	17.0	17.2	14.9
Speed $< 1.0$	18.3	18.0	16.7	17.1	14.8
Speed $\chi^2 < 2$	16.2	15.8	14.8	15.0	13.1
Matching $\chi^2 \leq 100$	16.1	15.7	14.7	14.9	13.0
$M_T > 200$ GeV	13.8	14.9	14.4	14.7	13.0
Speed $\chi^2$ event weight	14.4	15.6	15.2	15.4	13.6

Table A.5: Selection cut efficiencies for top squark MC events. See Sections A.1.3 and A.6 for discussion of the top squark charge survival efficiency and charge flipping.

Cut	Percent of top squark Events Passing Each Cut						
	100 GeV	150 GeV	200 GeV	250 GeV	300 GeV	350 GeV	400 GeV
Initial	100.0	100.0	100.0	100.0	100.0	100.0	100.0
Lumi reweighting	97.8	97.1	97.0	98.2	97.9	97.2	97.6
Beam weight	97.9	97.1	96.8	98.2	98.1	97.0	97.4
Remove bad runs and lbns	89.6	88.8	88.6	90.4	98.7	88.8	89.2
Event quality	85.7	84.7	84.7	86.4	85.8	85.1	85.5
$ \text{detector } \eta  < 2.0$	78.3	78.1	78.8	78.9	79.4	79.0	79.2
Medium quality	64.6	69.1	71.9	63.9	73.3	72.8	72.5
Number of layers $\geq 3$	61.4	66.3	69.4	60.8	70.7	70.3	69.8
Matched with central track	58.7	63.9	67.1	58.2	68.4	68.2	67.7
Track fit chi-square $< 4.00$	57.5	62.9	66.2	57.2	67.7	67.4	67.0
DCA $< 0.02$ for nSMT $> 0$ and DCA $< 0.2$ for nSMT $= 0$	56.9	62.3	65.6	56.6	67.2	66.9	66.5
N muons $\geq 1$	56.9	62.3	65.6	56.6	67.2	66.9	66.5
$ \text{detector } \eta  < 1.6$	52.0	59.3	63.4	52.0	65.7	65.7	65.3
Calorimeter isolation $< 2.50$ GeV	47.3	53.7	57.7	47.9	59.5	59.6	59.2
Track isolation $< 2.50$ GeV	46.0	52.0	55.8	47.0	57.3	57.3	56.6
muon_id_corr	44.0	49.5	52.9	44.9	54.1	54.0	53.4
muon_track_corr	39.2	43.7	46.4	39.9	47.1	47.0	46.4
muon_track_corr_lumi	39.4	43.9	46.6	40.0	47.4	47.3	46.6
muon_deltaR_corr	40.0	44.6	47.4	40.7	48.1	47.9	47.3
muon_iso_corr	39.1	43.5	46.1	39.8	46.8	46.7	46.1
Trigger Probability	24.9	27.6	29.3	25.3	29.4	29.3	28.8
Difference in A and C layer times	21.4	23.6	26.5	24.7	25.1	23.9	25.2
Timing for 2 muons	21.1	23.3	26.2	24.3	24.6	23.3	24.6
Acolinearity $< 0.05$ for 2 muons	21.1	23.2	26.0	24.1	24.3	23.1	24.3
$ \text{zAtPca}  < 40$ cm	19.6	21.6	24.2	22.4	22.6	21.4	22.6
Good beta and good $dE/dx$	15.2	16.0	17.0	14.5	13.5	11.1	10.0
$p_T > 60$ GeV	12.5	15.6	17.0	14.5	13.4	11.1	10.0
Speed $< 1.0$	12.1	15.3	16.8	14.8	13.4	11.1	10.0
Speed $\chi^2 < 2$	10.7	13.6	14.9	12.8	11.8	9.8	8.8
Matching $\chi^2 \leq 100$	10.6	13.5	14.8	12.7	11.7	9.8	8.8
$M_T > 200$ GeV	8.3	12.6	14.4	12.6	11.7	9.7	8.8
Speed $\chi^2$ event weight	8.6	13.2	15.2	13.3	12.4	10.3	9.3

Table A.6: Selection cut efficiencies for gaugino-like chargino MC events.

Cut	Percent of Gaugino-Like Chargino Events Passing Each Cut				
	100 GeV	150 GeV	200 GeV	250 GeV	300 GeV
Initial	100.0	100.0	100.0	100.0	100.0
Lumi reweighting	96.9	98.0	98.3	98.0	97.5
Beam weight	96.9	97.9	98.3	97.9	98.3
Remove bad runs and lbns	88.5	89.6	90.0	89.5	90.1
Event quality	84.5	85.8	86.1	85.6	86.4
$ \text{detector } \eta  < 2.0$	76.0	77.8	78.4	78.0	78.0
Medium quality	58.9	62.1	62.7	61.3	61.0
Number of layers $\geq 3$	56.0	59.1	59.5	58.2	57.6
Matched with central track	53.3	56.3	56.8	55.7	55.2
Track fit chi-square $< 4.00$	52.3	55.3	55.8	54.8	54.4
DCA $< 0.02$ for nSMT $> 0$ and DCA $< 0.2$ for nSMT $= 0$	51.7	54.7	55.4	54.3	53.8
N muons $\geq 1$	51.7	54.7	55.4	54.3	53.8
$ \text{detector } \eta  < 1.6$	45.8	49.4	50.5	49.6	49.4
Calorimeter isolation $< 2.50$ GeV	42.3	45.6	46.7	45.6	45.7
Track isolation $< 2.50$ GeV	41.3	44.6	45.7	44.7	44.9
muon_id_corr	39.7	42.7	43.6	42.7	42.9
muon_track_corr	35.7	38.2	38.9	38.1	38.1
muon_track_corr_lumi	35.8	38.4	39.1	38.2	38.3
muon_deltaR_corr	36.4	39.0	39.7	38.8	38.9
muon_iso_corr	35.6	38.1	38.8	38.0	38.1
Trigger Probability	22.7	24.3	24.7	24.2	24.1
Difference in A and C layer times	21.2	21.1	21.4	20.3	20.4
Timing for 2 muons	21.0	20.8	21.0	19.9	19.7
Acolinearity $< 0.05$ for 2 muons	20.9	20.8	20.8	19.7	19.6
$ \text{zAtPca}  < 40$ cm	19.5	19.4	19.5	18.3	18.3
Good beta and good $dE/dx$	14.9	13.1	11.7	9.4	7.9
$p_T > 60$ GeV	11.7	12.5	11.6	9.4	7.9
Speed $< 1.0$	11.2	12.3	11.5	9.4	7.9
Speed $\chi^2 < 2$	10.0	11.1	10.4	8.4	7.1
Matching $\chi^2 \leq 100$	9.9	11.0	10.3	8.4	7.0
$M_T > 200$ GeV	7.5	10.1	10.0	8.3	7.0
Speed $\chi^2$ event weight	7.8	10.6	10.6	8.8	7.4

Table A.7: Selection cut efficiencies for higgsino-like chargino MC events.

Cut	Percent of Higgsino-Like Chargino Events Passing Each Cut				
	100 GeV	150 GeV	200 GeV	250 GeV	300 GeV
Initial	100.0	100.0	100.0	100.0	100.0
Lumi reweighting	96.4	97.6	98.2	98.0	97.2
Beam weight	96.3	97.3	98.2	98.3	97.3
Remove bad runs and lbns	87.6	88.6	90.4	90.4	88.5
Event quality	83.8	84.7	86.4	86.6	84.7
$ \text{detector } \eta  < 2.0$	75.8	77.2	78.9	78.7	77.1
Medium quality	59.5	62.6	63.9	63.4	61.1
Number of layers $\geq 3$	56.5	59.6	60.8	60.3	58.0
Matched with central track	53.9	57.1	58.2	57.7	55.4
Track fit chi-square $< 4.00$	53.0	56.2	57.2	56.6	54.6
DCA $< 0.02$ for nSMT $> 0$ and DCA $< 0.2$ for nSMT $= 0$	52.4	55.6	56.6	56.1	53.9
N muons $\geq 1$	52.4	55.6	56.6	56.1	53.9
$ \text{detector } \eta  < 1.6$	46.7	50.6	52.0	51.7	50.0
Calorimeter isolation $< 2.50$ GeV	43.1	46.7	47.9	47.9	46.2
Track isolation $< 2.50$ GeV	42.2	45.8	47.0	47.0	45.3
muon_id_corr	40.5	43.9	44.9	44.9	43.1
muon_track_corr	36.3	39.2	39.9	39.9	38.3
muon_track_corr_lumi	36.4	39.4	40.0	40.1	38.5
muon_deltaR_corr	37.0	40.0	40.7	40.7	39.1
muon_iso_corr	36.1	39.1	39.8	39.8	38.2
Trigger Probability	23.1	25.0	25.3	25.3	24.2
Difference in A and C layer times	21.3	23.7	24.2	21.8	20.6
Timing for 2 muons	21.1	23.4	23.7	21.3	20.1
Acolinearity $< 0.05$ for 2 muons	21.0	23.3	23.6	21.1	19.9
$ \text{zAtPca}  < 40$ cm	19.5	21.7	21.9	19.7	18.5
Good beta and good $dE/dx$	15.1	15.0	13.7	10.7	8.5
$p_T > 60$ GeV	12.1	14.3	13.6	10.6	8.5
Speed $< 1.0$	11.6	14.1	13.5	10.6	8.5
Speed $\chi^2 < 2$	10.3	12.6	12.1	9.5	7.7
Matching $\chi^2 \leq 100$	10.3	12.6	12.0	9.5	7.6
$M_T > 200$ GeV	7.9	11.5	11.7	9.4	7.6
Speed $\chi^2$ event weight	8.3	12.2	12.4	10.0	8.1

## A.5 Background Estimation

The background was modeled with data for the single CMLLP analysis. The background was selected to be the events that passed the selection criteria described in

Section A.4, as well as having  $M_T < 200$  GeV.

### A.5.1 Background Normalization

It is optimal to normalize the background to the data in a signal-free region. As previously discussed, we imposed an analysis cut of  $\beta < 1$ , and in fact, most of the signal should have a speed less than 1. Thus, we could define a signal-free region with  $\beta > 1$ . Furthermore, one could define the signal-free background as events with  $\beta > 1$  and  $M_T < 200$  GeV and likewise, the signal-free data as events with  $\beta > 1$  and  $M_T > 200$  GeV. Let the number of background events be  $N_B$ , the number of normalized background events be  $N_{NB}$ , the number of signal-free background events be  $N_{SFB}$ , and the number of signal-free data events be  $N_{SFD}$ . Therefore, the normalized background was the number of background events times the number of signal-free data events, divided by the number of signal-free background events:

$$N_{NB} = N_B \frac{N_{SFD}}{N_{SFB}} \quad (\text{A.8})$$

### A.5.2 Differences in Kinematic Distributions and Additional Event Weight

It was noticed that there was a difference in the background and data distributions in  $\eta$ . This difference could be expected because one would expect high  $M_T$  events to have a higher chance of being in the forward regions than low  $M_T$  events. Thus, the different percentages of forward muons in the background and data resulted in different kinematic distributions. The difference in the  $\eta$  distributions causes a problem in the speed distributions because the speed resolution is different in the central and forward muon systems. The solution we imposed for this issue was to define an additional event weight.

The additional event weight was based on the  $|\text{det } \eta|$  distribution in the signal-free region (see Fig. A.14). The event weight was the ratio of signal-free data to signal-free background for each bin in  $|\text{det } \eta|$ . This event weight was applied to each background event. One obtains the most agreement between data and background when a large number of bins in the  $|\text{det } \eta|$  distribution is used. See Fig. A.15 for the  $\eta$  distribution for background and data, before and after the new event weight.

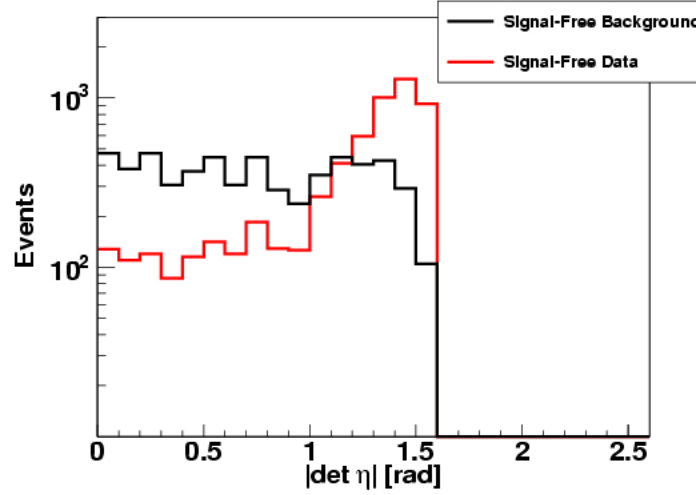


Figure A.14: The absolute value of the detector  $\eta$  distribution for signal-free background and signal-free data. The histograms in each plot have been normalized to have the same number of events.

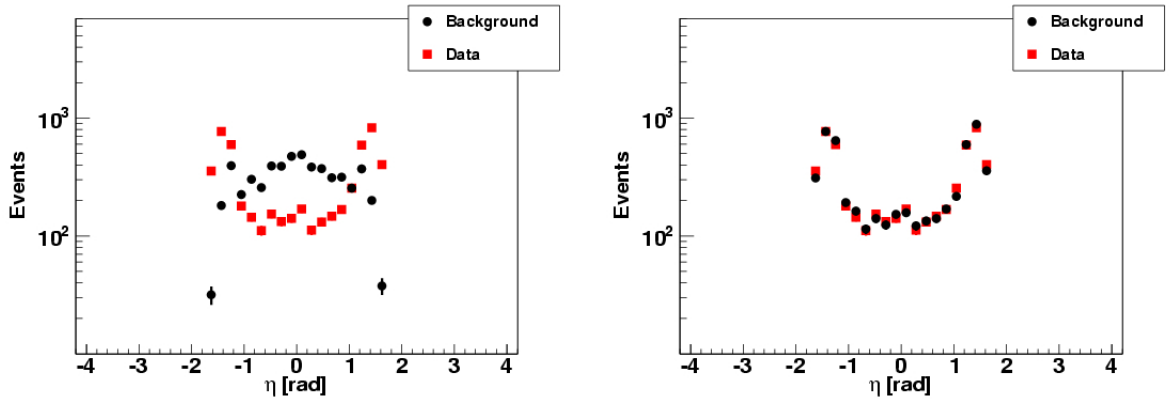


Figure A.15:  $\eta$  distribution for background and data, before the new event weight (left) and after (right). The histograms in each plot have been normalized to have the same number of events.

## A.6 Analysis Method

The key variables used for discrimination between signal and background were the speed and  $dE/dx$  (see Sections A.3.1 and A.3.2 for more information). The speed and  $dE/dx$  were highly anti-correlated for signal, and not for background. Figure A.16 shows the adjusted  $dE/dx$  as a function of  $\beta$  for data, background, and signal.

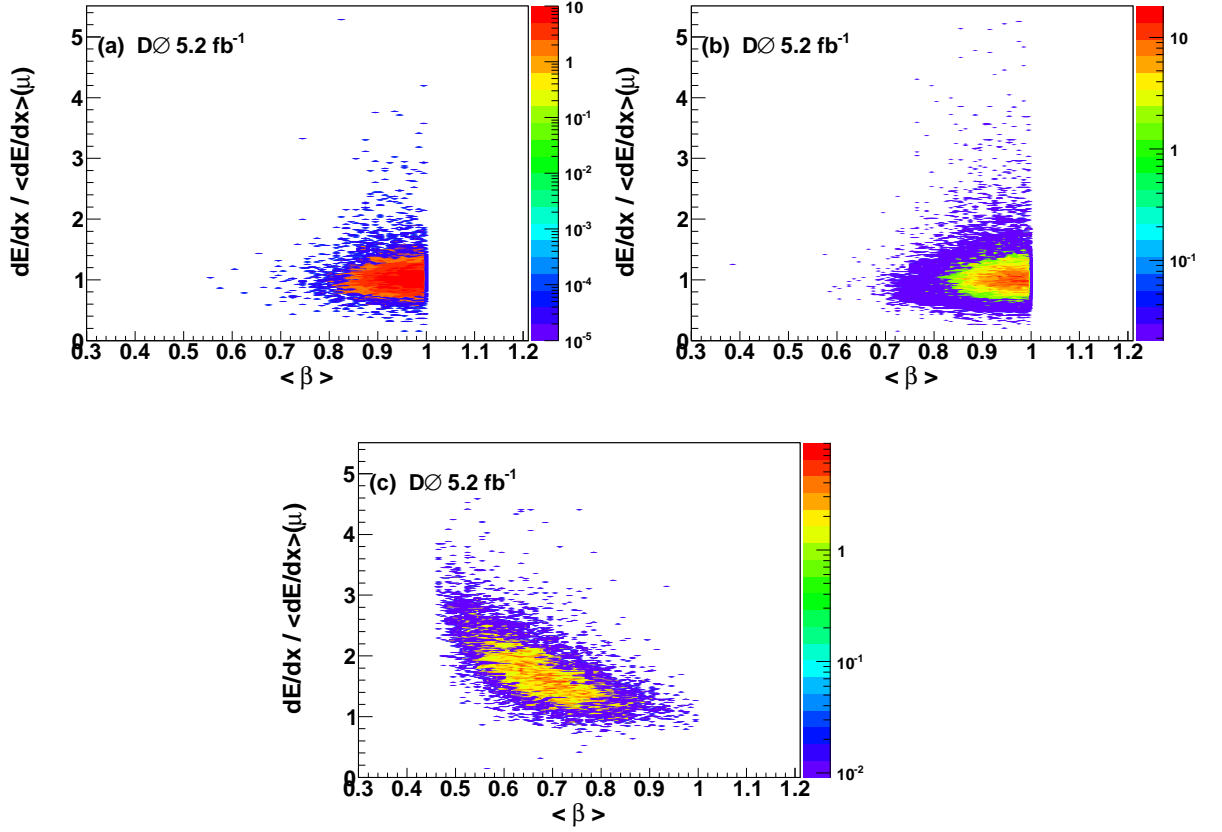


Figure A.16: Adjusted  $dE/dx$  as a function of  $\beta$  for data (a), background (b), and 300 GeV gaugino-like charginos (c). The contours indicate the numbers of events.

The final ntuples of events passing all the selection criteria were made, the background event weight was applied, and the background was normalized. After all of this, the final variable distributions, which are of the speed,  $dE/dx$ , and related variables, were made for signal, background, and data (see Fig. A.17 and A.18).

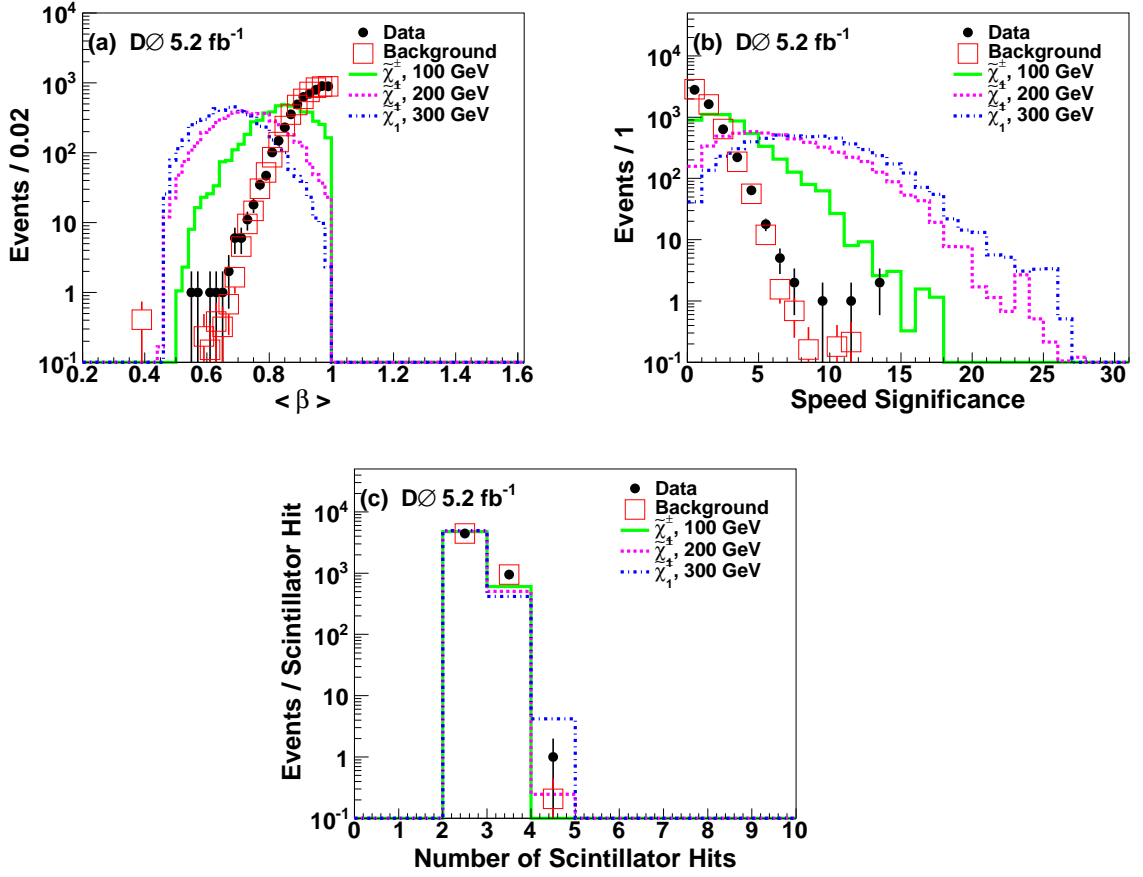


Figure A.17: Final distributions related to the speed for signal (100, 200, and 300 GeV gaugino-like charginos), background (single muon data with  $M_T < 200$  GeV), and data (single muon data with  $M_T > 200$  GeV). The speed distribution (a), speed significance distribution (b), and number of scintillator hits distribution (c). For each plot, the histograms have been normalized to have the same number of events.



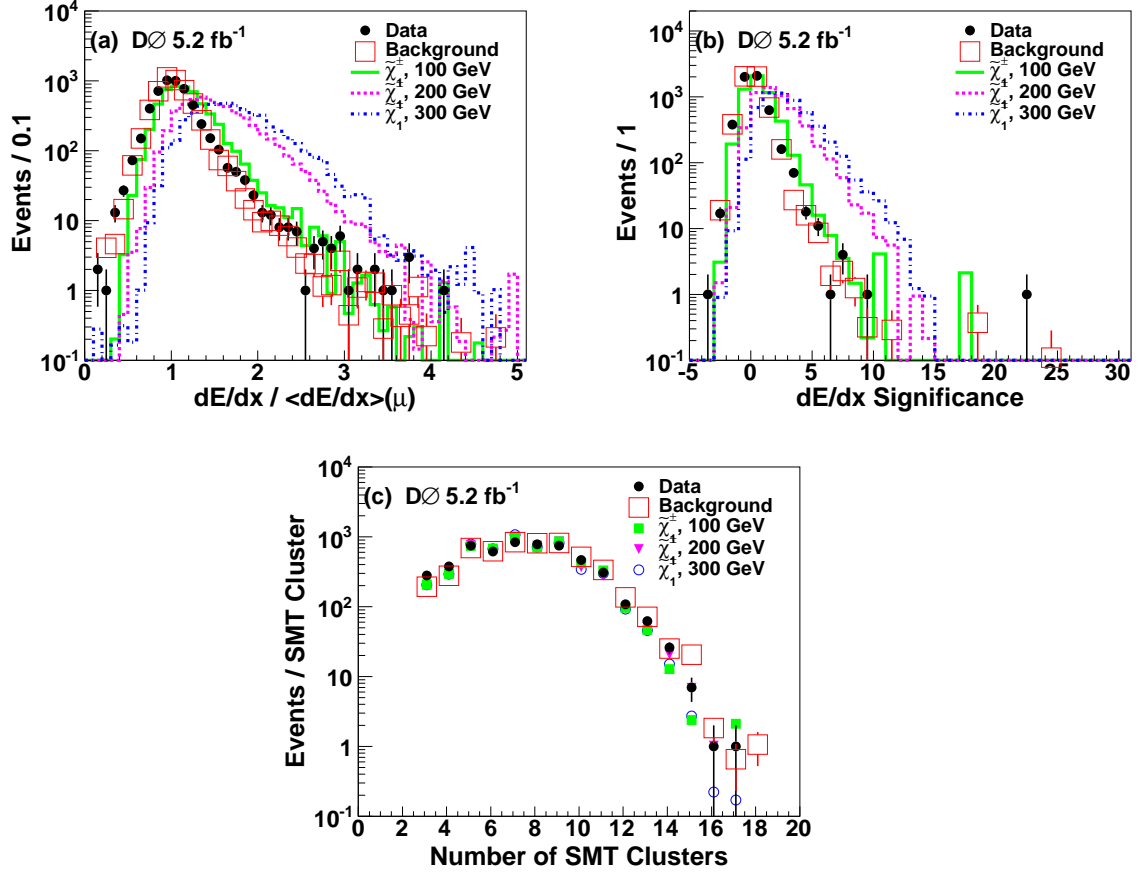


Figure A.18: Final distributions related to the  $dE/dx$  for signal (100, 200, and 300 GeV gaugino-like charginos), background (single muon data with  $M_T < 200$  GeV), and data (single muon data with  $M_T > 200$  GeV). The  $dE/dx$  distribution normalized to  $dE/dx$  from  $Z \rightarrow \mu\mu$  data (a),  $dE/dx$  significance distribution (b), and number of SMT clusters distribution (c). For each plot, the histograms have been normalized to have the same number of events.

These final variables, namely, the speed, speed significance, number of scintillator hits,  $dE/dx$ ,  $dE/dx$  significance, and number of SMT clusters, were the ones that were input to the Toolkit for Multivariate Analysis (TMVA) [265]. TMVA is a ROOT package designed to use multivariate techniques to separate signal from background. The TMVA correlation matrices for 300 GeV staus are shown in Fig. A.19. The results of the TMVA overtraining check, which compares the training and test samples for signal and background, are shown in Fig. A.20, for all of the stau mass points.

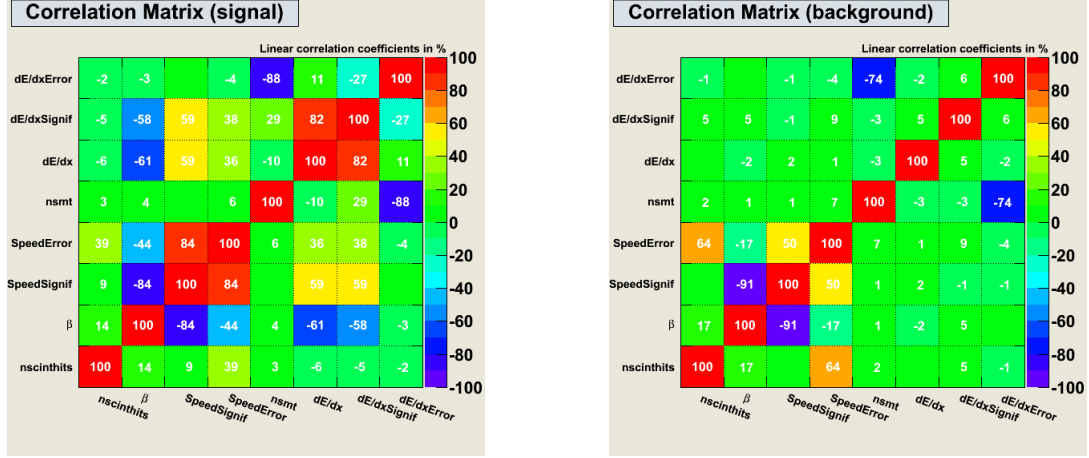


Figure A.19: TMVA correlation matrices for signal, in this case, a 300 GeV stau (left), and for background (right).

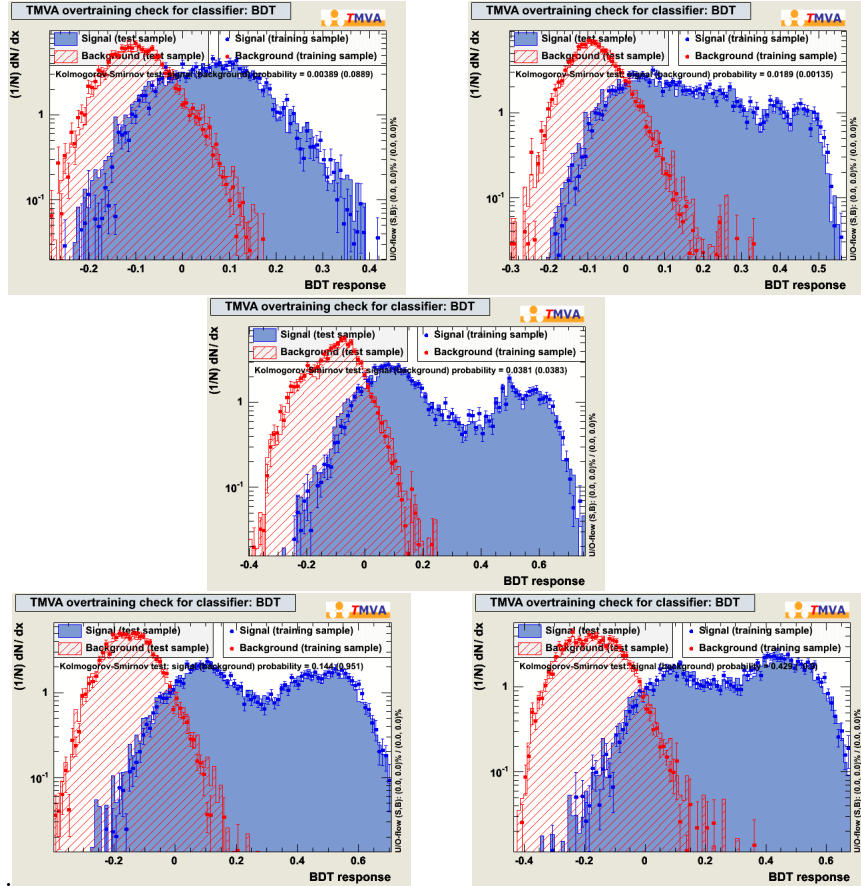


Figure A.20: TMVA overtraining check, which compares the training and test samples for signal and background, for the 100, 150, 200, 250, and 300 GeV staus.

In TMVA, the Boosted Decision Tree (BDT) method was used. One first trains

the BDT on the signal and background distributions to get “weights”. Then, these weights are applied to the signal, background, and data distributions to get the BDT output distributions. The BDT output distributions must be properly normalized to the expected number of events. In particular, the BDT distributions for signal must be normalized by the theoretical cross-section, times the total integrated luminosity, divided by the number of generated events. In addition, the top squarks can undergo charge flipping, and it is at this stage that the probability of a top squark being charged was applied. For the single CMLLP analysis, the probability of at least one top squark in the event being charged in all necessary regions of the detector is 38% (see Section A.1.3). This factor was applied in the top squark signal normalization as an additional multiplicative factor. See [256] for a complete description of the top squark charge flipping probability.

The BDT output distributions for the staus, top squarks, gaugino-like charginos, and higgsino-like charginos, after being normalized to the expected number of events, are shown in Fig. A.21, A.22, A.23, and A.24, respectively. These distributions, along with the systematic uncertainties, were then input to the Confidence Level Limit Evaluator (Collie) [266] to get 95% confidence level cross-section limits (see Section A.8).

Collie does not produce accurate results (especially not the  $-2\sigma$  expected cross-section) when there are bins with signal but no background. Thus, we explicitly required that the highest BDT bin in background was also the last bin for signal, for every signal and mass point. This procedure effectively creates one large bin at the end of the BDT distribution. However, we still obtained anomalous  $-2\sigma$  expected cross-section values for a few mass points where there are low background statistics in the last bin. Collie’s algorithm breaks down when one does not have enough background statistics. The problem was further corrected, for these signal and mass points only, by reducing the number of bins from 15 to 10. As the reader can see in

the BDT plots below, 10 bins were required for the 300 GeV and 400 GeV top squarks, the 300 GeV gaugino-like charginos, and the 250 GeV higgsino-like charginos. Note that changing the binning will, in general, also change the central value of the limits.

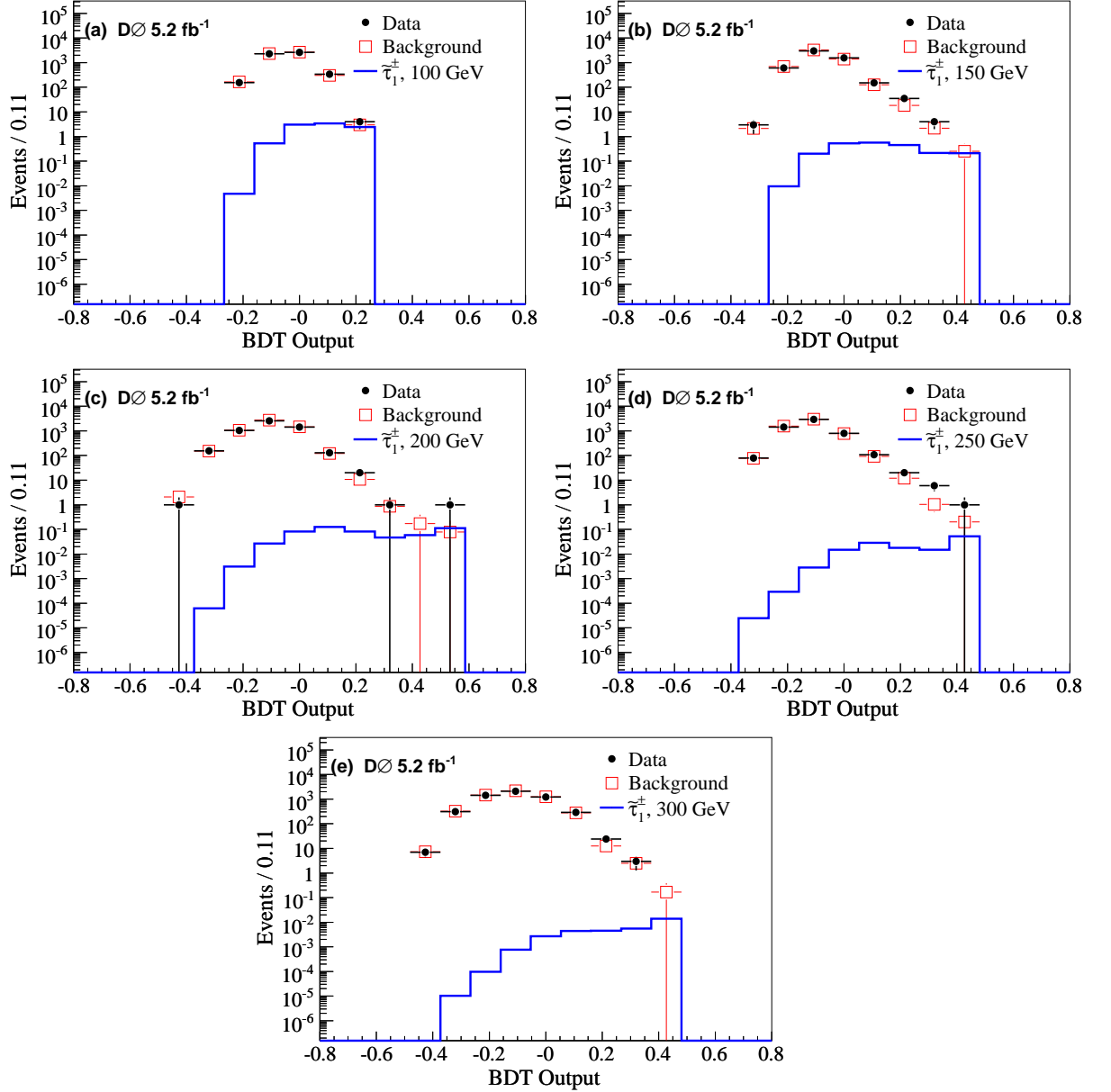


Figure A.21: Final BDT distributions for signal, background, and data. From left to right are displayed the 100, 150, 200, 250, and 300 GeV stau cases. For each plot, the signal histograms have been normalized to the expected number of events.

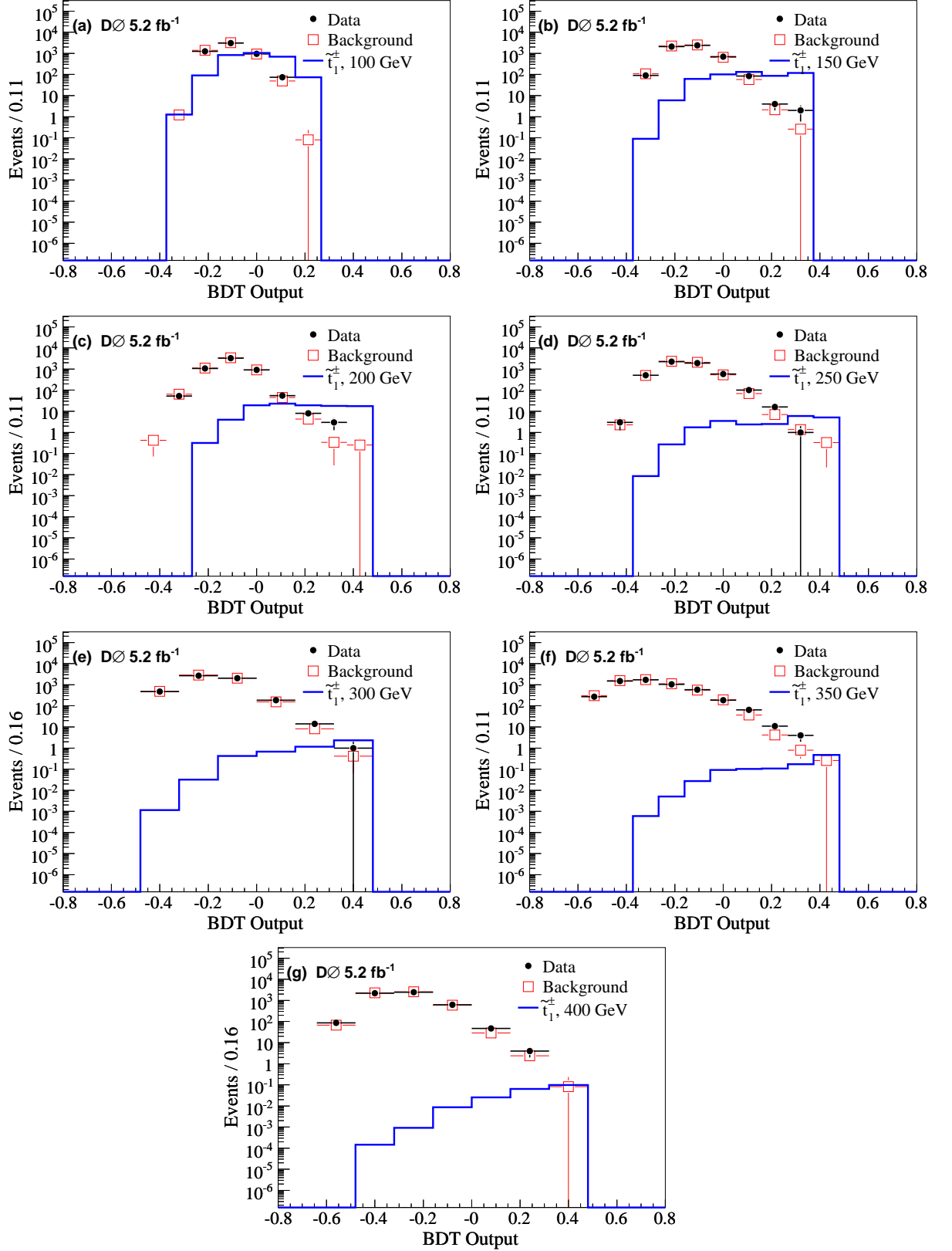


Figure A.22: Final BDT distributions for signal, background, and data. From left to right are displayed the 100, 150, 200, 250, 300, 350, and 400 GeV top squark cases. For each plot, the signal histograms have been normalized to the expected number of events.

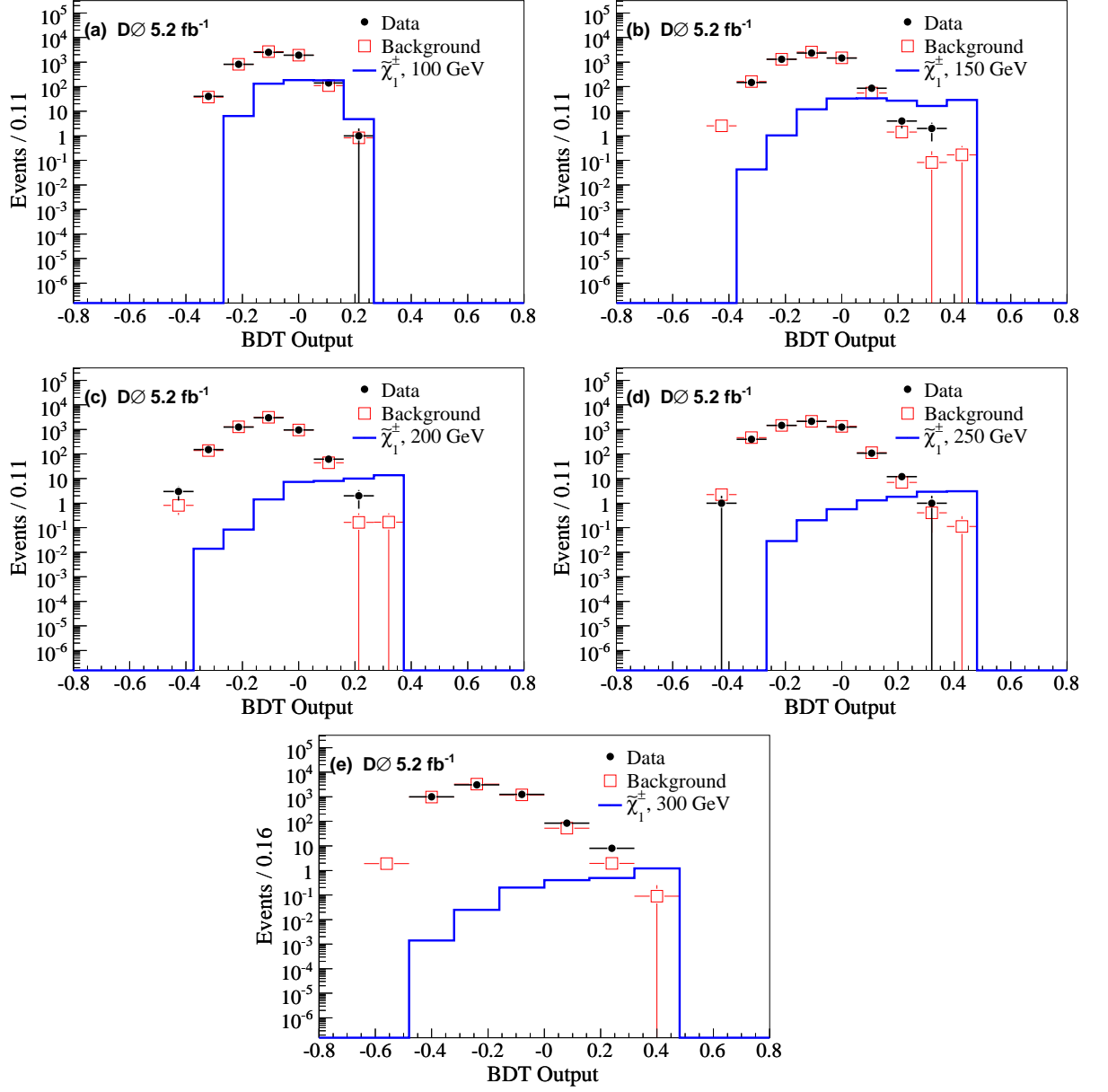


Figure A.23: Final BDT distributions for signal, background, and data. From left to right are displayed the 100, 150, 200, 250, and 300 GeV gaugino-like chargino cases. For each plot, the signal histograms have been normalized to the expected number of events.

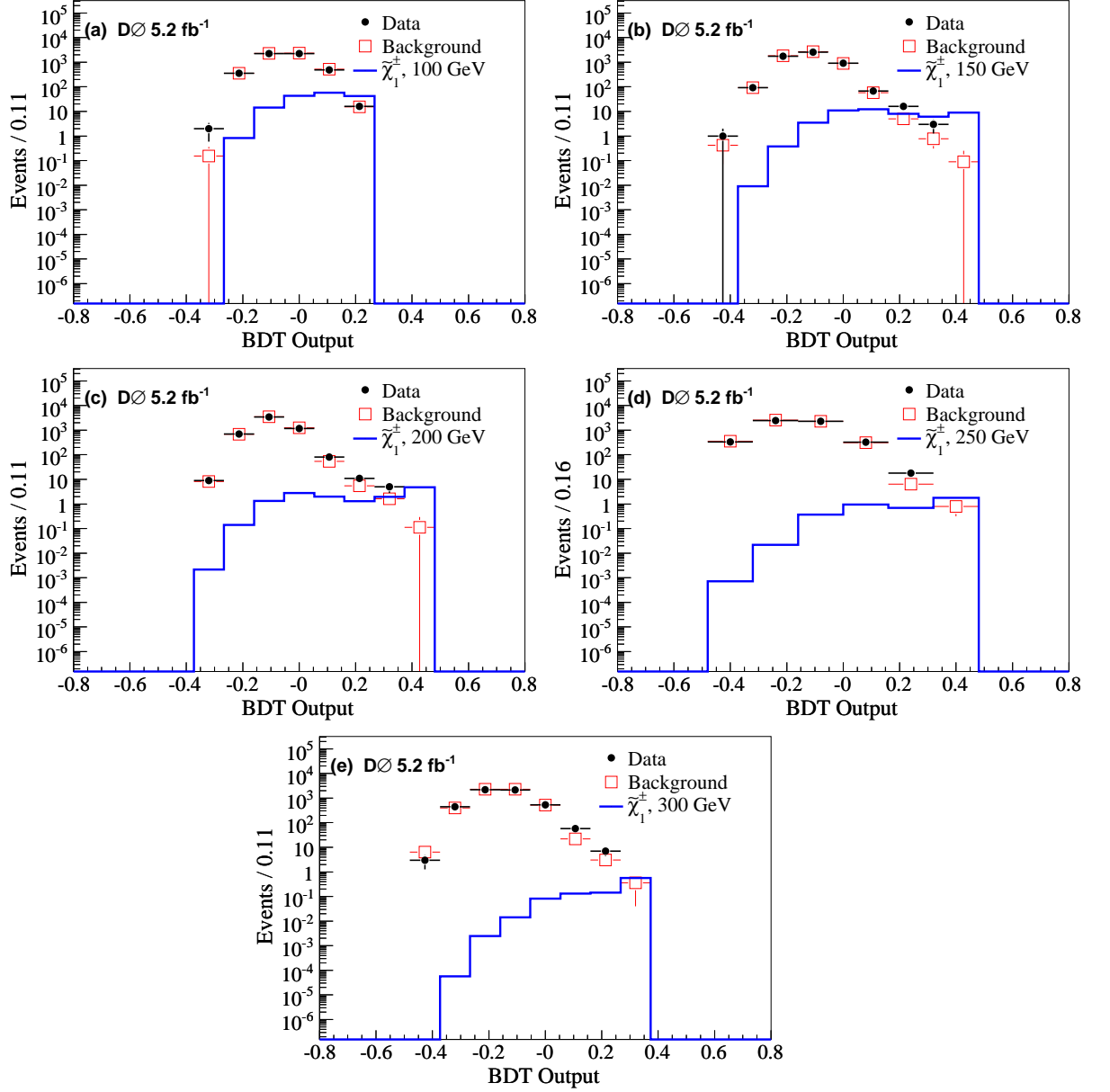


Figure A.24: Final BDT distributions for signal, background, and data. From left to right are displayed the 100, 150, 200, 250, and 300 GeV higgsino-like chargino cases. For each plot, the signal histograms have been normalized to the expected number of events.

## A.7 Systematic Uncertainties

Several choices made in the analysis could have a systematic effect on the results.

Each systematic uncertainty, besides the known typical systematic uncertainties, was

studied in turn by creating the variation in the final ntuples and then passing these ntuples through our version of `TMVAClassificationApplication.C` to obtain BDT distributions for each variation. One could determine how much these new BDT distributions varied from the original distributions. If the variation was constant for all bins of the BDT, then the systematic was taken to be a “flat” systematic uncertainty and was inputted appropriately into the Collie IO file. If the variation was not constant in the BDT bins, then the systematic was taken to be a “shape” systematic uncertainty and was inputted into Collie as such.

### A.7.1 Flat Systematic Uncertainties

A few systematic uncertainties, which are used in many D0 analyses, are well-known to be flat. These systematics include the luminosity uncertainty (6.1%) [267] and the muon identification uncertainty (2.1%). The muon identification uncertainty was the combination in quadrature of the muID uncertainty (1.2%), the muon track uncertainty (1.4%), and the muon isolation uncertainty (0.9%) [264]. These systematics were only applied to the MC, so therefore, only to the signal.

The rest of the systematics were studied one by one, comparing each BDT variation to the original BDT distributions. Many of these were found to be small and flat with respect to the shape of the BDT. The systematics that were found to be flat were: the background normalization uncertainty from the choice of the  $\beta$  cut (7.2%) and from the choice of the  $M_T$  cut (2.2%), the muon  $p_T$  smearing uncertainty (0.2%), the  $dE/dx$  correction uncertainty ( $<0.1\%$ ), the  $dE/dx$  smearing uncertainty (0.2%), and the speed  $\chi^2$  correction uncertainty (0.4%).

The analysis results could vary with the exact choice of background events. The background was normalized by taking the ratio of the number of signal-free data events to the number of signal-free background events. The signal-free data were data events with  $\beta > 1$  and  $M_T > 200$  GeV, and the signal-free background events



were data events with  $\beta > 1$  and  $M_T < 200$  GeV. The background normalization can be systematically varied by choosing different values to cut on  $\beta$ , for example, choose  $\beta$  cuts of 0.9 and 1.1. These two choices for  $\beta$  were made, and then the “ratio of ratios” was recomputed, where the “ratio of ratios” is:  $\frac{N_D}{N_{SFD}} / \frac{N_B}{N_{SFB}}$ . Subsequently, it was determined how much these new “ratios of ratios” differed from the original, and the average difference was taken as the  $\beta$  cut systematic:  $\pm 7.2\%$ . Likewise, the  $M_T$  cut can be varied to 180 and 220 GeV, and the computation of the new “ratios of ratios” and how they differed from the original gave an  $M_T$  cut systematic of  $\pm 2.2\%$ .

The muon  $p_T$  smearing is done as a processor within `vjets_cafe`. The  $\pm 1\sigma$  variations can be obtained by using the “shifted up parameters” and the “shifted down parameters”, respectively. The  $\pm 1\sigma$  variations were obtained and the BDT distributions were compared with the originals. For each signal (stau, top squark, gaugino-like chargino, and higgsino-like chargino) and mass point (100, 150, 200, 250, and 300 GeV/ $c^2$ ), the BDT distributions changed no more than  $\pm 0.2\%$ , which was taken to be the systematic for all signal samples and mass points.

Another systematic was to vary the choice of PDF, which was done using the `caf_pdfreweight v00-00-05 D0` package. For each signal (stau, top squark, gaugino-like chargino, and higgsino-like chargino) and mass point (100, 150, 200, 250, and 300 GeV/ $c^2$ ), the BDT distributions changed no more than  $\pm 0.2\%$ .

The  $dE/dx$  correction was made to the data to account for the shifts and downward slope in the graph of the mean  $dE/dx$  as a function of total integrated luminosity [263]. For each event, the correction was the mean  $dE/dx$  for the given integrated luminosity. We systematically varied this correction by using the mean  $dE/dx$  plus or minus its error, for the given integrated luminosity. This systematic was also relatively small and could be taken to be flat. For the background, the systematic was  $\pm 0.1\%$ , and for the signal, the systematic was  $\pm 0.02\%$ .

The MC  $dE/dx$  distributions were smeared slightly to maximize the agreement

with data. The smearing was optimized so that the  $Z \rightarrow \mu\mu$  MC distribution most agreed with the  $Z \rightarrow \mu\mu$  data distribution. For the systematic, we instead looked for the most agreement with the  $W \rightarrow \mu\nu$  data distribution. Again, the systematic gave flat results, with a fluctuation of  $\pm 0.2\%$ .

The speed  $\chi^2$  correction uncertainty was also taken to be a flat systematic. The speed  $\chi^2$  event weight for signal was derived based on the ratio of  $Z \rightarrow \mu\mu$  data to  $Z \rightarrow \mu\mu$  MC for each bin in the speed  $\chi^2$  distribution, so for the systematic,  $W \rightarrow \mu\nu$  data was used instead of  $Z \rightarrow \mu\mu$  data. The speed  $\chi^2$  distribution between  $Z \rightarrow \mu\mu$  and  $W \rightarrow \mu\nu$  data was very similar, so the systematic uncertainty was found to be small and flat:  $\pm 0.4\%$ .

### A.7.2 Shape Systematic Uncertainties

Systematics relating to the timing were also considered, and these were found to be shape systematics, meaning that they significantly altered the shape of the BDT distribution.

The first shape systematic varied the width of the level 1 (L1) timing gates, which are explicitly applied to the MC, by  $\pm 1$  ns to reflect the uncertainty in these widths. Figure A.25 shows plots for this systematic for one signal sample and mass point (the 300 GeV stau, in this case). On the left, one can see the original BDT distribution and the variations by  $\pm 1$  ns. On the right, one can see the ratio of the BDT with the systematic minus the BDT without the systematic, all divided by the BDT without the systematic. In other words, this plot shows how much the variations differ from the original. The “tight timing” plots correspond to a variation of -1 ns, while the “loose timing” plots correspond to +1 ns.

Secondly, the timing smearing systematic was taken to be a shape. The timing smearing was originally done with  $Z \rightarrow \mu\mu$  data timing distributions, so the smearing was redone using the  $W \rightarrow \mu\nu$  data distributions. See Fig. A.26 for plots relating to

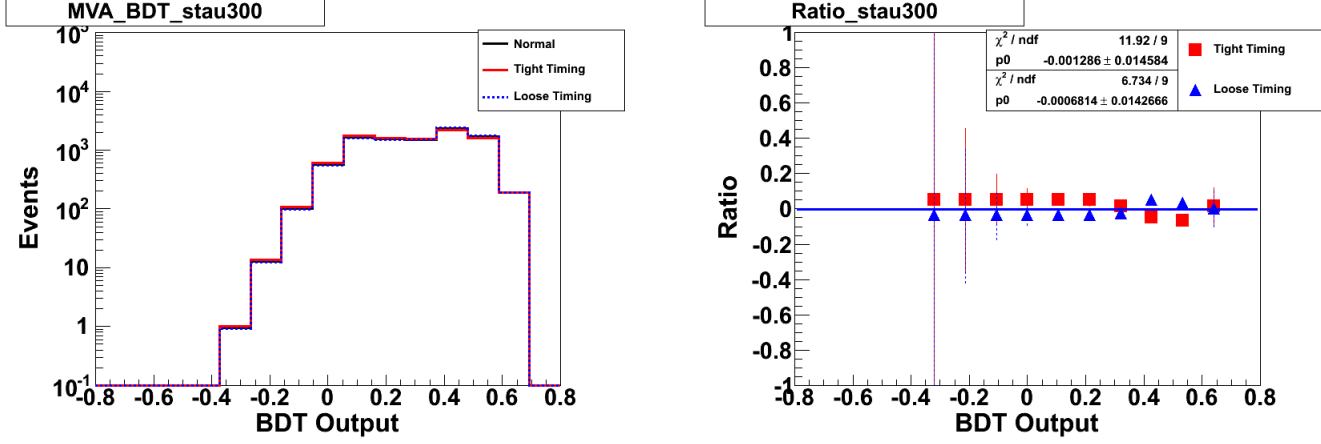


Figure A.25: Plots of the L1 timing gate systematic for the 300 GeV stau case. The BDT distributions for the original and the two variations (left), and how much each variation changed the original (right). The histograms in each plot have been normalized to have the same number of events.

this systematic, for the 100 GeV higgsino-like chargino case.

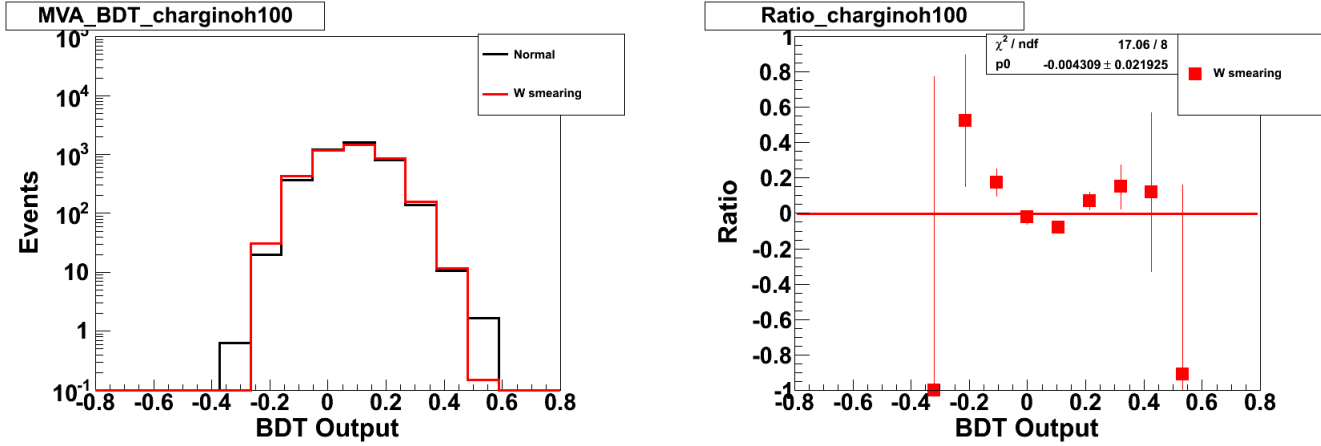


Figure A.26: Plots of the timing smearing systematic for the 100 GeV higgsino-like chargino case. The BDT distributions for the original and the variation (left), and how much the variation changed the original (right). The histograms in each plot have been normalized to have the same number of events.

The systematics are summarized in Table A.8.

Table A.8: Summary of systematic uncertainties.

Systematic Uncertainty	Background	Signal
Luminosity Uncertainty	-	Flat, $\pm 6.1\%$
Muon Identification Uncertainty	-	Flat, $\pm 2.1\%$
Background Normalization ( $\beta$ cut)	Flat, $\pm 7.2\%$	-
Background Normalization ( $M_T$ cut)	Flat, $\pm 2.2\%$	-
Muon $p_T$ Smearing Uncertainty	-	Flat, $\pm 0.2\%$
PDF Uncertainty	-	Flat, $< \pm 0.2\%$
$dE/dx$ Correction Uncertainty	Flat, $\pm 0.1\%$	Flat, $\pm 0.02\%$
$dE/dx$ Smearing Uncertainty	-	Flat, $\pm 0.2\%$
Speed $\chi^2$ Correction Uncertainty	-	Flat, $\pm 0.4\%$
L1 Timing Gate Uncertainty	-	Shape
Timing Smearing Uncertainty	-	Shape

## A.8 Results

A table of the expected number of events was obtained from the number of events in the signal-like region of the BDT distributions. A cut in the BDT was applied to define the signal-like region. However, this cut in the BDT was not optimized for the best expected limit, but rather, one cut (BDT value  $> 0.27$ ) was applied for each signal MC and each mass point. The BDT cut was not optimized for simplicity and clarity. The percentage of signal acceptance and numbers of predicted background and observed data events, as obtained from this BDT cut, are shown in Tables A.9-A.12. Please note that these tables are for illustrative purposes only and are not taken into account for the 95% CL limits.

Table A.9: Expected event table for staus.

Mass [GeV]	Signal Acceptance (%)	Predicted Background	Observed Data
100	$0.97 \pm 0.001(\text{stat.}) \pm 0.10(\text{sys.})$	$0 \pm 0(\text{stat.}) \pm 0(\text{sys.})$	0
150	$3.04 \pm 0.001 \pm 0.07$	$2.43 \pm 0.001 \pm 0.18$	4
200	$6.20 \pm 0.001 \pm 0.39$	$1.11 \pm 0.001 \pm 0.08$	2
250	$7.86 \pm 0.001 \pm 0.47$	$1.24 \pm 0.001 \pm 0.09$	7
300	$8.29 \pm 0.01 \pm 0.36$	$2.63 \pm 0.001 \pm 0.20$	3

Table A.10: Expected event table for top squarks.

Mass [GeV]	Signal Acceptance (%)	Predicted Background	Observed Data
100	$0.01 \pm 0.001(\text{stat.}) \pm 0.001(\text{sys.})$	$0 \pm 0(\text{stat.}) \pm 0(\text{sys.})$	0
150	$1.18 \pm 0.001 \pm 0.13$	$0.25 \pm 0.001 \pm 0.02$	2
200	$2.02 \pm 0.001 \pm 0.15$	$0.59 \pm 0.001 \pm 0.04$	3
250	$2.60 \pm 0.001 \pm 0.17$	$1.70 \pm 0.001 \pm 0.13$	1
300	$2.84 \pm 0.001 \pm 0.18$	$3.01 \pm 0.001 \pm 0.23$	2
350	$2.56 \pm 0.001 \pm 0.21$	$1.05 \pm 0.001 \pm 0.08$	4
400	$2.38 \pm 0.001 \pm 0.16$	$0.53 \pm 0.001 \pm 0.04$	1

Table A.11: Expected event table for gaugino-like charginos.

Mass [GeV]	Signal Acceptance (%)	Predicted Background	Observed Data
100	$0 \pm 0(\text{stat.}) \pm 0(\text{sys.})$	$0 \pm 0(\text{stat.}) \pm 0(\text{sys.})$	0
150	$3.16 \pm 0.001 \pm 0.20$	$0.25 \pm 0.001 \pm 0.02$	2
200	$3.60 \pm 0.001 \pm 1.39$	$0.17 \pm 0.001 \pm 0.01$	0
250	$5.33 \pm 0.001 \pm 0.41$	$0.51 \pm 0.001 \pm 0.04$	1
300	$4.59 \pm 0.001 \pm 0.47$	$0.59 \pm 0.001 \pm 0.04$	1

Table A.12: Expected event table for higgsino-like charginos.

Mass [GeV]	Signal Acceptance (%)	Predicted Background	Observed Data
100	$0.33 \pm 0.001(\text{stat.}) \pm 0.12(\text{sys.})$	$0 \pm 0(\text{stat.}) \pm 0(\text{sys.})$	0
150	$3.65 \pm 0.001 \pm 0.26$	$0.87 \pm 0.001 \pm 0.07$	3
200	$5.87 \pm 0.001 \pm 0.35$	$1.75 \pm 0.001 \pm 0.13$	5
250	$5.39 \pm 0.001 \pm 0.64$	$0.79 \pm 0.001 \pm 0.06$	2
300	$4.87 \pm 0.001 \pm 0.38$	$0.36 \pm 0.001 \pm 0.03$	0

Event displays of two candidate events are shown in Figures A.27 and A.28. For the first event (event # 12813686, run # 243293),  $\beta$  is 0.742, it has 2 scintillator hits, the adjusted  $dE/dx$  is 3.33, and there were 5 SMT clusters. For the second event (event # 22550709, run # 247800),  $\beta$  is 0.654, there were 2 scintillator hits, the adjusted  $dE/dx$  is 1.43, and there were 9 SMT clusters.



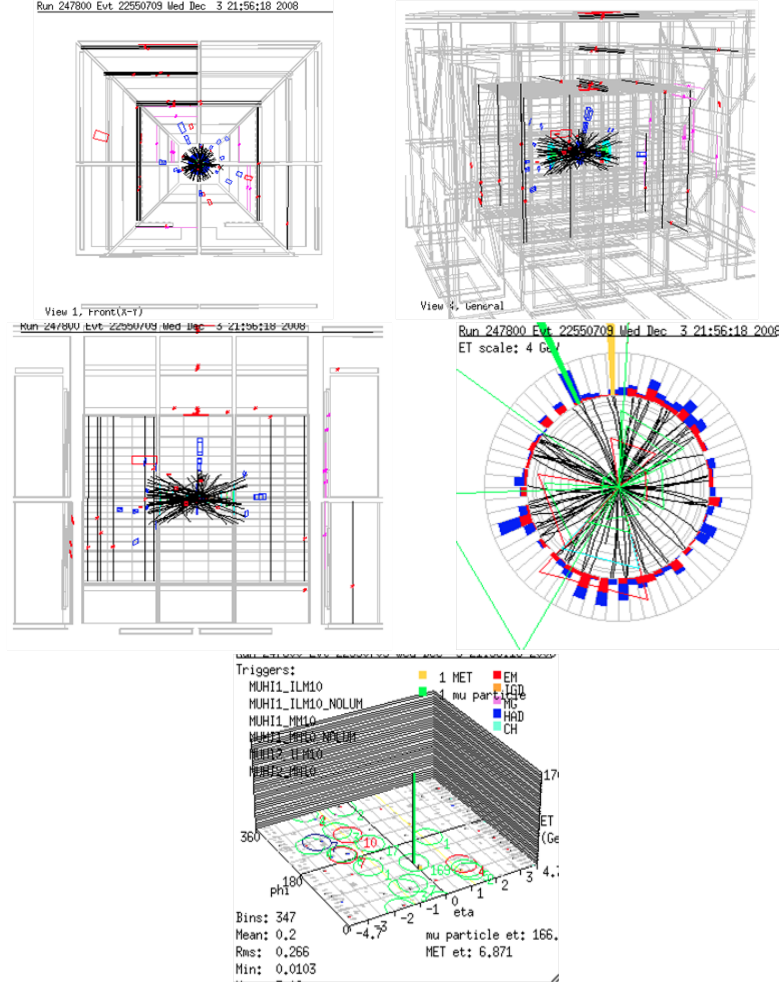


Figure A.28: Event displays for a candidate event (event # 22550709, run # 247800).

95% CL cross-section limits, as obtained with Collie's CLfit2, are shown in Tables A.13, A.14, A.15, A.16, and in Fig. A.29. Using the intersection of the observed 95% CL cross-section limit with the NLO limit, mass limits could be set for top squarks, gaugino-like charginos and higgsino-like charginos. The mass limits are 285 GeV for top squarks (assuming a charge survival probability of 38%), 267 GeV for gaugino-like charginos, and 217 GeV for higgsino-like charginos.

Figure A.14 also shows the top squark limits when there is no charge flipping. When there is no charge flipping, the top squark charge survival probability will be 84% for the single analysis, to take into account the fact that at production, not all top squarks are charged (see Section A.1.3). As can be seen in this figure, a mass

limit of 305 GeV could be set when there is no charge flipping.

Table A.13: NLO cross-sections and cross-section limits for staus.

Mass [GeV]	NLO Cross-Section [pb]	95% CL Limit [pb]	Expected Limit $\pm 1\sigma$ [pb]
100	0.0120	0.038	$0.025^{+0.011}_{-0.0075}$
150	0.0021	0.050	$0.018^{+0.0076}_{-0.0038}$
200	0.00050	0.013	$0.0066^{+0.0020}_{-0.0008}$
250	0.00010	0.015	$0.0055^{+0.0015}_{-0.0008}$
300	0.000030	0.006	$0.0053^{+0.0013}_{-0.0007}$

Table A.14: NLO cross-sections and cross-section limits for top squarks, assuming a charge survival probability of 38%.

Mass [GeV]	NLO Cross-Section [pb]	95% CL Limit [pb]	Expected Limit $\pm 1\sigma$ [pb]
100	15.6	0.70	$0.26^{+0.094}_{-0.078}$
150	1.58	0.081	$0.030^{+0.011}_{-0.0063}$
200	0.27	0.053	$0.021^{+0.0096}_{-0.0043}$
250	0.056	0.025	$0.020^{+0.0088}_{-0.0049}$
300	0.013	0.026	$0.016^{+0.0061}_{-0.0016}$
350	0.0032	0.032	$0.016^{+0.0046}_{-0.0024}$
400	0.0008	0.020	$0.016^{+0.0036}_{-0.0031}$

Table A.15: NLO cross-sections and cross-section limits for gaugino-like charginos.

Mass [GeV]	NLO Cross-Section [pb]	95% CL Limit [pb]	Expected Limit $\pm 1\sigma$ [pb]
100	1.33	0.44	$0.180^{+0.076}_{-0.051}$
150	0.240	0.033	$0.0120^{+0.0047}_{-0.0028}$
200	0.0570	0.014	$0.0070^{+0.0026}_{-0.00006}$
250	0.0150	0.010	$0.0072^{+0.0031}_{-0.0004}$
300	0.0042	0.014	$0.0084^{+0.0012}_{-0.0014}$

Table A.16: NLO cross-sections and cross-section limits for higgsino-like charginos.

Mass [GeV]	NLO Cross-Section [pb]	95% CL Limit [pb]	Expected Limit $\pm 1\sigma$ [pb]
100	0.3810	0.088	$0.087^{+0.038}_{-0.026}$
150	0.0740	0.038	$0.015^{+0.0049}_{-0.0033}$
200	0.0190	0.015	$0.0095^{+0.0018}_{-0.0017}$
250	0.0053	0.013	$0.0091^{+0.0047}_{-0.0013}$
300	0.0015	0.0103	$0.0077^{+0.0025}_{-0.0009}$



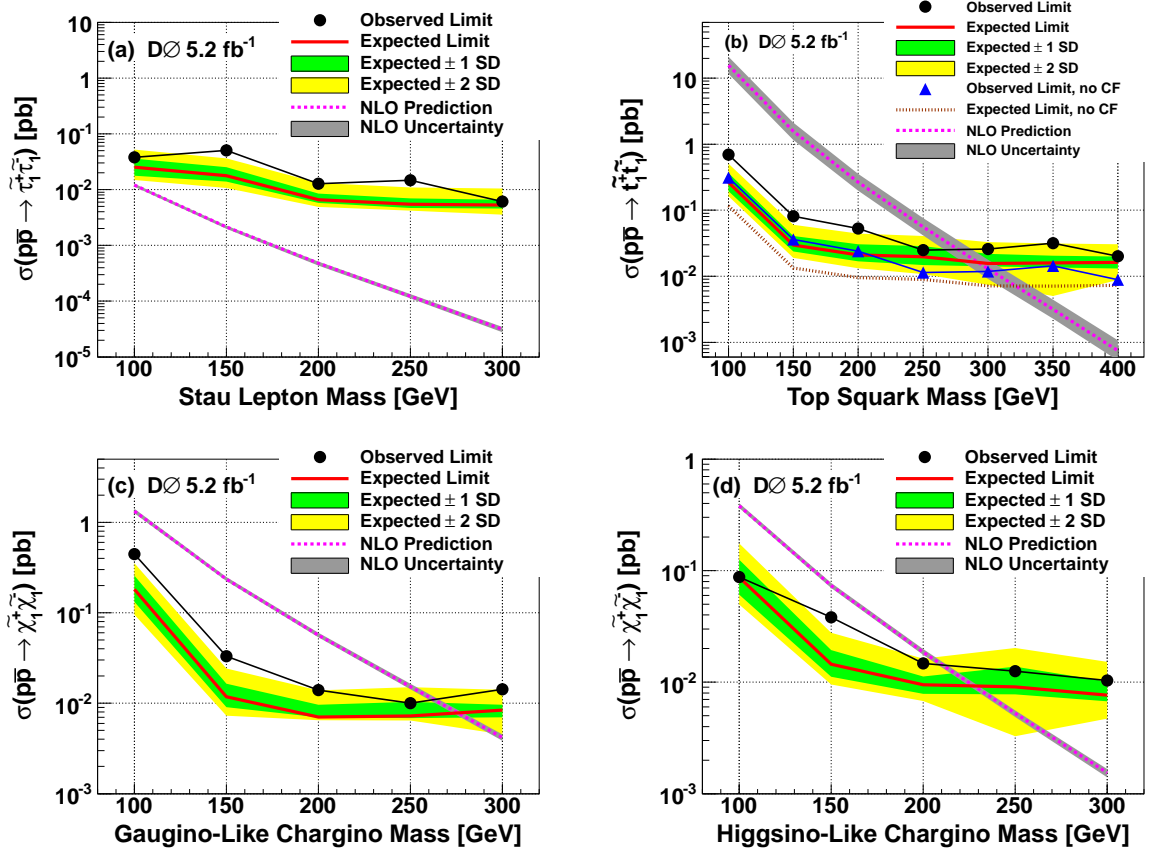


Figure A.29: 95% CL cross-section limits as a function of mass for stau (top left), top squarks (top right), gaugino-like charginos (bottom left), and higgsino-like charginos (bottom right). For the main top squark limits with the 1 and 2  $\sigma$  bands, a charge survival probability of 38% was assumed.

We could extend the results presented here by adding cascade decays to the pair produced signal samples we have worked with so far. The addition of cascades will increase our acceptance times cross-section and allow for improved limits. The cascade decays can be easily added to the stau MC because our stau signal is a particular GMSB model. We can add the following cascade decays: chargino1 pair decay, chargino1 neutralino2 decay, RH smuon decay, and selectron decay. The cross-sections and acceptances have been calculated for 100 GeV staus, and they are summarized in Table A.17. By comparing the total acceptance times cross-section with that of the 100 GeV stau pair alone, we can see that for the single analysis, the acceptance times cross-section would increase by 80% after including the cascade decays, for the 100

GeV stau case. However, this would not be enough to set a mass limit for the staus around 100 GeV, and so we did not pursue the cascade decays further.

Table A.17: Acceptance times cross-section for 100 GeV staus: pair produced and cascade decays.

	Acceptance	Cross Section [pb]	Acceptance*Cross Section [pb]
100 GeV stau pair	0.138	0.0122	0.00168
100 GeV stau through chargino1 pair decay	0.073	0.00786	0.000574
100 GeV stau through chargino1, neutralino2 decay	0.066	0.00467	0.000308
100 GeV stau through RH smuon decay	0.081	0.00457	0.000370
100 GeV stau through selectron decay	0.081	0.00457	0.000370
Total			0.00302

# Bibliography

- [1] Particle Data Group, “Review of Particle Physics,” *Chin. Phys.C* **38** (2014) 090001. [[link](#)].
- [2] D. Griffiths, *Introduction to Elementary Particles*. WILEY-VCH Verlag GmbH & Co., 2008.
- [3] F. Halzen and A. D. Martin, *Quarks and Leptons: An Introductory Course in Modern Particle Physics*. John Wiley and Sons, 1984.
- [4] S. F. Novaes, “Standard Model: An Introduction,” *arXiv e-print hep-ph/0001283* (2000) . [[link](#)].
- [5] G. S. Guralnik, “The History of the Guralnik, Hagen and Kibble Development of the Theory of Spontaneous Symmetry Breaking and Gauge Particles,” *Int. J. Mod. Phys. A* **24** (2009) 2601–2627. [[link](#)].
- [6] ATLAS Collaboration, “Observation of a new particle in the search for the Standard Model Higgs boson with the ATLAS detector at the LHC,” *Phys. Lett. B* **716** (2012) 1 – 29. [[link](#)].
- [7] CMS Collaboration, “Observation of a new boson at a mass of 125 GeV with the CMS experiment at the LHC,” *Phys. Lett. B* **716** (2012) 30 – 61. [[link](#)].

- [8] ATLAS Collaboration, “A Particle Consistent with the Higgs Boson Observed with the ATLAS Detector at the Large Hadron Collider,” *Science* **338** (2012) 1576 – 1582. [[link](#)].
- [9] CMS Collaboration, “A New Boson with a Mass of 125 GeV Observed with the CMS Experiment at the Large Hadron Collider,” *Science* **338** (2012) 1569 – 1575. [[link](#)].
- [10] A. Djouadi, “The anatomy of electroweak symmetry breaking: Tome I: The Higgs boson in the Standard Model,” *Phys. Rept.* **457** (2008) 1–216. [[link](#)].
- [11] M. Baak and R. Kogler, “The global electroweak Standard Model fit after the Higgs discovery,” *Proceedings - Rencontres de Moriond* (2013) . [[link](#)].
- [12] D. Kazakov, “Beyond the Standard Model (In Search of Supersymmetry),” *arXiv e-print hep-ph/0012288* (2001) . [[link](#)].
- [13] S. Carroll, *Spacetime and Geometry: An Introduction to General Relativity*. Addison Wesley, 2004.
- [14] S. Dodelson, *Modern Cosmology*. Elsevier Ltd., 2003.
- [15] J. H. Schwarz, M. B. Green, and E. Witten, *Superstring Theory*. Cambridge University Press, 1987.
- [16] C. Rovelli, *Quantum Gravity*. Cambridge University Press, 2007.
- [17] R. Davis, “Solar Neutrinos. II. Experimental,” *Phys. Rev. Lett.* **12** (1964) 303 – 305. [[link](#)].
- [18] SNO Collaboration, “Combined analysis of all three phases of solar neutrino data from the Sudbury Neutrino Observatory,” *Phys. Rev. C* **88** (2013) 025501. [[link](#)].

- [19] The Super-Kamiokande Collaboration, “Solar neutrino measurements in Super-Kamiokande-II,” *Phys. Rev. D* **78** (2008) 032002. [[link](#)].
- [20] Daya Bay Collaboration, “Observation of Electron-Antineutrino Disappearance at Daya Bay,” *Phys. Rev. Lett.* **108** (2012) 171803. [[link](#)].
- [21] T2K Collaboration, “Observation of Electron Neutrino Appearance in a Muon Neutrino Beam,” *Phys. Rev. Lett.* **112** (2014) 061802. [[doi](#)].
- [22] J. P. Ostriker and P. Steinhardt, “New Light on Dark Matter,” *Science* **300** (2003) 1909–1913. [[link](#)].
- [23] F. Zwicky, “On the Masses of Nebulae and of Clusters of Nebulae,” *Astrophysical Journal* **86** (1937) 217. [[link](#)].
- [24] V. Rubin, W. Ford, and N. Thonnard, “Extended Rotation Curves of High-Luminosity Spiral Galaxies.4. Systematic Dynamical Properties SA,” *Astrophysical Journal* **225** (1978) L107–L111. [[link](#)].
- [25] WMAP Collaboration, “Nine-year Wilkinson Microwave Anisotropy Probe (WMAP) Observations: Cosmological Parameter Results,” *The Astrophysical Journal Supplement Series* **208** (2013) 19. [[doi](#)].
- [26] WMAP Collaboration, “Nine-year Wilkinson Microwave Anisotropy Probe (WMAP) Observations: Final Maps and Results,” *The Astrophysical Journal Supplement Series* **208** (2013) 20. [[doi](#)].
- [27] Planck Collaboration, “Planck 2013 results. XVI. Cosmological parameters,” *Astronomy & Astrophysics* **571** (2014) A16. [[doi](#)].
- [28] LUX Collaboration, “First results from the LUX dark matter experiment at the Sanford Underground Research Facility,” *Phys. Rev. Lett.* **112** (2014) 091303. [[doi](#)].

- [29] XENON100 Collaboration, “Dark Matter Results from 225 Live Days of XENON100 Data,” *Phys. Rev. Lett.* **109** (2012) 181301. [[link](#)].
- [30] CDMS Collaboration, “Silicon Detector Dark Matter Results from the Final Exposure of CDMS II,” *Phys. Rev. Lett.* **111** (2013) 251301. [[doi](#)].
- [31] DAMA/LIBRA Collaboration, “First results from DAMA/LIBRA and the combined results with DAMA/NaI,” *Eur. Phys. J. C* **56** (2008) 333 – 355. [[link](#)].
- [32] PAMELA Collaboration, “Cosmic-Ray Positron Energy Spectrum Measured by PAMELA,” *Phys. Rev. Lett.* **111** (2013) 081102. [[link](#)].
- [33] IceCube Collaboration, “Evidence for High-Energy Extraterrestrial Neutrinos at the IceCube Detector,” *Science* **342** (2013) 1242856. [[link](#)].
- [34] J. A. Frieman, M. S. Turner, and D. Huterer, “Dark Energy and the Accelerating Universe,” *Annual Review of Astronomy and Astrophysics* **46** (2008) 385 – 432. [[link](#)].
- [35] High- $z$  Supernova Search Team, “Observational Evidence from Supernovae for an Accelerating Universe and a Cosmological Constant,” *The Astronomical Journal* **116** (1998) 1009. [[link](#)].
- [36] The Supernova Cosmology Project, “Measurements of  $\Omega$  and  $\Lambda$  from 42 High-Redshift Supernovae,” *The Astrophysical Journal* **517** (1999) 565. [[link](#)].
- [37] A. Sakharov, “Expanding Universe and the Appearance of a Nonuniform Distribution of Matter,” *Letters to Journal of Experimental and Theoretical Physics* **5** (1967) 24.

- [38] H. Haber and G. Kane, “The search for supersymmetry: Probing physics beyond the standard model,” *Phys. Rept.* **117** (1985) 75 – 263. [\[link\]](#).
- [39] S. P. Martin, “A Supersymmetry Primer,” *arXiv e-print* **hep-ph/9709356** (1997) . [\[link\]](#).
- [40] J. D. Lykken, “Beyond the Standard Model,” *arXiv e-print* **1005.1676** (2011) . [\[link\]](#).
- [41] T. Kaluza *Preus. Acad. Wiss.* **K 1** (1921) 966.
- [42] O. Klein *Zeit. Phys.* **37** (1926) 895.
- [43] T. Appelquist, A. Chodos, and P. Freund, eds., *Modern Kaluza-Klein Theo.* Menlo Park, 1987.
- [44] D. Bailin and A. Love, “Kaluza-Klein theories,” *Rep. Prog. Phys.* **50** (1987) 1087. [\[link\]](#).
- [45] N. Arkani-Hamed, S. Dimopoulos, and G. Dvali, “The hierarchy problem and new dimensions at a millimeter,” *Phys. Lett. B* **429** (1998) 263. [\[link\]](#).
- [46] N. Arkani-Hamed, S. Dimopoulos, and G. Dvali, “Phenomenology, astrophysics, and cosmology of theories with submillimeter dimensions and TeV scale quantum gravity,” *Phys. Rev. D* **59** (1999) 086004. [\[link\]](#).
- [47] L. Randall and R. Sundrum, “Large Mass Hierarchy from a Small Extra Dimension,” *Phys. Rev. Lett.* **83** (1999) 3370 – 3373. [\[link\]](#).
- [48] C. T. Hill and E. H. Simmons, “Strong dynamics and electroweak symmetry breaking,” *Phys. Rept.* **381** (2003) 235 – 402. [\[link\]](#).
- [49] M. Schmaltz and D. Tucker-Smith, “Little Higgs Theories,” *Annu. Rev. Nucl. Part. Sci.* **55** (2005) 229 – 270. [\[link\]](#).

- [50] M. Perelstein, “Little Higgs models and their phenomenology,” *Prog. Part. Nucl. Phys.* **58** (2007) 247 – 291. [[link](#)].
- [51] N. Arkani-Hamed, A. G. Cohen, and H. Georgi, “Electroweak symmetry breaking from dimensional deconstruction,” *Phys. Lett. B* **513** (2001) 232 – 240. [[link](#)].
- [52] N. Arkani-Hamed, T. Gregoire, J. G. Wacker, and A. G. Cohen, “Phenomenology of Electroweak Symmetry Breaking from Theory Space,” *JHEP* **2002** (2002) 020. [[link](#)].
- [53] Z. Chacko, H.-S. Goh, and R. Harnik, “Natural Electroweak Breaking from a Mirror Symmetry,” *Phys. Rev. Lett.* **96** (2006) 231802. [[link](#)].
- [54] M. J. Strassler and K. M. Zurek, “Echoes of a hidden valley at hadron colliders,” *Phys. Lett. B* **651** (2007) 374–379. [[link](#)].
- [55] M. J. Strassler, “Possible effects of a hidden valley on supersymmetric phenomenology,” *arXiv e-print hep-ph/0607160* (2006) . [[link](#)].
- [56] Y. Bai, M. Carena, and J. Lykken, “Dilaton-Assisted Dark Matter,” *Phys. Rev. Lett.* **103** (2009) 261803. [[link](#)].
- [57] N. Arkani-Hamed, D. P. Finkbeiner, T. R. Slatyer, and N. Weiner, “A theory of dark matter,” *Phys. Rev. D* **79** (2009) 015014. [[link](#)].
- [58] CERN Communications Group, “CERN FAQ: LHC the Guide,” *CERN-Brochure-2008-001-Eng* (2008) . [[link](#)].
- [59] O. S. Brüning, P. Collier, P. Lebrun, S. Myers, R. Ostojic, J. Poole, and P. Proudlock, *LHC Design Report*. CERN, 2004. [[link](#)].
- [60] L. Evans and P. Bryant, “LHC Machine,” *JINST* **3** (2008) S08001. [[link](#)].



- [61] <http://home.web.cern.ch/about/accelerators/large-electron-positron-collider>.
- [62] <http://lhc-machine-outreach.web.cern.ch/lhc-machine-outreach/>.
- [63] R. Bailey and P. Collier, “Standard Filling Schemes for Various LHC Operation Modes,” *LHC Project Note* **LHC-PROJECT-NOTE-323** (2003) . [link].
- [64] G. Arduini, W. Herr, E. Métral, and T. Pieloni, “Alternative bunch filling schemes for the LHC,” *LHC Project Note* **CERN-LHC-Project-note-401** (2007) . [link].
- [65] *The LHC Injection Sequencer*, vol. LHC-PROJECT-NOTE-323. 2014. [link].
- [66] <https://twiki.cern.ch/twiki/bin/view/CMSPublic/LumiPublicResults>.
- [67] <http://www.lhc-closer.es/1/3/9/0>.
- [68] <http://cms.web.cern.ch/>.
- [69] CMS Collaboration, *CMS Physics: Technical Design Report Volume 1: Detector Performance and Software*. CERN, 2006. [link].
- [70] CMS Collaboration, “CMS Physics Technical Design Report, Volume II: Physics Performance,” *J. Phys. G: Nucl. Part. Phys.* **34** (2007) 995. [link].
- [71] CMS Collaboration, “The CMS experiment at the CERN LHC,” *JINST* **3** (2008) S08004. [link].
- [72] D. Green, ed., *At the Leading Edge: The ATLAS and CMS LHC Experiments*. World Scientific Publishing Co. Pte. Ltd., 2010.

- [73] CMS Collaboration, *CMS Technical Design Report for the Level-1 Trigger Upgrade*. No. CERN-LHCC-2013-011. CMS-TDR-12. CERN, 2013. [link].
- [74] CMS Collaboration, “The CMS high level trigger,” *Eur. Phys. J. C* **46** (2006) 605 – 667. [link].
- [75] <https://twiki.cern.ch/twiki/bin/view/CMS/GlobalTriggerAvailableMenus>.
- [76] <http://j2eeps.cern.ch/cms-project-confdb-hltdev/browser/>.
- [77] <https://twiki.cern.ch/twiki/bin/view/CMS/TriggerStudies>.
- [78] T. Sjöstrand, S. Mrenna, and P. Skands, “PYTHIA 6.4 Physics and manual,” *JHEP* **2006** (2006) no. 05, 026. [link].
- [79] J. Alwall, M. Herquet, F. Maltoni, O. Mattelaer, and T. Stelzer, “MadGraph 5: going beyond,” *JHEP* **2011** (2011) 1 – 40. [link].
- [80] R. Brun, “GEANT - Detector Description and Simulation Tool,” *CERN Program Library Long Writeup W5013* (1993) . [link].
- [81] <http://wlcg.web.cern.ch/>.
- [82] <http://ultralight.caltech.edu/web-site/igrid/html/>.
- [83] A. K. Nayak, “Reconstruction of physics objects in the CMS detector,” *CMS Note CMS-CR-2013-019* (2013) . [link].
- [84] CMS Collaboration, “Particle-Flow Event Reconstruction in CMS and Performance for Jets, Taus, and MET,” *CMS Physics Analysis Summary CMS-PFT-09-001* (2009) . [link].
- [85] W. Erdmann, “Vertex reconstruction at the CMS experiment,” *J. Phys.: Conf. Ser.* **110** (2008) 092009. [link].

- [86] T. Speer and K. Prokofiev, “Vertex Fitting with the Kalman Filter Formalism in the ORCA Reconstruction Program,” *CMS Internal Note CMS-IN-2003-008* (2003) . [[link](#)].
- [87] G. Abbiendi, N. Adam, J. Alcaraz, N. Amapane, E. Antillon, R. Bellan, I. Belotelov, I. Bloch, C. Campagnari, T. Cox, A. Everett, A. Grelli, J. Goh, V. Halyo, A. Hunt, E. James, P. Kalavase, S. Kao, M. Konecki, D. Kovalskyi, V. Krutelyov, C. Liu, D. Miller, M. Mulders, N. Neumeister, D. Pagano, J. Pivarski, J. Ribnik, S. Stoynev, P. Traczyk, D. Trocino, J. Vlimant, and R. Wilkinson, “Muon Reconstruction in the CMS Detector,” *CMS Analysis Note CMS AN 2008/097* (2009) . [[link](#)].
- [88] CMS Collaboration, “The performance of the CMS muon detector in proton-proton collisions at  $\sqrt{s} = 7$  TeV at the LHC,” *JINST* **8** (2013) P11002. [[link](#)].
- [89] A. Everett and CMS Collaboration, “Muon reconstruction and identification in CMS,” *AIP Conference Proceedings* **1200** (2010) 701–704. [[link](#)].
- [90] I. Shipsey, N. Leonardo, M. Solmaz, M. D. Mattia, Z. Hu, and I. Tomalin, “Studies of Stand-Alone Muon Reconstruction for Displaced Muons,” *CMS Analysis Note CMS-AN-2011/487* (2011) . [[link](#)].
- [91] C. Liu and N. Neumeister, “Reconstruction of Cosmic and Beam-Halo Muons,” *CMS Note CMS NOTE-2008/001* (2008) . [[link](#)].
- [92] <https://twiki.cern.ch/twiki/bin/view/CMSPublic/SWGuideMuonId>.
- [93] CMS Collaboration, “Electron Reconstruction and Identification at  $\sqrt{s} = 7$  TeV,” *CMS Detector Performance Summaries CMS-DP-2010-032* (2010) . [[link](#)].

- [94] <https://twiki.cern.ch/twiki/bin/view/CMSPublic/SWGuideEgamma>.
- [95] W. Adam, R. Frühwirth, A. Strandlie, and T. Todor, “Reconstruction of Electrons with the Gaussian-Sum Filter in the CMS Tracker at the LHC,” *CMS Note CMS-NOTE-2005-001* (2005) . [link].
- [96] <https://twiki.cern.ch/twiki/bin/view/Main/%20EGammaScaleFactors2012>.
- [97] M. Cacciari, G. P. Salam, and G. Soyez, “The anti- $k_t$  jet clustering algorithm,” *JHEP* **2008** (2008) 063. [link].
- [98] CMS Collaboration, “Algorithms for b Jet Identification in CMS,” *CMS Physics Analysis Summary CMS BTV-09-001* (2009) . [link].
- [99] CMS Collaboration, “Performance of tau-lepton reconstruction and identification in CMS,” *JINST* **7** (2012) P01001. [link].
- [100] CMS Collaboration, “Missing transverse energy performance of the CMS detector,” *JINST* **6** (2011) P09001. [link].
- [101] M. Fairbairn, A. Kraan, D. Milstead, T. Sjöstrand, P. Skands, and T. Sloan, “Stable massive particles at colliders,” *Phys. Rept.* **438** (2007) 1–63. [link].
- [102] Z. Liu and B. Tweedie, “The Fate of Long-Lived Superparticles with Hadronic Decays after LHC Run 1,” *JHEP* **2015** (2015) 42. [doi].
- [103] K. Kohri and T. Takahashi, “Cosmology with long-lived charged massive particles,” *Phys. Lett. B* **682** (2010) 337–341. [link].
- [104] M. Byrne, C. Kolda, and P. Regan, “Bounds on charged, stable superpartners from cosmic ray production,” *Phys. Rev. D* **66** (2002) 075007. [link].

- [105] P. Smith, J. Bennett, G. Homer, J. Lewin, H. Walford, and W. Smith, “A search for anomalous hydrogen in enriched D<sub>2</sub>O, using a time-of-flight spectrometer,” *Nucl. Phys. B* **206** (1982) no. 3, 333 – 348. [[link](#)].
- [106] P. Dirac, “Quantised Singularities in the Electromagnetic Field,” *Proc. R. Soc. London* **133** (1931) 60. [[link](#)].
- [107] P. A. M. Dirac, “The Theory of Magnetic Poles,” *Phys. Rev.* **74** (1948) 817–830. [[link](#)].
- [108] M. Carena, D. Choudhury, R. A. Diaz, H. E. Logan, and C. E. M. Wagner, “Top-squark searches at the Fermilab Tevatron in models of low-energy supersymmetry breaking,” *Phys. Rev. D* **66** (2002) 115010. [[link](#)].
- [109] G. Giudice and R. Rattazzi, “Theories with gauge mediated supersymmetry breaking,” *Phys. Rept.* **322** (1999) 419 – 499. [[link](#)].
- [110] M. Dine and A. E. Nelson, “Dynamical supersymmetry breaking at low energies,” *Phys. Rev. D* **48** (1993) 1277–1287. [[link](#)].
- [111] M. Dine, A. E. Nelson, Y. Nir, and Y. Shirman, “New tools for low energy dynamical supersymmetry breaking,” *Phys. Rev. D* **53** (1996) 2658–2669. [[link](#)].
- [112] J. L. Feng and T. Moroi, “Fermilab Tevatron signatures of long-lived charged sleptons in gauge-mediated supersymmetry breaking models,” *Phys. Rev. D* **58** (1998) 035001. [[link](#)].
- [113] J. L. Feng, S. Su, and F. Takayama, “SuperWIMP gravitino dark matter from slepton and sneutrino decays,” *Phys. Rev. D* **70** (2004) 063514. [[link](#)].
- [114] J. L. Feng, S. Su, and F. Takayama, “Supergravity with a gravitino lightest supersymmetric particle,” *Phys. Rev. D* **70** (2004) 075019. [[link](#)].

- [115] C.-H. Chen, M. Drees, and J. F. Gunion, “Nonstandard string-SUSY scenario and its phenomenological implications,” *Phys. Rev. D* **55** (1997) 330–347. [\[link\]](#).
- [116] G. F. Giudice, R. Rattazzi, M. A. Luty, and H. Murayama, “Gaugino mass without singlets,” *JHEP* **1998** (1998) 027. [\[link\]](#).
- [117] L. Randall and R. Sundrum, “Out of this world supersymmetry breaking,” *Nucl. Phys. B* **557** (1999) 79 – 118. [\[link\]](#).
- [118] J. F. Gunion and S. Mrenna, “Study of SUSY signatures at the Fermilab Tevatron in models with near mass degeneracy of the lightest chargino and neutralino,” *Phys. Rev. D* **62** (2000) 015002. [\[link\]](#).
- [119] J. L. Feng and T. Moroi, “Supernatural supersymmetry: Phenomenological implications of anomaly-mediated supersymmetry breaking,” *Phys. Rev. D* **61** (2000) 095004. [\[link\]](#).
- [120] G. Giudice and A. Romanino, “Split supersymmetry,” *Nucl. Phys. B* **699** (2004) 65. [\[link\]](#).
- [121] N. Arkani-Hamed and S. Dimopoulos, “Supersymmetric unification without low energy supersymmetry and signatures for fine-tuning at the LHC,” *JHEP* **2005** (2005) 073. [\[link\]](#).
- [122] R. Barbier, C. Berat, M. Besancon, M. Chemtob, A. Deandrea, E. Dudas, P. Fayet, S. Lavignac, G. Moreau, E. Perez, and Y. Sirois, “R-Parity-violating supersymmetry,” *Phys. Rept.* **420** (2005) 1 – 195. [\[link\]](#).
- [123] P. W. Graham, D. E. Kaplan, S. Rajendran, and P. Saraswat, “Displaced Supersymmetry,” *JHEP* **149** (2012) 1 – 32. [\[link\]](#).

- [124] P. Langacker and G. Steigman, “Requiem for a fractionally charged, massive particle,” *Phys. Rev. D* **84** (2011) 065040. [[link](#)].
- [125] C. S. Aulakh, K. Benakli, and G. Senjanovic, “Reconciling High-Scale Left-Right Symmetry with Supersymmetry,” *Phys. Rev. Lett.* **79** (1997) 2188–2191. [[link](#)].
- [126] CDF Collaboration, “Search for Doubly Charged Higgs Bosons Decaying to Dileptons in  $p\bar{p}$  Collisions at  $\sqrt{s} = 1.96$  TeV,” *Phys. Rev. Lett.* **93** (2004) 221802. [[link](#)].
- [127] CDF Collaboration, “Search for Long-Lived Doubly Charged Higgs Bosons in  $p\bar{p}$  Collisions at  $\sqrt{s} = 7$  TeV,” *Phys. Rev. Lett.* **95** (2005) 071801. [[link](#)].
- [128] A. Maiezza, M. Nemevsek, and F. Nesti, “Lepton Number Violation in Higgs Decay,” *Phys. Rev. Lett* **115** (2015) 081802. [[doi](#)].
- [129] M. J. Strassler and K. M. Zurek, “Discovering the Higgs through highly-displaced vertices,” *Phys. Lett. B* **661** (2008) 263 – 267. [[link](#)].
- [130] A. Falkowski, J. Ruderman, T. Volansky, and J. Zupan, “Hidden Higgs decaying to lepton jets,” *JHEP* **05** (2010) 077. [[link](#)].
- [131] A. Falkowski, J. Ruderman, T. Volansky, and J. Zupan, “Discovering Higgs Boson Decays to Lepton Jets at Hadron Colliders,” *Phys. Rev. Lett.* **105** (2010) 241801. [[link](#)].
- [132] S. Jung and H.-S. Lee, “Untracked Signals of Supersymmetry at the LHC,” *arXiv e-print* **1503.00414** (2015) . [[link](#)].
- [133] K. Hamaguchi, Y. Kuno, T. Nakaya, and M. M. Nojiri, “Study of late decaying charged particles at future colliders,” *Phys. Rev. D* **70** (2004) 115007. [[link](#)].

- [134] G. D. Kribs, A. Martin, and T. S. Roy, “Supersymmetry with a chargino NLSP and gravitino LSP,” *JHEP* **01** (2009) 023. [[link](#)].
- [135] A. Freitas, F. D. Steffen, N. Tajuddin, and D. Wyler, “Axinos in Cosmology and at Colliders,” *JHEP* **1106** (2011) 036.
- [136] D. Griffiths, *Introduction to Electrodynamics*. Prentice Hall, 1999. [[link](#)].
- [137] G. Hooft, “Magnetic monopoles in unified gauge theories,” *Nucl. Phys. B* **79** (1974) 276 – 284. [[link](#)].
- [138] A. Polyakov, “Particle spectrum in quantum field theory,” *JETP Lett.* **20** (1974) 194. [[link](#)].
- [139] E. Huguet and P. Peter, “Bound states in monopoles: sources for UHECR?,” *Astropart. Phys.* **12** (2000) 277 – 289. [[link](#)].
- [140] S. D. Wick, T. W. Kephart, T. J. Weiler, and P. L. Biermann, “Signatures for a cosmic flux of magnetic monopoles,” *Astropart. Phys.* **18** (2003) 663 – 687. [[link](#)].
- [141] Y. Cho and D. Maison, “Monopole configuration in Weinberg-Salam model,” *Phys. Lett. B* **391** (1997) 360 – 365. [[link](#)].
- [142] Y. Yang, “Dually charged particle-like solutions in the Weinberg-Salam theory,” *Proc. R. Soc. Lond. A* **454** (1998) 155 – 178. [[link](#)].
- [143] Y. Yang, *Solitons in Field Theory and Nonlinear Analysis*. Springer, 2001.
- [144] W. S. Bae and Y. M. Cho, “Finite Energy Electroweak Dyon,” *arXiv e-print hep-th/0210299* (2002) . [[link](#)].
- [145] S. P. Ahlen, “Stopping-power formula for magnetic monopoles,” *Phys. Rev. D* **17** (1978) 229 – 233. [[link](#)].



- [146] S. P. Ahlen and K. Kinoshita, “Calculation of the stopping power of very-low-velocity magnetic monopoles,” *Phys. Rev. D* **26** (1982) 2347 – 2363. [\[link\]](#).
- [147] S. Ahlen, “Monopole Energy Loss and Detector Excitation Mechanisms,” in *Magnetic Monopoles*, J. Carrigan, Richard A. and W. Trower, eds., vol. 102 of *NATO Advanced Science Institutes Series*, pp. 259–290. Springer US, 1983. [\[link\]](#).
- [148] R. Mackeprang and A. Rizzi, “Interactions of coloured heavy stable particles in matter,” *Eur. Phys. J. C* **50** (2007) 353–362. [\[link\]](#).
- [149] R. Mackeprang and D. Milstead, “An updated description of heavy-hadron interactions in Geant-4,” *Eur. Phys. J. C* **66** (2010) 493–501. [\[link\]](#).
- [150] J. Alimena, S. Banerjee, S. Cho, D. Cutts, M. Eads, and Y. Xie, “A study of time-of-flight for the charged massive long-lived particle search,” *D0Note* **6141** (2011) . [\[link\]](#).
- [151] CMS Collaboration, “Searches for long-lived charged particles in pp collisions at  $\sqrt{s} = 7$  and 8 TeV,” *JHEP* **07** (2013) 122. [\[link\]](#).
- [152] P. Meade, M. Papucci, and T. Volansky, “Odd Tracks at Hadron Colliders,” *Phys. Rev. Lett.* **109** (2012) 031801. [\[link\]](#).
- [153] P. Fayet, “Spontaneously broken supersymmetric theories of weak, electromagnetic and strong interactions,” *Phys. Lett. B* **69** (1977) 489 – 494. [\[doi\]](#).
- [154] P. Fayet, “Massive gluinos,” *Phys. Lett. B* **78** (1978) 417 – 420. [\[doi\]](#).

- [155] G. R. Farrar and P. Fayet, “Phenomenology of the production, decay, and detection of new hadronic states associated with supersymmetry,” *Phys. Lett. B* **76** (1978) 575 – 579. [[link](#)].
- [156] A. Arvanitaki, S. Dimopoulos, A. Pierce, S. Rajendran, and J. Wacker, “Stopping gluinos,” *Phys. Rev. D* **76** (2007) 055007. [[link](#)].
- [157] P. W. Graham, K. Howe, S. Rajendran, and D. Stolarski, “New measurements with stopped particles at the LHC,” *Phys. Rev. D* **86** (2012) 034020. [[link](#)].
- [158] T.P.Wangler and K.R.Crandall, “Beam Halo in Proton Linac Beams,” *Proceedings of International Linac Conference* (2000) . [[link](#)].
- [159] H1 Collaboration, “A direct search for stable magnetic monopoles produced in positron-proton collisions at HERA,” *Eur. Phys. J. C* **41** (2005) 133 – 141. [[link](#)].
- [160] *Search for long-lived particles with the ATLAS detector*, vol. arXiv:1408.6360. 2014. [[link](#)].
- [161] *Thinking outside the beamspot: Other SUSY searches at the LHC (long-lived particles and R-parity violation)*. 2015. [[link](#)].
- [162] ALEPH Collaboration, “Search for pair-production of long-lived heavy charged particles in  $e^+e^-$  annihilation,” *Phys. Lett. B* **405** (1997) 379–388. [[link](#)].
- [163] DELPHI Collaboration, “Search for heavy stable and long-lived particles in  $e^+e^-$  collisions at  $\sqrt{s} = 189$  GeV,” *Phys. Lett. B* **478** (2000) 65–72. [[link](#)].
- [164] L3 Collaboration, “Search for heavy neutral and charged leptons in  $e^+e^-$  annihilation at LEP,” *Phys. Lett. B* **517** (2001) 75–85. [[link](#)].

- [165] OPAL Collaboration, “Search for stable and long-lived massive charged particles in  $e^+e^-$  collisions at  $\sqrt{s} = 130$  to  $209$  GeV,” *Phys. Lett. B* **572** (2003) 8–20. [[link](#)].
- [166] H1 Collaboration, “Measurement of Anti-Deuteron Photoproduction and a Search for Heavy Stable Charged Particles at HERA,” *Eur. Phys. J. C* **36** (2004) 413. [[doi](#)].
- [167] CDF Collaboration, “Search for Long-Lived Charged Massive Particles in  $p\bar{p}$  Collisions at  $\sqrt{s} = 1.8$  TeV,” *Phys. Rev. Lett.* **90** (2003) 131801. [[link](#)].
- [168] CDF Collaboration, “Search for Long-Lived Massive Charged Particles in  $1.96$  TeV  $p\bar{p}$  Collisions,” *Phys. Rev. Lett.* **103** (2009) 021802. [[link](#)].
- [169] D0 Collaboration, “Search for Long-Lived Charged Massive Particles with the D0 Detector,” *Phys. Rev. Lett.* **102** (2009) 161802. [[link](#)].
- [170] D0 Collaboration, “Search for charged massive long-lived particles,” *Phys. Rev. Lett.* **108** (2012) 121802. [[link](#)].
- [171] D0 Collaboration, “Search for charged massive long-lived particles at  $\sqrt{s} = 1.96$  TeV,” *Phys. Rev. D* **87** (2013) 052011. [[link](#)].
- [172] ATLAS Collaboration, “Search for heavy long-lived charged particles with the ATLAS detector in pp collisions at  $\sqrt{s} = 7$  TeV,” *Phys. Lett. B* **703** (2011) 428–446. [[link](#)].
- [173] ATLAS Collaboration, “Search for stable hadronising squarks and gluinos with the ATLAS experiment at the LHC,” *Phys. Lett. B* **701** (2011) 1–19. [[link](#)].
- [174] ATLAS Collaboration, “Search for massive long-lived highly ionising particles with the ATLAS detector at the LHC,” *Phys. Lett. B* **698** (2011) 353–370. [[link](#)].

- [175] ATLAS Collaboration, “Searches for heavy long-lived sleptons and  $R$ -hadrons with the ATLAS detector in pp collisions at  $\sqrt{s} = 7$  TeV,” *Phys. Lett. B* **720** (2013) 277 – 308. [[link](#)].
- [176] ATLAS Collaboration, “Search for long-lived, multi-charged particles in pp collisions at  $\sqrt{s} = 7$  TeV using the ATLAS detector,” *Phys. Lett. B* **722** (2013) 305 – 323. [[link](#)].
- [177] ATLAS Collaboration, “Search for heavy long-lived multi-charged particles in pp collisions at  $\sqrt{s} = 8$  TeV using the ATLAS detector,” *Eur. Phys. J. C* **75** (2015) 362. [[doi](#)].
- [178] ATLAS Collaboration, “Search for metastable heavy charged particles with large ionisation energy loss in pp collisions at  $\sqrt{s} = 8$  TeV using the ATLAS experiment,” *Eur. Phys. J. C* **75** (2015) 407. [[doi](#)].
- [179] CMS Collaboration, “Search for heavy stable charged particles in pp collisions at  $\sqrt{s} = 7$  TeV,” *JHEP* **2011** (2011) no. 3, 24. [[link](#)].
- [180] CMS Collaboration, “Search for fractionally charged particles in pp collisions at  $\sqrt{s} = 7$  TeV,” *Phys. Rev. D* **87** (2013) 092008. [[link](#)].
- [181] CMS Collaboration, “Search for heavy long-lived charged particles in pp collisions at  $\sqrt{s} = 7$  TeV,” *Phys. Lett. B* **713** (2012) 408–433. [[link](#)].
- [182] LHCb Collaboration, “Search for long-lived heavy charged particles using a ring imaging Cherenkov technique at LHCb,” *arXiv e-print* **arXiv:1506.09173** (2015) . [[link](#)].
- [183] CMS Collaboration, “Constraints on the pMSSM, AMSB model and on other models from the search for long-lived charged particles in proton-proton collisions at  $\sqrt{s} = 8$  TeV,” *Eur. Phys. J. C* **75** (2015) 325. [[doi](#)].

- [184] J. L. Feng, S. Iwamoto, Y. Shadmi, and S. Tarem, “Long-Lived Sleptons at the LHC and a 100 TeV Proton Collider,” *arXiv e-print* **arXiv:1505.02996** (2015) . [[link](#)].
- [185] T. B. Collaboration, “Search for Long-Lived Particles in  $e^+e^-$  Collisions,” *Phys. Rev. Lett.* **114** (2015) 171801. [[doi](#)].
- [186] D0 Collaboration, “Search for Neutral, Long-Lived Particles Decaying into Two Muons in  $p\bar{p}$  Collisions at  $\sqrt{s} = 1.96$  TeV,” *Phys. Rev. Lett.* **97** (2006) 161802. [[link](#)].
- [187] D0 Collaboration, “Search for Long-Lived Particles Decaying into Electron or Photon Pairs with the D0 Detector,” *Phys. Rev. Lett.* **101** (2008) 111802. [[link](#)].
- [188] ATLAS Collaboration, “Search for long-lived, weakly interacting particles that decay to displaced hadronic jets in proton-proton collisions at  $\sqrt{s} = 8$  TeV with the ATLAS detector,” *Phys. Rev. D* **92** (2015) 012010. [[doi](#)].
- [189] ATLAS Collaboration, “Search for pair-produced long-lived neutral particles decaying in the ATLAS hadronic calorimeter in  $pp$  collisions at  $\sqrt{s} = 8$  TeV,” *PLB* **743** (2015) 15–34. [[link](#)].
- [190] ATLAS Collaboration, “Search for displaced vertices arising from decays of new heavy particles in 7 TeV  $pp$  collisions at ATLAS,” *Phys. Lett. B* **707** (2012) 478. [[link](#)].
- [191] ATLAS Collaboration, “Search for a Light Higgs Boson Decaying to Long-Lived Weakly Interacting Particles in Proton-Proton Collisions at  $\sqrt{s} = 7$  TeV with the ATLAS Detector,” *Phys. Rev. Lett.* **108** (2012) 251801. [[link](#)].

- [192] ATLAS Collaboration, “Search for long-lived, heavy particles in final states with a muon and a multi-track displaced vertex in proton-proton collisions at  $\sqrt{s} = 8$  TeV with the ATLAS detector,” *ATLAS Conference Note* **ATLAS-CONF-2013-092** (2013) . [link].
- [193] ATLAS Collaboration, “Search for massive, long-lived particles using multitrack displaced vertices or displaced lepton pairs in pp collisions at 8TeV with the ATLAS detector,” *arXiv e-print* **arXiv:1504.05162** (2015) . [link]. submitted to Phys. Rev. D.
- [194] CMS Collaboration, “Search in leptonic channels for heavy resonances decaying to long-lived neutral particles,” *JHEP* **2013** (2013) 1. [link].
- [195] CMS Collaboration, “Search for long-lived particles that decay into final states containing two electrons or two muons in proton-proton collisions at  $\sqrt{s} = 8$  TeV,” *Phys. Rev. D* **91** (2015) 052012. [doi].
- [196] I. Shipsey, N. Leonardo, M. Solmaz, M. D. Mattia, and Z. Hu, “Search for long-lived particles decaying to final states that include dimuons reconstructed using the muon chambers only,” *CMS Analysis Note* **CMS-EXO-14-012** (2014) . [link].
- [197] CDF Collaboration, “Search for heavy metastable particles decaying to jet pairs in  $p\bar{p}$  collisions at  $\sqrt{s} = 1.96$  TeV,” *Phys. Rev. D* **85** (2012) 012007. [link].
- [198] D0 Collaboration, “Search for Resonant Pair Production of Neutral Long-Lived Particles Decaying to  $b\bar{b}$  in  $p\bar{p}$  Collisions at  $\sqrt{s} = 1.96$  TeV,” *Phys. Rev. Lett.* **103** (2009) 071801. [link].
- [199] LHCb Collaboration, “Search for long-lived particles decaying to jet pairs,” *Eur. Phys. J. C* **75** (2015) 152. [doi].

- [200] CMS Collaboration, “Search for long-lived neutral particles decaying to quark-antiquark pairs in proton-proton collisions at  $\sqrt{s} = 8$  TeV,” *Phys. Rev. D* **91** (2015) 012007. [[doi](#)].
- [201] ATLAS Collaboration, “Search for long-lived neutral particles decaying into lepton jets in proton-proton collisions at  $\sqrt{s} = 8$  TeV with the ATLAS detector,” *JHEP* **2014** (2014) 88. [[doi](#)].
- [202] CDF Collaboration, “Search for Supersymmetry with Gauge-Mediated Breaking in Diphoton Events with Missing Transverse Energy at CDF II,” *Phys. Rev. Lett.* **104** (2010) 011801. [[link](#)].
- [203] CMS Collaboration, “Search for new physics with long-lived particles decaying to photons and missing energy in pp collisions at  $\sqrt{s} = 7$  TeV,” *JHEP* **2012** (2012) 172. [[doi](#)].
- [204] CMS Collaboration, “Search for long-lived particles in events with photons and missing energy in proton-proton collisions at  $\sqrt{s} = 7$  TeV,” *Phys. Lett. B* **722** (2013) 273 – 294. [[link](#)].
- [205] CMS Collaboration, “Search for long-lived neutral particles decaying to photons with missing energy in proton-proton collision at  $\sqrt{s} = 8$  TeV,”.
- [206] CMS Collaboration, “Search for displaced photons using conversions at 8 TeV,”.
- [207] CMS Collaboration, “Search for "Displaced Supersymmetry" in events with an electron and a muon with large impact parameters,” *Phys. Rev. Lett.* **114** (2015) 061801. [[doi](#)].

- [208] ATLAS Collaboration, “Search for anomaly-mediated supersymmetry breaking with the ATLAS detector based on a disappearing-track signature in pp collisions at  $\sqrt{s} = 7$  TeV,” *Eur. Phys. J. C* **72** (2012) 1 – 20. [[link](#)].
- [209] ATLAS Collaboration, “Search for charginos nearly mass degenerate with the lightest neutralino based on a disappearing-track signature in pp collisions at  $\sqrt{s} = 8$  TeV with the ATLAS detector,” *Phys. Rev. D* **88** (2013) 112006. [[link](#)].
- [210] CMS Collaboration, “Search for disappearing tracks in proton-proton collisions at  $\sqrt{s} = 8$  TeV,” *JHEP* **2015** (2015) 96. [[doi](#)].
- [211] D0 Collaboration, “Search for Stopped Gluinos from  $p\bar{p}$  Collisions at  $\sqrt{s} = 1.96$  TeV,” *Phys. Rev. Lett.* **99** (2007) 131801. [[link](#)].
- [212] G. Farrar, R. Mackeprang, D. Milstead, and J. Roberts, “Limit on the mass of a long-lived or stable gluino,” *JHEP* **2011** (2011) 1–17. [[link](#)].
- [213] ATLAS Collaboration, “Search for long-lived stopped  $R$ -hadrons decaying out-of-time with pp collisions using the ATLAS detector,” *Phys. Rev. D* **88** (2013) 112003. [[link](#)].
- [214] ATLAS Collaboration, “Search for decays of stopped, long-lived particles from 7 TeV pp collisions with the ATLAS detector,” *Eur. Phys. J. C* **72** (2012) 1–21. [[link](#)].
- [215] CMS Collaboration, “Search for Stopped Gluinos in pp Collisions at  $\sqrt{s} = 7$  TeV,” *Phys. Rev. Lett.* **106** (2011) 011801. [[link](#)].
- [216] CMS Collaboration, “Search for decays of stopped long-lived particles produced in proton-proton collisions at  $\sqrt{s} = 8$  TeV,” *Eur. Phys. J. C* **75** (2015) 1. [[doi](#)].



- [217] J. Pinfold, R. Du, K. Kinoshita, B. Lorazo, B. Price, and M. Regimbald, “A search for highly ionizing particles produced at the OPAL intersection point at LEP,” *Phys. Lett. B* **316** (1993) 407 – 411. [[link](#)].
- [218] CDF Collaboration, “Direct Search for Dirac Magnetic Monopoles in  $p\bar{p}$  Collisions at  $\sqrt{s} = 1.96$  TeV,” *Phys. Rev. Lett.* **96** (2006) 201801. [[link](#)].
- [219] G. R. Kalbfleisch, K. A. Milton, M. G. Strauss, L. Gamberg, E. H. Smith, and W. Luo, “Improved Experimental Limits on the Production of Magnetic Monopoles,” *Phys. Rev. Lett.* **85** (2000) 5292 – 5295. [[link](#)].
- [220] G. R. Kalbfleisch, W. Luo, K. A. Milton, E. H. Smith, and M. G. Strauss, “Limits on production of magnetic monopoles utilizing samples from the D0 and CDF detectors at the Fermilab Tevatron,” *Phys. Rev. D* **69** (2004) 052002. [[link](#)].
- [221] C. Cowden, S. Wilbur, N. Akchurin, S. W. Lee, M. Mulhearn, and S. Worm, “Search for Dirac Magnetic Monopoles in pp Collisions at  $\sqrt{s} = 8$  TeV,” *CMS Physics Analysis Summary* **EXO-12-005** (2014) .
- [222] ATLAS Collaboration, “Search for magnetic monopoles and stable particles with high electric charges in 8 TeV pp collisions with the ATLAS detector,” *arXiv e-print* **1509.08059** (2015) . [[link](#)].
- [223] L. Patrizzii and M. Spurio, “Status of Searches for Magnetic Monopoles,” *Annu Rev Nucl Part S* **65** (2015) 279 – 302. [[doi](#)].
- [224] <https://twiki.cern.ch/twiki/bin/viewauth/CMS/DelayedSingleMuons>.
- [225] <https://cmswbm.web.cern.ch/cmswbm/>.

- [226] C.S.Hill and M.Rodenburg, “Search for stopped long-lived particles produced in pp collisions at  $\sqrt{s} = 8$  TeV,” *CMS Analysis Note* **CMS AN 2013/398** (2014) . [[link](#)].
- [227] T. Sjöstrand, S. Mrenna, and P. Skands, “A brief introduction to PYTHIA 8.1,” *Comput. Phys. Communc.* **178** (2008) no. 05, 852 – 867. [[doi](#)].
- [228] GEANT4 collaboration, “Geant4: A simulation toolkit,” *Nucl. Instrum. Methods A* **506** (2003) 250 – 303. [[doi](#)].
- [229] GEANT4 collaboration, “Geant4 developments and applications,” *IEEE Trans. Nucl. Sci.* **53** (2006) 270 – 278. [[doi](#)].
- [230] B. Allanach, M. Battaglia, G. Blair, M. Carena, A. De Roeck, A. Dedes, A. Djouadi, D. Gerdes, N. Ghodbane, J. Gunion, H. Haber, T. Han, S. Heinemeyer, J. Hewett, I. Hinchliffe, J. Kalinowski, H. Logan, S. Martin, H.-U. Martyn, K. Matchev, S. Moretti, F. Moortgat, G. Moortgat-Pick, S. Mrenna, U. Nauenberg, Y. Okada, K. Olive, W. Porod, M. Schmitt, S. Su, C. Wagner, G. Weiglein, J. Wells, G. Wilson, and P. Zerwas, “The Snowmass Points and Slopes: benchmarks for SUSY searches,” *Eur. Phys. J. C* **25** (2002) 113 – 123. [[link](#)].
- [231] H. Baer, F. E. Paige, S. D. Protopescu, and X. Tata, “ISAJET 7.69: A Monte Carlo event generator for pp,  $p\bar{p}$ , and  $e^+e^-$  reactions,” *arXiv e-print* **hep-ph/0312045** (2003) . [[link](#)].
- [232] L. Quertenmont, T. Adams, G. Bruno, A. Meneguzzo, C. Nuttens, J. Chen, V. Veeraraghavan, K. Rybinska, M. Kazana, P. Zalewski, C. Carrillo, C. Farrell, J. Hauser, J. Turkewitz, and Y. Kubota, “Search for Heavy Stables Charged Particles with the CMS detector,” *CMS Analysis Note* **CMS AN 2012/293** (2013) . [[link](#)].

- [233] <http://cmslxr.fnal.gov/source/SimG4Core/CustomPhysics/plugins/RHStopTracer.cc>.
- [234] [http://cmslxr.fnal.gov/source/SimG4Core/CustomPhysics/python/Exotica\\_HSCP\\_SIM\\_cfi.py#0023](http://cmslxr.fnal.gov/source/SimG4Core/CustomPhysics/python/Exotica_HSCP_SIM_cfi.py#0023).
- [235] <https://twiki.cern.ch/twiki/bin/viewauth/CMS/DelayedSingleMuonsAnalysisInstructions>.
- [236] <https://twiki.cern.ch/twiki/bin/viewauth/CMS/DelayedSingleMuonsAdditionalAnalysisNotes>.
- [237] S. Chauvie, P. Nieminen, and M. G. Pia, “Geant4 Model for the Stopping Power of Low Energy Negatively Charged Hadrons,” *IEEE Trans. Nucl. Sci.* **54** (2007) 578 – 584. [doi].
- [238] [http://cmslxr.fnal.gov/lxr/source/Configuration/Generator/python/UndergroundCosmicMu\\_cfi.py?v=CMSSW\\_7\\_2\\_3](http://cmslxr.fnal.gov/lxr/source/Configuration/Generator/python/UndergroundCosmicMu_cfi.py?v=CMSSW_7_2_3).
- [239] [https://cmssdt.cern.ch/SDT/lxr/source/RecoMuon/MuonSeedGenerator/plugins/CosmicMuonSeedGenerator.cc?v=CMSSW\\_7\\_2\\_0\\_pre6](https://cmssdt.cern.ch/SDT/lxr/source/RecoMuon/MuonSeedGenerator/plugins/CosmicMuonSeedGenerator.cc?v=CMSSW_7_2_0_pre6).
- [240] [https://cmssdt.cern.ch/SDT/lxr/source/RecoMuon/StandAloneTrackFinder/src/StandAloneTrajectoryBuilder.cc?v=CMSSW\\_7\\_2\\_0\\_pre6](https://cmssdt.cern.ch/SDT/lxr/source/RecoMuon/StandAloneTrackFinder/src/StandAloneTrajectoryBuilder.cc?v=CMSSW_7_2_0_pre6).
- [241] CMS Collaboration, “Muon Reconstruction and Identification Improvements for Run-2 and First Results with 2015 Run Data,” *CMS Detector Performance Summaries* **CERN-CMS-DP-2015-015** (2015) 1–15. [link].
- [242] J. Alimena and D. Cutts, “A Study of Displaced Standalone Muon Reconstruction,” *CMS Note* **CMS-AN-2015/035** (2015) . [link].

- [243] [https://cmssdt.cern.ch/SDT/lxr/source/RecoMuon/Configuration/python/RecoMuonPOnly\\_cff.py?v=CMSSW\\_7\\_2\\_0\\_pre6](https://cmssdt.cern.ch/SDT/lxr/source/RecoMuon/Configuration/python/RecoMuonPOnly_cff.py?v=CMSSW_7_2_0_pre6).
- [244] CMS Collaboration, “CMS Luminosity Based on Pixel Cluster Counting - Summer 2013 Update,” *CMS Public Analysis Note* **CMS-PAS-LUM-13-001** (2013) . [[link](#)].
- [245] T. Junk, “Confidence level computation for combining searches with small statistics,” *Nucl. Instrum. Methods A* **434** (1999) 435 – 443. [[doi](#)].
- [246] A. L. Read, “Presentation of search results: the CL s technique,” *J Phys G* **28** (2002) 2693. [[doi](#)].
- [247] R. Cousins and V. Highland, “Incorporating systematic uncertainties into an upper limit,” *Nucl. Instrum. Methods A* **320** (1992) 331. [[doi](#)].
- [248] CMS Collaboration, “TSG Plots for CHEP2015 in Okinawa, Japan, 13-17 April 2015,” *CMS Note* **L1 Trigger DPG Results** (2015) 1–22. [[link](#)].
- [249] J. Alimena, S. Bannerjee, S. Cho, D. Cutts, M. Eads, S. Park, and Y. Xie, “A Search for Charged Massive Long-Lived Particles at D0,” *D0Note* **6156** (2011) . [[link](#)].
- [250] S. Banerjee, T. Bose, D. Cutts, M. Eads, and Y. Xie, “A Search for Charged Massive Stable Particles at D0 RunII,” *D0Note* **5653** (2008) . [[link](#)].
- [251] Y. Xie, *A Search for Charged Massive Long-Lived Particles Using the D0 Detector*. PhD thesis, Brown University, 2009. [[link](#)].
- [252] J. Alimena, S. Banerjee, S. Cho, D. Cutts, M. Eads, S. Park, and Y. Xie, “Combined Results For Charged Massive Long-Lived Particle Search at D0,” *D0Note* **6253** (2011) . [[link](#)].

- [253] M. Eads and D. Hedin, “A Search for Charged Massive Stable Particles at D0,” *D0Note* **4965** (2005) . [link].
- [254] M. Eads, *A Search for Charged Massive Stable Particles at D0*. PhD thesis, Northern Illinois University, 2005. [link].
- [255] S. P. Martin, S. Moretti, J. Qian, and G. W. Wilson, “Direct investigations of supersymmetry: subgroup summary report,” *CERN Conference Note* **CERN-TH-2001-343. DCPT-2001-114. FERMILAB-CONF-2001-371-T. IPPP-2001-57** (2001) . [link].
- [256] J. Alimena, S. Banerjee, S. Cho, D. Cutts, M. Eads, S. Park, and Y. Xie, “Stable Stop Quark Production,” *D0Note* **6075** (2011) . [link].
- [257] <http://pythia6.hepforge.org/examples/main78.f>.
- [258] R. Mackeprang, *Stable Heavy Hadrons in ATLAS*. PhD thesis, University of Copenhagen, 2007. [link].
- [259] P. D. Grannis and M. J. Shochet, “The Tevatron Collider Physics Legacy,” *Annual Review of Nuclear and Particle Science* **63** (2013) no. 1, .  
<http://www.annualreviews.org/doi/pdf/10.1146/annurev-nucl-102212-170621>.
- [260] S. Holmes, R. S. Moore, and V. Shiltsev, “Overview of the Tevatron collider complex: goals, operations and performance,” *JINST* **6** (2011) T08001.  
[link].
- [261] D0 Collaboration, “The upgraded D0 detector,” *Nucl. Instrum. Methods A* **565** (2006) 463–537. [link].
- [262] J. Alimena, S. Banerjee, S. Cho, D. Cutts, M. Eads, S. Park, and Y. Xie, “p20 SingleMuonOR Trigger Study for the Charged Massive Long-lived Particle Search,” *D0Note* **6069** (2010) . [link].

- [263] J. Alimena, S. Banerjee, S. Cho, D. Cutts, M. Eads, M. Klein, E. Teich, and Y. Xie, “A study of  $dE/dx$  for the charged massive long-lived particle search,” *D0Note* **6033** (2011) . [[link](#)].
- [264] O. Brandt, S. Cho, M. Cooke, M. Eads, D. Hedin, A. Santos, B. Tuchming, Y. Yatsunenko, and S. Youn, “Muon Identification Certification for the Summer 2009 Extended Dataset (Run IIb-1 and -2),” *D0Note* **6025** (2010) . [[link](#)].
- [265] A. Hoecker, P. Speckmayer, J. Stelzer, J. Therhaag, E. von Toerne, and H. Voss, “TMVA 4: Toolkit for Multivariate Data Analysis with ROOT,” *arXiv e-print physics/0703039* (2009) . [[link](#)].
- [266] W. Fisher, “Collie: A Confidence Level Limit Evaluator,” *D0Note* **5595** (2010) . [[link](#)].
- [267] D0 Collaboration, “The D0 experiment’s integrated luminosity for Tevatron Run IIa,” *Fermilab Preprint* **FERMILAB-TM-2365** (2007) . [[link](#)].